
THE UNIVERSITY *of* EDINBURGH

# Experimental study of tidal turbines loading and performance in oblique waves and currents

*Rodrigo Andres Martinez Mejia*


THE UNIVERSITY *of* EDINBURGH

A thesis submitted for the degree of

**Doctor of Philosophy**

of

**The University of Edinburgh**.

Institute for Energy Systems

School of Engineering

September 2, 2020

To Angie & Evie Mae Martinez

# Abstract

Tidal energy exploitation is at an early development stage. World wide, installed capacity for tidal energy is 18 MW. In Europe only, installed capacity for wind is 168 GW. Levelised Cost of Energy (LCOE) projections for tidal energy are estimated at 328 £/MWh by 2025. In contrast, LCOE for onshore and offshore wind are 60 £/MWh and 100 £/MWh, respectively. These costs need to be reduced to improve the long-term economic viability of the sector. High costs of tidal turbines are, in part, the result of load uncertainties caused by the highly variable flows turbines experience. Turbine performance and loading are measured for a 1:15 scale model tested in the FloWave circular, combined wave and current basin at the University of Edinburgh, UK. Three different flow directions were tested. Each of them were also combined with three different regular waves in four different directions. Fifteen physical quantities were measured including flow velocity, wave height, rotational speed and rotor and foundation loads. It was found that wave height or period have no significant impact on the average loading of the turbine. However, waves not-normal to the rotor plane showed a lower influence on the turbine average loading than waves normal to the rotor plane. In addition, the presence of waves increases the load fluctuations in the rotor by almost a factor of three. Rotor loading relative to the rotor's angular position experience three dips during a single rotation associated to the passage of the blades in front of the support tower. Analysis in the frequency domain to identify key frequencies with potential impact is presented. The frequency of the wave-induced loads can be observed on the rotor load spectra, where the peaks associated with waves have the highest amplitude, followed by the frequency of the blades passing in front of the support tower.

# Acknowledgements

I would like to thank the following people for the involvement, support and encouragement throughout the duration of this research:

- My wife, Angie for her motivation and encouragement. For always being there and putting up with me during stressful times.
- My family: for their unconditional love and support, even from the other side of the world.
- Professor Tom Bruce for his supervision of the project and sharing all his experience.
- Dr Grégory Payne for his supervision and technical guidance with the turbine and tank testing.
- FloWave staff: Tom, Jeff, Donald, Sam and Martin. Without their guidance the experiments wouldn't have been possible.

This research was funded by the scholarship awarded by Consejo Nacional de Ciencia y Tecnología (CONACYT).

# Contents


**1 Introduction** **1**

1.1 Renewable Energy . . . . . 1
1.2 Tidal Energy . . . . . 2
1.3 Tidal Energy Resource in Scotland . . . . . 3
1.4 Examples of horizontal axis tidal turbines . . . . . 4
1.5 Examples of tidal stream energy projects . . . . . 7
1.6 Uncertainties and limitations of full-scale devices . . . . . 9
1.7 Aim and objectives . . . . . 10
1.8 Structure of thesis . . . . . 11

**2 Technical background** **13**

2.1 Scope of technical background . . . . . 13
2.2 Tidal stream energy conversion; the rotor and its environment . . . 13
2.2.1 Flow velocity . . . . . 15
2.2.2 Flow asymmetry . . . . . 16
2.2.3 Turbulence . . . . . 18
2.2.4 Waves . . . . . 20
2.2.5 Wave-current interaction . . . . . 22
2.3 Turbine loading and performance . . . . . 23
2.4 Model, laboratory and scaling effects . . . . . 32
2.5 Fatigue loading . . . . . 35

**3 Literature review** **37**
3.1 Scope of literature review . . . 37
3.2 Field measurements of tidal stream . . . 37
3.3 Laboratory turbine testing . . . 39
3.3.1 Tests under in-line current-only conditions . . . 41
3.3.2 Tests under yawed current-only conditions . . . 46
3.3.3 Tests under combined wave and current conditions . . . 50
3.4 Field turbine testing . . . 55
3.5 Summary of findings . . . 59

**4 Experimental set-up** **63**
4.1 Experimental facility . . . 63
4.1.1 Basin instrumentation . . . 65
4.2 Turbine model . . . 66
4.2.1 Turbine instrumentation . . . 67
4.3 Data logging . . . 72
4.4 Summary . . . 72

**5 Design of test matrix** **75**
5.1 Testing parameters . . . 75

**6 Flow characterisation** **81**
6.1 Introduction . . . 81
6.2 Methodology . . . 81
6.3 Data quality checking . . . 82
6.3.1 Frequency spectra smoothing . . . 83
6.3.2 Wave gauge data checking . . . 83
6.4 Results . . . 87
6.4.1 Flow velocity . . . 87
6.4.2 Turbulence intensity . . . 90
6.4.3 Frequency analysis . . . 90
6.4.4 Current direction . . . 97
6.5 Discussion . . . 99
6.6 Conclusion . . . 102

**7 Turbine testing** **103**
7.1 Introduction . . . 103
7.2 Methodology . . . 103

7.3 Data quality control . . . 105
7.3.1 Blade root bending moment (RBM) . . . 105
7.3.2 Support structure load cell . . . 106
7.3.3 Thrust transducer . . . 107
7.4 Turbine characterisation under current-only conditions with a range of TSR values . . . 108
7.5 Turbine testing at fixed TSR for all current and wave conditions . . . 111
7.5.1 Turbine performance under waves and current at fixed TSR - influence of wave period . . . 112
7.5.2 Turbine performance under waves and current at fixed tip-speed-ratio - influence of wave angle . . . 114
7.5.3 Rotational speed analysis . . . 116
7.5.4 Timeseries analysis of loading fluctuations due to waves . . . 117
7.5.5 Loading dependency on rotor angular position . . . 118
7.5.6 Loading on support structure . . . 125
7.5.7 Frequency domain analysis . . . 127
7.6 Summary of findings . . . 136

**8 Conclusions** **139**

**References** **143**

**Appendices** **160**

**A RBM calibration tables** **161**

**B Test matrix** **163**

**C Time series - all tests** **165**

**D Author contributions** **185**

# List of Figures


1.1 Level of tidal resources across Europe. Source: Aqua-RET (2012) . 3

1.2 Tidal energy Atlas of Scotland for a) Spring peak flow and b) Neap peak flow. The Pentland Firth is identified by the blue oval on (a). Reproduced from http://www.renewables-atlas.info/ © Crown Copyright. . . . . 5

1.3 Horizontal axis turbines: a) M100 (Nova Innovation, 2017); b) Orbital O2 2MW (Orbital Marine, 2018); c) D10 (Sabella, 2017); d) CoRMaT (Nautricity, 2017); e) PLAT-O (Sustainable Marine Energy Ltd, 2017); f) EvoPod (Oceanflowenergy, 2017); g) AR1500 (Atlantis Resources, 2017); h) AH1000 MK1 (Andritz Hydro Hammerfest, 2017) . . . . . 8

2.1 Flow variables a turbine is typically subjected to in a marine environment. The quantities and abbreviations are described in the main body of the chapter. . . . . 14

2.2 Mean flow velocity depth profiles taken at the west coast of Scotland, UK showing a power law approximation of $1/8^{th}$. Data from Martinez et al. (2019). . . . . 17

2.3 Mean mid-depth flow velocity measurements taken at the west coast of Scotland, UK showing a flow asymmetry of about 15°. Data from Martinez et al. (2019). . . . . 17

2.4 Typical representation of the turbulence energy spectrum. Adapted from Barba (2017). Vertical axis $E(K)$ represents the energy content of the eddies and the horizontal axis $K$ represents the scale of the eddies. . . . . 19

2.5 Classification of the spectrum of ocean waves according to Munk (1950). Vertical axis is relative wave height. Adapted from Munk (1950). . . . . 21

2.6 Actuator disc model of a tidal turbine. Numbers indicate location identifiers. The rotor is assumed to be infinitely thin. Flow goes from left to right. . . . . 24
2.7 Example of a von Karman vortex street showing vortex shedding. Taken from van Dyke (1982) . . . . . 29
2.8 St number for cylinders in steady flow plotted against Re. Solid line is for smooth surfaces and dashed line for rough surfaces. Adapted from Lienhard (1966) . . . . . 30
2.9 Drag coefficient for cylinder. From White (2010) . . . . . 31
2.10 Typical steel S-N curve (top) and Stress-Strain curve (bottom). From SIEMENS (2019) . . . . . 36

3.1 Locations of the flow measurements studies around the British Isles. a) British Isles; b) Orkney, Scotland. Adapted from Nilfanion (2017). 39
3.2 Progression of testing complexity (added variables). . . . . 40
3.3 Typical parameters measured during a turbine model laboratory testing. . . . . 40
3.4 Front view of the rotor identifying the blades, the stanchion and rotational direction. This schematic is used when analysing polar plots. $\phi$ corresponds to the rotor angular position. . . . . 43
3.5 Angle-averaged root bending moment (RBM) of blade 1 (B1) for current-only case with $TI = 3\%$ and $TSR = 6.87$. Expressed as a percentage of the average RBM. Adapted from Payne et al. (2017b) 43
3.6 The left axis is the power spectra of the RBM coefficient of blade 1 (Eq. 3.1), the right axis is the spectral density of the streamwise flow velocity and the horizontal axis is the frequency normalised by the rotor rotational frequency $f_0$. Reproduced from Payne et al. (2018) 44
3.7 Standard deviation of $C_T$ for three $TI$ levels. From Vinod et al. (2017) 46
3.8 Power coefficient ($C_P$) vs tip speed ratio ($TSR$) curves at different yaw angles ($\beta$) with pitch angle of 20°. Adapted from Bahaj et al. (2007b). . . . . 48
3.9 Thrust coefficient ($C_T$) vs tip speed ratio ($TSR$) curves at different yaw angles ($\beta$) with pitch angle of 20°. Adapted from Bahaj et al. (2007b). . . . . 49
3.10 $C_T$ at maximum $C_P$ ($TSR = 4$) for different yaw angles at 0.75 m/s. From Fabre et al. (2015) . . . . . 50
3.11 Turbine mounted on catamaran. From Jeffcoate et al. (2016) . . . . 58

3.12 Turbine mounted on tug boat. a) test rig, b) water level, c) speed log, d) turbine, e) breaking resistor and f) control and data acquisition systems. From Starzmann et al. (2013) . . . . . 58
3.13 Turbine mounted in subsea testing rig. From Xu et al. (2016) . . . . 59

4.1 View of the circular FloWave basin. Yellow overhead crane and gantry for accessibility and the mounting of instrumentation are visible. . . . . 64
4.2 Plan view of the basin showing coordinates, measurements and quadrants for easier reference . . . . . 64
4.3 Plan view showing the exact position of the turbine fixed on the basin's floor relative to the geometric centre of the basin. . . . . 65
4.4 a) Turbine mounted on the basin floor (shown in the floor's raised position, out of the water); b) section view of the turbine with its main components identified and key dimensions. From Payne et al. (2017b). . . . . 67
4.5 Turbine diagram with dimensions and basin's instrumentation location. All dimensions in mm. . . . . 68
4.6 Motor diagram. . . . . 69
4.7 Motor control cabinet designed, built and commissioned by the author. All dimension in mm. . . . . 70
4.8 Slip ring (red circle) mounted in the shaft cage of the turbine. The front of the turbine is on the left-hand side of the image. . . . . 70
4.9 Torque and thrust transducer mounted on the turbine. . . . . 71
4.10 Close up of the blades mounted on the root bending moment transducers mounted to the hub. 1: Hub; 2: RBM flexures; 3: blades; 4: nacelle nose. . . . . 72
4.11 Data acquisition cabinet designed, built and commissioned by the author. All dimension in mm. . . . . 73

5.1 Plan view of the basin indicating current (solid) and wave (dashed) angles selected for testing. Blue circular marker represents the location where the turbine will be positioned. $u$ is the flow component perpendicular to the rotor plane, $v$ is the flow component transversal to the turine axis (drive shaft) and $w$ is the vertical flow component. 77
5.2 Tests name coding key . . . . . 78

6.1 Front view of the rotor plane delimited by the dashed circle. Wave gauges (yellow lines) and flow velocity measurement points (red crosses). Flow components in the stream-wise ($u$), transverse ($v$) and vertical ($w$) directions indicated by the arrows. . . . . 82
6.2 Comparison of streamwise velocity $u$ for spectral analysis in case C1 (top) and C3-W11 (bottom). Logarithmic down-sampling vs *pwelch* function. . . . . 84
6.3 Randomly selected case C1-W11 to show wave gauges data before and after filtering. . . . . 85
6.4 Close-up for the comparison of the wave gauges signal with and without filter. Case C1-W11. . . . . 85
6.5 Wave mean amplitude (dashed lines) and standard deviation (shaded) from to wave gauges for wave case C2-W21 . . . . . 86
6.6 Spatial variation for a wave of Tw=2.2 s at the FloWave basin. From Draycott et al. (2016) . . . . . 87
6.7 Comparison between the prescribed velocity (red dashed line), the velocity component $u$ and the resultant magnitude $U$ using $uv$ and $uvw$ flow components. Each $x$ position corresponds to each of the test cases. Figure for representative purposes only using turbine testing data rather than flow characterisation. All measurements are at hub height ($z = -1$ m). . . . . 88
6.8 Flow velocity $U$ depth profiles. Power law approximation of $1/10^{th}$ also shown. . . . . 89
6.9 Contours of time-averaged, flow velocities, $U$, in rotor plane for: C1 (top), C2 (middle) and C3 (bottom), based upon the nine-point measurements. Values in m/s. . . . . 91
6.10 Plan view of the basin with velocity vectors for a 0.8 m/s current. Vector length is proportional to velocity at measurement point relative to input velocity. Nominal test area shown by grey dashed rectangle; 15 m diameter raiseable floor shown as a grey circle. Red rectangle gives approximate position of the turbine. Adapted from Noble et al. (2015). . . . . 92
6.11 Turbulence intensity ($TI$) depth profiles . . . . . 92
6.12 Contours of time-averaged, turbulence intensity, $TI$ (%), in rotor plane for: C1 (top), C2 (middle) and C3 (bottom), based upon the nine-point measurements. . . . . 93

6.13 Spectral comparison of the flow components for Case C3. The Kolmogorov turbulent decay slope is included for comparison. . . . . 94
6.14 Spectral comparison exploring the effect of yaw angle in $U$ with no waves. . . . . 95
6.15 Spectral comparison of $U$ in flow characterisation and during turbine testing for case C1. . . . . 95
6.16 Spectral comparison of $U$ for current case C3 with wave W1 (Tw=2s) from different directions (0°, 45° and 135°). . . . . 96
6.17 Spectral comparison of $U$ at different depths (z=1.6, 1.3, 1, 0.7 and 0.4m) for case C1-W21 (H=91 mm; Tw=2.5 s). . . . . 96
6.18 Effect of water depth on the wave induced velocity. Case C1-W21. Zoomed in from Figure 6.17. . . . . 97
6.19 Top: current direction variation from the mean (red dashed line) during a one second period. Bottom: Histogram of the measured current angle during the whole duration of a test. Flow measurement at hub height for case C3. . . . . 98
6.20 Current direction $\beta$ at hub height for all test cases with error bars showing standard deviation. Horizontal axis is divided in three sections: 0°, -10° and -20°. Dashed lines indicate target current angle. . 98
6.21 Depth profiles of current incident angles at rotor plane. Each line represents each current angle case seen from the front of the rotor. . 99
6.22 Contours of time-averaged, flow direction, $\beta$, in rotor plane for: C1 (top), C2 (middle) and C3 (bottom), based upon the nine-point measurements. Values in degrees (°) . . . . . 100
6.23 Vectrino probe geometry. The emitter is located in the centre while four (only three shown in diagram) protruding arms represent the receivers. . . . . 101

7.1 Front view of the turbine rotor with relative location of Vectrino (green) and wave gauges (yellow) . . . . . 105
7.2 Time series of $RBM1$, $RBM2$ and $RBM3$. Case C1, no waves. . . . . 106
7.3 Sample for outlier removal in loadcell data for case C1. Overview of the whole time series . . . . . 107
7.4 Sample for outlier removal in loadcell data for case C1. Zoom in of the largest peak showing removal by interpolation from Figure 7.3 . 107
7.5 Extract of thrust signal before and after removing hydrostatic pressure for case C1-W21 . . . . . 108

7.6 Variation of $C_T$ with $TSR$. Error bars indicate $C_T$ standard deviation. Three yaw angles: C1:0°, C2:−10° and C3:−20°. No waves. C1 markers shifted by 0.05 to the left and C3 markers shifted by 0.05 to the right to avoid overlaps and improve visibility. . . . . 109
7.7 Standard deviation of $C_T$ normalised by the average $C_T$. Three yaw angles: C1:0°, C2:−10° and C3:−20°. No waves. C1 markers shifted by 0.05 to the left and C3 markers shifted by 0.05 to the right to avoid overlaps and improve visibility. . . . . 110
7.8 Variation of $C_P$ with $TSR$. Error bars indicate $C_P$ standard deviation. Three yaw angles: C1:0°, C2:−10° and C3:−20°. No waves. C1 markers shifted by 0.05 to the left and C3 markers shifted by 0.05 to the right to avoid overlaps and improve visibility. . . . . 110
7.9 Standard deviation of $C_P$ normalised by the average $C_P$. Three yaw angles: C1:0°, C2:−10° and C3:−20°. No waves. C1 markers shifted by 0.05 to the left and C3 markers shifted by 0.05 to the right to avoid overlaps and improve visibility. . . . . 111
7.10 $C_T$ plots comparing the influence of wave period. Error bars indicate $C_T$ standard deviation. Plots grouped by wave angle: a) 0°, b) 45°, c)135° and d)-45°. $TSR$=7. Three flow angles: C1:0°, C2:−10° and C3:−20°. . . . . 113
7.11 $C_P$ plots comparing the influence of wave period. Error bars indicate $C_P$ standard deviation. Waves at a) 0°, b) 45°, c)135° and d)-45°. $TSR$=7. Three flow angles: C1:0°, C2:−10° and C3:−20°. . 114
7.12 $C_T$ plots comparing the influence of wave angle. Error bars indicate $C_T$ standard deviation. Plots grouped by wave period: a) Tw=2.0 s, b) Tw=2.5 s, c) Tw=3.0 s. $TSR$=7. Three flow angles: C1:0°, C2:−10° and C3:−20°. . . . . 115
7.13 $C_P$ plots comparing the influence of wave angle. Error bars indicate $C_P$ standard deviation. Plots grouped by wave period: a) Tw=2.0 s, b) Tw=2.5 s, c) Tw=3.0 s. $TSR$=7. Three flow angles: C1:0°, C2:−10° and C3:−20°. . . . . 116
7.14 Histogram of rotational speed for case C1. Pink line represents the target rotational speed of 90 RPM. . . . . 117
7.15 Time series of wave gauges (left axis) and thrust T (right axis). Case C3-W12. . . . . 118
7.16 Time series of wave gauges (left axis) and torque $\tau$ (right axis). Case C3-W12. . . . . 119

7.17 Polar plots of rotor loads and rotational speed variations as percentage of the mean values for cases C1, C2 and C3 . . . . . 121
7.18 Polar plots of rotor loads and rotational speed variations (% from mean values) for all waves at 0° with -10° yaw. . . . . 122
7.19 Polar plots of rotor loads and rotational speed variations (% from mean values) for all waves at 0° with 0° yaw. . . . . 123
7.20 Polar plots of rotor loads and rotational speed variations (% from mean values) for waves with Tw=2.5 s, at all angles with -20° yaw. . 124
7.21 Polar plots rotor loads and rotational speed variations (% from mean values) for case C3-W23. . . . . 126
7.22 $\overline{\mathrm{T}}$ and $\overline{\mathrm{Fx}}$ comparison. Top to bottom: Current-only cases at 0°, -10° and -20°. . . . . 127
7.23 Difference between $\overline{\mathrm{Fx}}$ and $\overline{\mathrm{T}}$ from Figure 7.22. . . . . 128
7.24 Spectral density of $C_T$ (left) and $U_0$ (right) against frequency normalised by the rotational frequency of the turbine $f_0$. Case C3-W32. 129
7.25 Spectral density of $C_P$ (left) and $U_0$ (right) against frequency normalised by the rotational frequency of the turbine $f_0$. Case C3-W32. 130
7.26 $S_{C_T}$ with current at -20°, exploring influence of wave angle with wave period Tw=2.0 s. . . . . 131
7.27 Zoom of the peak of the $S_{C_T}$ spectra from Figure 7.26 associated with the waves with period Tw=2.0 s. . . . . 131
7.28 $S_{C_T}$ with current at -10°, exploring influence of wave angle with wave period Tw=2.0 s. . . . . 132
7.29 $S_{C_T}$ spectra with current at 0°, exploring influence of wave angle with wave period Tw=2.0 s. . . . . 132
7.30 $S_{C_P}$ with current at -20°, exploring influence of wave angle with wave period Tw=2.0 s. . . . . 133
7.31 $S_{C_T}$ comparison of waves W1, W2 and W3 at 315° with a current angle of 0° . . . . . 133
7.32 Spectral $C_P$ comparison of cases C1-W11, C2-W22 and C3-W33. . 134
7.33 Comparison between spectral density of the three $C_{RBM}$ against frequency normalised by the rotational frequency of the turbine $f_0$. Case C3-W32. . . . . 135
7.34 Comparison between spectral density of $C_T$ and $C_{RBM}$ and $S_{C_{\Sigma RBM}}$ against frequency normalised by the rotational frequency of the turbine $f_0$. Case C3-W32. . . . . 135

C.1 Thrust signals for all tests at $\beta = 0°$ . . . 166
C.2 Thrust signals for all tests at $\beta = 10°$ . . . 167
C.3 Thrust signals for all tests at $\beta = 20°$ . . . 168
C.4 Torque signals for all tests at $\beta = 0°$ . . . 170
C.5 Torque signals for all tests at $\beta = 10°$ . . . 171
C.6 Torque signals for all tests at $\beta = 20°$ . . . 172
C.7 RBM signals for all tests at $\beta = 0°$ . . . 174
C.8 RBM signals for all tests at $\beta = 10°$ . . . 175
C.9 RBM signals for all tests at $\beta = 20°$ . . . 176
C.10 Load cell signals for all tests at $\beta = 0°$ . . . 178
C.11 Load cell signals for all tests at $\beta = 10°$ . . . 179
C.12 Load cell signals for all tests at $\beta = 20°$ . . . 180
C.13 Wave gauges signals for all tests at $\beta = 0°$ . . . 182
C.14 Wave gauges signals for all tests at $\beta = 10°$ . . . 183
C.15 Wave gauges signals for all tests at $\beta = 20°$ . . . 184

# List of Tables


1.1 HATT developers. . . . . 5
1.2 Leased tidal sites in the UK. . . . . 9

2.1 List of Froude scaling factors *S* for common parameters. . . . . 35

3.1 Summary of flow characteristics from field measurements at potential tidal sites . . . . . 38
3.2 Summary of findings of current-only tidal turbine testing. . . . . 47
3.3 Summary of findings of yawed current-only tidal turbine testing. . . 51
3.4 Summary of findings of combined wave and current turbine testing. 56
3.5 Summary of findings of wave-induced fatigue loads. . . . . 57
3.6 Summary of findings of field tidal turbine testing. . . . . 60

4.1 Turbine design parameters and instrumentation rated values . . . . . 68

5.1 Wave periods and heights selected for testing. . . . . 77
5.2 FloWave tests matrix . . . . . 78
5.3 Tests database after code assignment . . . . . 79

A.1 Calibration table for RBM1. Output columns are at different lever arm lengths. Data provided by manufacturer Applied Measurements Ltd. . . . . 161
A.2 Calibration table for RBM2. Output columns are at different lever arm lengths. Data provided by manufacturer Applied Measurements Ltd. . . . . 161
A.3 Calibration table for RBM3. Output columns are at different lever arm lengths. Data provided by manufacturer Applied Measurements Ltd. . . . . 162

B.1 Test Matrix . . . . . 163

# Nomenclature

| | | |
|---|---|---|
| $\alpha$ | Exponent in power law | $-$ |
| $\beta$ | Flow angle ($\beta = 0^\circ$ for head on to rotor) | $^\circ$ |
| $\mu$ | Dynamic viscosity | $kg/(m \cdot s)$ |
| $\nu$ | Kinematic viscosity | $m^2/s$ |
| $\omega$ | Wave angular frequency | $rad/s$ |
| $\omega_{rotor}$ | Rotor angular velocity | $rad/s$ |
| $\phi$ | Rotor angular position | $^\circ$ |
| $\rho$ | Fluid density | $kg/m^3$ |
| $\sigma$ | Apparent wave angular frequency | $rad/s$ |
| $\overline{\tau}$ | Time-averaged torque | $Nm$ |
| $\tau$ | Time-varying torque | $Nm$ |
| $\theta$ | Wave propagation angle ($\theta = 0^\circ$ for head on to rotor) | $^\circ$ |
| $A_{rotor}$ | Rotor swept area | $m^2$ |
| $A_{tank}$ | Tank cross section area | $m^2$ |
| $A_{tower}$ | Support structure projected area | $m^2$ |
| $C_D$ | Drag coefficient | $-$ |
| $C_P$ | Power coefficient | $-$ |
| $C_T$ | Thrust coefficient | $-$ |

| | | |
|---|---|---|
| $D$ | Rotor diameter | $m$ |
| $d$ | Water depth | $m$ |
| $f$ | Frequency | $Hz$ |
| $f_0$ | Rotor rotational frequency | $Hz$ |
| $F_D$ | Drag force | $N$ |
| Fr | Froude number | – |
| $Fx$ | Load cell load in the $x$ direction | $N$ |
| $Fy$ | Load cell load in the $y$ direction | $N$ |
| $Fz$ | Load cell load in the $z$ direction | $N$ |
| $g$ | Acceleration due to gravity | $m/s^2$ |
| $H$ | Wave height | $m$ |
| $k$ | Wave number | – |
| $L$ | Wavelength | $m$ |
| $l$ | Characteristic length | $m$ |
| $\ell$ | Integral lengthscale | $m$ |
| $Mx$ | Load cell moment around the $x$ axis | $Nm$ |
| $My$ | Load cell moment around the $y$ axis | $Nm$ |
| $Mz$ | Load cell moment around the $z$ axis | $Nm$ |
| $P$ | Power | $W$ |
| $r$ | Rotor radius | $m$ |
| $RBM$ | Root Bending Moment | $Nm$ |
| Re | Reynolds number | – |
| $RPM$ | Rotor speed in revolutions per minute | $RPM$ |
| $S$ | Spectral density of $x$ physical quantity | $x^2Hz^{-2}$ |

| | | |
|---|---|---|
| $SD$ | Standard deviation | – |
| St | Strouhal number | – |
| $\overline{\mathrm{T}}$ | Time-averaged thrust | $N$ |
| T | Time-varying thrust | $N$ |
| t | Time | s |
| $TI$ | Turbulence intensity | % |
| $TSR$ | Tip-speed ratio | – |
| Tw | Wave period | $s$ |
| $\overline{U}$ | Single point, time-averaged flow velocity resultant from $u$, $v$ and $w$ | $m/s$ |
| $U$ | Single point velocity magnitude from $u$, $v$ and $w$ | $m/s$ |
| $\overline{U_0}$ | Rotor-area- and time-averaged flow velocity | $m/s$ |
| $U_0$ | Flow velocity averaged over rotor swept area | $m/s$ |
| $U_d$ | Depth-averaged flow velocity | $m/s$ |
| $U_z$ | Flow velocity as a function of height in the water column | $m/s$ |
| $u$ | Time-varying streamwise flow velocity component (in $x$ direction) | $m/s$ |
| $v$ | Time-varying transverse flow velocity component (in $y$ direction) | $m/s$ |
| $w$ | Time-varying vertical flow velocity component (in $z$ direction) | $m/s$ |
| $z$ | Vertical elevation in the water column | $m$ |
| $z_0$ | Seabed roughness | $m$ |

**Abbreviations**

| | |
|---|---|
| ADV | Acoustic Doppler Velocimetry |
| BEM | Blade Element Momentum |
| CapEx | Capital Expenditure |

| | |
|---|---|
| CFD | Computational Fluid Dynamics |
| CNC | Computer Numerical Control |
| EMEC | European Marine Energy Centre |
| EnFAIT | Enabling Future Arrays in Tidal |
| EPSRC | Engineering and Physical Sciences Research Council |
| FDEL | Fatigue Damage Equivalent Load |
| FEA | Finite Element Analysis |
| FFT | Fast Fourier Transform |
| FS | Factor of safety |
| HATT | Horizontal Axis Tidal Turbine |
| I/O | Inputs and Outputs |
| IFREMER | French Research Institute for Sea Exploitation |
| LCOE | Levelised Cost of Energy |
| LDV | Laser Doppler Velocimetry |
| MCT | Marine Current Turbines |
| NE | Northeast |
| NI | National Instruments |
| NW | Northwest |
| OH | OpenHydro |
| OpEx | Operational expenditure |
| PSD | Power Spectral Density |
| PTO | Power Take-Off |
| ReDaPT | Reliable Data Acquisition Platform for Tidal |
| RMS | Root mean square |

| | |
|---|---|
| SE | Southeast |
| SME | Sustainable Marine Energy Ltd. |
| SW | Southwest |
| TEC | Tidal Energy Converter |
| TGL | Tidal Generation Ltd. |
| VHFR | Very High Frequency Radars |
| WG | Wave gauge |
| X-MED | eXtreme loading of Marine Energy Devices |

# Chapter 1

# Introduction

## 1.1 Renewable Energy

Due to the ever-greater urgency to address global warming issues, the Renewable Energy Directive (European Union, 2018) proposed that at least 27% of the EU energy should be from renewable sources by 2030. In this Directive, the UK had a national interim target of 15% by 2020. According to the Department for Business Energy & Industrial Strategy (2019b), on its Digest of UK Energy Statistics 2019, the UK's share of renewable energy sources in 2017 was of 33%, with 31.1% used for electricity generation, 7.3% for heat and 6.2% for transport. These figures already surpass the Directive's goals.

Additionally to the EU Renewable Energy Directive, The Scottish Government (2013) set a target of generating the equivalent of 100% of Scotland's electricity demand from renewable energy sources by 2020, with the added challenge of maintaining the country as a global lead in tidal and wave energy developments. In 2019, the equivalent to 74.6% of electricity consumption in Scotland was from renewable energy sources (The Scottish Government, 2019). This figure is equivalent to 54.9% of the UK renewable energy generation (Department for Business Energy & Industrial Strategy, 2019a). Compared with other renewable sources such as wind and solar photovoltaics, tidal energy has the potential to generate 20% of the UK energy demand (The British Government, 2013). World wide, installed capacity for tidal energy is $\sim$18 MW (Collombet, 2018). In Europe, total net installed capacity for

wind is ∼168 GW (Fraile and Mbistrova, 2018). Tidal energy is still at a relatively early stage on its maturity and needs continued research into fundamentals of machine loading and performance in realistic conditions to enhance reliability and cost effectiveness.

## 1.2 Tidal Energy

One of the reasons tidal energy has such a potential lies on sea water density. It is over 800 times higher than air and, as it will be detailed in Section 2.3, the power generated by a turbine is directly proportional to the density of the fluid, the swept area of the rotor and the cube of the flow velocity. Such a large density means that the flow does not need to be as fast as the wind speed used in the wind industry for generating electricity and tidal turbine rotors do not need to be as large as wind turbines to generate a similar power output. The vast amount of power available in tidal currents is an important driver that encourages the development of a commercially available technology. Another important driver for the development of commercial devices is the energy security. The International Energy Agency (2019) defines energy security as "the uninterrupted availability of energy sources at an affordable price". Tides are highly predictable compared to the unpredictable nature of other renewable energy sources. This predictability means that it is exactly known when would a backup energy source would need to step in and supply electricity during slack waters.

One of the main drawbacks of tidal energy is associated to the high costs it currently has. According to the Department of Energy and Climate Change (2013), the levelised cost of electricity (LCOE) from tidal stream sources is expected to reduce from 190 £/MWh in 2025 to 171 £/MWh by 2030 for shallow water deployments, and from 148 £/MWh to 129 £/MWh for deep water deployments. This is still not a competitive generation method compared to onshore wind turbines of over 5 MW capacity which is forecasted to have an LCOE of 97 £/MWh by 2030. The high LCOEs are mainly attributed to the high costs of capital and operational expenditure, CapEx and OpEx respectively. A solution to lower the LCOE is to

reduce CapEx by optimising the structural design of the device whilst maintaining the device's performance and survivability. A possible approach is to lower the factors of safety (FS) that account for the design and performance uncertainties arising from loads in naturally occurring flows. A way to have a better understanding of the impact these loads have on a tidal turbine is physical testing of scale models under realistic testing conditions. In order to recreate realistic conditions, a sound understanding of the marine environment is needed.

## 1.3 Tidal Energy Resource in Scotland

In recent years, research and development on tidal energy in the UK has grown steadily. It is not a surprise since most of Europe's tidal energy resource levels are concentrated around the British Isles (as shown qualitatively in Figure 1.1). It is also noticeable some concentrations around the Iberian Peninsula, south of Italy and Turkey.


**Figure 1.1:** Level of tidal resources across Europe. Source: Aqua-RET (2012)

The UK waters, as reported by The British Government (2013), contain around 50% of Europe's theoretical tidal energy resource and a UK extractable resource of around 4% of the overall supply with the technologies available in 2013. However, this measurement does not include all the islands that surround the British Isles.

The Scottish Government (2018) reported that Scotland is comprised of more than 800 islands. This gives way to numerous narrow channels, seaways and firths between the different islands which can contain strong tidal currents. However, exploitation of this potential in these locations might be hindered by their location far from large population centres.

The conversion of this theoretical resource into a technical resource depends upon the conversion technologies. The technologies that are emerging most strongly (Chapter 3) are designed for locations where flow speed is of the order of 2 m/s or greater.

The waters surrounding Scotland have strong currents as can be seen in Figure 1.2. The areas with potential tidal sites are Orkney and Shetland (including the Pentland Firth), the West of Scotland (including the Hebrides) and the Irish Sea. The difference between Spring and Neap peak flows around the British Isles is emphasised by comparing Figures 1.2a and 1.2b. The Spring tides at the Pentland Firth (blue oval) contain the fastest flows reaching up to 4 m/s. In contrast, the Neap tides at the same location contain flow speeds that hardly exceed 2 m/s.

The Pentland Firth (blue oval in Figure 1.2), located between Orkney and Caithness in mainland Scotland, contains the highest tidal energy concentration in the world according to Neill et al. (2017). It has been the focus of multiple research studies, with power potential estimates varying from 1-2 GW averaged over a tidal cycle (Black & Veatch Consulting Ltd, 2005; Adcock et al., 2013; Vennell, 2013) to 18 GW at peak flow (Salter and Taylor, 2007). Such estimates variations are mainly attributed not just to how accessible the energy sources are with present technologies while keeping a competitive LCOE compared to other energy sources but also to the methodologies utilised to calculate these estimates.

## 1.4 Examples of horizontal axis tidal turbines

As it has been seen in previous sections, the UK waters contain a large theoretical resource of renewable tidal stream energy. This has led to a plethora of approaches to harness the tides energy. Amongst the most common approaches are horizontal

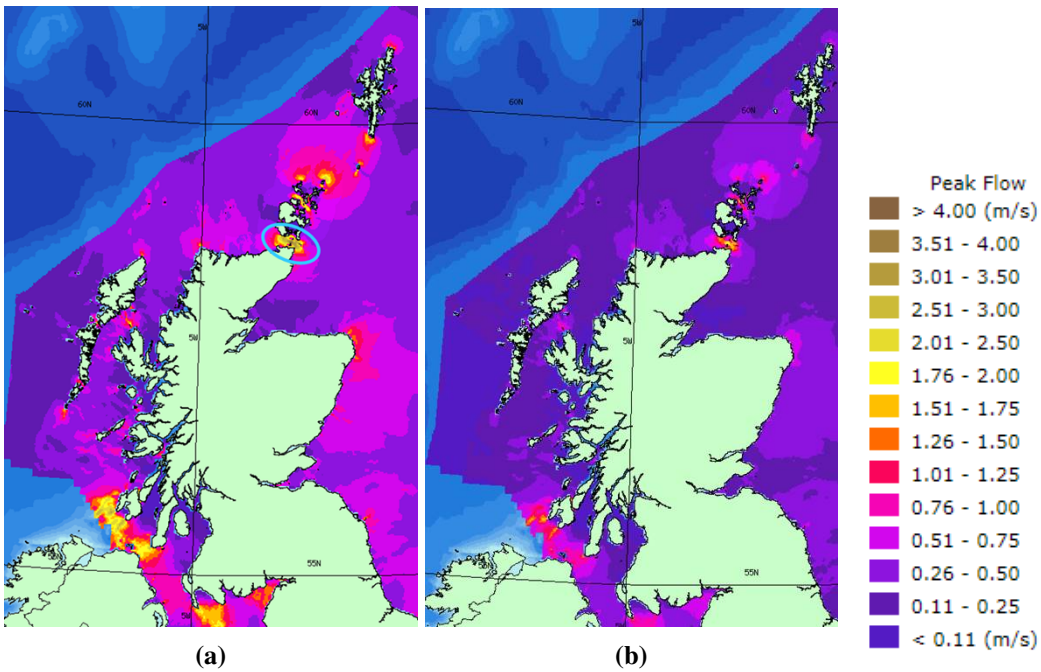


**(a)** **(b)**

**Figure 1.2:** Tidal energy Atlas of Scotland for a) Spring peak flow and b) Neap peak flow. The Pentland Firth is identified by the blue oval on (a). Reproduced from http://www.renewables-atlas.info/ © Crown Copyright.

axis tidal turbines (HATT), cross-flow tidal turbines (vertical or horizontal), tidal kites and oscillating hydrofoils. However, despite the different technologies developed, the last years have seen a significant technology convergence on HATTs. One reason might be that HATTs have taken inspiration and knowledge from available technology in the wind industry and applied it to the marine environment. Hence transferable skills and knowledge from the wind industry have pushed this type of tidal energy converter (TEC) to the forefront. There are a few successful –and some not-so-successful– stories of full-scale turbines. This section contains a brief description of some of the available full-scale technologies listed in Table 1.1.

**Table 1.1:** HATT developers.

| Developer | Device | Rated power | Figure 1.3 |
|---|---|---|---|
| Nova Innovation | M100 | 1 MW | a |
| Orbital Marine | Orbital O2 | 2 MW | b |
| Sabella | D10 | 1 MW | c |
| Nautricity | CoRMaT | 0.5 MW | d |
| Sustainable Marine Energy | PLAT-O | N/A | e |
| OceanFlowEnergy | EvoPod | N/A | f |
| SIMEC Atlantis | AR1500 | 1.5 MW | g |
| Andritz Hydro Hammerfest | AH1000 | 1 MW | h |

One of the companies with successful sea trials is the Scottish company Nova Innovations. They have two deployment sites, one which started in 2016 under the project Enabling Future Arrays in Tidal (EnFAIT) in Bluemull Sound in Shetland, Scotland with three 100 kW M100 turbines (Figure 1.3a) and a recently leased site in Bardsey Island, North Wales that will assess the technical feasibility and environmental impact for later deployments.

Another Scottish company with successful sea trials is Orbital Marine (formerly known as ScotRenewables). Their 2 MW concept, the Orbital O2, is a 72 m long floating barge with two 20 m rotors mounted at the end of two hinged arms (Figure 1.3b). Each turbine has a rated power of 1 MW at flow speeds of 2.5 m/s. They were awarded an agreement for lease from the Crown Estate in 2012 for the development of a tidal array at Lashy Sound, Orkney

Sabella is a French company with a gravity tripod-mounted turbine, the D10 turbine (Figure 1.3c). It comprises six blades with a symmetrical profile which allows the turbine to operate at ebb and flow without the need of yaw control. The turbine has a rated power of 1 MW. One round of tests has been performed and a subsequent round is planned off the coast of Ushant Island, France.

Another Scottish company is Nautricity. They promote a contra-rotating 500 kW tidal turbine: the CoRMaT (Figure 1.3d). This design is their second-generation device with successful proof of concept testing (Clarke et al., 2007, 2009) and now commercially available.

Scottish company Sustainable Marine Energy LTD (SME), based in Edinburgh, has two working models: The PLAT-O (Figure 1.3e) and the PLAT-I. They are platform based concepts tuned for offshore and inshore usage, respectively. The approach of SME is to use commercially available rotors from German company Schottel and mount them on pontoon platforms of their own design. The PLAT-O is designed to float at the desired height in the water column via a taut mooring. The number of turbines can be modified to the different requirements. Plat-O has been tested at FloWave by Fabre et al. (2015) and at Cranfield University's towing tank by Bivol et al. (2017). On the other hand, their Plat-I model has been tested

at FloWave by Jeffcoate and McDowell (2017). A more detailed insight into these studies is presented in Chapter 3.

OceanFlowEnergy has a turbine concept called EvoPod (Figure 1.3f). This model has been successfully tested at different scales in both tanks and sea. PIV measurements at laboratory scale of the EvoPod's wake have been done by Good et al. (2011). Sea trials have been conducted in several instances: Atcheson et al. (2015) measured the wake of a towed 1:10 scale version at Montgomery Lough, Northern Ireland and Jeffcoate et al. (2014, 2015, 2016) analysed the performance difference of the turbine between towing the turbine in a lake and moored in a tidal site; they also compared the effects of different submergence distances and the interaction between two turbines in different array combinations.

SIMEC Atlantis owns the 2 MW turbine AR2000 with 20 m rotor diameter. A smaller version, the 1.5 MW AR1500 (Figure 1.3g) with an 18 m diameter rotor was one of the first turbines to be installed along with Andritz Hydro Hammerfest 1.5 MW turbine AH1000 (Figure 1.3h) between mainland Scotland and the island of Stroma under the MeyGen project. This project was leased to generate up to 398 MW from the tidal currents. The project is made up of several phases. The first phase of the project consists of four 1.5 MW turbines. The second phase will incorporate two of the newer AR2000. Subsequent phases have no specifics regarding technologies to be installed in order to achieve its full potential.

## 1.5 Examples of tidal stream energy projects

As presented in the previous sections, the advancement in tidal energy technologies in recent years has led to the development of several full-scale projects. Some projects might be for demonstration with single devices but some others are multi-device, multi megawatt arrays. An overview of the current leased tidal sites around the UK isles is presented in Table 1.2. There are several leased sites, some of them are under development already and some of them still in the design stages. However, regardless of the stage the projects currently are, the UK is the country with the highest installed capacity for tidal energy in the world (Edge et al., 2017).


**(a)** **(b)**

**(c)** **(d)**

**(e)** **(f)**

**(g)** **(h)**

**Figure 1.3:** Horizontal axis turbines: a) M100 (Nova Innovation, 2017); b) Orbital O2 2MW (Orbital Marine, 2018); c) D10 (Sabella, 2017); d) CoRMaT (Nautricity, 2017); e) PLAT-O (Sustainable Marine Energy Ltd, 2017); f) EvoPod (Oceanflowenergy, 2017); g) AR1500 (Atlantis Resources, 2017); h) AH1000 MK1 (Andritz Hydro Hammerfest, 2017)

The increase in projects around the UK and tidal turbine developers points that the sector is on the right path, even though it is still in a early stage.

**Table 1.2:** Leased tidal sites in the UK.

| Site | Tenant | Status | Capacity |
|---|---|---|---|
| Fair Head | Fair Head Tidal Energy Park | Pre-planning | 100 MW |
| Torr Head | Tidal Ventures | Consented | 100 MW |
| Holyhead Deep | Minesto | Consented | 10 MW |
| Isle of Wight | Isle of Wight Council | Consented | 30 MW |
| West Anglesey | Menter Môn | Pre-planning | N/A |
| Bardsey Sound | Nova Innovation | Pre-planning | 0.5 MW |
| Ness of Duncansby | SIMEC Atlantis Energy | In development | 100 MW |
| Westray South | DP Energy | In development | 200 MW |
| Fall of Warness | EMEC | Operational | N/A |
| Sound of Islay | SIMEC Atlantis Energy | Pre-construction | 10 MW |
| Pentland Firth | SIMEC Atlantis Energy | In construction | 398 MW |
| Bluemull Sound | Nova Innovation | In construction | 0.6 MW |
| Shapinsay Sound | EMEC | Operational | N/A |
| Lashy Sound | Orbital Marine Power | In development | 10 MW |
| Sanda Sound | Oceanflow Energy | In construction | >0.5 MW |
| Stronsay Firth | EMEC | In planning | N/A |
| Islay Demo Zone | EMEC | In planning | N/A |
| Mull of Galloway | SIMEC Atlantis Energy | In planning | 30 MW |
| Portland Bill | SIMEC Atlantis Energy | In planning | 30 MW |
| Strangford Lough | SIMEC Atlantis Energy | In planning | 30 MW |
| West Islay | DP Energy | In planning | 30 MW |

Data obtained from http://www.thecrownestate.co.uk

## 1.6 Uncertainties and limitations of full-scale devices

The economic potential and environmental attraction of harnessing tidal energy is clear. However, despite considerable progress and successful deployments, there is still research to be done to fully understand how these devices react to real sea conditions. Not knowing the detailed characteristics of flows in potential tidal sites leaves levels of uncertainty that could potentially be dealt with only by over-engineering the devices, leading to higher CapEx and LCOE. Higher costs could ultimately make tidal energy not economically or commercially feasible. As will be shown in the detailed review in Chapter 3, the vast majority of studies upon which these devices and their performance estimations have been based are for the simplest cases of current and wave parameters. Early research projects were conducted in towing tanks. Roughly speaking, this type of facilities have an idealised flow where no turbulence or velocity depth profiles are present (Salvatore et al., 2014). They

also lack wave-current interaction effects, while in reality, flow changes with time and space. Within a tidal cycle, the flow speed will change from almost 0 m/s to its maximum potential. In the most favourable cases, flow direction between flood an ebb is close to 0° but in several locations, the flow direction between flood and ebb can be up to 20°. Like these, several other phenomena (e.g. turbulence, seabed roughness, waves) influence the flow a turbine will be subjected to. Chapter 2 will look into detail at these phenomena.

## 1.7 Aim and objectives

In this chapter, the importance of transitioning to renewable energy sources was discussed. Tidal energy has evident advantages over other renewable energy sources (e.g. a high level of predictability). It has been shown that the distribution of European tidal stream resources concentrates in British waters and, as a consequence, the number of technologies and projects in the UK is high. Research and development on tidal energy technologies in the UK is strong. As an example, according to the European Commission's Community Research and Development Information Service (CORDIS) datasets, under the EU Horizon 2020 program, an investment of around £100 million has been granted solely to tidal energy projects from 2014 to 2020. However, there is still the need to fully comprehend the real flow phenomena that occur at potential tidal sites and to assess the impact these phenomena have on tidal stream energy converters (e.g. wave-current interaction).

The aim of this thesis is to investigate the influence of more realistic current and wave conditions on the performance and loading characteristics of a horizontal axis tidal turbine. The specific objectives of the research are:

- To quantify the influence of current misalignment on loading and on performance of a tidal turbine via thrust and power coefficients, $C_T$ and $C_P$, respectively.
- To determine the influence of the presence of waves with difference in periods and direction on the loading and on performance of a tidal turbine, again via thrust and power coefficients, $C_T$ and $C_P$.

- To investigate the influence of current misalignment and the presence of waves on the loading and on performance of a tidal turbine according to the rotor's absolute angular position.

- In the frequency domain, to explore and quantify the influence of waves - collinear and non-collinear - with current upon the loading experienced by the rotor.

Ahead of the main research phase addressing the above four principal objectives, three substantial preparation tasks are required:

- To complete the design, assembly and commissioning of the turbine and its associated control cabinets.

- To carry out 'bare basin' measurements of currents and waves in order that the inflow and incident waves are well characterised before the turbine is placed.

- To characterise the turbine's performance under 'ideal' conditions of zero yaw current-only inflow, in order that the influences being exported in the main objectives can be clearly identified.

## 1.8 Structure of thesis

Chapter 2 presents a theoretical background on technical concepts of fluid mechanics concepts related to flow-structure interactions, the loading and performance of tidal turbines and, the model, laboratory and scaling effects. A review of academic literature on field measurements and tidal turbine tests is presented in Chapter 3. The experimental set-up is presented in Chapter 4. Chapter 5 describes the design and implementation of the test matrix. A detailed description of the testing basin and associated flow characteristics is provided in Chapter 6 and the results of the turbine tests are presented in Chapter 7. Finally, Chapter 8 concludes the thesis. In the appendices, time series of all measurements for all tests conditions, along with journal publications in which the author is main or contributing author are included.

# Chapter 2

# Technical background

## 2.1 Scope of technical background

Ahead of the critical review of the relevant literature in Chapter 3, this section attempts to provide the necessary technical background to understand the terminology and concepts used throughout this work. The section commences with some basic concepts of the hydrodynamic phenomena surrounding tidal stream turbines in real sea conditions. It then moves to fluid-structure interaction and how these interactions have a direct impact on the loading and performance of a tidal stream turbine. It then finishes with effects that are specific to model and laboratory testing, scaling and array effects. The reader should finish this chapter with a better understanding of the basic flow-structure interaction concepts that are related to tidal turbines and the operational principles of a tidal turbine.

## 2.2 Tidal stream energy conversion; the rotor and its environment

The flow a tidal turbine is subjected to is influenced by different physical variables. Figure 2.1 shows a tidal turbine in a generalised marine environment. On the left hand side of the figure, the different flow phenomena found in the ocean are depicted. On the right hand side the turbine and the typical fluid-structure interactions are shown.

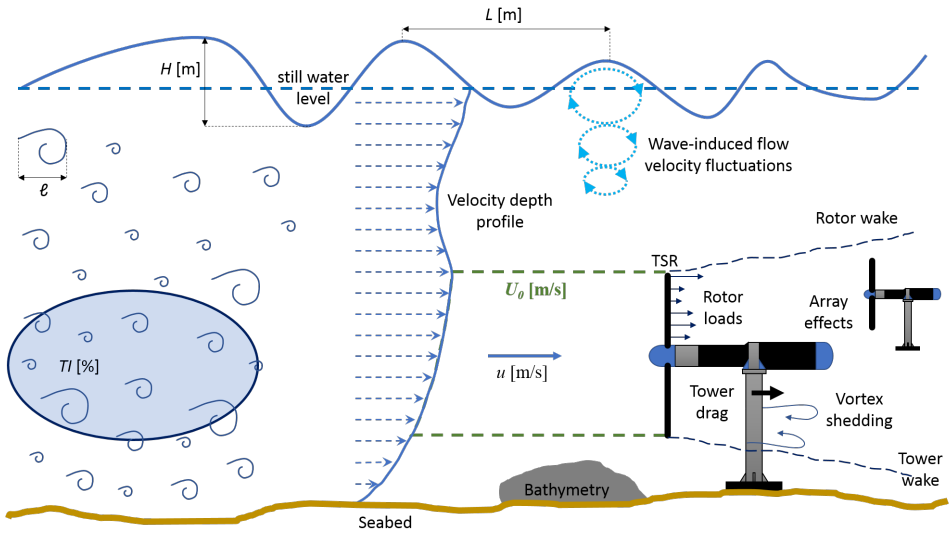


**Figure 2.1:** Flow variables a turbine is typically subjected to in a marine environment. The quantities and abbreviations are described in the main body of the chapter.

The flow velocity in a tidal channel will be influenced by flow velocity fluctuations around the average flow velocity known as turbulence (Section 2.2.3). This turbulence is comprised of large, energy-containing eddies that in turn are comprised of smaller eddies and so on until the energy dissipates into heat by viscous forces. The sources of turbulence are also depicted in Figure 2.1; seabed roughness, bathymetry and waves will contribute to the generation of turbulence. Some in a larger scale than the others. These sources of turbulence have also an influence on the flow velocity at different depths of the water column. As a result, the real variation in flow velocity with depth is very far from an uniform flow. This variation gives the flow velocity a unique 'shape' along the water column called the velocity depth profile (Section 2.2.1). Although the velocity depth profile is very site-specific, it is common to fit a power-law to the velocity depth profile for ease of analysis. However, in reality no flow is as uniform as a power-law.

The fact that these factors are unique to each potential tidal site makes it imperative that the flow at each potential deployment site is measured and characterised precisely.

### 2.2.1 Flow velocity

The way the flow velocity a turbine sees is quantified is shown in Figure 2.1. It can be a single point measurement $U$, or any of its components: horizontal velocity component $u$, transverse velocity component $v$ or vertical velocity component $w$. It can be the spatial-average of all the single-point measurements performed within the rotor area $U_0$ or, the velocity depth profile depicted by the vertical curve created by all the arrows across the full water column ($U_z$).

#### Velocity depth profile

The velocity depth profile is the variability the flow velocity experiences along the depth of the water column (Figure 2.1). The flow velocity can be influenced by many factors, like the bathymetry, shear currents, waves, man-made obstacles and many more.

The seabed roughness consists of sand ripples, dunes, vegetation, stones and any other surface feature found on the seabed. These features slow down the flow layers closest to the seabed adding shear to the flow, thus creating a boundary layer. On the other hand, bathymetry is all the different features, like trenches, ditches, bends and any large obstacles found in the seabed. Bathymetry acts in a similar way as seabed roughness. However, the larger sizes of these features create larger turbulent flow structures. The maximum size of these flow structures is constricted to be the size of the bathymetry feature that produced them. The maximum size a flow structure can be is known as integral length scale (Section 2.2.3).

Waves have a direct influence on the velocity field under them. This influence gives the water particles an orbital motion as can be seen in Figure 2.1. These orbital motions decrease in size as the water depth increases. In the same way that seabed roughness and bathymetry result in shearing in the lower part of the water column generating turbulence, these orbital motions result in shear forces in the upper part of the water column.

All these factors will give the velocity profile a unique shape for each location. However, it is common to use a power law to describe the shape of a velocity depth profile (Soulsby et al., 1993; Sellar and Wakelam, 2018).

$$U_z = \left(\frac{z}{z_0 \cdot d}\right)^{1/\alpha} U_d \tag{2.1}$$

where $U_z$ is the flow velocity as a function of the height $z$ in the water column, $z_0$ is the bed roughness $d$ is the water depth, $U_d$ the depth-averaged velocity and $\alpha$ the power coefficient.

A typical value for the power coefficient $\alpha$ is 7. However, any given site could be described by many other power law values. The one-hour averaged data shown in Figure 2.2 was collected from an undisclosed location on the west of Scotland (Martinez et al., 2019). A power law of $1/8^{th}$ is fitted to show how much the velocity depth profile can change during a tidal cycle of 12 hours at the same location. Depth profiles play an important role in tidal turbine loading as the flow velocity at the top of the rotor will be different than the flow velocity at the bottom of the rotor. This depth variation in the flow velocity will create an uneven loading on the rotor. The grey area shown in Figure 2.2 represents the rotor of a common tidal turbine whose diameter is half the depth of the water (not dissimilar to the set-up used in the current work). Focusing on the fastest line to the right of the figure (06:52), the flow velocity at the bottom of the rotor is about 2.2 m/s whereas at the top of the rotor is just above 4.8 m/s. In Section 2.3 it will be seen that thrust is proportional to $U_z^2$. This means that the thrust experienced at the top of the rotor would be $\sim 4$ times more than the thrust experienced at the bottom of the rotor.

### 2.2.2 Flow asymmetry

A tidal flow is not characterised only by the flow velocity and the turbulence intensity. Another important factor is the flow asymmetry. Flow asymmetry is the angular difference between the mean flood direction and the mean ebb direction. Similar to Figure 2.2, the data presented in Figure 2.3 is from the west coast of Scotland. The data shows a flow asymmetry of 20° between flood (NE direction) and ebb (SW direction). This value is site specific and can vary greatly from one site to another. As an example of how much flow directionality can change from site to site, according to Harrison (2015), flow asymmetry at Fall of Warness, Scotland is

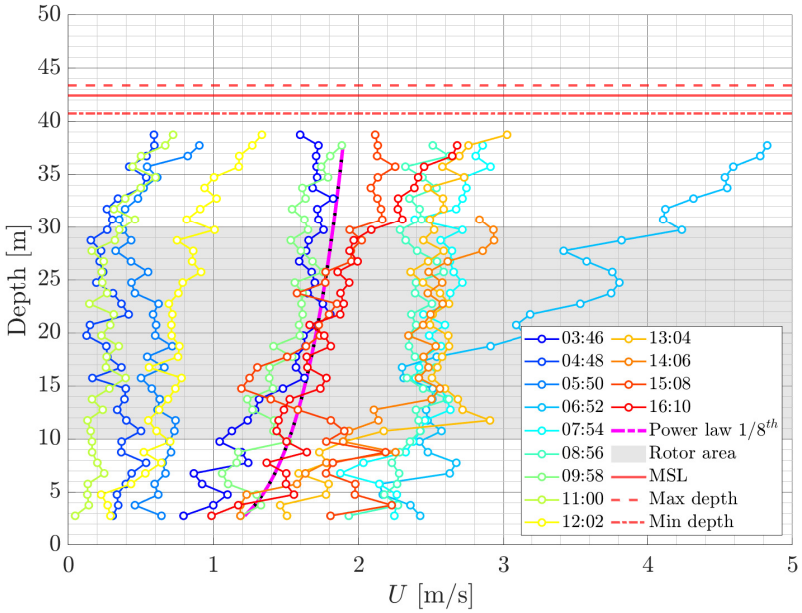


**Figure 2.2:** Mean flow velocity depth profiles taken at the west coast of Scotland, UK showing a power law approximation of $1/8^{th}$. Data from Martinez et al. (2019).

of 5°. As it will be seen in Chapter 7, flow misalignment has an important influence on the rotor loading and performance as tidal turbines are usually not able to turn the rotor in the direction of the flow.

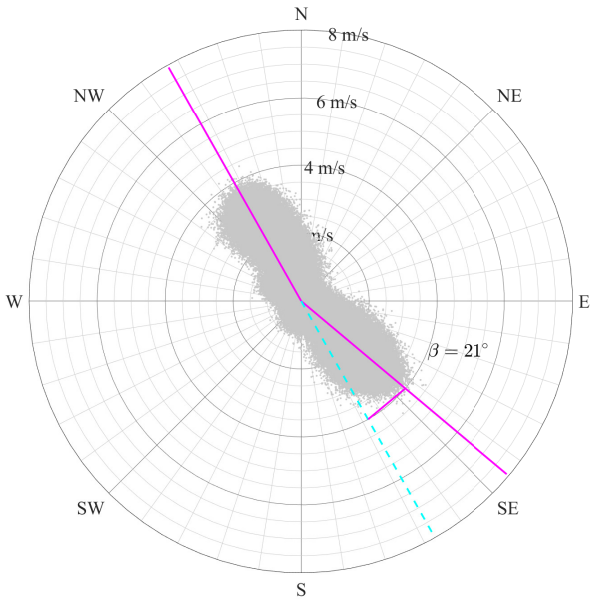


**Figure 2.3:** Mean mid-depth flow velocity measurements taken at the west coast of Scotland, UK showing a flow asymmetry of about 15°. Data from Martinez et al. (2019).

### 2.2.3 Turbulence

Flow velocity and direction change constantly with time at different scales. These fluctuations, as will be seen in Chapter 3, have a direct impact on a the turbine loading.

Turbulence is defined as the stochastic change in velocity and pressure within a fluid. It is characterised by the presence of eddies, vortices and other turbulent flow structures. The onset of turbulence can be roughly predicted by the Reynolds number (Re), which is the ratio of inertial to viscous forces in a flow. It is defined as:

$$\mathrm{Re} = \frac{\rho U L}{\mu} \tag{2.2}$$

where $\rho$ is the fluid density, $U$ is the flow velocity, $L$ is the characteristic length and $\mu$ is the dynamic viscosity of the fluid. This non-dimensional parameter will be discussed in more detail in Section 2.4.

Looking at Equation (2.2), it can be deduced that fluids flowing through or past a body that have large characteristic lengths and/or have high speeds and/or have low viscosity tend to be associated with turbulent flow (higher Re), whereas those fluids flowing through or past a body which has smaller characteristic length and/or have slow velocity and/or have high viscosity tend towards laminar flow (lower Re).

A quantitative measure of the turbulence is the turbulence intensity $TI$. It is defined as the ratio of the flow fluctuations around the mean flow velocity (Equation 2.3). $TI$ has a direct impact in the loading of a turbine. Higher levels of $TI$ ($\sim 20\%$) can increase loading standard deviations by up to 2-3 times the values of a site with low $TI$ levels ($\sim 5\%$) (Mycek et al., 2014). $TI$ is expressed as:

$$TI = \frac{u\prime}{\overline{u}} \tag{2.3}$$

where $u\prime$ is the standard deviation of the streamwise flow velocity (Equation 2.4) and $\overline{u}$ is the average streamwise velocity.

$$u\prime = \sqrt{\frac{1}{N-1}\sum_{i=1}^{N}|u_i - \overline{u}|^2} \tag{2.4}$$

where $N$ is the number of measured samples.

## Energy cascade

A feature of turbulence is the energy cascade. It refers to the way the energy contained in the larger scale turbulent eddies transfers into smaller scale eddies until the energy is dissipated via viscous friction in the form of heat (see e.g. Pope, 2000). There are three ranges (Figure 2.4), the first one on the left in which the energy is produced and the eddies have the largest sizes, the middle one is where the flow motions are determined by inertial effects and lastly, the dissipation range in which the energy is dissipated into heat. The size of the eddies in the production range is known as integral length scales.

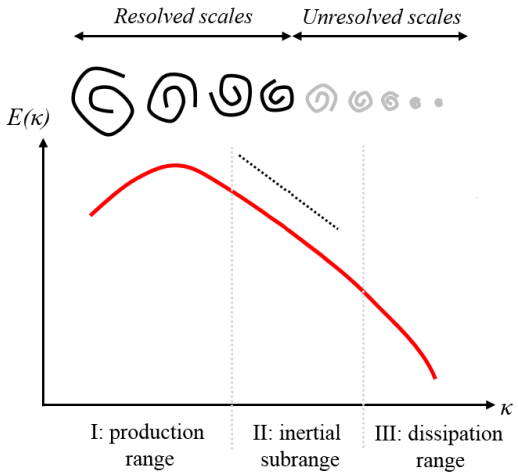


**Figure 2.4:** Typical representation of the turbulence energy spectrum. Adapted from Barba (2017). Vertical axis $E(K)$ represents the energy content of the eddies and the horizontal axis $K$ represents the scale of the eddies.

## Integral length scales

The size of the energy containing eddies in a turbulent flow is defined as the integral length scale. This measure is the distance over which two-point flow velocity components of an eddy are correlated. According to Blackmore et al. (2016), it can be interpreted as representative of the size of the turbulent eddies that contain the

largest amount of energy. O'Neill et al. (2004) mentions that defining the length scales is important to understanding the mechanics of energy production and dissipation and to suitably define an area or volume for experimental and numerical investigations. The maximum size of these eddies is defined by the characteristic length of the body. For example, the size of the largest eddies generated by a turbine rotor will be the size of the rotor. All these eddies surrounding a turbine will have a direct impact in the turbine loading.

### 2.2.4 Waves

Another contribution of velocity flow fluctuations to the turbulence comes from waves. Figure 2.1 shows two key parameters defining an ocean wave: wave height ($H$), which is the distance between the highest (crest) and lowest (trough) points of a wave and the wavelength ($L$), which is the distance between two neighbouring crests. Third and fourth parameters that are not represented in Figure 2.1 are the wave period $Tw$ and wave direction $\theta$. In an idealised sea state, waves have fixed parameters. However, in reality the four parameters have significantly different values, from calm seas to stormy conditions. Irregular sea states are a superposition and interference of several different waves, each with its own height, period, wavelength and direction. The height of irregular waves is expressed using the significant wave height ($H_0$), which is usually defined as four times the standard deviation of the surface elevation. In laboratory testing, however, it is common practice to use regular waves. The choice of regular waves not only provides with repeatability but it also allows for a better characterisation of the device and a better understanding of the hydrodynamic interactions between the device and each of the wave parameters. There are, however, some laboratory testing of tidal turbines in irregular waves (e.g. Porter et al. (2018); Draycott et al. (2019)).

According to Munk's (1950) ocean waves classification (Figure 2.5), waves with periods 1 s $< Tw >$ 30 s (blue lines) have the largest relative height ($H/H_0$) within the whole ocean wave spectrum and are classified as ordinary gravity waves. This type of waves are the ones a tidal turbine will be subjected to more frequently. In the Figure, wave periods around 7 s are the ones with the largest relative height.

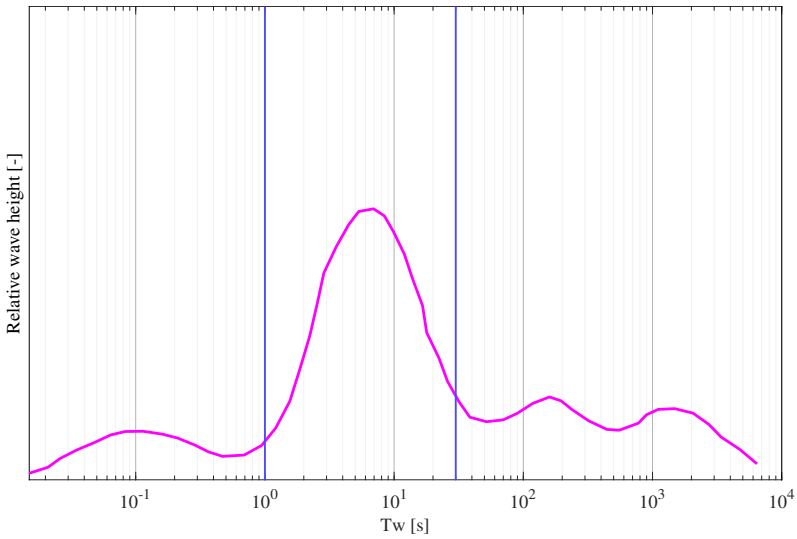


**Figure 2.5:** Classification of the spectrum of ocean waves according to Munk (1950). Vertical axis is relative wave height. Adapted from Munk (1950).

As seen in Figure 2.1, the influence of the waves in the flow velocity extends down the water column. How deep the influence goes depends on $H$ and $Tw$. This influence in the flow velocity can be quantified with linear wave theory using the general approach for intermediate waters (see, for example, Hedges (1987); Dean and Dalrymple (1984)). This theory helps estimate the horizontal particle velocity at a desired depth (circular arrows under a wave in Figure 2.1). This velocity is expressed as:

$$u = \frac{H}{2} \cdot \frac{\cosh\left[k\left(d+z\right)\right]}{\sinh\left(kd\right)} \cdot \omega \cdot \cos\left(kx - \omega t\right) \tag{2.5}$$

where $H$ is wave height, $\omega$ is the wave frequency, $k$ is wave number, $d$ is water depth, $z$ is height in the water column, $x$ is the distance travelled in the streamwise direction and $t$ the time elapsed. $z = 0$ at seawater level (SWL) and is positive vertically upwards.

The maximum horizontal particle velocity is:

$$u_{max} = \frac{H}{2} \cdot \frac{\cosh\left[k\left(d+z\right)\right]}{\sinh\left(kd\right)} \cdot \omega \tag{2.6}$$

To find the wavenumber $k = \frac{2\pi}{L}$, is necessary to find the wavelength $L$ first as:

$$L = \frac{gTw^2}{2\pi} \tanh\left(\frac{2\pi d}{L}\right) \tag{2.7}$$

where $g$ is acceleration due to gravity.

### 2.2.5 Wave-current interaction

Waves superimposed on a mean current experience a Doppler shift, which is the change in frequency of a wave from the reference frame of an observer who is moving relative to the wave source. This change in frequency is defined as:

$$\sigma = \omega - kU \tag{2.8}$$

where $\omega$ is the rotational frequency of the waves seen from a reference frame in which $U$ is the current velocity, $\sigma$ is the rotational frequency of the waves seen from a reference frame in which $U = 0$ (i.e. the viewer is moving with the current).

Free propagating waves only exist when the angular frequency $\omega$ and wavenumber $k$ satisfy the frequency dispersion relation. The dispersion relation for intermediate waters according to (e.g.) Peregrine (1976) is defined as:

$$\Omega = \sqrt{gk \tanh kd} \tag{2.9}$$

and:

$$\Omega^2 = \sigma^2 \tag{2.10}$$

Combining Equations (2.8), (2.9) and (2.10) to have a dispersion relation with Doppler shift:

$$\omega = kU \pm \sqrt{gk \tanh kd} \tag{2.11}$$

adding the Doppler shift from Equation (2.11) in Equation (2.6) gives:

$$u_{max} = \frac{H}{2} \cdot \frac{\cosh\left[k\left(d+z\right)\right]}{\sinh\left(kd\right)} \cdot \left(kU \pm \sqrt{gk \tanh kd}\right) \tag{2.12}$$

which is the horizontal velocity of a water particle influenced by wave and current. This horizontal particle velocity is of an oscillatory nature and it will either make the flow faster or slower depending on the direction the particle is moving at a specific time.

The wave period has a direct influence in the cyclic loading of a turbine. If the waves have a short period, there will be more waves in a given time than with higher periods. This frequency is related to the fatigue loading of a turbine.

## 2.3 Turbine loading and performance

Now that the main flow phenomena have been introduced, the next step is to understand how these phenomena interact with the different components of a turbine subjected to a tidal flow. In this section, aerodynamics of blades are not discussed as they do not play a direct role in the scope of these experiments or subsequent analysis and interpretation. If the reader wishes to deepen their knowledge in this matter, a good start is Hansen (2008).

Most of the knowledge applied in tidal stream turbines has been taken and modified from the wind energy sector. In the next pages, a general background of the theory involved in the design of tidal turbines is discussed. Each of the concepts can be further studied in the references provided.

### Actuator disc theory

One of the most basic tools to quantify the loading and performance of a tidal turbine is the actuator disc model like the one showed in Figure 2.6. It is a one-dimensional tool based on linear momentum theory that is typically used to, in a basic manner, quantify the thrust generated and power extracted from the flow by an ideal rotor (blue rectangle). For this, the rotor has to be placed in a stream tube delimited by the solid black lines shown in Figure 2.6. In this theory, it is assumed that no water flows across the stream tube and that the water flows from left to right. Also, the water is assumed to be incompressible and inviscid. The rotor is assumed to have an infinite number of blades and to be infinitely thin. The thrust experienced by the rotor is uniform over the whole rotor area and the wake of the rotor is

assumed to be non-rotating. The theory also makes the assumption that the mass of water flowing through the whole system is conserved. The numbers in Figure 2.6 indicate locations: (1) far upstream of the rotor, (2) just upstream of the rotor, (3) just downstream of the rotor and (4) far downstream of the rotor.

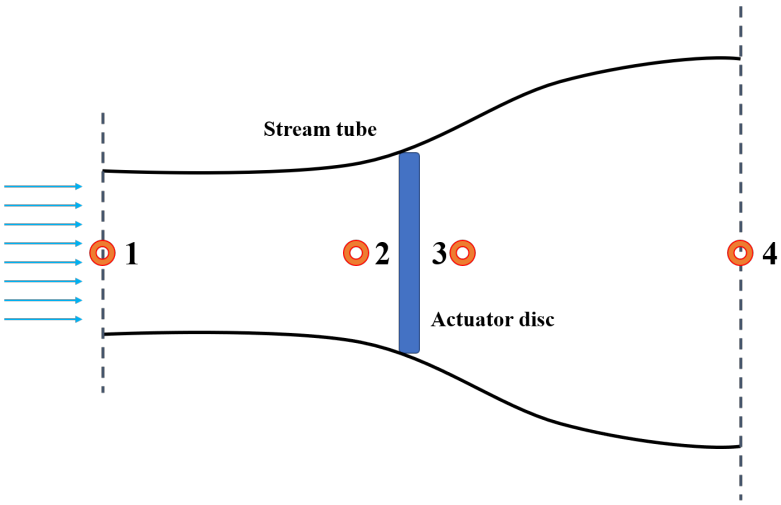


**Figure 2.6:** Actuator disc model of a tidal turbine. Numbers indicate location identifiers. The rotor is assumed to be infinitely thin. Flow goes from left to right.

In this section, the reader is taken step by step through the development of the non-dimensional quantities that characterise the loading and performance of a rotor: power and thrust coefficients, $C_P$ and $C_T$ respectively.

Consider that the mass of water per unit time that flows through any cross-section of the stream tube at any given time is defined by $\rho Q = \rho AU$. This flow rate must be the same throughout the whole stream tube, therefore:

$$\rho A_1 U_1 = \rho A_2 U_2 = \rho A_3 U_3 = \rho A_4 U_4 \tag{2.13}$$

Conservation of linear momentum says that the force of the water exerted on the rotor (thrust) is equal and opposite to the net force of all the water flowing through the stream tube:

$$T = \rho Q (U_1 - U_4) \tag{2.14}$$

where $Q$ is the flow rate.

On each side of the rotor no work is done. Therefore, it is possible to apply Bernoulli's equation to each side of the rotor:

$$p_1 + \frac{1}{2}\rho {U_1}^2 = p_2 + \frac{1}{2}\rho {U_2}^2 \tag{2.15}$$

$$p_3 + \frac{1}{2}\rho {U_3}^2 = p_4 + \frac{1}{2}\rho {U_4}^2 \tag{2.16}$$

Assuming that $p = p_1 = p_4$ and $U = U_2 = U_3$ and solving for $p_2$ and $p_3$, respectively:

$$p_2 = p + \frac{1}{2}\rho \left(U_1^2 + U^2\right) \tag{2.17}$$

$$p_3 = p + \frac{1}{2}\rho \left(U_4^2 + U^2\right) \tag{2.18}$$

Taking into consideration that $F = A_{rotor}p$, the thrust on the rotor can be expressed as the sum of the forces on either side of the rotor assuming that points (2) and (3) on Figure 2.6 are so close to each other that the area on both sides is the same ($A_{rotor} = A_2 = A_3$):

$$T = A_{rotor}(p_2 - p_3) \tag{2.19}$$

Solving Equation (2.19) for $p_2$ and $p_3$ replacing with equations (2.17) and (2.18) we get:

$$T = \frac{1}{2}\rho A_{rotor} \left(U_1^2 - U_4^2\right) \tag{2.20}$$

Equating thrust values from equations (2.14) and (2.20) we obtain:

$$\rho A_{rotor} U \left(U_1 - U_4\right) = \frac{1}{2}\rho A_{rotor} \left(U_1^2 - U_4^2\right) \tag{2.21}$$

Remembering factorising rules: $m^2 - n^2 = (m-n)(m+n)$:

$$U = \frac{U_1 + U_4}{2} \tag{2.22}$$

There is a flow velocity variation between points (1) and (2) of Figure 2.6 induced by the rotor. This variation, in terms of $U_1$ and $U_2$ is known as the axial induction factor $a$:

$$a = \frac{U_1 - U}{U_1} \tag{2.23}$$

This implies:

$$U = U_1 (1 - a) \tag{2.24}$$

Equating $U_2$ values from equations (2.22) and (2.24) and solve for $U_4$ we obtain:

$$\frac{U_1 + U_4}{2} = U_1 (1 - a) \tag{2.25}$$

$$U_4 = U_1 (1 - 2a) \tag{2.26}$$

To obtain the power $P$ generated by the rotor, the thrust force from Equation (2.20) has to be multiplied by the flow velocity at the rotor $U$:

$$P = \frac{1}{2} \rho A_{rotor} U \left( U_1^2 - U_4^2 \right) \tag{2.27}$$

Applying the same factoring rule as before:

$$P = \frac{1}{2} \rho A_{rotor} U (U_1 - U_4)(U_1 + U_4) \tag{2.28}$$

and substituting $U$ and $U_4$ from Equations (2.24) and (2.26), respectively, we obtain the power $P$:

$$P = \frac{1}{2} \rho A_{rotor} U_1^3 4a (1 - a)^2 \tag{2.29}$$

In order to make this measure of power comparable with the power generated by devices of different characteristics under different flow and wave conditions, it is important to find a common ground by normalising it.

## Power coefficient

The power coefficient ($C_P$) is a non-dimensional measure of the power extracted from the flow by the rotor divided by the power available in the water in the absence of the rotor (Equation 2.29):

$$C_P = \frac{\text{Rotor power}}{\text{Power in the water}} \tag{2.30}$$

$$C_P = \frac{P}{\frac{1}{2} \cdot \rho \cdot A_{rotor} \cdot U_1^3} \tag{2.31}$$

where $P$ is the power generated by the rotor, $\rho$ is the water density, $A_{rotor}$ is the rotor area and $U_1$ is the flow velocity measured.

### Lanchester-Betz limit

Regardless of how efficient a turbine is, there is a maximum amount of power a turbine can extract from the flow. This limit is known as the Lanchester-Betz limit. If all the energy of the incoming flow were to be extracted, the flow velocity in location (3) in Figure 2.6 would be zero and the turbine would have no wake. In reality, this is not the case. This limit is associated to the expansion of the stream-tube in the wake of the turbine due to the flow velocity deficit. Therefore, the cross-section upstream of the rotor is smaller than the disc area and the cross-section downstream of the rotor is larger than the disc area. This change in the cross-section along the stream-tube is what limits the maximum power a turbine could theoretically extract from the flow. When $P$ from Equation (2.31) is replaced by Equation (2.29), we get :

$$C_P = 4a(1-a)^2 \tag{2.32}$$

Differentiating Equation (2.32) and equating to zero yields the maximum power ($C_{P_{MAX}}$) a turbine can extract from the flow:

$$\frac{dC_P}{da} = 4\,(1-a)\,(1-3a) = 0 \tag{2.33}$$

solving for $a$:

$$a = \frac{1}{3} \tag{2.34}$$

replacing $a$ on Equation (2.32) gives us $C_{P_{MAX}}$:

$$C_{P_{MAX}} = 4 \cdot \frac{1}{3}\left(1-\frac{1}{3}\right)^2 = \frac{16}{27} = 0.5926 \tag{2.35}$$

This means that a turbine cannot extract more than $\sim 60\%$ of the flow energy.

## Thrust coefficient

The incoming flow not only generates a torque that, in turn, generates power but it goes hand in hand with thrust loading. Similar to $C_P$, the thrust coefficient ($C_T$) is a non-dimensional measure of the thrust experienced by a turbine's rotor during power extraction.

For calculating the coefficients, the following definition is used:

$$C_T = \frac{\text{Thrust force}}{\text{Dynamic force}} \tag{2.36}$$

$$C_T = \frac{T}{\frac{1}{2} \cdot \rho \cdot A_{rotor} \cdot U_1^2} \tag{2.37}$$

where $T$ is the thrust experienced by the rotor, $\rho$ is the water density, $A_{rotor}$ is the rotor area and, $U_1$ is the flow velocity measured.

It is worth noting that the $C_T$ is related to $U^2$, whereas $C_P$ is related to $U^3$ (Equation 2.31). meaning that $C_P$ is more sensitive than $C_T$ to small changes in the inflow velocity.

## Tip-speed-ratio

Tip-speed-ratio ($TSR$) is the ratio between the tangential speed at the tip of the blades and the flow velocity perpendicular to the rotor plane. When looking into the loading and performance of a turbine, $C_T$ and $C_P$ are usually plotted against the $TSR$ of the rotor. This allows for a better comparison of different turbines regardless of the rotor diameter, flow velocity or wave conditions.

$$TSR = \frac{\text{tangential speed of tip blade}}{\text{flow velocity}} \tag{2.38}$$

$$TSR = \frac{\omega_{rotor} r}{U_1} \tag{2.39}$$

where $\omega_{rotor}$ is the rotor's rotational speed in rad/s, $r$ is the rotor radius and $U_1$ is the flow velocity measured.

## Vortex shedding

Going back to Figure 2.1, the flow past the support structure of a turbine could potentially generate vortex shedding. According to White (2010), vortex shedding (Figure 2.7) is the phenomena that occurs when a fluid flows past a body, generating oscillations in the fluid behind the body and in the body itself. The vortex shedding frequency $f$ in Equation (2.40) depends on the size of the body and the speed of the fluid. Vortex shedding can lead to fatigue loads that could potentially damage turbine components. It is also related to the non-dimensional Strouhal number St.

**Figure 2.7:** Example of a von Karman vortex street showing vortex shedding. Taken from van Dyke (1982)

$$f = \frac{U \cdot \mathrm{St}}{D} \tag{2.40}$$

where $f$ is the vortex shedding frequency, $U$ is the flow velocity, St is the Strouhal number and $D$ is the diameter of the cylinder. The Strouhal number is non-dimensional. It is associated to a flow at speed $U$ past a submerged body with a characteristic geometry (Lienhard, 1966). The number describes the mechanics of oscillating flows. The St number for cylinders can be selected from graphs as a function of Re (Figure 2.8).

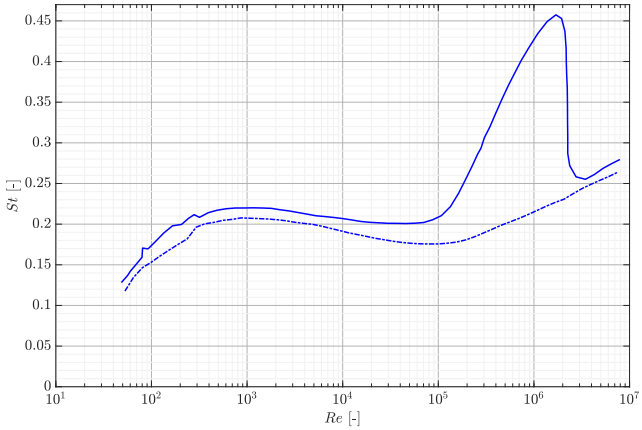


**Figure 2.8:** St number for cylinders in steady flow plotted against Re. Solid line is for smooth surfaces and dashed line for rough surfaces. Adapted from Lienhard (1966)

## Drag force

The drag force is the resistive force acting between the flow and a submerged obstacle (White, 2010). In the case of a tidal turbine, the drag force of the tower needs to be calculated as it is not accounted for in the Actuator Disc Theory. The drag force of a generic cylindrical tower can be expressed as:

$$F_D = \frac{1}{2} \cdot \rho \cdot U^2 \cdot C_D \cdot A_{tower} \tag{2.41}$$

where $\rho$ is the water density, $U$ is the flow velocity, $C_D$ the drag coefficient, in this case of a cylinder perpendicular to the flow and $A_{tower}$ the projected area of the tower (generally a rectangle) that gives the influence of the size.

The drag coefficient ($C_D$) is a dimensionless quantity that quantifies the influence of the shape of the body on the drag force experienced in a moving fluid (see e.g. White, 2010). Figure 2.9 shows the $C_D$ for a cylinder against Re.

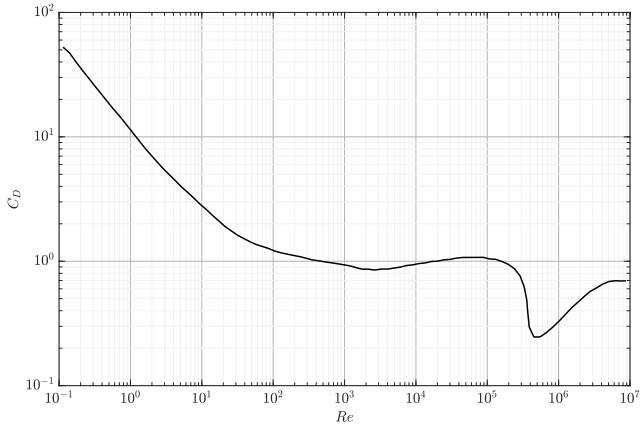


**Figure 2.9:** Drag coefficient for cylinder. From White (2010)

## Array effects

Once the hydrodynamics of a turbine in a marine environment are estimated, further effects can be considered. Such is the case of array effects. In order to capture as much energy as possible from the flow at a high energetic site, multiple turbines should be installed in arrays. The device within an array will interact between its neighbouring devices. A turbine's wake will have a direct impact on the loading and performance of the devices behind it. Careful planning has to be taken into consideration when designing an array layout. Relative position between turbines will play an important part in the performance of the whole array. Using 15 cross-flow turbines in 5 different layouts, Sutherland et al. (2018) observed a variation of up to 19% on the $C_P$ of individual turbines within the arrays, indicating that the positioning of the turbines is important. An increasing streamwise spacing between turbines increase power output, as well as staggering row arrangements. And, the lateral spacing between turbines has a 'sweet spot' in which an optimal blockage was observed. Ouro et al. (2019) noted that the $C_P$ of turbines 8 diameters (8D) behind another row of turbines had a 30% deficit. This means that further spacing should be considered when designing an array. If a 20 m rotor was used, a steamwise gap between turbines should be not less than 160 m ($8D = 8 \times 20 = 160$).

## 2.4 Model, laboratory and scaling effects

When testing a scaled device in a laboratory, several effects need consideration. The nature of scale testing in a controlled environment lacks variables that will be present in the real world that might have an impact in the full-scale devices. These effects are called, model, laboratory and scaling effects.

### Model effects

Model effects are those that are specific to either a scale model or a full-scale model but not both. Examples of model effects are relative surface roughness. If a scale model and a full-scale device use the same materials, the surface roughness relative to the size of the scale model and full-scale device will be different and could have implications in the fluid-structure interactions. In real marine conditions, there is wind in the sea surface that could have an impact in floating turbines. Water density and salinity will also be different. The presence of animals and potential risk of collisions is also something that would not be present in scale model testing.

### Laboratory effects

Laboratory effects refer to any flow feature specific to a laboratory in particular. Gaurier et al. (2015) did a 'Round Robin' test campaign in which they tested the same scale tidal turbine model in four different facilities: two towing tanks and two recirculating tanks. The main difference was the onset turbulence which, in turn, has a direct impact in the loads fluctuations. Compared to recirculating tanks, towing tanks present no turbulence intensity and no velocity depth profile (Salvatore et al., 2014). A laboratory effect associated to recirculating tanks was observed by Payne et al. (2018), where the current had a transverse asymmetry in the tank due to the two impellers rotating in the same direction to generate the current. Like these examples, each facility will have its unique characteristics and careful characterisation of the flow should be performed prior to any device testing. Other examples of laboratory effect include wave generation method (hinged paddle, piston, etc.) and how these waves are absorbed (artificial beaches or dynamic paddles). Another laboratory effect that depends on the facility and the model is the blockage ratio.

### Blockage ratio

A limitation of laboratory testing is the finite extent of the cross-section of flumes and tanks where a model rotor occupies a fraction of the entire cross-sectional area of the facility. As this ratio increases, more flow is forced through the rotor as there is nowhere else it can go, increasing the $C_P$ to unrealistic values that can exceed the Betz limit seen in Chapter 2 (Garrett and Cummins, 2007; Schluntz and Willden, 2015). This is known as blockage ratio and is defined as:

$$\text{Blockage ratio} = \frac{A_{rotor}}{A_{tank}} \tag{2.42}$$

where $A_{rotor}$ is the swept area of the rotor and $A_{tank}$ is the cross-sectional area of the testing facility. Typically, it is preferred to have blockage ratios below 0.05 to avoid any influence on the $C_P$.

## Scaling effects

There are three forces that play a major role in the interaction between structures and fluids: inertial, viscous and gravitational forces (see e.g. Thiébaut, 2015). And, depending on the phenomenon investigated, the relative magnitude of these forces will vary (see e.g. Payne, 2008). This relative magnitude is characterised by two non-dimensional ratios: the Reynolds number (Re) and the Froude number (Fr). For an in-depth analysis on scaling effects, see, for example, Newman (1977).

### Reynolds similitude

For tidal turbines, Re is usually calculated based on the blade chord. For the case of the cylindrical support structure, the Re number is based on the diameter of the tower.

In case of laboratory testing of tidal turbines, blade aerodynamics will be governed by Re as will vortex shedding and drag forces.

As per Equation (2.2), Re is the ratio between inertial and viscous forces:

$$\text{Re} = \frac{\text{Inertial forces}}{\text{Viscous forces}} = \frac{F_i}{F_v} \propto \frac{\rho U^2 l^2}{\mu U l} = \frac{\rho U l}{\mu} = \frac{U l}{\nu} \tag{2.43}$$

where:

$$\nu = \frac{\mu}{\rho} \tag{2.44}$$

where $\rho$ is the water density, $U$ the flow velocity, $l$ is characteristic linear dimension, $\mu$ the kinematic viscosity and $\nu$ the dynamic viscosity.

## Froude similitude

Waves are gravity-driven so using Froude scaling when dealing with wave related phenomena is logical as it relates inertial and gravitational forces (Schmitt and Elsäßer, 2017).

The ratio between inertial and gravitational forces is given by the Froude number Fr:

$$\text{Fr} = \frac{\text{Inertial forces}}{\text{Gravitational forces}} = \frac{F_i}{F_g} \propto \frac{\rho U^2 l^2}{\rho g l^3} \tag{2.45}$$

where $g$ is the gravitational acceleration and $l$ a characteristic length.

The Froude similarity between scale model (sub-indices M) and full scale (sub-indices F) is given by:

$$\frac{U_M^2}{g l_M} = \frac{U_F^2}{g l_F} \tag{2.46}$$

$$\frac{U_M}{\sqrt{g l_M}} = \frac{U_F}{\sqrt{g l_F}} \tag{2.47}$$

Solving for $U_F$:

$$U_F = U_M \sqrt{\frac{l_F}{l_M}} \tag{2.48}$$

Where the scale factor $S$:

$$S = \frac{l_F}{l_M} \tag{2.49}$$

then:

$$U_F = U_M \sqrt{S} \tag{2.50}$$

Table 2.1 shows the scaling factors $S$ for common parameters.

**Table 2.1:** List of Froude scaling factors $S$ for common parameters.

| **Physical parameter** | **Scaling factor** $S$ | **Equivalent unit** |
|---|---|---|
| Length | $S$ | m |
| Volume | $S^3$ | $m^3$ |
| Time | $\sqrt{S}$ | s |
| Velocity | $\sqrt{S}$ | m/s |
| Acceleration | 1 | $m/s^2$ |
| Mass | $S^3$ | kg |
| Density | 1 | $kg/m^3$ |
| Force | $S^3$ | N |
| Pressure | $S$ | $kg/m^2$ |
| Torque | $S^4$ | Nm |
| Power | $S^{3.5}$ | Nm/s |
| Angle | 1 | $^\circ$ |
| Angular velocity | $\sqrt{1/S}$ | rad/s |
| Angular acceleration | $1/S$ | $rad/s^2$ |

As presented by McCombes and Iyer (2012), the rotor loads are dominated by the wave forces. Thus, Froude similitude was chosen for scaling the rotor dimensions and wave and current parameters. The application of Froude scaling on the rotor dimensions is presented in Chapter 4. The flow parameters scaling is reviewed in Chapter 5. It is worth mentioning that when assuming a Froude similitude ($Fr_M = Fr_F$), achieving Reynolds similitude ($Re_M = Re_F$) is not possible.

## 2.5 Fatigue loading

Fatigue loads are any loads that fluctuate over a period of time. According to Shigley and Mischke (1989), materials can fail under the action of these cyclic loads at stress levels that are below the ultimate strength of the material or even below the yield strength. Figure 2.10 shows the stress-cycles (S-N) curve (top) and the stress-strain curve (bottom) of steel. Some of the characteristic points match in both curves, like ultimate strength and yield strength. If a combination of stress and

number of cycles fall between the yield strength and endurance limit on the S-N curve, a material will fail at stresses below the yield strength. Hence, consideration must be taken when designing a component that will experience fatigue loads. Any cyclic loads that fall below the endurance limit will not have a negative impact on the material.

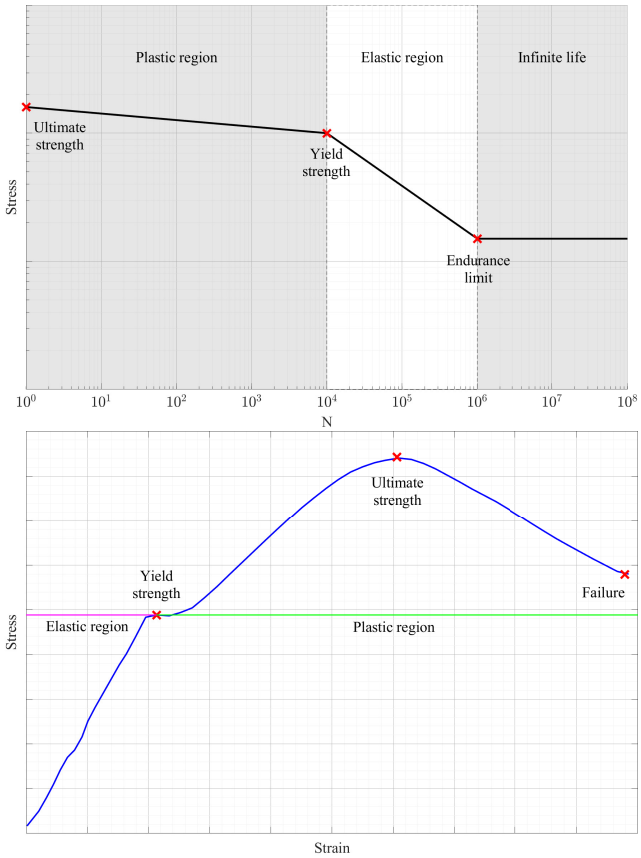


**Figure 2.10:** Typical steel S-N curve (top) and Stress-Strain curve (bottom). From SIEMENS (2019)

# Chapter 3

# Literature review

## 3.1 Scope of literature review

This section commences with a review on field measurement studies to have a better understanding of how real flows behave at potential tidal sites. It then moves on to a review of turbine model testing in current-only conditions and in combined waves and currents, both in laboratories and tidal sites suitable for small-scale models.

## 3.2 Field measurements of tidal stream

In order to define the model testing conditions that are representative of real sea conditions, and to understand model testing limitations, flow velocity, turbulence intensity ($TI$) and flow directionality have to be studied. The focus of this review is on studies conducted in the British Isles waters. The most commonly used measuring tools are Acoustic Doppler Current Profiler (ADCP) and Acoustic Doppler Velocimeter (ADV).

In Table 3.1, a summary of the different studies in which field measurements have been performed is presented, together with maps (Figure 3.1). Mean speeds in promising tidal sites are typically in the range of 2.5 m/s with associated maxima above 4 m/s. $TI$ average values roughly range between 10% and 12% per tidal cycle. These parameters are used to select the current conditions for the model tests conducted in the present study (Chapter 5).

**Table 3.1:** Summary of flow characteristics from field measurements at potential tidal sites

| **Reference** | **Location** | **Mean $U_d$ [m/s]** | **Max $U_d$ [m/s]** | **TI [%]** | **Max flow asymmetry** | **Depth profile power law** |
|---|---|---|---|---|---|---|
| McCann et al. (2008) | EMEC, Kirkwall, UK | 1.6 | 1.9 | 11 | 10° | $1/7^{th}$ |
| Sutherland et al. (2013) | EMEC, Fall of Warness, UK | 2.4 | 4 | 10 | 4° | N/A |
| Easton et al. (2011) | Inner Sound, Pentland Firth, UK | 2.5 | 4.5 | N/A | 25° | N/A |
| Easton (2013) | Inner Sound, Pentland Firth, UK | 2.5 | 3.2 | N/A | 20° | N/A |
| Goddijn-Murphy et al. (2013) | Inner Sound, Pentland Firth, UK | 2.7 | 4.0 | N/A | 20° | N/A |
| Evans (2014) | Ramsey Sound, Pembrokeshire, UK | 2.5 | 3.8 | N/A | 20° | N/A |
| Milne et al. (2013) | Sound of Islay, UK | 1.0 | 2.5 | 12-13 | 5° | N/A |
| Thiébaut and Sentchev (2016) | Dover Strait, UK | 1.0 | 2.5 | N/A | 10° | $1/6^{th} - 1/7^{th}$ |
| Lewis et al. (2017) | Isle of Anglesey, UK | 1.0 | 1.5 | N/A | 10° | $1/7^{th}$ |
| Gooch et al. (2009) | Puget Sound (four sites), Washington, USA | 0.72-1.95 | 2.12-3.95 | N/A | 0.52°-1.12° | $1/5^{th} - 1/10^{th}$ |
| Sellar and Wakelam (2018) | EMEC, Fall of Warness, UK | 2.77 | 3.4 | 10 | 7° | $1/7^{th}$ |

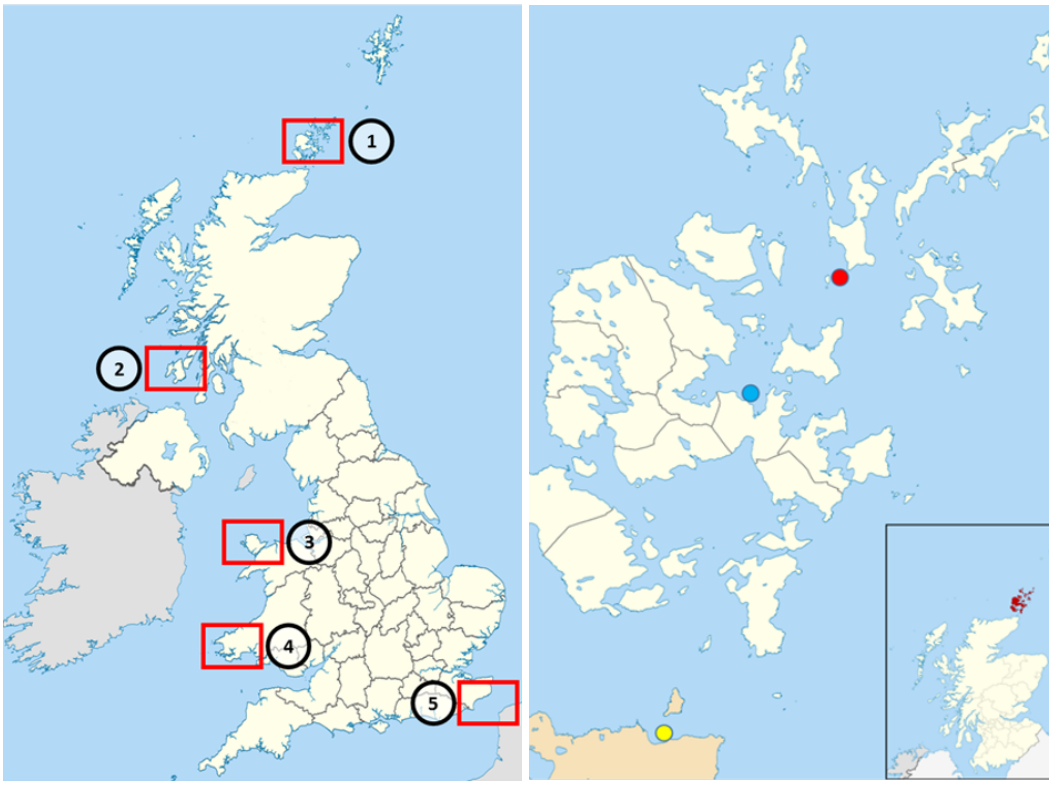


**(a)** ① Orkney, ② Sound of Islay, ③ Isle of Anglesey, ④ Ramsey Sound and ⑤ Dover Strait.

**(b)** Red - Fall of Warness; Blue - Kirkwall; Yellow - Inner Sound, Pentland Firth.

**Figure 3.1:** Locations of the flow measurements studies around the British Isles. a) British Isles; b) Orkney, Scotland. Adapted from Nilfanion (2017).

## 3.3 Laboratory turbine testing

In the exploration of the technical background of Chapter 2, Figure 2.1 showed the different flow variables a turbine is subjected to during a typical laboratory test. For the purpose of structuring this literature review, Figure 3.2 shows a simplified diagram on how the complexity of turbine model testing progresses. The simplest case is that of current-only, in which only flow velocity and $TI$ are considered. Moving to the right, the addition of a yaw angle adds an additional layer of complexity to the tests. Looking down, the superposition of waves and different various angles between waves and current create the most complex tests for which several variables have to be considered and analysed. In the case of towing tank testing, $TI$ does not exist as the flow is stationary and the turbine moves through it. For recirculating tank tests, a current is generated by means of pumps, impellers or similar. Some of

the facilities, like the French Research Institute for Exploitation of the Sea (IFREMER), use flow conditioning screens that control the *TI*. Figure 3.3 shows the typical parameters measured during a laboratory test. Most of the studies presented herein measure rotor thrust and torque and some also incorporate measurements of the blade root bending moments. As will be seen, most of the laboratory studies operate the turbine under constant speed control whereas very few prefer the use of constant torque.

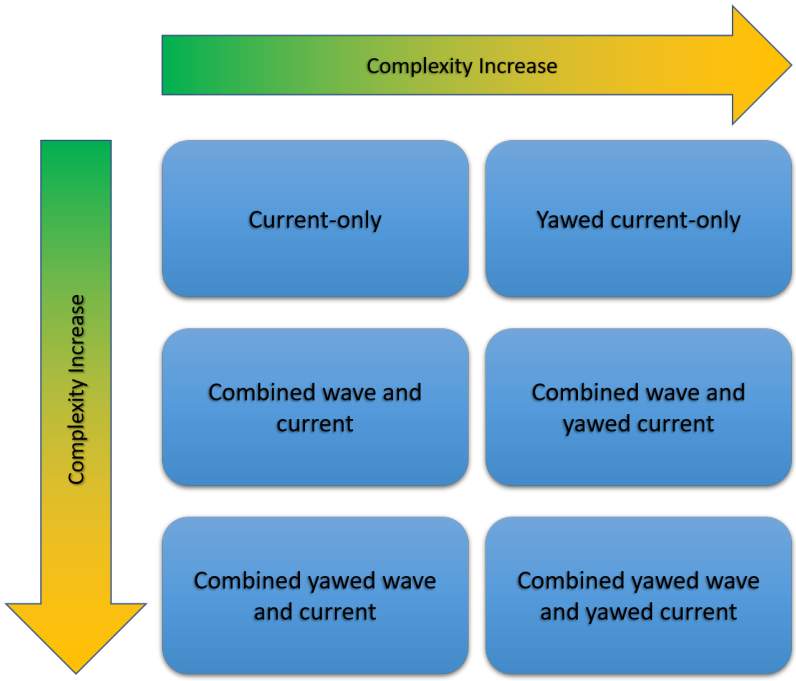


**Figure 3.2:** Progression of testing complexity (added variables).

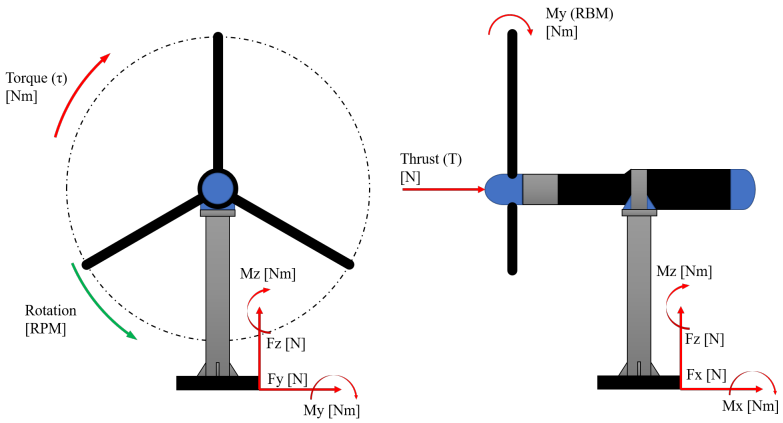


**Figure 3.3:** Typical parameters measured during a turbine model laboratory testing.

### 3.3.1 Tests under in-line current-only conditions

There is an extensive literature on tidal turbine testing based upon physical models. The most basic form of testing is when the current is perpendicular to the rotor plane (Figure 3.2). These tests mainly focus on the effect of different $TSR$, flow velocity and $TI$ on the turbine's performance and loading through the power and thrust coefficients, $C_P$ and $C_T$ respectively.

Doman et al. (2015) ran a series of tests in a towing tank with carriage velocity of 0.5, 0.8, 0.9 and 1.0 m/s within a $TSR$ range of $\sim$2-7 for each velocity. The model was a 1:20 scale turbine with a 0.762 m diameter rotor with NREL S814 blades profile. For velocities above 0.5 m/s, peak $C_P$ and $C_T$ were recorded at $TSR \approx 3.5$ and 4.5, respectively. At 0.5 m/s, the coefficients were lower than for the rest of the velocities due to the low Re number at 0.5 m/s.

With an unconventional six-bladed rotor, Morandi et al. (2016) used a 0.4 m diameter model with inflow velocities varying from 0.78 to 3.0 m/s. The turbine tested was a 1:25 scale model of the Sabella full-scale turbine, a turbine with symmetrical (elliptical) blade profile. The turbine was tested at the CNR-INSEAN recirculating water tank in Rome, over a $TSR$ range of 0 to 5. Similar to Doman et al. (2015), at the lower flow velocities the model shows lower coefficients due to the lower Re number. Peak performance was observed at $TSR \approx 2.5$.

Looking at the performance coefficients in the frequency domain, Chamorro et al. (2013) used a 0.8 m diameter rotor equipped with NACA 44 blade profile at a recirculating tank with flow velocity of 0.4 m/s. A maximum $C_P$ of 0.45 was observed at $TSR$=5.8. In addition, two distinct regimes in the frequency domain were observed: a low frequency range where the $C_P$ seems to be governed by the flow's energy cascade (Kolmogorov slope) and a high frequency range where the $C_P$ seems to be independent of the flow's turbulence. It is also observed that the rotational frequency of the turbine falls within the slower, responsive range of the spectra while the harmonics fall in the higher range. This frequency domain approach forms the basis of some of the present work presented in Chapter 7.

The University of Edinburgh designed and developed a 1.2 m diameter turbine under The Engineering and Physical Sciences Research Council (EPSRC) Extreme Loading of Marine Energy Devices due to Waves, Current, Flotsam and Mammal Impact (X-MED) project. Detail on the turbine design and build is given in Payne et al. (2017a). The turbine was tested by Payne et al. (2017b, 2018) at IFREMER, France with $U$=0.8 m/s and two different $TI$ values (3% and 12%), achieved by use of grids upstream of the turbine. Exploring the turbine instantaneous power in the frequency domain, two distinct sections were observed, one below the turbine rotational frequency $f_0$ where the power spectrum follows the flow velocity spectrum and a second section above the rotational frequency where mechanical, electrical and tower shadow effect have an influence in the power. These findings are in agreement with Chamorro et al. (2013). It was observed that features found on the onset flow spectrum were correlated to features also found on the rotor loads spectrum. The angle averaged root bending moment of blade B1 (Figure 3.4) for the current-only case with $TI = 3\%$ and $TSR = 6.87$ is shown in Figure 3.5. Relating Figure 3.5 to Figure 3.4, the support tower is represented by the dotted black line and the three blades by the green dashed lines. The down-facing notch is associated with the tower shadow effect. The right-to-left asymmetry is believed to be caused by the current generation method at the flume, where both pumps rotate in the same direction, transferring a moment to the flow.

Extending their research to explore the influence of $TI$, Payne et al. (2017a) found that an increase in $TI$ from 3% to 12% caused the $C_T$ and $C_P$ standard deviation to increase from 3% to 10% and from 5% to 18%, respectively. This was a reminder that the level of $TI$ has a direct impact on the loading and performance of the turbine. In addition, Payne et al. (2018) performed a more in-depth analysis of the loading in the frequency domain and average loading on the supporting structure. It was noted that the load spectra are correlated to the upstream flow but only up to half the rotational frequency for the root bending moment coefficient $C_{RBM1}$ (defined by Equation 3.1) and up to three times the rotational frequency for thrust. The magnitude of the peaks associated with the rotational frequency is similar to the

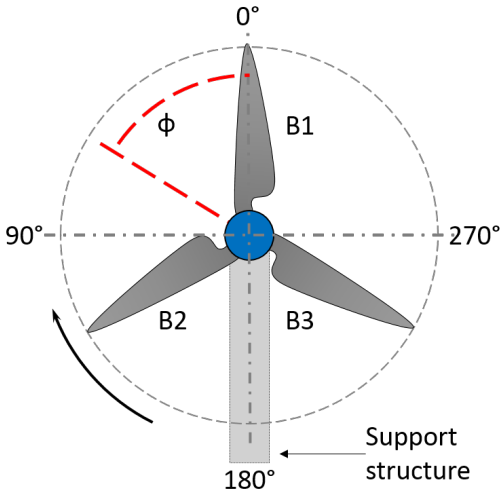


**Figure 3.4:** Front view of the rotor identifying the blades, the stanchion and rotational direction. This schematic is used when analysing polar plots. $\phi$ corresponds to the rotor angular position.

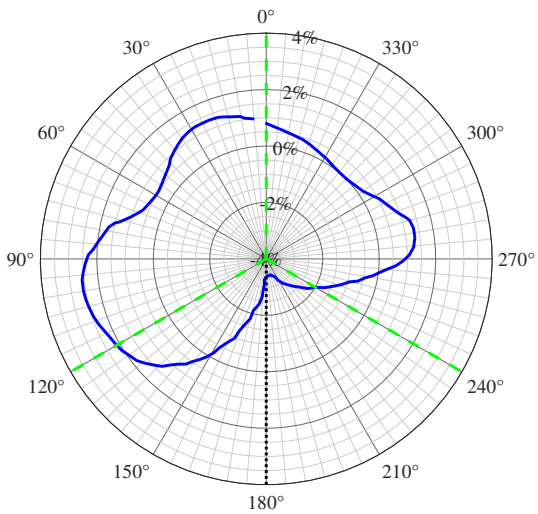


**Figure 3.5:** Angle-averaged root bending moment (RBM) of blade 1 (B1) for current-only case with $TI = 3\%$ and $TSR = 6.87$. Expressed as a percentage of the average RBM. Adapted from Payne et al. (2017b)

magnitude of the peaks associated with the turbulence loads at lower frequencies. For frequencies $f/f_0 > 1$, where $f_0$ is the rotor rotational frequency, the spectra of the $RBM1$ coefficient ($S_{C_{RBM1}}$) have steeper slopes than the flow velocity spectra as seen on Figure 3.6. The forces acting on the rotor plus support structure in the flow direction show mean values of around 10% higher than the thrust average values

acting on the rotor only. However, these values decrease as $TSR$ increases. A more in-depth discussion of the model characteristics is presented in Chapter 4.

$$C_{RBM_1} = \frac{RBM}{\frac{1}{3} \cdot D \cdot \left(\frac{1}{2} \cdot \rho \cdot A_{rotor} \cdot \overline{U^2}\right)} \tag{3.1}$$

where $D$ is the rotor diameter, $\rho$ is the water density, $A_{rotor}$ is the rotor area and $U$ is the flow velocity.

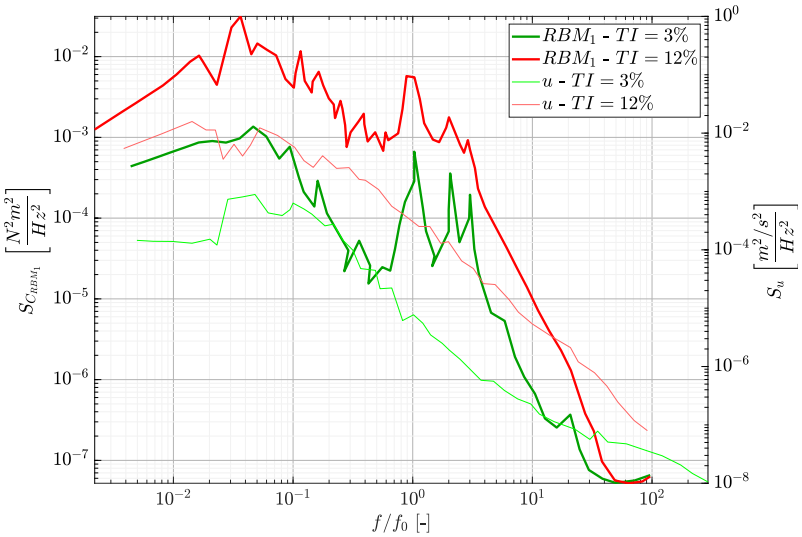


**Figure 3.6:** The left axis is the power spectra of the RBM coefficient of blade 1 (Eq. 3.1), the right axis is the spectral density of the streamwise flow velocity and the horizontal axis is the frequency normalised by the rotor rotational frequency $f_0$. Reproduced from Payne et al. (2018)

## Turbulence-induced loading

A number of studies have explored the influence of inflow turbulence intensity $TI$ on rotor performance and loading.

Mycek et al. (2014) carried out tests in a recirculating tank with 5 different flow velocities ranging from 0.4 to 1.2 m/s using a 0.7 m rotor with a NACA-63-419 blade profile. It was observed that the turbine behaviour is weakly dependent upon the two ambient $TI$ values tested (3% and 15%). In both cases, an optimal $TSR$ range of 3-6 was observed with maximum $C_P$ at $TSR \approx 4$. The $C_T$ curves for both $TI$ cases were almost superimposed. The $C_P$ behaviour at $TI$=3% agrees with results from Bahaj et al. (2007a) and Maganga et al. (2010). The $C_P$ values stay

close to each other except for the lowest flow velocity. At $TI$=15%, the values are more apart from each other. In both cases, the $C_P$ values increase with flow velocity. For $TSR > 3$, standard deviation values for $C_P$ and $C_T$ are up to 2.5 times higher for $TI = 15\%$ than for $TI = 3\%$.

Blackmore et al. (2015) made use of two turbines, Southampton University's and the one of IFREMER (e.g. Gaurier et al., 2015). The Southanmpton rotor had 0.8 m diameter with NACA 48 blades fitted, and the IFREMER rotor 0.7 m diameter with an unreported blade profile. Both turbines were tested at IFREMER's recirculating tank. The turbines were tested under six different inflow conditions with $TI$ ranging from 4.6% to 25% and integral length scales from 0.15 to 0.76 m. It was concluded that for the extreme cases tested, increasing the $TI$ can reduce $C_P$ and $C_T$ by over 10% and an increase in integral length scales can increase the $C_P$ and $C_T$ by over 10%. The rotors experienced an increase in torque and thrust fluctuations for increasing $TI$ values. Increasing the integral length scales show an even larger increase in these fluctuations.

The following year, Blackmore et al. (2016) with the Southampton University turbine expanded their results by adding blade root bending moments analysis. From their tests, higher $TI$ reduces average values of $C_P$, $C_T$ and blade root bending moments but increases their fluctuations. Higher integral length scales increase the performance coefficients and blade root bending moments with fluctuations higher than the ones experienced by an increased $TI$, in line with the findings of Mycek et al. (2014). *RBM* fluctuations were seen to increase up to five times for the most extreme $TI$ case compared to the lower $TI$ cases.

Vinod et al. (2017) tested a small 0.14 m diameter rotor in a recirculating tank with three $TI$ levels (1.5%, 3.7% and 9.2%). The $C_P$ and $C_T$ mean values for the different $TI$ levels remained almost unaffected but the standard deviation values in Figure 3.7 are twice as high for the higher $TI$ case at $TSR >$3.5.

Mullings et al. (2017) made further analysis on the experiments performed by Payne et al. (2017b). They concluded that to be representative of the nature of a tidal cycle, it is better to consider a variable $TI$ instead of the typically-used constant

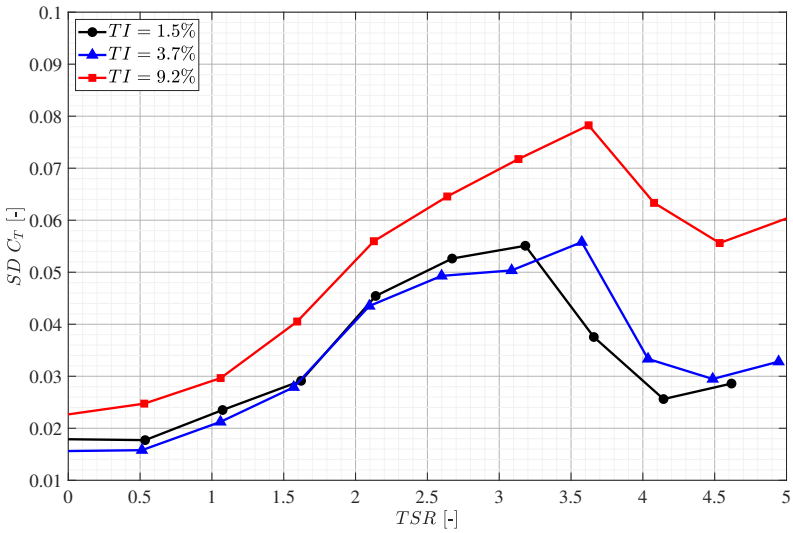


**Figure 3.7:** Standard deviation of $C_T$ for three $TI$ levels. From Vinod et al. (2017)

values, with the latter overestimating the loading. However, the effects of waves on the rotor are greater than the effects of $TI$. They also observed that regular waves usually used in laboratory studies over-estimate the more realistic irregular waves found in real sea conditions by a factor of 1.5-2.

The general consensus is that as $TI$ increases, the standard deviation of the loads increases while average values remain unchanged. The same behaviour is observed when increasing the integral length scales but at higher rates.

Table 3.2 shows a brief summary of the different testing parameters for all the current-only studies presented in this section. Most of the studies utilised different blade profiles, giving each model a characteristic loading and performance profile. Due to the variety of rotor designs and test conditions in all the studies, all the coefficient data have different $TSR$ values at which the maximum $C_P$ was observed.

### 3.3.2 Tests under yawed current-only conditions

Some studies assess the effect of yaw angle between the main flow direction and the turbine's axis, i.e. conditions when the turbine is yawed with respect to the dominant flow direction.

One of the first studies utilising an instrumented turbine model was Bahaj et al. (2007b). They used a 0.8 m rotor in a towing tank and cavitation tunnel at two different rotor depths. Inflow speeds ranged from 0.8 to 1.5 m/s and the yaw an-

**Table 3.2:** Summary of findings of current-only tidal turbine testing.

| Reference | D [m] | U [m/s] | Blade profile | Notes |
|---|---|---|---|---|
| Doman et al. (2015) | 0.762 | 0.5-1.0 | NREL S814 | Max $C_P$ at $TSR \approx 4$ |
| Morandi et al. (2016) | 0.4 | 2.76 | Symmetrical ellipse | Max $C_P$ at $TSR \approx 2.5$ |
| Chamorro et al. (2013) | 0.8 | 0.4 | NACA 44 | Max $C_P$ at $TSR \approx 5.8$ |
| Payne et al. (2017a) | 1.2 | 0.8 | NACA 63-8xx | Max $C_P$ at $TSR \approx 6.5$ |
| Tian et al. (2018) | 1.2 | 0.5 | FF-77-W | Max $C_P$ at $TSR \approx 6$ |
| Mycek et al. (2014) | 0.7 | 0.4-1.2 | NACA-63-419 | Max $C_P$ at $TSR \approx 4$. At higher $TI$ values, the $SD$ of $C_P$ and $C_T$ are up to 2.5 times higher than for lower $TI$ values |
| Blackmore et al. (2015) | 0.7-0.8 | 0.7-0.8 | NACA 48xx | Max $C_P$ at $TSR \approx 6.5$. Integral lengthscales have a higher impact on the turbine performance than ambient $TI$ |
| Vinod et al. (2017) | 0.14 | 0.86 | SG6043 | Max $C_P$ at $TSR \approx 4.5$. At higher $TI$ values, the $SD$ of $C_P$ and $C_T$ are up to 2 times higher than for lower $TI$ values |

gle between the main current direction and the rotor shaft varied from 0° to 30°. Findings indicate that the highest performance for the turbine model with NACA 63-8xx blade profiles was at $TSR = 5-7$ with a blade pitch angle of 20° (Figures 3.8 and 3.9). The power coefficient ($C_P$) of the turbine decreases as the yaw angle increases. This is as would be expected qualitatively due to the rotor experiencing only an in-line component of the total flow. From the two rotor depths, the closest to the surface has reduced coefficients. Batten et al. (2007, 2008) validated their numerical method with the experiments performed by Bahaj et al. (2007b). Their Blade Element Momentum (BEM) model matches the experimental $C_P$ for $TSR<7$ but it under-predicts the $C_T$ by about 10%.

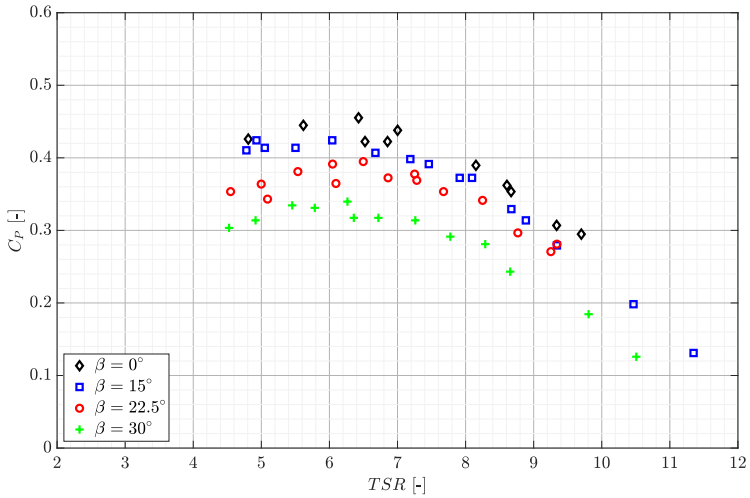


**Figure 3.8:** Power coefficient ($C_P$) vs tip speed ratio ($TSR$) curves at different yaw angles ($\beta$) with pitch angle of 20°. Adapted from Bahaj et al. (2007b).

Maganga et al. (2009) tested a 0.7 m diameter turbine at IFREMER with five different current angles (-10°, 0°, 10°, 15° and 20°) and three different turbulence conditions (5%, 8% and 25%). They concluded that the yaw angle caused a significant loss of power and a seemingly unaffected thrust for yaw angles lower than 10° and thrust values of up to 15% lower for yaw angles over 10°. At -10° yaw the torque is higher than at 0° yaw. In a subsequent publication, Maganga et al. (2010) presented further analysis on the same tests conducted at IFREMER. In this subsequent work, it was confirmed that the thrust suffers little-to-no effect for yaw angles up to ±10°. However, for higher angles thrust can be up to 15% lower. Torque

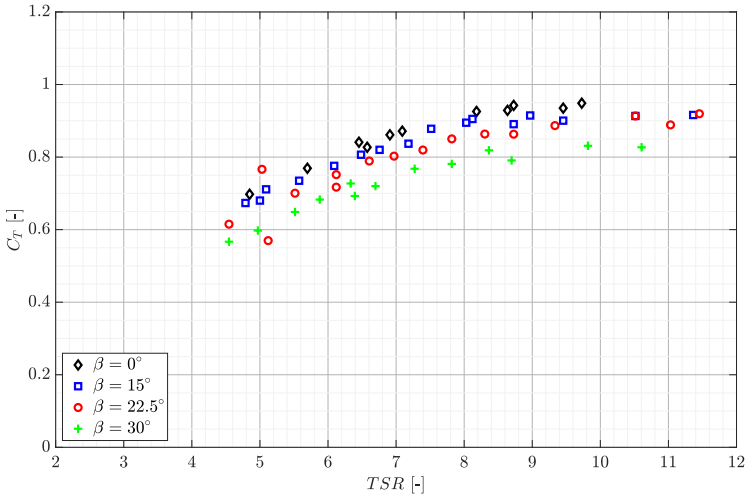


**Figure 3.9:** Thrust coefficient ($C_T$) vs tip speed ratio ($TSR$) curves at different yaw angles ($\beta$) with pitch angle of 20°. Adapted from Bahaj et al. (2007b).

reduces as the angle of the incoming flow increases. Contrary to their previous publication, the torque data does not show the highest values at -10°. Unfortunately, this observation is not commented upon by the authors. Analysis in the frequency domain of the thrust force does not show any significant differences between the different yaw angles. $C_P$ and $C_T$ curves with $TSR$ are not reported. $TI$ of 25% shows a 15% reduction in $C_P$ compared to $TI$=8%.

Fabre et al. (2015), based on the full-scale PLAT-O device (see Chapter 1), designed a model of two pontoons and one rotor with a 0.571 m diameter to assess the influence of the structure on the turbine performance. Tests were in a towing tank with carriage velocity of 0.75 m/s. The maximum $C_P$ and $C_T$ were reported at $TSR \approx 4$. The results show a 7% increase in $C_P$ when the turbine is mounted with the pontoons compared to the isolated turbine. In the cases with yaw angle of 5°, 10°, 15° and 20°, $C_P$ and $C_T$ decrease as the yaw angle increases. $C_T$ decreases as the yaw angle increases at a higher rate than $C_P$. It was observed that power evolves with the cube of the cosine of the yaw angle. $C_T$ at maximum $C_P$ is compared at different yaw angles to understand the mechanical loads when the power production is at its highest. In the $C_T$ case, there is no clear trend between the isolated turbine and the pontoon mounted (Figure 3.10).

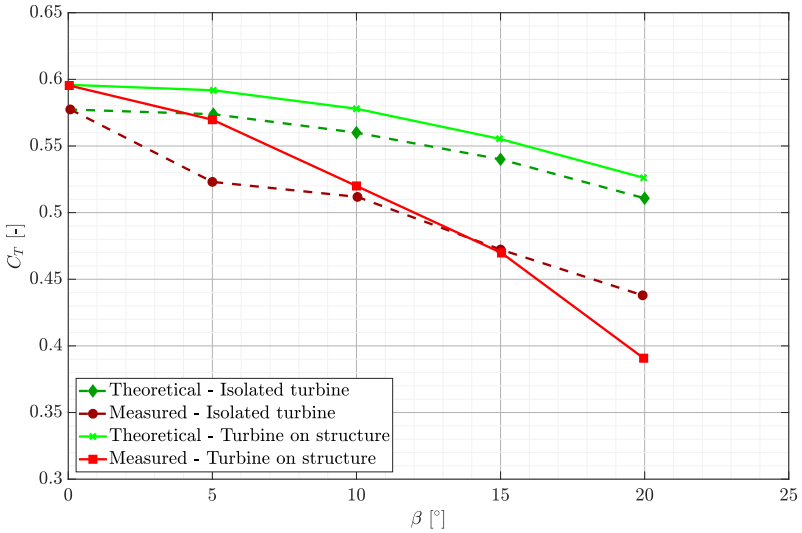


**Figure 3.10:** $C_T$ at maximum $C_P$ ($TSR = 4$) for different yaw angles at 0.75 m/s. From Fabre et al. (2015)

Table 3.3 summarises the different testing parameters for all the yawed current studies in this section. The main consensus is that as yaw angle increases, the power and thrust coefficients decrease. This impact is not as noticeable for small yaw angles ($\beta \approx 10°$).

### 3.3.3 Tests under combined wave and current conditions

Potential tidal sites are not free from the presence of waves and these waves have an influence on the flow and therefore, on the devices. Despite the waves approaching from a predominant direction in the field, waves from all directions are possible. Most of the studies in the literature utilise the same incidence angle for current and waves, with the situation of opposing waves studied in a few cases, mostly, the studies agree that wave-induced forces influence loading fluctuations rather than average loads.

Barltrop et al. (2006) studied blade root bending moment of a 0.35 m diameter rotor with blade profile NREL S814 in the Strathclyde University towing tank. The range of carriage speeds was from 0 to 1.6 m/s, the wave height was 0.15 m, at wave frequencies of 0.5 and 0.833 Hz. The bending moments were observed to fluctuate greatly, especially with the steeper waves. The bending moments calculated numerically showed higher values when the waves were normal to the rotor's plane. Sub-

**Table 3.3:** Summary of findings of yawed current-only tidal turbine testing.

| Reference | D [m] | U [m/s] | H [mm] | Tw [s] | Blade profile | Notes |
|---|---|---|---|---|---|---|
| Bahaj et al. (2007b) | 0.8 | 0.8-1.5 | N/A | N/A | NACA 63-8xx | Max $C_P$ at $TSR \approx 6$. |
| Maganga et al. (2009) | 0.7 | 0.75 | N/A | N/A | Undisclosed | No $C_P$ values reported. Higher the $TI$, lower the $C_P$. Yaw angles lower than 10° show no effect on the loading. |
| Fabre et al. (2015) | 0.571 | 0.8 | N/A | N/A | Undisclosed | Max $C_P$ at $TSR \approx 4$. As yaw angle increase, $C_P$ and $C_T$ decrease. |

sequently, Barltrop et al. (2007) upgraded their rotor to a 0.4 m diameter with blade profile NREL S814. Carriage speed used ranged from 0.1 to 1.4 m/s. Wave height and frequency ranged from 0.02 to 0.14 m and 0.5 to 0.833 Hz, respectively. It was observed that an increase in wave height increases the average values of torque and thrust. The torque signal showed more sensitivity to the wave height increase. An increase in rotational speed from 90 to 127 RPM, showed a near-doubling of the torque and thrust signals. When testing the turbine at fixed $TSR \approx 2.34$ with a range of rotational speeds and flow velocities, the torque suffers a reduction at around 110 RPM which becomes more noticeable for waves with higher frequency. This reduction in torque implies a stall condition which, as a consequence, generates a peak in the thrust. Time histories of thrust show that peak values of thrust can be double the mean values in the absence of waves. Instantaneous torque values can vary by up to 40% when the highest waves are applied.

Lust et al. (2013) used a 0.8 m diameter rotor in a towing tank with flow velocity of 1.68 m/s and two different wave conditions (H=0.18 m, Tw=2.3 s and H=0.09 m, Tw=1.6 s) at two different rotor depths. Their BEM model generally agreed with the experiments, but it overestimated $C_P$ and underestimated $C_T$ at $TSR > 7$. Peak $C_P$ was observed at $TSR \approx 6.5$ in both the experiments and the BEM modelling. Turbine performance was not observed to be dependent upon waves, although a small increment in $C_P$ was visible when the rotor was closer to the surface, maybe associated with the influence of the waves on the current velocity known as Stokes drift. Maximum and minimum values of torque and thrust happen at wave crests and troughs, respectively, as expected. Rotational speed fluctuations are also noticeable with the addition of waves. From the same institution and in the same facilities but with a 0.46 m turbine, Luznik et al. (2013) observed that average turbine loading was unaffected with and without waves. However, in the presence of waves the turbine could not operate at $TSR < 5$ due to the induced stall by the wave-induced fluctuations in torque.

Galloway et al. (2014) tested a 0.8 m diameter rotor turbine with blade profile NACA 48 with varying thickness in a towing tank. The tests included five yaw

angles (-15°, 0°, 7.5°, 15° and 22.5°) and four wave conditions (H=0.075-0.15 m and Tw=1.33-2.86 s). It was observed that the maximum *RBM* could increase by a factor of 1.75 the median value when the yaw angle was perpendicular to the rotor plane and the wave height and frequency were 0.1 m and 2.86 Hz, respectively. The wave period was found to have more significant effect on the blade loads than the wave height. It was observed that out-of-plane blade root bending moment is more sensitive to waves than to yaw angles. However, when considering the rotor as a whole, the yaw angle has a greater influence, reducing $C_P$ and increasing $C_T$ for increasing yaw angles.

Fernandez-Rodriguez et al. (2014) used a 0.27 m diameter turbine in a recirculating tank with a flow velocity of 0.46 m/s and two opposing wave conditions. Frequency analysis between current-only and current-with-wave showed no difference in the trend of the thrust force spectra except for the additional peaks associated with the wave period. This phenomenon was also observed by Payne et al. (2017a).

### Wave-induced loading fluctuations

The following studies have similar findings in which the addition of waves to the incoming inflow has little influence on the mean performance and loading of the turbine, but the standard deviation or fluctuations around the mean values are seen to increase by up to three times compared to the cases with no waves.

Galloway et al. (2010) tested at a towing tank a 0.8 m diameter rotor with blade profile NACA 48 with varying thickness. $C_P$ and $C_T$ at yaw angle $\beta = 22.5°$ with no waves showed little-to-no difference to the 0° yaw case. At $\beta = 15°$ the coefficients showed lower values than the 0° yaw case and at $\beta = 22.5°$ the coefficients were even lower. $C_P$ and $C_T$ values at 0° yaw angle with waves showed the same values as the no-waves condition. In contrast, the 25° yaw angle case showed a reduction of 20% in $C_P$ compared to the 0° yaw angle case. Torque and thrust fluctuations can be greater than 35% of the mean rotor loads when waves are present. Subsequently, Galloway et al. (2011) compared the power and thrust coefficients from their previous tests against BEM modelling with blockage correction. This validation showed a good agreement between the numerical and experimental data.

Gaurier et al. (2013) tested a 0.9 m rotor and de Jesus Henriques et al. (2014a) a 0.5 m rotor, both using a recirculating tank. Gaurier et al. (2015) used a 0.6 m/s current with waves ranging from 0.14 to 0.8 m and 0.42 to 2.0 Hz. de Jesus Henriques et al. (2014a) used a 0.46 m/s current with two wave forms (H=0.041 m; Tw=0.71 s and H=0.078 m; Tw=0.91 s). Both research groups observed that the wave-induced load fluctuations show a standard deviation two to three times higher than for the current-only case. These fluctuations represent a significant contribution to risk of failure. Average $C_P$ and $C_T$ values remained unchanged with the addition of waves, in line with the earlier findings of Barltrop et al. (2007).

Ordonez-Sanchez et al. (2016) tested a turbine with a 0.5 m diameter with a Wortmann FX 63-37 blade profile at the CNR-INSEAN towing tank in Rome, Italy. Two flow velocities (0.5 and 1 m/s) and three wave heights (0.4, 0.3 and 0.2 m) with Tw=2 s were tested. As found by previous authors, average $C_P$ and $C_T$ values remained unchanged for wave cases but standard deviation increased with waves. There was a pattern in the RBM time series spanning over several cycles that linked the blades' position in the water column and the passage of the waves, indicating a relationship between the wave period, blade angular position and rotational frequency.

de Jesus Henriques et al. (2014b, 2016) performed experiments with a 0.5 m turbine with a variant of the Wortmann FX 63-137 blade profile in a flow velocity of 0.92 m/s at the University of Liverpool recirculating flume. They explored the influence of blade pitch angle ranging from 3° to 18° with 3° increments on the performance of their turbine under the influence of three wave conditions (H=0.058, 0.082 and 0.113 m and Tw=0.81, 0.75 and 0.69 s. Agreeing qualitatively with Ordonez-Sanchez et al. (2016) and Gaurier et al. (2013), it was found that mean values of $C_P$ and $C_T$ remain unchanged while standard deviation values increased almost eight-fold for $C_P$ and three-fold for $C_T$ when compared with the current-only case. Increasing the blade pitch angle above 6° proved to lower thrust at a higher rate than power. Additionally, standard deviation of power and thrust also increased with the pitch angle above 6°.

Guo et al. (2017), with a 0.8 m rotor turbine in a towing tank with carriage speeds of 0.56 and 0.68 m/s and wave height ranging from 0.05 to 0.10 m and wave period ranging from 1.0 to 3.0 s noted that a disturbance of 15% of the mean flow velocity due to the passing waves can induce fluctuations on the loads up to 50% of the mean.

Tables 3.4 and 3.5 show a brief summary of the different testing parameters for all the combined wave and current studies discussed in this section. The main findings are that average $C_P$ and $C_P$ are not affected by the addition of waves. However, the *SD* of the coefficients can be up to eight times larger than the current-only cases.

## 3.4 Field turbine testing

Some studies have been performed in natural bodies of water including lakes and tidal sites suitable for small-scale devices. In the case of lakes, turbulence intensity levels are comparable to those of towing tanks. Conditions in tidal sites suitable for small-scale devices are closer to the conditions found in recirculating flumes. One of the advantages of using natural bodies of water is the possibility to use larger scale models and multi-device arrays.

In the UK, The University of Belfast designed and developed a 1.5 m diameter, 4-bladed turbine (Figure 3.11) leading to several research outcomes. One of these research outcomes is from Jeffcoate et al. (2014). In their research, they tested the turbine in steady waters at Montgomery Lough, NI, UK with a towing catamaran and in a turbulent environment moored at Strangford Lough Narrows, NI, UK. The turbine has a maximum $C_P$ of 0.31 at $TSR$=3.1 for the lake tests and 0.24 at $TSR$=3 for the moored tests, which represent a 24% reduction in power. The moored tests have higher temporal variations in power, torque and RPM compared to the lake tests. Atcheson et al. (2015) produced some tests in the same lake with a 1:10 scale version of the EvoPod turbine (Chapter 1). The $TI$ during the tests was 8-9%. The maximum $C_P$ value (0.33-0.37) for the three different flow velocities observed happened at $TSR \approx 3$. An increase of 0.3 m/s caused the average mechanical power to double. Frost et al. (2017) compared the performance of this turbine in a wave

**Table 3.4:** Summary of findings of combined wave and current turbine testing.

| Reference | D [m] | U [m/s] | H [mm] | Tw [s] | Blade profile | Notes |
|---|---|---|---|---|---|---|
| Barltrop et al. (2006) | 0.35 | 0-1.6 | 150 | 1.2-2.0 | NREL S814 | Steeper waves have higher influence on load fluctuations. Waves normal to rotor plane lead to the largest *RBM*. |
| Barltrop et al. (2007) | 0.4 | 1.0-1.4 | 20-140 | 1.2-2.0 | NREL S814 | At lower flow velocities, average torque values increase. Wave height has a greater impact on torque for longer waves. |
| Lust et al. (2013) | 0.8 | 1.68 | 90-180 | 1.6-2.3 | NACA 63-618 | Max $C_P$ at $TSR \approx 6$. Waves do not affect turbine performance unless rotor is close to the surface. Max and min load values follow wave crests and troughs. |
| Luznik et al. (2013) | 0.46 | 0.6 | 76 | 1.7 | E387 | Wave-induced fluctuations limits turbine operation to $TSR > 5$. |
| Galloway et al. (2014) | 0.8 | 0.9 | 75-150 | 1.3-2.8 | NACA 48XX | Waves have a greater impact on individual blade loads. Yaw angle has a greater impact on rotor loads. |
| Fernandez-Rodriguez et al. (2014) | 0.27 | 0.46 | 70 | 0.7-1.5 | Gottingen 804 | Max $C_P$ at $TSR \approx 4.5$. In the frequency domain, the addition of waves shows no impact. |

**Table 3.5:** Summary of findings of wave-induced fatigue loads.

| Reference | D [m] | U [m/s] | H [mm] | Tw [s] | Blade profile | Notes |
|---|---|---|---|---|---|---|
| Galloway et al. (2010) | 0.8 | 0.9 | 100 | 1.3 | NACA 48XX | $C_P$ and $C_T$ reduce as yaw angle increases. |
| Gaurier et al. (2013) | 0.9 | 0.6 | 140-800 | 0.5-2.3 | NACA 63418 | Max $C_P$ at $TSR \approx 4.5$. Average $C_P$ and $C_T$ are not affected by addition of waves. *SD* values of $C_P$ and $C_T$ were observed 2-3 times higher than current-only cases. |
| Ordonez-Sanchez et al. (2016) | 0.5 | 0.5-1.0 | 200-400 | 2.0 | Wortmann FX 63-37 | Max $C_P$ at $TSR \approx 3.5$. Average $C_P$ and $C_T$ are not affected by addition of waves. |
| de Jesus Henriques et al. (2014b) | 0.5 | 0.46-0.92 | 41-113 | 0.6-0.9 | Wortmann FX 63-137 | |
| Guo et al. (2017) | 0.8 | 0.56-0.68 | 50-100 | 1-3 | NACA 63-8xx | Max $C_P$ at $TSR \approx 5$. Small ($\sim 15\%$) wave-induced flow disturbances induce load fluctuation of around 50%. |

and towing tank and in a tidal channel. The peak $C_P$ for field testing and flume testing were 0.382 at $TSR$=4.7 and 0.44 at $TSR$=4.6 respectively.

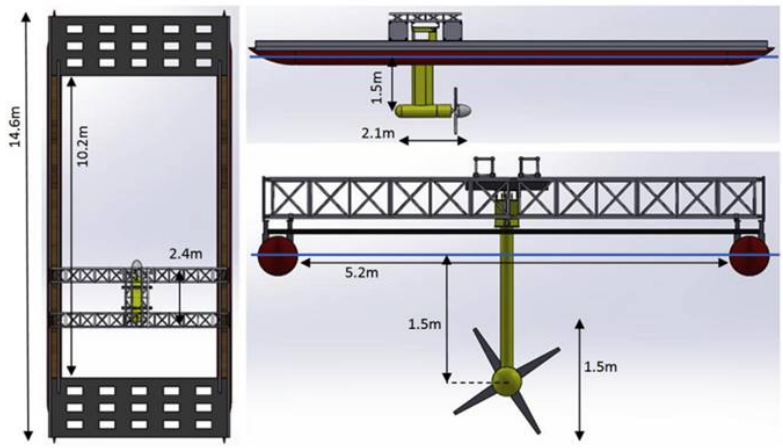


**Figure 3.11:** Turbine mounted on catamaran. From Jeffcoate et al. (2016)

Starzmann et al. (2013) mounted a 4 m diameter off-the-shelf Schottel rotor to the bow of a tug boat (Figure 3.12) and pushed it off the harbour of Rotterdam, Netherlands. Similar to Jeffcoate et al. (2014), no significant turbulence or velocity shear were observed at the site. Two sets of blades were used, a rigid one and a passive adaptive one. For the rigid blades, the $C_P$ curves showed good agreement between the experimental data and CFD simulations up to $TSR \approx 7$. For $TSR > 7$, the CFD overestimated the $C_P$ values. The passive adaptive blades showed a decrease in $C_P$ and $C_T$ as the velocity exceeded the design velocity.

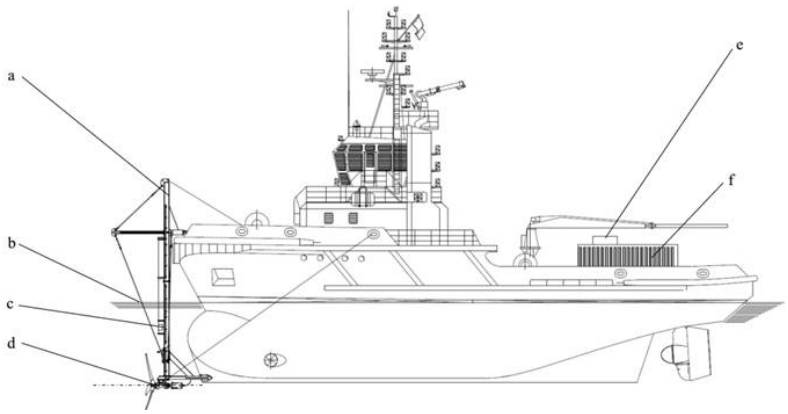


**Figure 3.12:** Turbine mounted on tug boat. a) test rig, b) water level, c) speed log, d) turbine, e) breaking resistor and f) control and data acquisition systems. From Starzmann et al. (2013)

In China, Xu et al. (2016), tested a 7.5 m diameter turbine (Figure 3.13) in a tidal channel. They reported a mean flow velocity of 2 m/s with slower ebb velocities and a flow misalignment between ebb and flow of about 10°. Their turbine showed a controlled $C_P$ of 0.388 at $TSR$=7 in flows with speeds ranging from 1.0 to 1.6 m/s.

**Figure 3.13:** Turbine mounted in subsea testing rig. From Xu et al. (2016)

### Turbulence-induced fatigue loads

Table 3.6 shows a brief summary of the different testing parameters and main results for all the field turbine tests presented in this section. In general, the higher $TI$ levels found on real tidal sites have a greater impact on the $C_P$ and $C_T$ than in laboratory testing.

## 3.5 Summary of findings

From the field measurements studies reviewed on this Chapter, the flow velocity typically varies from 1.0 up to 4.5 m/s at potential tidal sites. The flow asymmetry between ebb and flood goes from a fairly straight flow with 4° difference up to 25°. Turbulence intensity levels have an overall mean of 10%. The wave direction is independent of the tidal flow direction. In the field, although there is a predominant wave direction, there will be occasions when the wave direction varies from this.

The main results of each study reviewed in this section along with their main current and wave testing parameters were shown in Tables 3.2 to 3.6.

**Table 3.6:** Summary of findings of field tidal turbine testing.

| Reference | D [m] | U [m/s] | H [mm] | Tw [s] | Blade profile | Notes |
|---|---|---|---|---|---|---|
| Jeffcoate et al. (2014) | 1.5 | - | - | - | Eppler E387 | Max $C_P$ at $TSR \approx 3$. Tidal site showed a $C_P$ reduction of 25% due to high $TI$ levels. |
| Atcheson et al. (2015) | 0.46 | 0.6 | 76 | 1.7 | Eppler E387 | Max $C_P$ at $TSR \approx 3$ at three different flow velocities. |
| Xu et al. (2016) | 7.5 | 2 | - | - | NACA 634xx | Above rated flow velocity (1.6 m/s) rotor power decreased. |

Independently from model size, several of the presented studies agree that flow misalignment and $TI > 15\%$ influence the mean power and rotor loads. $TI < 15\%$ and the presence of waves have little impact on average loads and performance. However, they have a direct influence on the load variability, leading to high standard deviations. Some of the studies investigated the influence of the hub height on the wave effects on the turbine. For the present work, given that the tower height cannot be modified, this parameter will not be studied.

To the author's knowledge, the influence of non collinear waves and currents has not been explored in a controlled environment at a medium size scale at the time of testing, perhaps in part due to the limited number of testing facilities capable of producing such conditions. This gives an opportunity to create a unique set of testing conditions that will contribute to the state of the art. Therefore, the focus of this study is to explore the influence of oblique waves and currents on a scale model tidal turbine, with the aim of reducing design uncertainty and reducing associated costs.

# Chapter 4

# Experimental set-up

In this Chapter, the testing facility and turbine model are presented in two sub-sections. Each sub-section contains an in-depth description of the instrumentation used to measure the different variables. In the basin section, the instruments for measuring flow velocity and wave height are described. For the turbine, instruments to measure torque, thrust, root bending moment and structural loading at the base of the tower are introduced, along with a brief description of the motor, the slip ring and the electrical cabinets.

## 4.1 Experimental facility

The FloWave facility, shown in Figure 4.1, is located at The University of Edinburgh, Scotland, UK. It is a 25 m diameter circular basin with a 2 m working depth and a 15 m diameter elevating floor. A maximum current of 1.6 m/s is generated by 28 5-bladed, 1.7 m diameter impellers arranged around the full circumference of the basin. The basin is optimised to generate waves with a maximum height of 700 mm at 2 s period. Multi-directional wave generation is achieved by 168 absorbing flap type wave makers, also arranged around the full circumference. The elevating floor facilitates access to the basin bottom when setting up models and instrumentation. This facility has the advantage of creating flow and waves independently at any given angle (Robinson et al., 2015a). The basin was specifically designed to support tidal and wave energy research and development in intermediate water depths at a 1:20 Froude scale by bridging the gap between small scale

laboratory studies (i.e. narrow recirculating flumes) and field trials. At 1:20 scale, FloWave can replicate full-scale currents of up to 12 knots (6 m/s) and 28 m waves in an area of approximately 2 $km^2$.

**Figure 4.1:** View of the circular FloWave basin. Yellow overhead crane and gantry for accessibility and the mounting of instrumentation are visible.

In Figure 4.2, a plan view diagram of the 25 m diameter basin and the 15 m diameter elevating floor are shown along with the basin coordinate system and a quadrant-based compass points for easy reference later in this work.

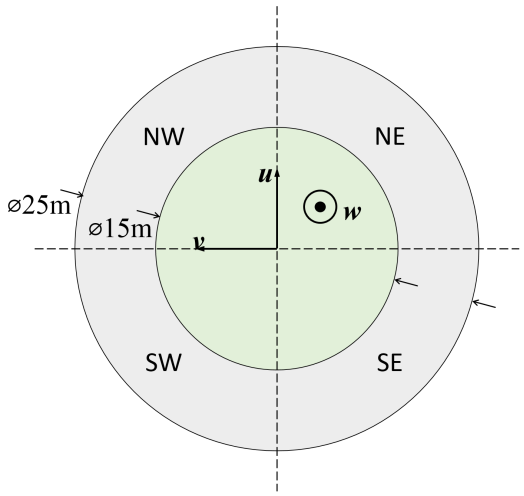


**Figure 4.2:** Plan view of the basin showing coordinates, measurements and quadrants for easier reference

The exact location of the turbine relative to the geometrical centre of the basin is shown in Figure 4.3. The streamwise measurement of 1.64 m is from the centre of the basin to the centre of the load cell. The distance from the centre of the load cell

to the rotor plane is 0.4D (diameters) or 0.486 m. The total distance of the centre of the basin to the rotor plane is 2.126 m.

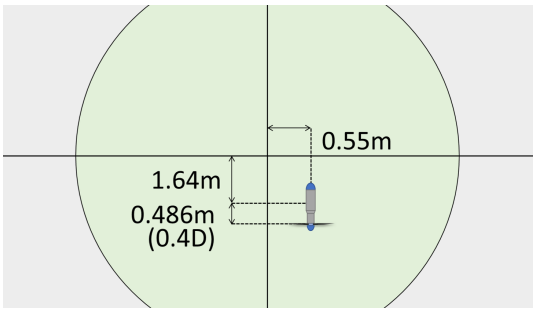


**Figure 4.3:** Plan view showing the exact position of the turbine fixed on the basin's floor relative to the geometric centre of the basin.

### 4.1.1 Basin instrumentation

#### Flow velocity

An Acoustic Doppler Velocimeter (ADV) was used for all flow measurements. The specific instruments used was a Vectrino Profiler manufactured by Nortek. This instrument can measure flow velocities up to 3.0 m/s at a sample rate of up to 100 Hz in three dimensions. This model in particular can measure 30 mm velocity profiles with a 1 mm vertical resolution. In these experiments, however, only the measurement in the middle of the velocity profile was used. It has an accuracy of $\pm$ 0.1 mm/s. Full details can be found on Nortek Group (2017).

#### Wave height

Wave elevation was measured using resistive wave gauges. This type of gauges measure the resistance between a pair of semi-submerged parallel rods. Depending on the wave height, the circuit is closed at different lengths of the rods. The resistance measured is proportional to the wave height. These were sampled at 64 Hz, enough samples per second for the wave periods of 2.0, 2.5 and 3.0 seconds. The wave gauges were calibrated by FloWave staff every day before testing to avoid any uncertainties.

## 4.2 Turbine model

The turbine model used for the tests was designed and built at the University of Edinburgh for the Engineering and Physical Sciences Research Council (EPSRC) funded project 'X-MED' (EP/J010235/1). It consists of a 1:15 scale, 1.2 m diameter rotor that represents a generic 18 m diameter horizontal axis tidal turbine at full scale based on Froude similitude. The blade profile is a NACA 63-8XX series made of aluminium, manufactured by computer numerical control (CNC) machining. According to Payne et al. (2017a), the blade profile was selected so the model's performance would match the performance curve of a full-scale turbine. As is common practice in model testing, these experiments were conducted under speed control to achieve constant $TSR$ values. When using Froude similitude for scaling the flow parameters (Chapter 5), it is not possible to match the blade hydrodynamics between the scale model and the full-scale device by matching the Re numbers between the two as it is impossible to satisfy both Froude and Reynolds scaling simultaneously. However, by matching the blade performance curves and $TSR$ values between the scale model and the full-scale device, the blade hydrodynamics are scaled. Figure 4.4a shows the turbine mounted on the load cell fixed on the basin's floor. All the instrumentation is kept protected inside the black and silver cylindrical sleeves as seen in Figure 4.4b.

The author had direct involvement in the assembly of the turbine, design and fabrication of mounting and transportation frames, design and fabrication of centring aids for mounting the shaft through the bearings and dynamic seals, hand polishing of all the blades prior to anodising, design, manufacture and installation of water leakage sensors in the turbine, build of all the connectors of the turbine and cabinets, including IP67 rated ones, design and build of the electrical cabinets, turbine commissioning at FloWave and turbine testing at IFREMER. And lastly, design, commission-build and foam-line wooden crates to keep all the equipment safe during international shipping.

Figure 4.5 shows the front and side view diagrams of the turbine with dimensions and the location of the Vectrino and wave gauges.

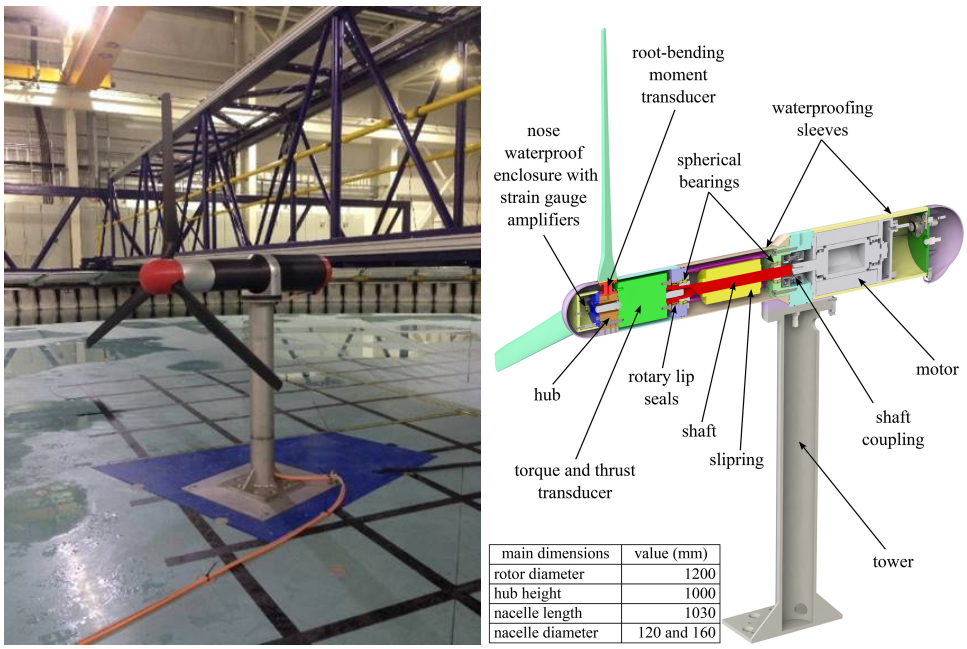


**(a)** **(b)**

**Figure 4.4:** a) Turbine mounted on the basin floor (shown in the floor's raised position, out of the water); b) section view of the turbine with its main components identified and key dimensions. From Payne et al. (2017b).

### 4.2.1 Turbine instrumentation

The turbine model is fitted with a torque and thrust transducer mounted upstream of the dynamic seals to avoid any parasitic loads due to friction between the shaft and the dynamic seals or the slip ring. It also includes sensors measuring the stream-wise root bending moment at the root of each blade. A resolver records the absolute angular position of the rotor. The main difference between a resolver and an encoder is that the output signal of the former is analogue, whereas the output signal of the latter is digital.

All the turbine sensors are sampled synchronously at 256 Hz with the same data acquisition system through different channels. This sampling frequency was chosen because at this frequency the noise floor of the different instruments already shows in the plots. Even if there were load oscillations at higher frequencies, they would not be identifiable.

The root bending moment load cells developed a fault during the tests which will be discussed in Chapter 7. Although a detailed explanation of the different

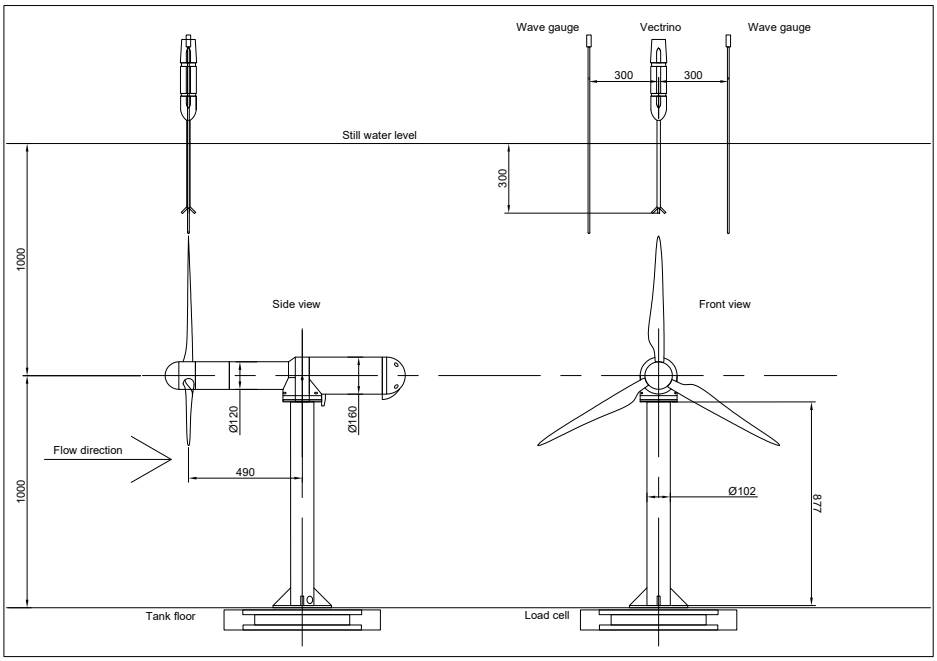


**Figure 4.5:** Turbine diagram with dimensions and basin's instrumentation location. All dimensions in mm.

components is presented below, further specifications can be found in Payne et al. (2017a).

A simplified overview of the design parameters and the rated values of the selected instruments to measure each parameter is presented in Table 4.1.

**Table 4.1:** Turbine design parameters and instrumentation rated values

| **Parameter** | **Design value** | **Instrument rated value** |
|---|---|---|
| Thrust | 120 N | 640 N |
| Torque | 26 Nm | 50 Nm |
| RBM | 62 Nm | 93 Nm |

## Motor

The motor/generator used in the turbine is shown in Figure 4.6. It is an Alxion 145ST4M017 with continuous torque rating of 26 Nm and a peak torque of 110 Nm. The motor is brushless with a permanent magnet rotor. It is fitted with an angular resolver used for feedback control of the motor and to record absolute angular position. The resolver has an angular precision of 0.01667°.

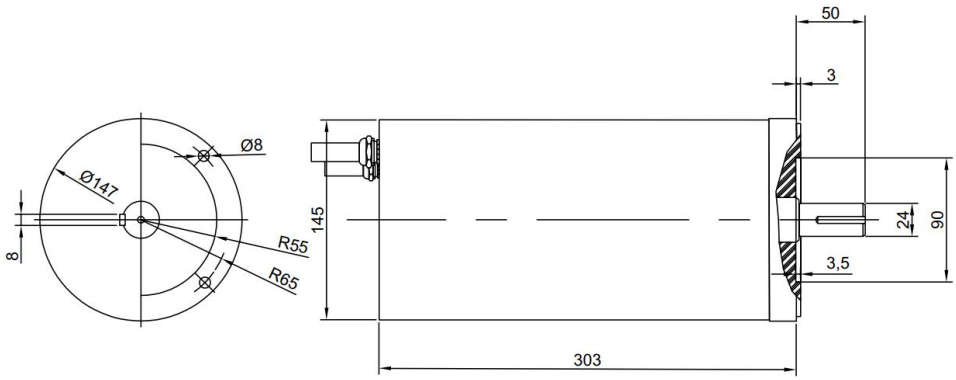


**Figure 4.6:** Motor diagram.

The motor is supplied by a 400 VAC mains supply through a Moog DS2000 drive. This drive is capable of controlling the motor as a break/generator. The drive is accompanied by a recovery resistor to dump any generated electricity by the motor, a miniature circuit breaker and a 30 mA residual current device (RCD). The main function of the RCD is to protect the system in case of a short circuit caused by water ingress. A 24 V power supply feeds the motor drive. The control drive, along with its recovery resistor and all associated circuitry are installed in the power and control cabinet shown in Figure 4.7. The cabinet is fitted with an active ventilation system, consisting of a fan at the bottom sucking cool air in and a ventilation hole at the top to push out the hot air. The main design requirement was to keep any power cable as far as possible from any data cable and if any crossing between these two was needed, it should be done at 90°. Also, the load resistor is kept in a purpose-made aluminium sleeve to minimise electrical noise. The design of the cabinet layout, selection and sourcing of the components and the cabinet build was performed mainly by the author.

## Slip ring

Routing the cabling of the torque and thrust transducer and the RBM sensors from the rotating side of the turbine to the non-rotating side of the turbine is achieved with an 18-way Moog AC6349-18 slip ring. To reduce electrical noise, the grounding screen of the instrumentation cable is also routed through the slip ring. The position of the slip ring is shown in Figure 4.8.

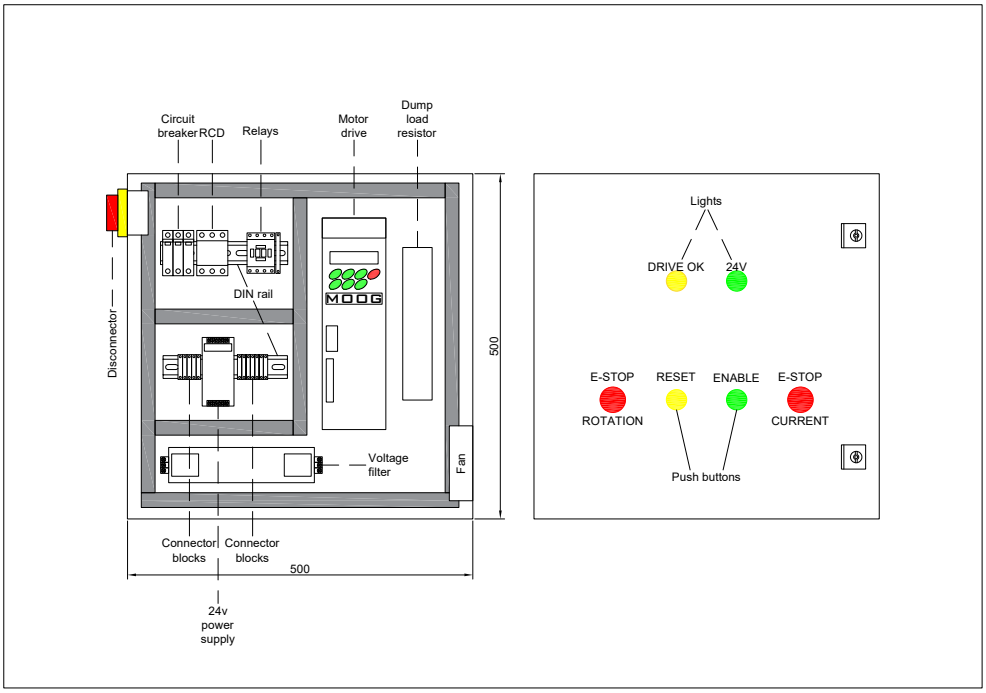


**Figure 4.7:** Motor control cabinet designed, built and commissioned by the author. All dimension in mm.

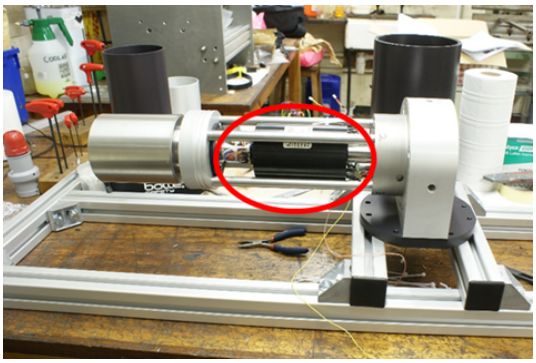

**Figure 4.8:** Slip ring (red circle) mounted in the shaft cage of the turbine. The front of the turbine is on the left-hand side of the image.

## Torque and thrust transducer

The transducer shown in Figure 4.9 was custom made by Applied Measurements Ltd in the UK. It has a maximum measurable load of 640 N in thrust and 50 Nm in torque. These rated load values were calculated with a safety factor of 2 from the Blade Element Momentum (BEM) model used to design the rotor. It is waterproof and is equipped with 18 throughways to pass cables from the shaft to the hub for the signals and power supply of the *RBMs*.

**Figure 4.9:** Torque and thrust transducer mounted on the turbine.

### Root bending moment transducer

The flexures where the root bending moment transducers fix the blades to the hub are seen in Figure 4.10. They were designed with a maximum streamwise out-of-plane (*My* in Figure 3.3) moment of 62 Nm using the BEM load predictions as a baseline. Later, with aid of Finite Element Analysis (FEA) with the software SolidWorks Simulation, a maximum stress of 54 MPa was calculated. The flexures were designed by Payne et al. (2017a) and built in-house at the mechanical workshop of the engineering department. Applied Measurements Ltd (AM) was in charge of mounting the strain gauges on the flexures, waterproofing and calibration of the strain gauges. Calibration data can be found in Appendix A. The strain gauges are connected to individual signal amplifiers located in the nacelle nose (Figure 4.10). The strain gauges amplifiers were also supplied by AM and have an output of 4-20 mA and a bandwidth of 1 kHz. An extra calibration following the tank testing performed by the author confirmed the values supplied by Applied Measurements. During testing, some anomalies were observed in some of the data obtained from the *RBMs*. These issues are presented in Chapter 7.3.

### Tower load cell

A 6 degrees-of-freedom load cell, an AMTI Biomechanics Force Platform model OR6-7, was mounted between the turbine tower and the basin bottom. It measures maximum loads of 4448 N in $Fz$, and 2224 N in $Fx$ and $Fy$. Its maximum mea-

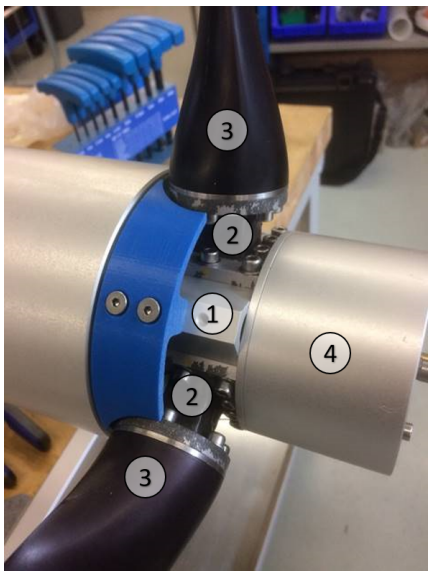


**Figure 4.10:** Close up of the blades mounted on the root bending moment transducers mounted to the hub. 1: Hub; 2: RBM flexures; 3: blades; 4: nacelle nose.

surable moments are 600 Nm for $Mz$, 1100 Nm for $Mx$ and $My$ (see Figure 3.3 for definitions).

## 4.3 Data logging

For logging the data, an acquisition system was mounted on a purpose-built cabinet (Figure 4.11) with a National Instruments (NI) chassis cDAQ-9174 fitted with a NI9401 digital I/O module to log the resolver signal from the motor, a NI9203 current analogue input module for the *RBM* sensors and the torque and thrust transducer and a NI9205 voltage module for the tower load cell. The grounding screens of all the data cables were connected to the cabinet at their point of entry to avoid electric noise polluting the signals. To protect the data acquisition system, an in-line fuse was adapted into the NI chassis' power supply. This cabinet was designed and built by the author.

## 4.4 Summary

In this chapter, the working ranges of the basin were presented along with its main characteristics. The turbine model used in this work was introduced with detailed

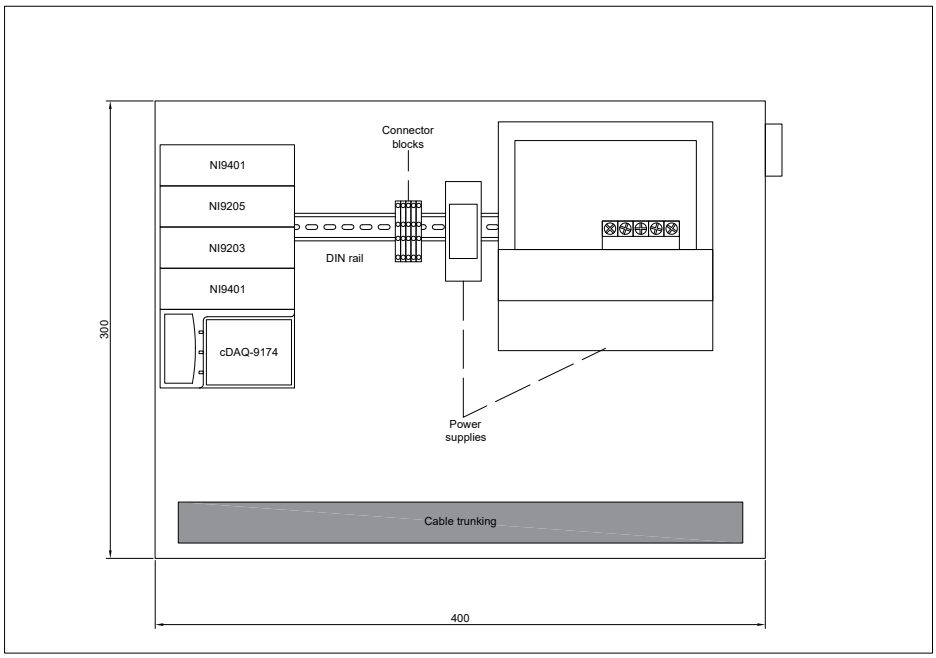


**Figure 4.11:** Data acquisition cabinet designed, built and commissioned by the author. All dimension in mm.

explanation of its instrumentation. In addition, clarification of the extent of involvement of the author was presented.

FloWave used their own data acquisition system for the Vectrino, wave gauges and load cell data. At the end of the testing campaign, the raw data was delivered through a cloud-based, file-sharing system managed by the University of Edinburgh.

# Chapter 5

# Design of test matrix

The whole test campaign was divided in three phases: *flow characterisation*, *turbine characterisation under current-only conditions* and *turbine testing at fixed TSR for all current and wave conditions.*

Flow characterisation is aimed to understand how the onset flow behaves with the turbine out of the water. Flow measurements are made where the turbine rotor would be mounted when testing it. Flow parameters are similar to those the turbine was subjected to. An in-depth explanation of these tests is in Chapter 6.

Turbine characterisation under current-only conditions explores a range of $TSR$ values by keeping a constant flow velocity and investigating a range of rotational speeds to create $C_P$ and $C_T$ curves of the turbine. These tests were conducted only with current, no waves. An in-depth explanation of these tests is in Chapter 7.

Turbine testing at fixed $TSR$ for all current and wave conditions explores the effects of oblique waves and currents at a fixed rotational speed and flow velocity. An in-depth explanation of these tests is in Chapter 7.

## 5.1 Testing parameters

The current and waves parameters selected for the turbine testing were a close representation of real sea states, as reviewed in Chapter 2. A flow velocity of 0.8 m/s was selected. This is the design speed for the turbine model presented by Payne et al. (2017a). At 1:15 Froude scaling, it corresponds to a full-scale velocity of 3.1 m/s which, according to McNaughton et al. (2015) in Chapter 2, is a realistic

flow velocity for deployment at sites such as the European Marine Energy Centre (EMEC). From the findings presented in Table 3.1, three current angles (0°, 10° and 20°) were chosen for the present tests.

The wave directions were chosen to provide a broad range of conditions within the testing time allocated and the technical capability of the facility. Five different wave angles (0°, 45°, 135° and -45°) were chosen. In that context, tests with opposing waves at 180° were not carried out as it limits the range of wave period available due to the Doppler shift seen on Section 2.2.5. Waves at 90° were also excluded because the associated wave-induced velocity will be parallel to the rotor disc and will therefore have limited influence on its load.

As with almost all physical modelling campaigns, the selection of the test matrix is constrained by the available facility time. In general, the starting point is an ambition to complete the largest number of tests possible, but other considerations are crucial. The main constraint is the allocated time for use of the facility. Then, installation of the turbine and equipment at the beginning of the campaign and the dismounting at the end of the allocated time. Finally, the time it takes for the tank to settle down before new flow conditions can be generated and the actual testing time. All these considerations are discussed in detail in this Chapter.

Figure 5.1 shows a top view of the basin, with a blue circular marker representing the location at which the turbine was positioned. The dashed lines represent the wave angles selected for testing and the solid, coloured lines, represent the current angles chosen.

Wave heights and periods were chosen to produce (according to linear wave theory) a horizontal wave induced velocity at hub height of 0.1 m/s, bearing in mind that this condition would only apply for the collinear waves and current case.

Three wave periods Tw (2.0, 2.5 and 3.0 s) were chosen that fell within the working range of the wave makers. For a 1:15 scale, using Froude similitude from Chapter 2.4 (Table 2.1), the selected wave periods are roughly equivalent to 7.5, 9.6 and 11.6 s at full scale, respectively. These full-scale periods cover a range of relatively common conditions in the UK waters. Then, with the aid of linear wave

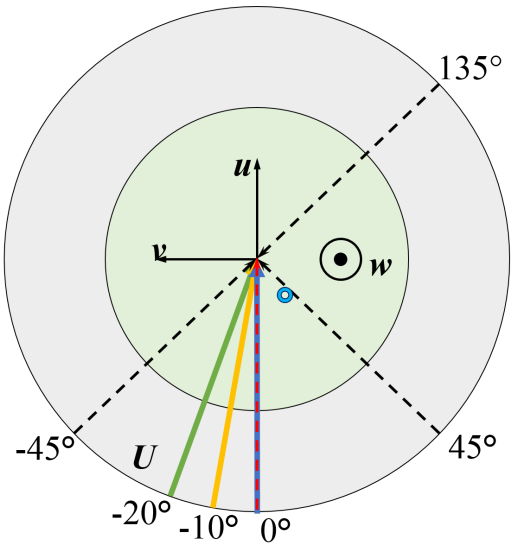


**Figure 5.1:** Plan view of the basin indicating current (solid) and wave (dashed) angles selected for testing. Blue circular marker represents the location where the turbine will be positioned. $u$ is the flow component perpendicular to the rotor plane, $v$ is the flow component transversal to the turine axis (drive shaft) and $w$ is the vertical flow component.

**Table 5.1:** Wave periods and heights selected for testing.

| Tw [s] | 2 | 2.5 | 3 |
|---|---|---|---|
| H [m] | 0.102 | 0.091 | 0.086 |

theory (see Section 2.2.5), and solving Equation (2.12) for wave height H with the aid of Equation (2.11) gives the wave parameters presented in Table 5.1. Having the wave parameters and flow velocity scaled down using Froude similitude will allow to explore correctly the combined influence of waves and currents.

Once the current velocity, current angles, wave heights and periods were selected, a matrix with all the possible combinations was generated in Table 5.2, with a total of 36 tests including the current-only cases C1, C2 and C3.

In an attempt to simplify communication, a code system was created for naming specific tests. They apply for both flow characterisation and turbine testing. For the turbine characterisation tests, referring to each test by their current angle and $TSR$ is enough. Figure 5.2 shows the process to create the code, where C stands for current and W for waves.

**Table 5.2:** FloWave tests matrix

| Current angle | Tw=2s H=102mm | Tw=2.5s H=91mm | Tw=3s H=86mm |
|---|---|---|---|
| 0 | - | - | - |
| 0 | 0 | 0 | 0 |
| 0 | 45 | 45 | 45 |
| 0 | - | 135 | 135 |
| 0 | 315 | 315 | 315 |
| -10 | - | - | - |
| -10 | 0 | 0 | 0 |
| -10 | 45 | 45 | 45 |
| -10 | - | 135 | 135 |
| -10 | 315 | 315 | 315 |
| -20 | - | - | - |
| -20 | 0 | 0 | 0 |
| -20 | 45 | 45 | 45 |
| -20 | - | 135 | 135 |
| -20 | 315 | 315 | 315 |

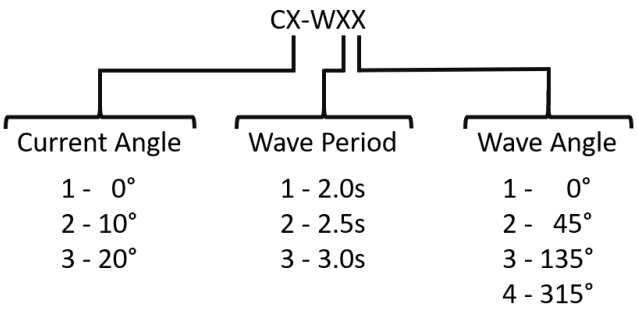


**Figure 5.2:** Tests name coding key

In Table 5.3 the final tests code is arranged in the same fashion as in Table 5.2. For the cases where there are no waves, only the current part is shown: C1, C2 and C3. All the W13 waves do not exist because at the moment of trying them in the basin, the specific combination of H=102 mm and Tw=2 s at $\theta = 135°$ did not reach the centre of the basin.

The testing times selected varied depending on the test type. All the tests had a 32 s excess at the beginning to allow for the waves reach the turbine's location. This ramp-up time was removed during data processing. For the flow characterisation tests, a duration of 128 s was selected. For the turbine characterisation tests

**Table 5.3:** Tests database after code assignment

| C1 | | |
|---|---|---|
| C1-W11 | C1-W21 | C1-W31 |
| C1-W12 | C1-W22 | C1-W32 |
| - | C1-W23 | C1-W33 |
| C1-W14 | C1-W24 | C1-W34 |
| C2 | | |
| C2-W11 | C2-W21 | C2-W31 |
| C2-W12 | C2-W22 | C2-W32 |
| - | C2-W23 | C2-W33 |
| C2-W14 | C2-W24 | C2-W34 |
| C3 | | |
| C3-W11 | C3-W21 | C3-W31 |
| C3-W12 | C3-W22 | C3-W32 |
| - | C3-W23 | C3-W33 |
| C3-W14 | C3-W24 | C3-W34 |

under current-only conditions, a duration of 256 s was selected as current-only conditions do not present the high levels of velocity fluctuations as the combined wave and current conditions do. The turbine tests at fixed $TSR$ for all current and wave conditions were logged for 512 s. These durations were selected to capture all the frequency spectrum that is contained in the flow. The more flow perturbations, the longer the measurements should be. Hence, the tests with waves have longer durations.

In addition to the testing time, a basin settling time between each test had to be considered. From communications with FloWave, the basin settling time for current angle and start-up was considered as 10 minutes and for any change in wave period or angle to be 3 minutes. These settling times allow for any parasitic flow velocity or wave reflections in the basin from previous conditions tested to dissipate. In the case of turbine characterisation, only a 30 s settling time was considered as the only change that was required was a change in the turbine rotational speed.

On top of all the time calculated, a round of tests with the turbine using mock instrumentation had to be included to avoid any damage to the turbine or the instrumentation in case something went wrong with flow parameters never tested before. These tests had a duration of 256 s and normal settling times.

The overall testing time calculated was of 34 hours plus half a day required to set-up the turbine in the tank and half a day for decommissioning. A facility access of 10 days was allocated for this project thanks to the School of Engineering through the Funded Resource Allocation (FRA). All required testing, setting-up, decommissioning and unexpected troubleshooting had to happen within this allocated time.

# Chapter 6

# Flow characterisation

## 6.1 Introduction

In order to have a clear understanding of the incident flow the turbine was going to be subjected to, a campaign of flow characterisation tests was carried out in the 'bare basin' without the turbine model in place. This section describes the methodology, tested conditions and findings. The main objective is to characterise the flow within the rotor area. For this, flow velocity and wave height were recorded. In this section, analysis of the flow velocity in time- and frequency-domain, turbulence intensity, flow direction and wave-induced fluctuations is presented.

## 6.2 Methodology

These tests were performed without the turbine and measurements of the flow velocity were taken in the plane where the rotor would be.

A view of the rotor seen from the front is shown in Figure 6.1. The evenly-spread velocity point-measurement locations on the rotor plane are represented by the red crosses. The dashed line represents the rotor swept area. There are nine points within the rotor area plus one above and one below the rotor at the vertical centre-line. The vertical line of point-measurements is used to create the velocity and $TI$ depth profiles presented in this Chapter.

The yellow lines seen in Figure 6.1 show the position of the wave gauges for the full duration of the testing campaign. The wave gauges are in line with the rotor plane.

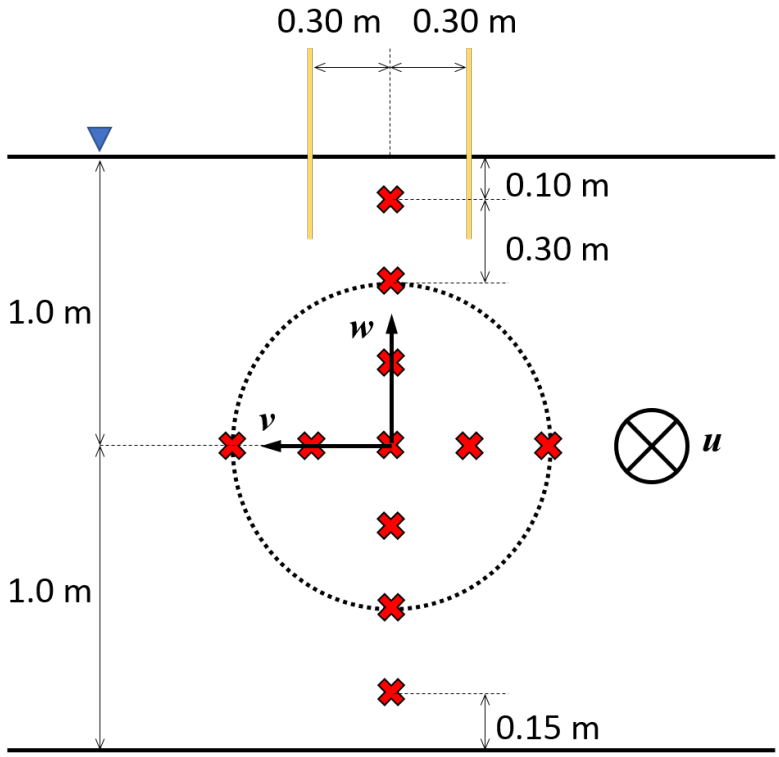


**Figure 6.1:** Front view of the rotor plane delimited by the dashed circle. Wave gauges (yellow lines) and flow velocity measurement points (red crosses). Flow components in the stream-wise ($u$), transverse ($v$) and vertical ($w$) directions indicated by the arrows.

Due to time constraints during the tests, only cases C1, C2 and C3 have the full velocity mapping array shown in Figure 6.1. For all the cases with waves, only the hub height measurements were carried out.

## 6.3 Data quality checking

Before being able to perform any analysis with the data, pre-processing is required to 'clean up' the acquired voltage signals. This involves the identification and removal of noise spikes, careful smoothing and/or cropping to minimise undesired noise which would adversely affect the post-processing analysis. Throughout, it is essential to ensure that useful information is not lost or distorted by this pre-processing.

### 6.3.1 Frequency spectra smoothing

Frequency analysis helps understand how the flow velocity is influenced by waves and to understand the turbulent nature of the flow. Turbulence is further discussed in Section 6.4.2. The spectral density curves shown in this thesis were obtained by averaging components over bins whose frequency widths are evenly distributed on a log scale. This means that high frequency bins contain a wider frequency range than low frequency bins which leads to curves being smoother toward higher frequencies. The effect of this 'smoothing' method for cases C1 and C3-W11 is shown in Figure 6.2, where the raw data (blue) converted into frequency domain using Welch's method is compared with the 'smoothed' data (orange) in a log-log plot. The Welch's method approach is estimated with the MATLAB function *pwelch*. The basic principle of the Welch's method is that it returns the power spectral density (PSD) estimate of the input signal using Welch's overlapped segment averaging estimator. A description and appraisal of Welch's method is given in Solomon Jr. (1991). In Figure 6.2 it can be seen that the trend and the peaks remain once the 'smoothing' is applied. The peak associated to the waves in case C3-W11 is easily distinguishable. In Chapter 7, this method is also used to identify key frequencies in the loading of the turbine and to see the influence of the waves as a function of water depth. The 'smoothing' method was chosen for the frequency domain analysis due to its ability to show all the frequency features in the signal present with the *pwelch* function while keeping a neater view of the data.

### 6.3.2 Wave gauge data checking

A time series of the wave gauges signal for case C1-W11 is shown in Figure 6.3, with a 'zoomed-in' part of the series shown in Figure 6.4. The figures show both wave gauges data with a raw and filtered version plotted against time.

Figure 6.4 contains noise at 16 Hz. This noise is believed to be caused by vortex-induced vibrations on the wave gauge rods generated by the passing flow. For this, a simple low-pass filter with moving average was chosen, the MATLAB *smooth* function. In Figure 6.4 the effect of the smoothing can be appreciated.

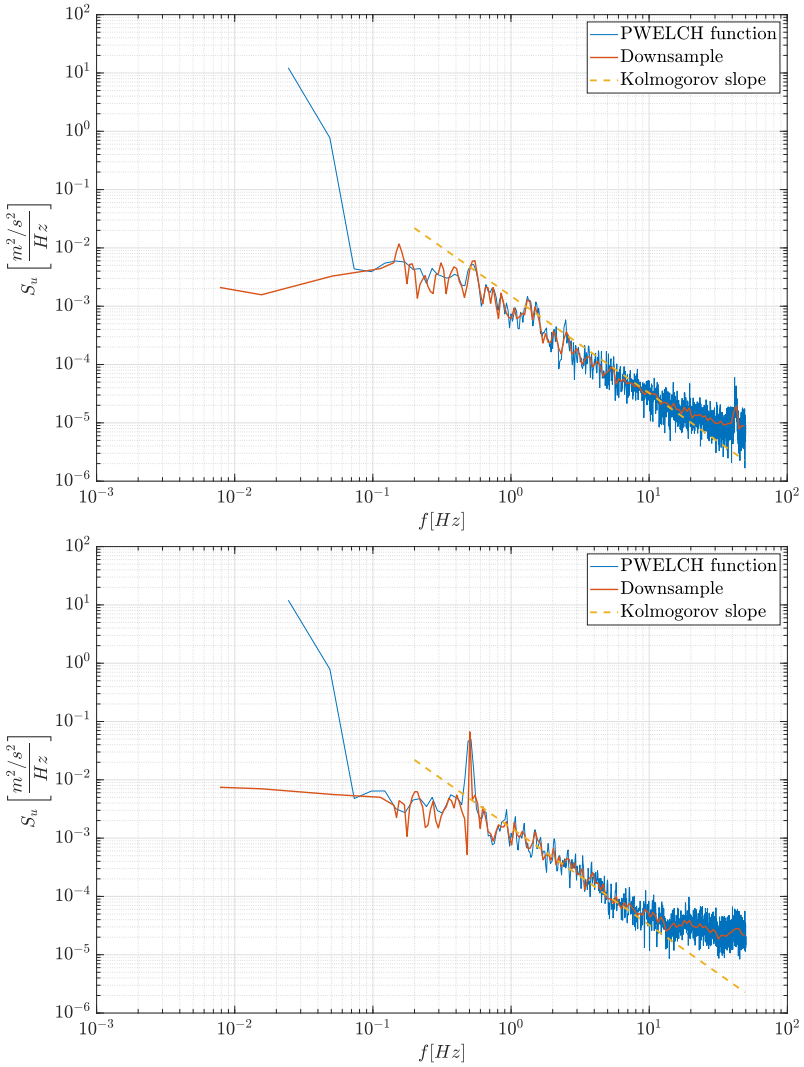


**Figure 6.2:** Comparison of streamwise velocity *u* for spectral analysis in case C1 (top) and C3-W11 (bottom). Logarithmic down-sampling vs *pwelch* function.

To check the accuracy of the wave height, once the data was smoothed, the crest and trough values of the wave time series were identified. Next, the mean and standard deviation of the crest and trough peaks were calculated. Figure 6.5 shows time series of case C1-W21 in which the blue and red markers indicate the crest and trough peaks, respectively. The dashed lines indicate the mean values of the whole time series crests and troughs and the shading indicates the standard deviation of the crest and trough values. The basis of the code is to identify the peaks in two steps once the data has been smoothed. First, the crest peaks are identified using the MATLAB *findpeaks* function. This function finds the local

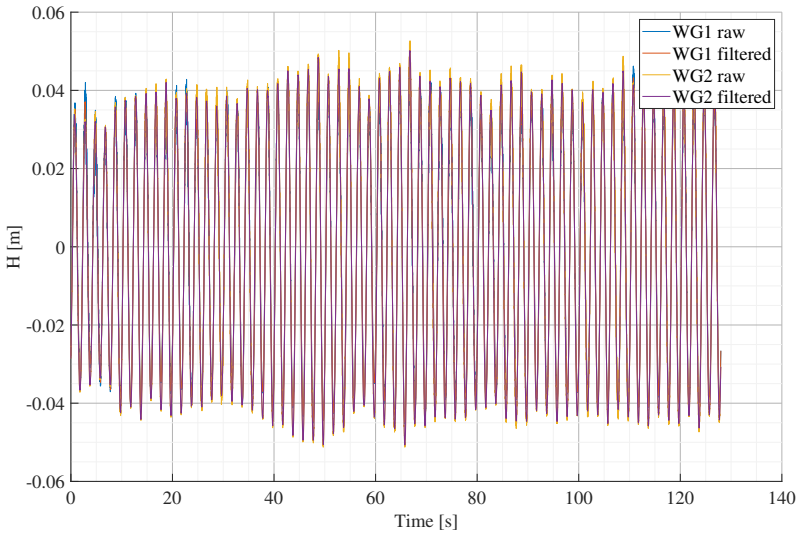


**Figure 6.3:** Randomly selected case C1-W11 to show wave gauges data before and after filtering.

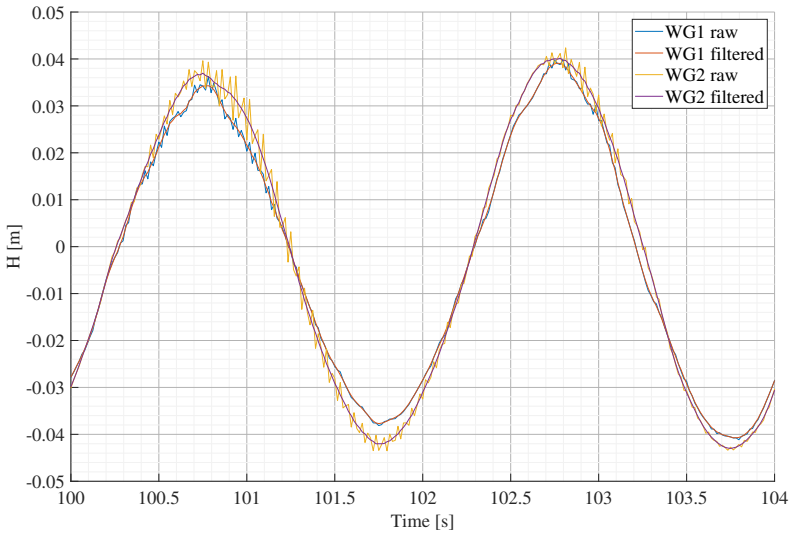


**Figure 6.4:** Close-up for the comparison of the wave gauges signal with and without filter. Case C1-W11.

maxima (peaks) comparing a data point with its neighbouring points. A minimum distance of 120 samples between peaks was selected to be close to the distance between the crests for the slowest period of 2 s which at 64 Hz sampling rate is 124 samples. The trough peaks were identified using the same *findpeaks* function on the inverted wave gauge time series. Next, the mean and standard values for crest and trough are calculated for both wave gauges. Lastly, the wave height can be calculated by measuring the distance between average values of crest and trough.

It can be seen that the average trough minima throughout a time series (dashed lines) are significantly different between the two wave gauges signals. Also, the standard deviation of the crests and troughs for both wave gauges is fairly high. This is thought to be caused by different factors, the spatial and temporal variability in the flow caused by how the current is injected into the tank from under the wave paddles and how the impellers and the wave makers try to generate straight current and waves from a circular array. These factors will have a direct impact in the wave characteristics. Another important factor is the the absence of passive absorption in the basin (beach). In this particular design, the wave makers opposite to the wave makers generating the waves measure and absorb the waves accordingly. This method, if not adjusted properly, could still let some wave reflection bounce off the wave makers back towards the centre of the basin. There are also limits on the frequencies which can be effectively absorbed by the wave makers due to limitations of their stroke and controls systems.

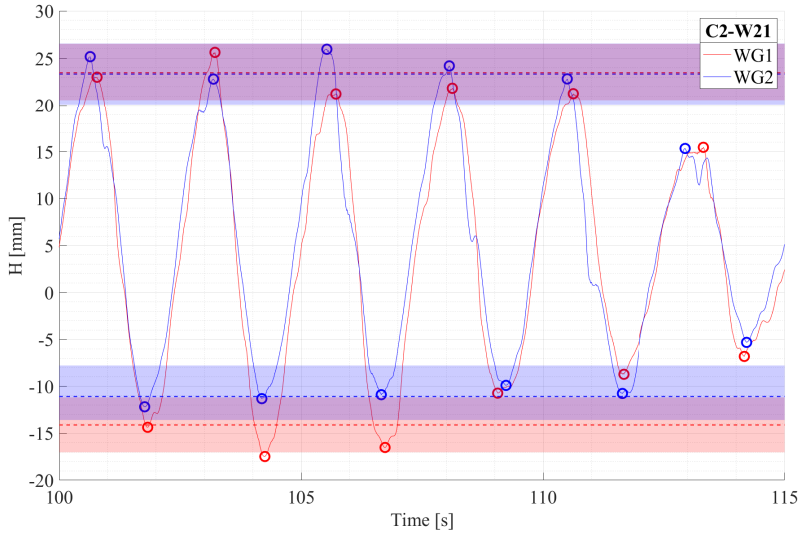


**Figure 6.5:** Wave mean amplitude (dashed lines) and standard deviation (shaded) from to wave gauges for wave case C2-W21

An example by Draycott et al. (2016) on how the circular array of wave makers at FloWave cannot generate straight waves is shown in Figure 6.6. In the Figure, the relative wave height between the prescribed wave height and the measured wave can vary as much as $\pm 10\%$.

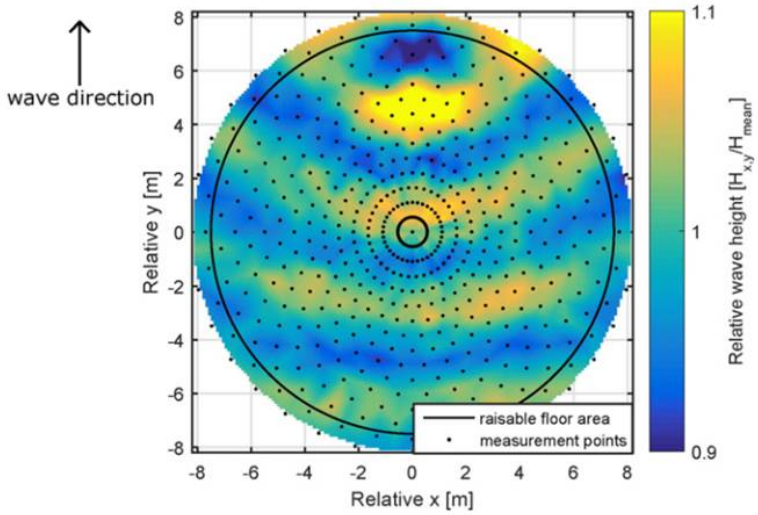


**Figure 6.6:** Spatial variation for a wave of Tw=2.2 s at the FloWave basin. From Draycott et al. (2016)

## 6.4 Results

### 6.4.1 Flow velocity

The measured flow velocity at hub height had to be checked to know how close it was from the nominal flow velocity of 0.8 m/s. As there are three different current angles, a comparison between the time-averaged velocity's streamwise component $\overline{u}$ and the time-averaged velocity magnitude $\overline{U} = \overline{\sqrt{u^2+v^2}}$ (Figure 5.1) of all the turbine tests is presented in Figure 6.7. The influence of including or not the vertical flow component $w$ is also shown in the Figure. The horizontal axis is divided in three areas: flow at 0°, at 10° and 20°. Each angular section contains every test identified by its unique code. From the figure, it can be observed that the vertical flow component $w$ (Figure 5.1) has an influence of under 1% in the calculation of $\overline{U}$. Therefore, it was decided not to include it in the calculations. It is also possible to see that $\overline{u}$ and $\overline{U}$, are below the nominal flow velocity of 0.8 m/s for tests with C1 and above the nominal flow velocity for C2 and C3. This difference has no intuitive explanation as the impellers speed was set constant at 96 RPM for all tests.

Flow velocity depth profiles are shown in Figure 6.8. Three profiles are shown, one for each of the current angles. Error bars represent the flow velocity standard

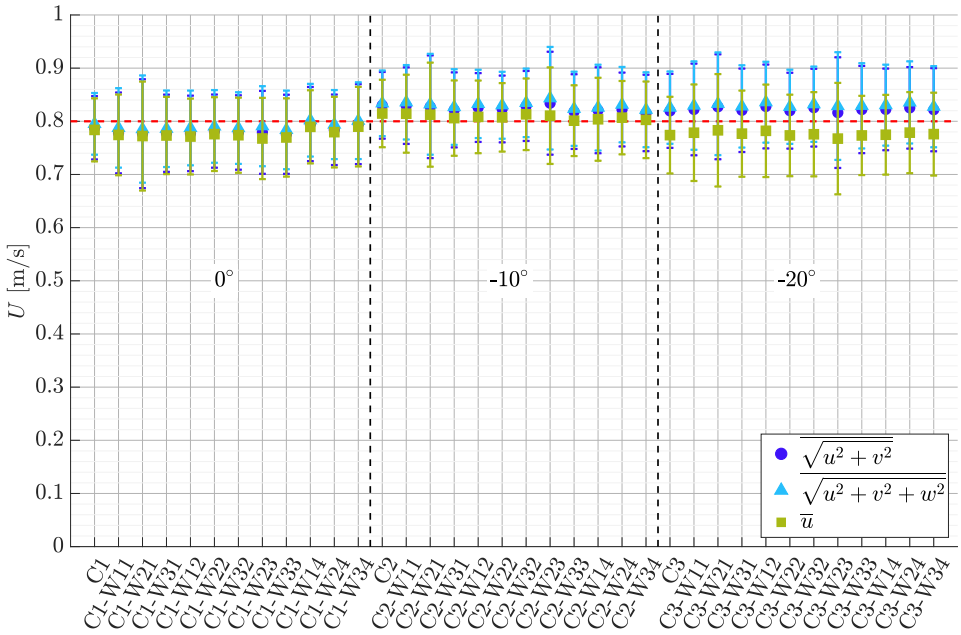


**Figure 6.7:** Comparison between the prescribed velocity (red dashed line), the velocity component $u$ and the resultant magnitude $U$ using $uv$ and $uvw$ flow components. Each $x$ position corresponds to each of the test cases. Figure for representative purposes only using turbine testing data rather than flow characterisation. All measurements are at hub height ($z = -1$ m).

deviation at each measurement location. A power law approximation of $1/10^{th}$ is fitted. For comparison, a typical power law approximation used to describe field velocity depth profiles is $1/7^{th}$. However, as seen in Chapter 2, different sites can be described by different power laws. It can be seen in the figure that in all the cases the behaviour is similar. *SD* values are high due to the turbulence-induced fluctuations around the average flow velocity. As expected, it can be seen that closer to the bottom of the basin the velocity is slower. This is due to bed friction-induced velocity shear profile and also due to the way in which the water is projected from the turning vanes in the basin (see Robinson et al. (2015b) for a CFD simulation and Noble et al. (2015) for experimental results). The three profiles show speeds increasing steadily with increasing height above the bed up to the 1m depth level. They then show a flat profile before suddenly increasing close to the water surface. These velocity profiles share the same qualitative trends with those given by Noble et al. (2015) for the same basin. Such characteristics include the flatter central part

of the profiles and the difference of almost 0.15 m/s between the slower bottom part and the faster top part of the profiles.

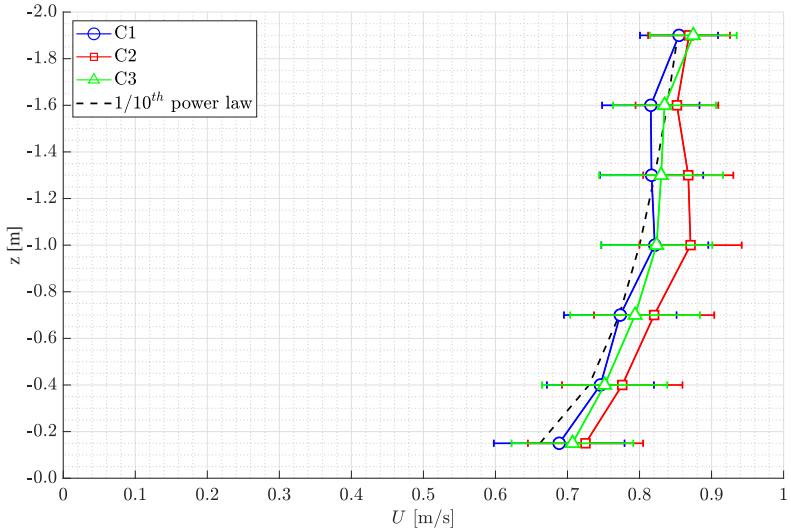


**Figure 6.8:** Flow velocity $U$ depth profiles. Power law approximation of $1/10^{th}$ also shown.

Figure 6.9 shows three different rotor area velocity maps, based upon nine point-measurements represented by red crosses. The spatial-average between these nine-point measurements is identified as $U_0$ (top left corner of each panel). The dashed circle shows the rotor disc area. The subfigures are for cases: C1 (top), C2 (middle) and C3 (bottom). It can be observed that for C1 and C3, the left-hand side of the rotor disc experiences a faster current with a relative increase to the rotor averaged velocity $U_0$ of 8.5% and 7.7% respectively. C1 presents less velocity variation throughout the rotor area measurements although at the rotor axis position, the velocity is slightly higher than the rotor area average. All the cases show a transverse profile with the left-hand side showing faster velocities than the right side. On the other hand, C1 and C3 show depth profiles that are not as fast as C2 at mid depth. These variations in flow are not dissimilar to the streamlines shown in Figure 6.10, where the straighter flow happens at the centre of the basin. Because of these spatial variations, the use of a spatial-averaged velocity ($U_0$) was adopted rather than only using the hub height velocity in order to have a more accurate representation of the flow across the rotor area. This rotor averaging method was also chosen by Blackmore et al. (2016) when they noticed that in cases where the

velocity fluctuations were sufficiently strong, the Betz limit appeared to be exceeded when using a single hub height velocity measurement. This method allows for high point-specific velocity fluctuations to average out with the other point measurements within the rotor area.

### 6.4.2 Turbulence intensity

Flow turbulence is one of the main causes of fluctuations observed in a turbine's loading; therefore, it is of great importance to calculate it. Bare basin measurements at FloWave carried out by Noble et al. (2015) and Sutherland et al. (2017) reported turbulence intensity values between 5% and 11% in the stream-wise direction. Figure 6.11 shows a depth profile of the $TI$ for the three current angles with no waves. As expected, the $TI$ tends to increase as the depth increases due to the lower values of the denominator in Equation (2.3). It also shows a correlation with the velocity depth profiles shown in Figure 6.8. At higher flow velocities, lower $TI$ and at lower flow velocities higher $TI$.

To understand how the $TI$ behaves across the rotor area, Figure 6.12 shows $TI$ contours in the rotor area for C1 (top), C2 (middle) and C3 (bottom). Visually, case C3 shows the highest $TI$ levels and C2 the lowest. C1 has the highest values towards the centre, whereas C2 shows the opposite. C3 shows a more homogeneous $TI$ across the whole area but with a maximum of 11%, the highest amongst the three cases.

### 6.4.3 Frequency analysis

Exploring the velocity data in the frequency domain allows exploration of whether the nature of the turbulence is realistic and follows the -5/3 slope in the inertial subrange of the energy cascade (Figure 2.4) proposed by Kolmogorov (e.g. Thorpe, 2007; O'Connor et al., 2010).

Figure 6.13 shows the spectral density of the incident velocity components $u$, $v$, and $w$ of case C3 at hub height plotted against frequency. Both axes use a logarithmic scale. Two distinct regions of the spectrum are identifiable in the figure. For frequencies below 0.2 Hz, the trend of the spectra of the three velocity

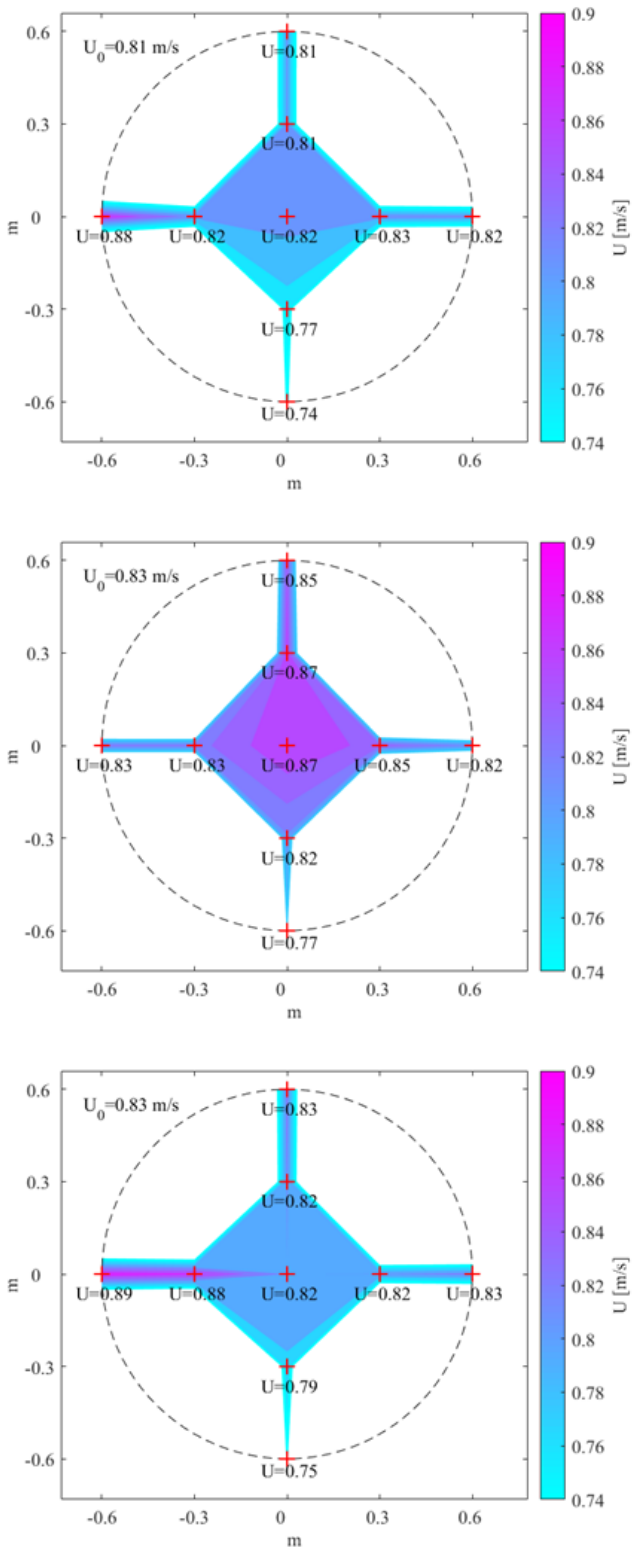


**Figure 6.9:** Contours of time-averaged, flow velocities, $U$, in rotor plane for: C1 (top), C2 (middle) and C3 (bottom), based upon the nine-point measurements. Values in m/s.

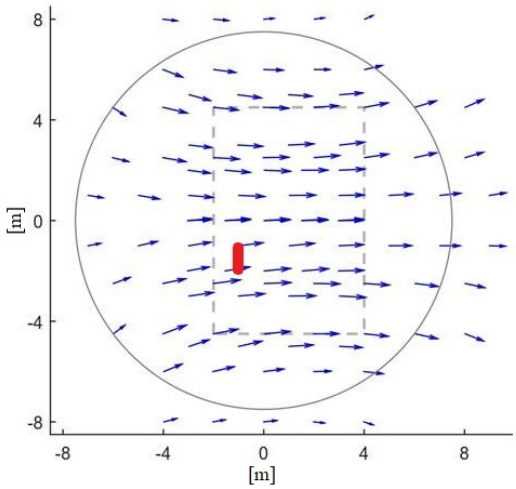


**Figure 6.10:** Plan view of the basin with velocity vectors for a 0.8 m/s current. Vector length is proportional to velocity at measurement point relative to input velocity. Nominal test area shown by grey dashed rectangle; 15 m diameter raiseable floor shown as a grey circle. Red rectangle gives approximate position of the turbine. Adapted from Noble et al. (2015).

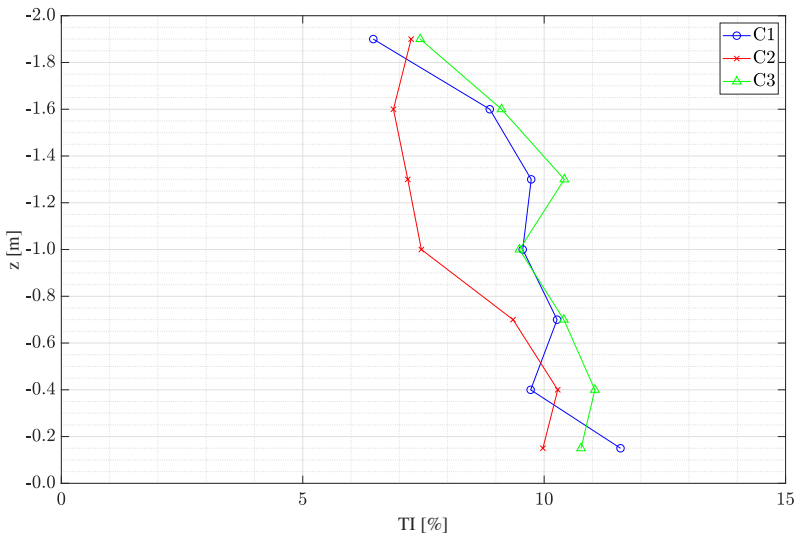


**Figure 6.11:** Turbulence intensity ($TI$) depth profiles

components is broadly horizontal, corresponding to the energy containing range in which the energy is being produced. For frequencies starting at around 1 Hz, the fall away of the spectral density indicates the inertial sub-range, where the energy starts cascading to smaller sized eddies. All the velocity components are observed to follow closely the Kolmogorov slope of -5/3, indicating that measured flow is similar to the idealised case of 3D isotropic homogeneous turbulent flow conditions

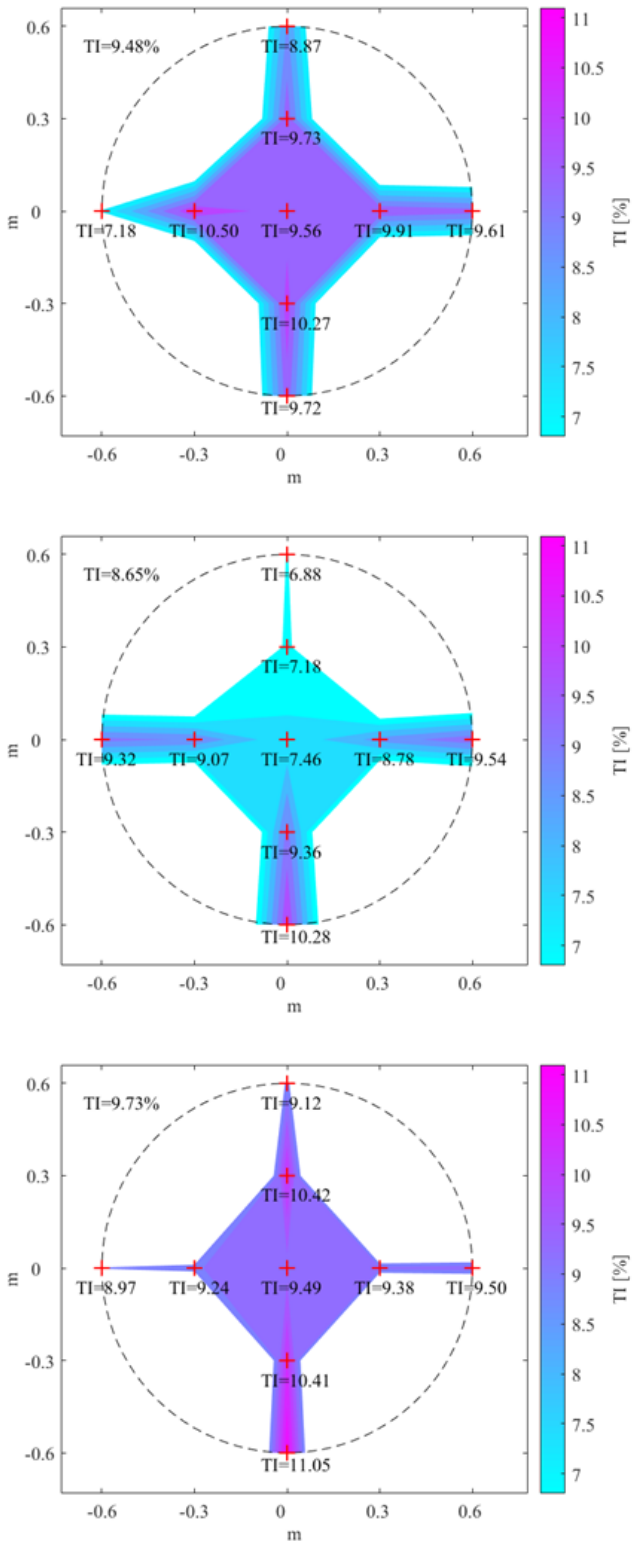


**Figure 6.12:** Contours of time-averaged, turbulence intensity, $TI$ (%), in rotor plane for: C1 (top), C2 (middle) and C3 (bottom), based upon the nine-point measurements.

modelled by Kolmogorov's theory. The levelling-off of the spectra for $u$ and $v$ components at the highest frequencies (above 30 Hz) is due to the limits of the instrumentation and is discussed further in Section 6.5.

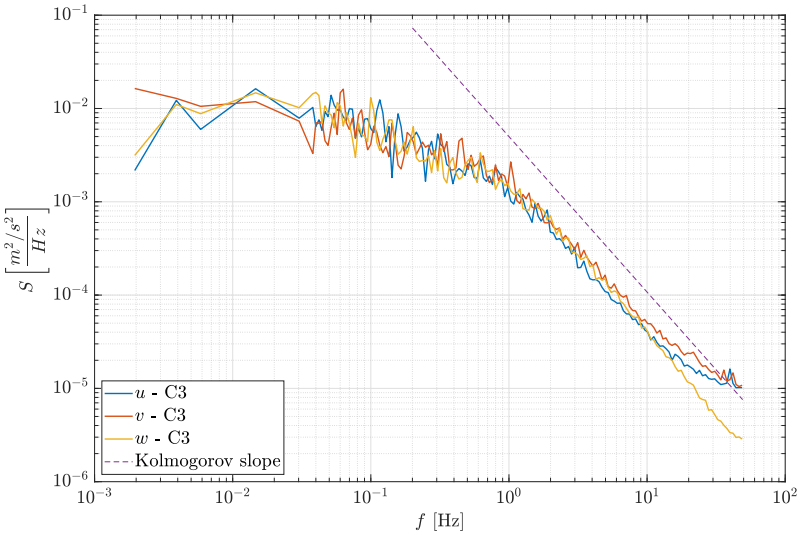


**Figure 6.13:** Spectral comparison of the flow components for Case C3. The Kolmogorov turbulent decay slope is included for comparison.

Figure 6.14 shows the spectral density of the resultant velocity magnitude $U$ of the onset flow at hub height of cases C1, C2 and C3. The spectra are very similar for the three current directions.

Comparing Figure 6.13 and 6.14, it can be seen that $U$ has a similar spectral density to the individual velocity components $u$, $v$ and $w$. Henceforth, to simplify the presentation of the spectra, $S_U$ will replace the separate use of the components' spectra $S_u$, $S_v$ and $S_w$.

To check if the velocity spectrum behaves similarly during the turbine tests, a comparison between the base case C1 with and without turbine is presented in Figure 6.15. It is possible to see a correlation between the two curves except for the spikes in the turbine testing case (blue). This peak is associated to the passage of the blades in front of the support structure. At 90 RPM, the rotational frequency is 1.5 Hz but when multiplied by 3 [blades] the blade passing frequency is 4.5 Hz, frequency of the peak seen in the figure. From the figure, it would be safe to assume that the flow with and without the turbine behave in a similar fashion, confirming the turbulent nature of the flow.

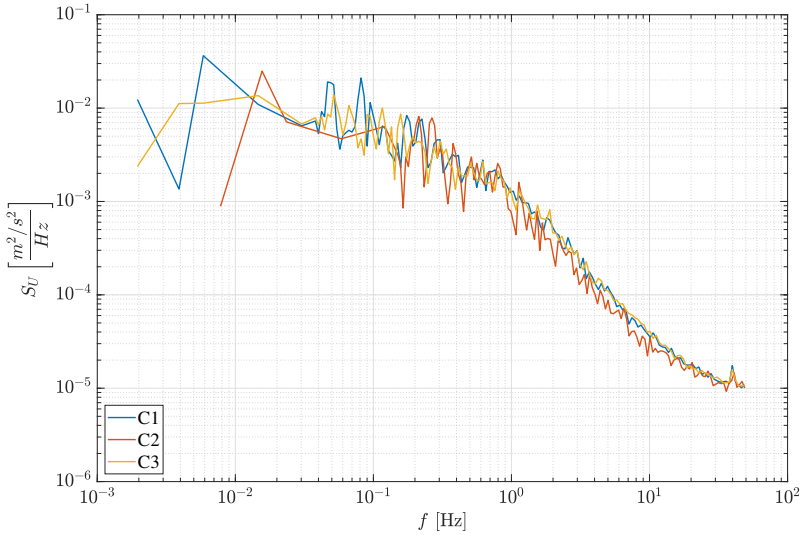


**Figure 6.14:** Spectral comparison exploring the effect of yaw angle in $U$ with no waves.

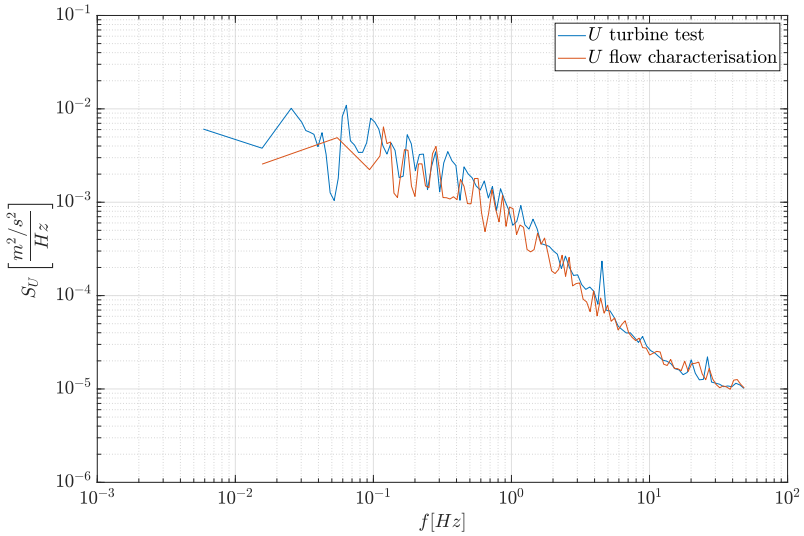


**Figure 6.15:** Spectral comparison of $U$ in flow characterisation and during turbine testing for case C1.

The influence of waves in the velocity spectra was explored by the addition to case C3 of wave W1 (period Tw=2.0 s; height H=102 mm) from three different directions: 0°, 45° and 315°. Figure 6.16 shows the resulting spectral density functions of the velocity $U$. It is interesting to note that the spectral peaks associated with the wave period are about an order of magnitude higher than those associated with turbulence. This implies that at the wave frequency, the energy contained in the waves is more significant than the energy contained in the turbulence.

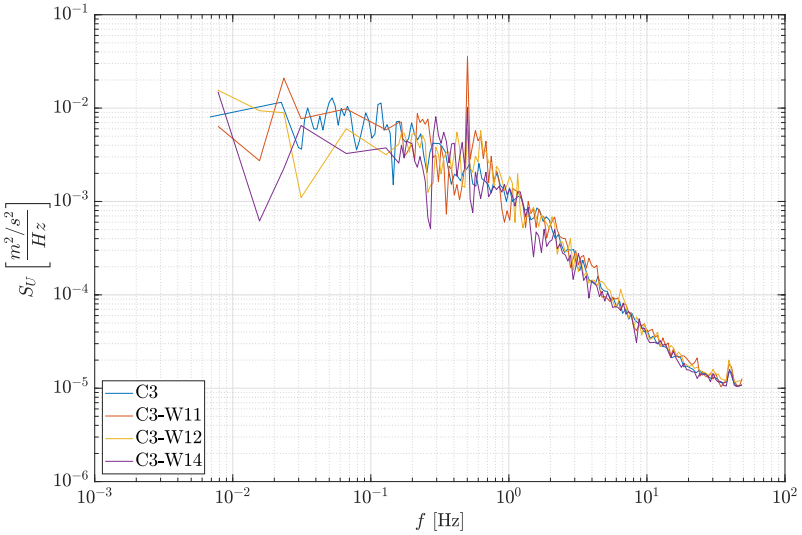


**Figure 6.16:** Spectral comparison of $U$ for current case C3 with wave W1 (Tw=2s) from different directions (0°, 45° and 135°).

A frequency spectral view of $U$ for case C1-W21 at different depths is presented in Figure 6.17. A close-up of the peaks associated to the waves is shown in Figure 6.18.

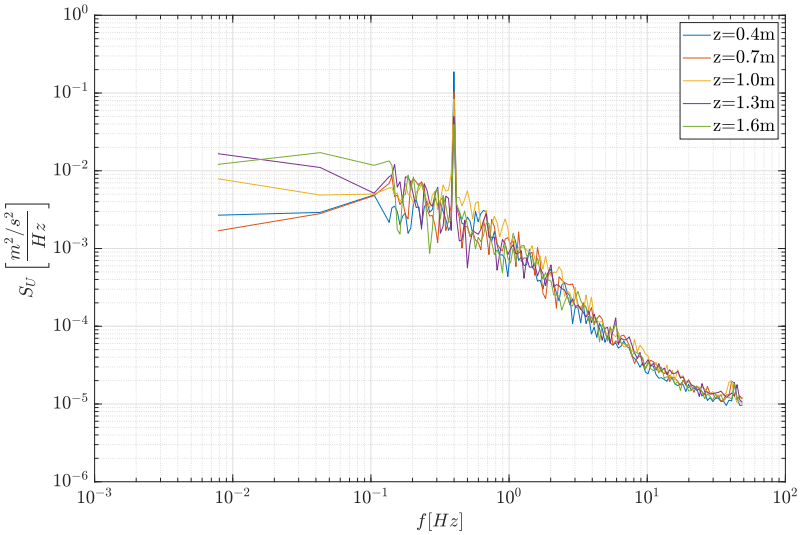


**Figure 6.17:** Spectral comparison of $U$ at different depths (z=1.6, 1.3, 1, 0.7 and 0.4m) for case C1-W21 (H=91 mm; Tw=2.5 s).

Figure 6.18 shows the expected reduction in wave velocity with elevation below still water level.

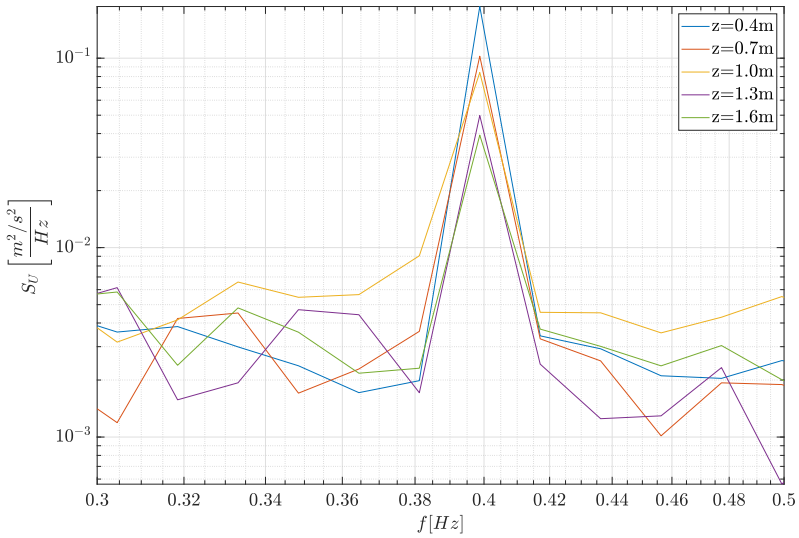


**Figure 6.18:** Effect of water depth on the wave induced velocity. Case C1-W21. Zoomed in from Figure 6.17.

### 6.4.4 Current direction

Exploring the current angle variation in the time domain, the bottom plot of Figure 6.19 shows a histogram of the current angle of current-only case C3 at -20°. $\mu$ is the mean angle and $\sigma$ is the standard deviation. The minimum angle experienced in the 256 s is -5° and a maximum of 40°, an average of 16.1° (4° below the prescribed 20°) and a standard deviation of 5.9°. The top panel shows the angle variation at hub height over a period of 1 s for the same case. Within a second, a range of angles from 8° to 22° is observed. The high variability observed in this figure leads to a high standard deviation equivalent to 36% the average angle.

Figure 6.20 shows the current direction for all test cases in similar fashion as Figure 6.7 with prescribed current angles represented by the red dashed lines. It can be seen that the cases at 0° recorded a higher current angle of about 2°, the cases at 10° are close to 10° and the cases at 20° have lower values of around 18°.

Figure 6.21 shows the depth profiles for cases C1 (blue), C2 (red) and C3 (green). All the profiles show the same trend: higher angles at the top and bottom, decreasing towards mid-depth with the smallest angles at hub height. This consistent trend is thought to be associated to the current generation method.

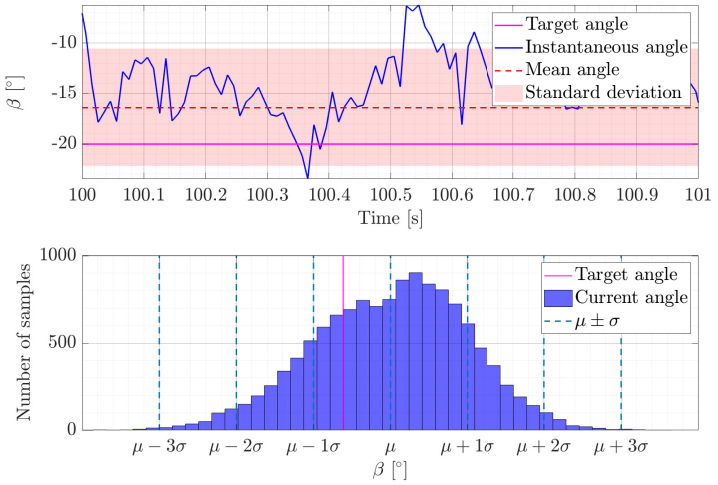


**Figure 6.19:** Top: current direction variation from the mean (red dashed line) during a one second period. Bottom: Histogram of the measured current angle during the whole duration of a test. Flow measurement at hub height for case C3.

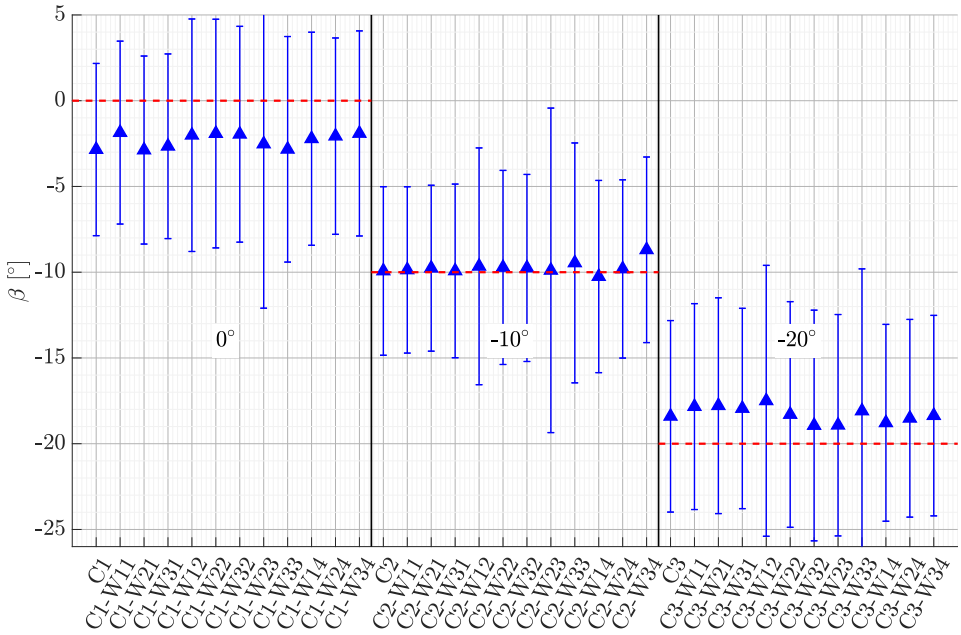


**Figure 6.20:** Current direction $\beta$ at hub height for all test cases with error bars showing standard deviation. Horizontal axis is divided in three sections: 0°, -10° and -20°. Dashed lines indicate target current angle.

Figure 6.22 shows the spatial variation of the inflow angle within the rotor area for C1 (top), C2 (middle) and C3 (bottom). For case C1, the minimum deviation measured from the prescribed angle (0°) is -3.93° and the maximum is 2.35°. The spatial-averaged angle over the rotor plane is -1°. For C2, the highest measured

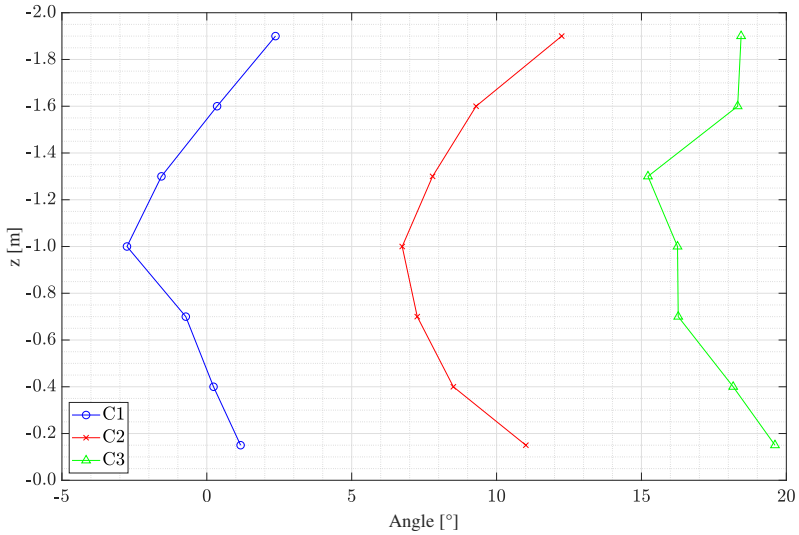


**Figure 6.21:** Depth profiles of current incident angles at rotor plane. Each line represents each current angle case seen from the front of the rotor.

angle is 9.29° and the lowest is 5.62° with a rotor-averaged angle of 7°. Lastly, C3 presents maximum and minimum values of 19.13° and 14.11°, respectively, and a rotor-averaged angle of 16.77°. In cases C2 and C3, $\Delta\beta$ values indicate the angle difference between each point and the same point from the 0° case. In all cases, the average angle over the nine measurement points of the rotor plane is lower than the prescribed angle. The reason for this is not known but it is presumed to be related to the way the current is generated, where the angular resolution of the tank is driven by the set number of impellers.

## 6.5 Discussion

A feature of the spectral density data in Figure 6.13 is an apparent levelling off of some of the flow components spectral densities for the highest frequencies. This so-called 'noise floor' can be seen in Figure 6.13, where at higher frequencies, the curves tend to depart from the trend of the velocity spectral density into a plateau. This noise floor is associated with all the white noise from the sensors.

Another feature seen in Figure 6.13 is the difference at which this noise floor appears depending on the velocity component. The explanation for this lies in the Vectrino probe geometry shown in Figure 6.23. The noise floor can be seen in Figure 6.13, where the $u$ and $v$ curves start to become horizontal and detach from the

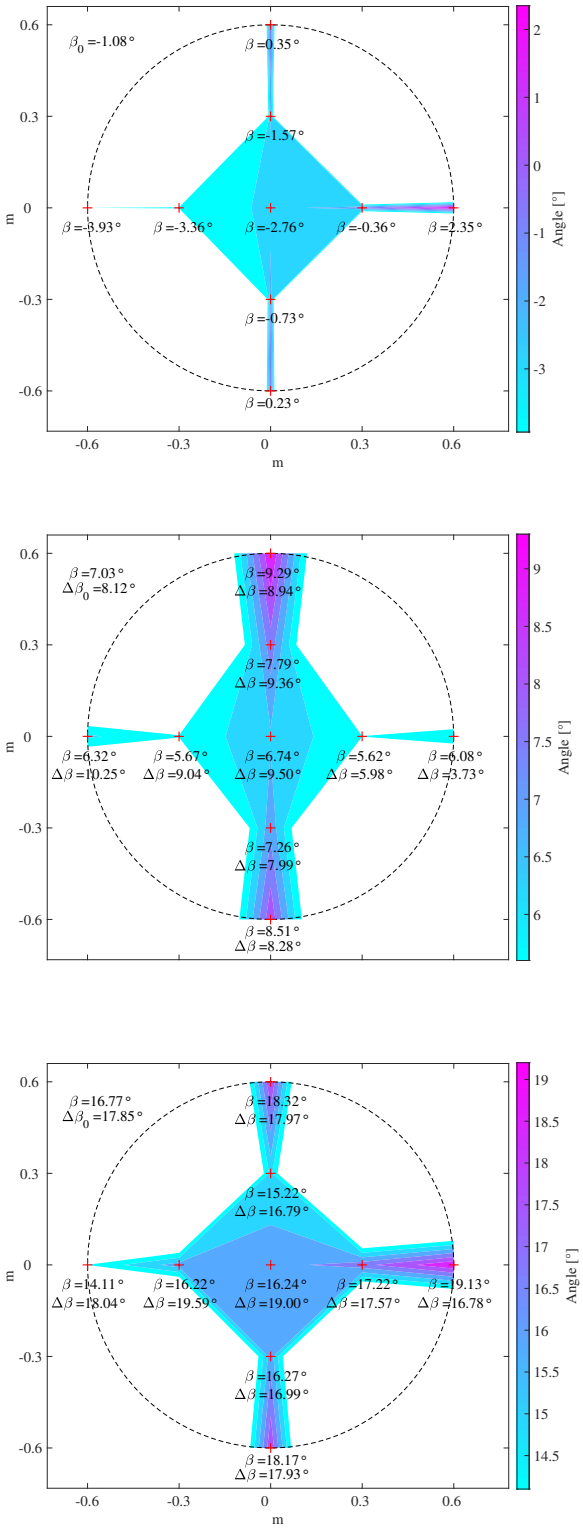


**Figure 6.22:** Contours of time-averaged, flow direction, $\beta$, in rotor plane for: C1 (top), C2 (middle) and C3 (bottom), based upon the nine-point measurements. Values in degrees (°)

-5/3 slope at around 10 Hz. Meanwhile, the vertical component *w* keeps following the -5/3 slope up to 50 Hz. This difference is due to the 60° angle at which the probe receivers are mounted relative to the emitter. The vertical direction is therefore 'better aligned' with the receiver's compared horizontal, giving a higher precision in the readings as compared to the longitudinal direction. This phenomenon was also observed by Harding et al. (2014). It is worth noting that the instrument was never rotated between tests and the impellers' rotational velocity input values were always the same.

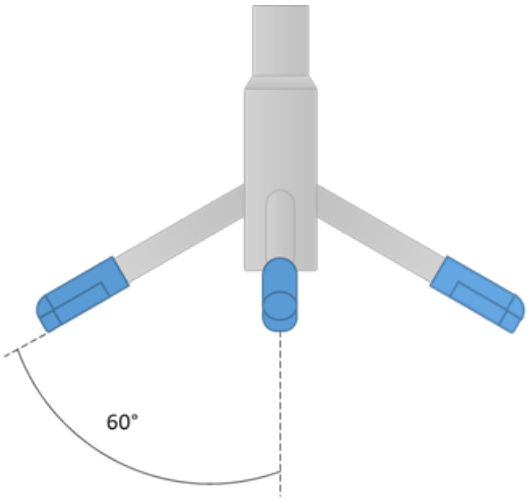


**Figure 6.23:** Vectrino probe geometry. The emitter is located in the centre while four (only three shown in diagram) protruding arms represent the receivers.

As seen in this section, the flow velocity spatial variation present in the rotor area makes it unreliable to use only hub height measurements when normalising and comparing results. Unfortunately, the only tests with measurements recorded at different rotor plane positions are without waves. Therefore, all normalising and comparing will be done with C1, C2 and C3 cases only. The use of these current-only cases however, will allow to isolate the effects waves have on the turbine.

It has been seen that flow velocity and current angle present non-uniformity within the rotor area of up to 10% from the prescribed values. One of the possible reasons for these spatial non-uniformities could be due to the relatively short length of the tests and the lack of repeats for any of the tests. However, despite this non-uniformity, the quality of the data and the different conditions tested gave

confidence that the data is fit for purpose and it is now possible to move on to the next stage of the data analysis with the turbine tests.

## 6.6 Conclusion

Flow characterisation consisted of a set of tests where the turbine was not mounted in the basin in order to quantify the flow conditions the turbine was going to be exposed to. The test conditions comprised of three current angles (0°, -10° and -20°) with flow velocity of 0.8 m/s. Flow characterisation tests were only performed with the current-only cases C1, C2 and C3. Flow measurements were performed with an ADV and a set of two wave gauges.

The wave gauges data went through a filtering process utilising the *smooth* MATLAB function and a despiking method by means of threshold exceedance identification and linear interpolation. As all the flow characterisation tests were performed without waves, wave height is explored in Chapter 7.

The flow velocity presented a depth profile similar to a $1/10^{th}$ power law, with velocities closer to the water surface up to 22% faster than the flow closest to the bottom of the basin. The flow velocity measured within the rotor area presented spatial variability of $\pm 9\%$ of the prescribed velocity of 0.8 m/s. Analysis of the flow velocity in the frequency domain show that the flow velocity follows closely a -5/3 slope, meaning that the flow behaves as the idealised case of turbulent flows. $TI$ levels also present a depth profile with the higher levels closer to the bottom of the basin, where the slowest flows were observed. The lowest $TI$ recorded was 6.8% and the highest 11%. The average current direction for all the cases at prescribed 0° was observed at -2°, for prescribed -10° was -10° and for -20° was -18.5°.

# Chapter 7

# Turbine testing

## 7.1 Introduction

In this Chapter, the turbine tests performed with the 1.2 m rotor diameter turbine introduced in Chapter 4 are presented. The turbine was subjected to a combination of oblique wave and current conditions. The objectives of these tests are to explore the influence the selected flow conditions on the turbine model with the non-dimensional power and thrust coefficients, to quantify the loading dependency on the rotor angular position and to identify key frequencies in the turbine loading.

## 7.2 Methodology

The turbine tests are divided in two phases: turbine characterisation under current-only conditions and turbine testing at fixed $TSR$ for all current and wave conditions.

The turbine characterisation tests are aimed at characterising the turbine's power and thrust coefficients ($C_P$ and $C_T$) without waves across a range of $TSR$ values. In these tests, the flow velocity remained fixed at a nominal value of 0.8 m/s and the rotor speed was varied from 45 to 95 RPM. During the first tests performed with this turbine (Payne et al., 2017a), the rotor experienced instabilities where the rotor would stop spinning and start jerking. The only way to stop the instabilities was to increase the rotational speed manually. These instabilities were witnessed only at $TSR < 4$. Hence, a $TSR$ range of 4.25 to 7.5 was chosen. It is thought a large ratio between the moment of inertia of the turbine rotor on the one hand and of the turbine motor on the other hand leads to these instabilities. This issue is also

probably compounded by the fact that the drivetrain shaft has a degree of compliancy due to the presence of the torque transducer between the rotor and the motor. However, these instabilities did not strongly influence the test matrix plan, nor at all influence the gathered data.

The turbine tests at fixed $TSR$ aim to understand how the rotor, blade and support structure loading behave over a mixed range of current directions, wave angles and wave periods and heights. In this case, as shown previously in Figure 5.1, three different current angles (solid lines) in combination with three wave conditions at four different angles (dashed lines) were used. The figure also shows the turbine position and the flow components convention. These tests were performed at a fixed $TSR$ of 7 with prescribed nominal flow velocity of 0.8 m/s and turbine speed of 90 RPM.

All the turbine characterisation tests under current-only conditions were performed at three different current angles as shown in Figure 5.1, and were based upon a measurement duration of 256 s as indicated in Chapter 5. This time is equivalent to approximately 384 rotor revolutions at 90 RPM. The turbine tests at fixed $TSR$ for all current and wave conditions were based upon a measurement duration of 512 s. This time is equivalent to approximately 768 rotor revolutions at 90 RPM and 256 waves for Tw=2 s, 205 waves for Tw=2.5 s and 170 waves for Tw=3 s.

For calculating the power and thrust coefficients, $C_P$ and $C_T$ respectively, equations 2.37 and 2.31 were used. In this case however, the time-averaged flow velocity $\overline{U}$ is replaced by the rotor-area- and time-averaged $\overline{U}_0$ (value shown top left of each panel in Figure 6.9).

The front view schematic of the rotor area seen in Figure 7.1 shows the position of the Vectrino (green) and the wave gauges (yellow lines). The latter are in the same positions as in the flow characterisation tests. The coordinates system is also shown. Note that due to the presence of the rotor, the Vectrino had to be positioned 0.1 m above the rotor. For an in-depth description of the experimental set-up refer to Chapter 4.

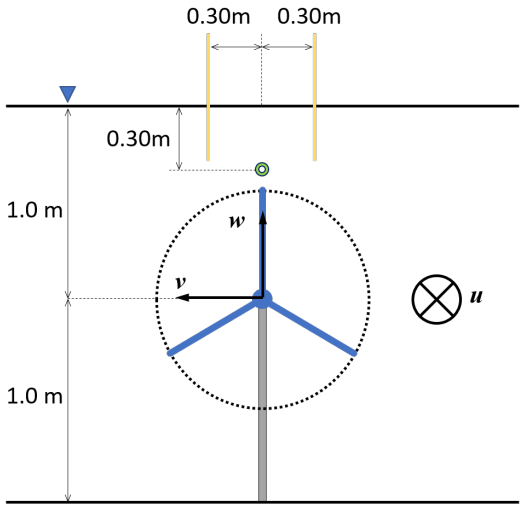


**Figure 7.1:** Front view of the turbine rotor with relative location of Vectrino (green) and wave gauges (yellow)

## 7.3 Data quality control

All the raw recorded signals went through an initial pre-processing quality check to ensure noise levels are kept to a minimum, outliers removed and faulty sensors identified so the data is fit for analysis.

### 7.3.1 Blade root bending moment (RBM)

During the tests, live feed of the root bending moment measurements of blade number three (*RBM*3) presented values outside the instrument's range due to a drift towards zero (Figure 7.2). These out-of-range levels showed flattened maxima peaks. In the post-processing of the data, with aid of MATLAB, this fault on the *RBM*3 signal was observed in all cases with the exception of cases C3-W23, C3-W33, C3-W14, C3-W24 and C3-W34. As will be seen later in this Chapter, it was decided not to use the data of *RBM*3 in the present analysis. The fault is believed to be due to a fault in the waterproofing of the *RBM* sensors or creeping in the strain gauge binding. For case C3, sensor *RBM*2 showed saturation levels. Visual check was performed to cross-check the data quality of all the signals for each individual test.

The *RBM* data has to go through a three-step process to be ready to use. Firstly, the raw data from the sensors needs to be converted from mA to Nm. This was done using calibration matrices provided by the manufacturer (Appendix A). These ma-

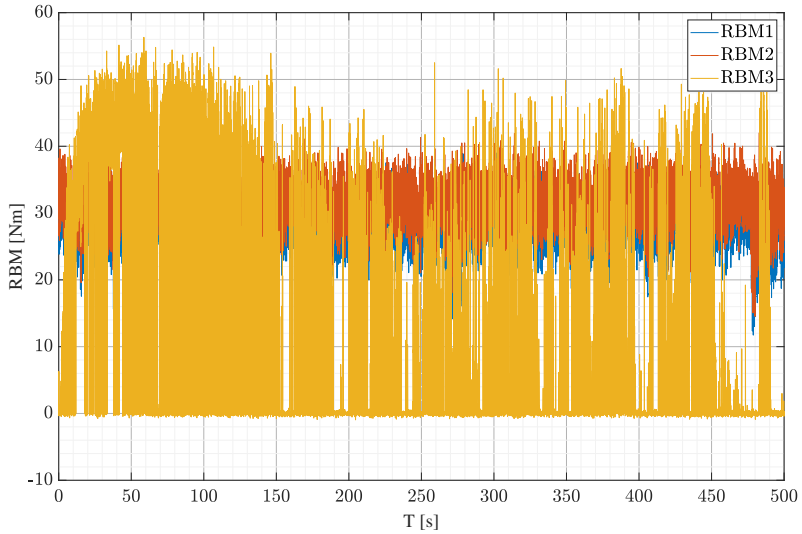


**Figure 7.2:** Time series of *RBM*1, *RBM*2 and *RBM*3. Case C1, no waves.

trices contain mA values of the *RBM*'s outputs at five different lever arm distances with six different forces. Secondly, the logged data from the zeroing tests performed with the turbine stationary and in still water is subtracted from the *RBM* time series. Finally, detection of outliers larger than three times the standard deviation of the signals are removed and replaced by linear interpolation.

### 7.3.2 Support structure load cell

The support structure load cell data presented large outliers up to five times the mean amplitude (Figure 7.3a, blue) that needed to be removed. The source of these outliers is believed to be electric noise as all of these outliers are one sample long. Considering a sample frequency of 256 Hz (0.003 s), a one-sample spike of over five times the mean value is not physically possible. The process utilised to identify the outliers was to find one-sample peaks that would fall outside an envelope of $\pm 10\%$ the mean value of the time series. Removing the outliers was done by linear interpolation between the two neighbouring samples. In Figure 7.3, a time series of the streamwise load cell force Fx for case C1-W21 is shown in raw (blue) and filtered (orange). A close-up of this same timeseries is shown in Figure 7.4, where the outlier removal and interpolation of the adjacent points to replace said outlier is seen.

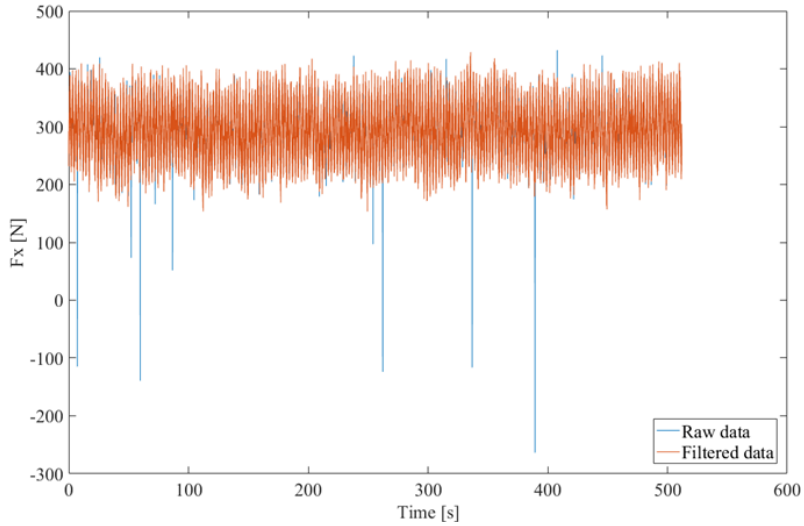


**Figure 7.3:** Sample for outlier removal in loadcell data for case C1. Overview of the whole time series

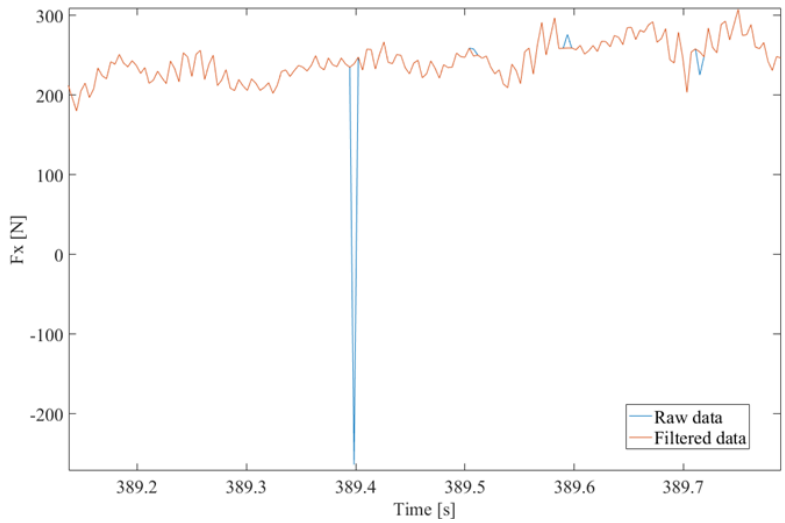


**Figure 7.4:** Sample for outlier removal in loadcell data for case C1. Zoom in of the largest peak showing removal by interpolation from Figure 7.3

### 7.3.3 Thrust transducer

When the turbine is submerged, the water column above the turbine applies a hydrostatic pressure to the thrust transducer. This pressure is then translated into a thrust force by the transducer. To remove this hydrostatic load, once the turbine is submerged the instruments are logged with the turbine and the flow still. During the data quality control these values are then subtracted from the measurements (Figure 7.5).

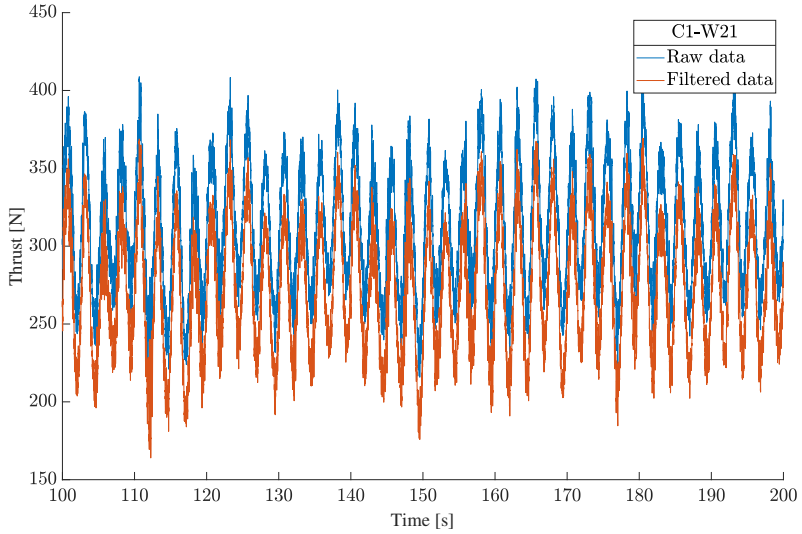


**Figure 7.5:** Extract of thrust signal before and after removing hydrostatic pressure for case C1-W21

## 7.4 Turbine characterisation under current-only conditions with a range of TSR values

In this section, the loading and performance of the turbine under current-only conditions over a $TSR$ range is presented. This is achieved by using the non-dimensional power and thrust coefficients ($C_P$ and $C_T$) introduced in Section 2.3 with Equations 2.31 and 2.37 and their respective standard deviation values. For this, the time-averaged torque $\overline{\tau}$ and thrust $\overline{\mathrm{T}}$ are used.

In Figure 7.6 the $C_T$ data for the three flow angles C1, C2 and C3 without waves is presented against $TSR$. The error bars indicate the $C_T$ standard deviation based on the full length of the coefficient time series. The 0° and -10° curves are almost overlapping whereas the -20° has lower values. The overlapping between the 0° and -10° curves might seem counter-intuitive as Bahaj et al. (e.g. 2007a) showed a decreasing trend that goes with the increasing yaw angle. However, Maganga et al. (2009, 2010) obtained similar results where the difference between 0° and 10° yaw is almost unnoticeable but the values above 10° start dropping as the yaw angle increases. This discrepancy is thought to be associated to the yaw angles tested in each work. Bahaj et al. (2007a) used yaw angles of 0°, 15°, 22.5° and 30° whereas

Maganga et al. (2009, 2010) used 0°, 10°, 15° and 20°. Perhaps, if Bahaj et al. (2007a) had tested at 10°, they could have witnessed similar results as Maganga et al. (2009, 2010) and this work.

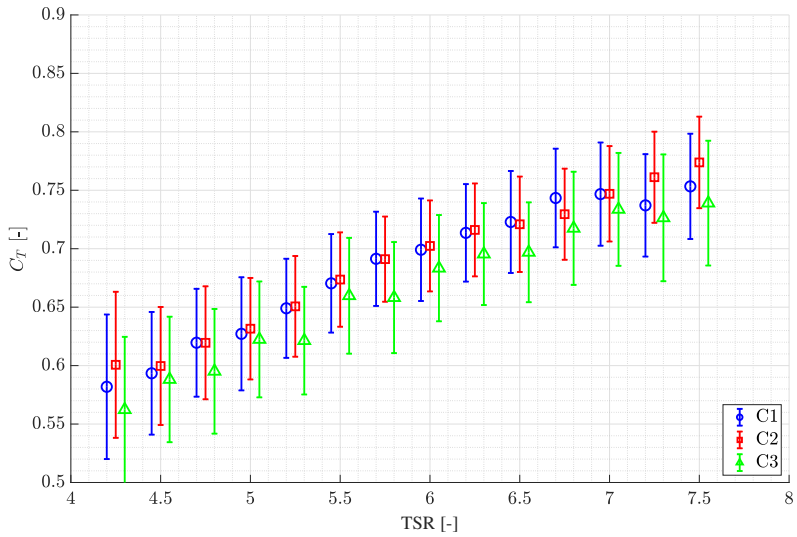


**Figure 7.6:** Variation of $C_T$ with $TSR$. Error bars indicate $C_T$ standard deviation. Three yaw angles: C1:0°, C2:$-10°$ and C3:$-20°$. No waves. C1 markers shifted by 0.05 to the left and C3 markers shifted by 0.05 to the right to avoid overlaps and improve visibility.

Figure 7.7 shows the standard deviation in $C_T$ normalised by the average $C_T$ for each flow angle case. For the three cases, the *SD* presents a convex shape with lowest values at around $TSR$=6. The highest values are for case C3. Case C1 has similar values (within 5%) to case C2 for $TSR < 7$. For $TSR > 7$, the normalised *SD* values for C2 are 20% higher than C1. For C3, the normalised *SD* values are 40% higher than C1 when $TSR > 7$. Another gap of 40% between C3 and the other two cases is seen at $TSR \approx 5.75$. Although there seems to be a pattern between the yaw angles, there are still discrepancies of unknown nature that do not allow to establish conclusions.

Figure 7.8 shows the $C_P$ variation with $TSR$ covering the three yaw angles cases (C1, C2 and C3) without waves. The error bars indicate the $C_P$ standard deviation. In this case, the data do not follow the same intuitive variation with yaw that was followed by $C_T$. The $C_P$ for the C2 case is marginally ($\sim 5\%$) higher than the C1 case. The C3 data show the lowest values, typically by about 10%. This

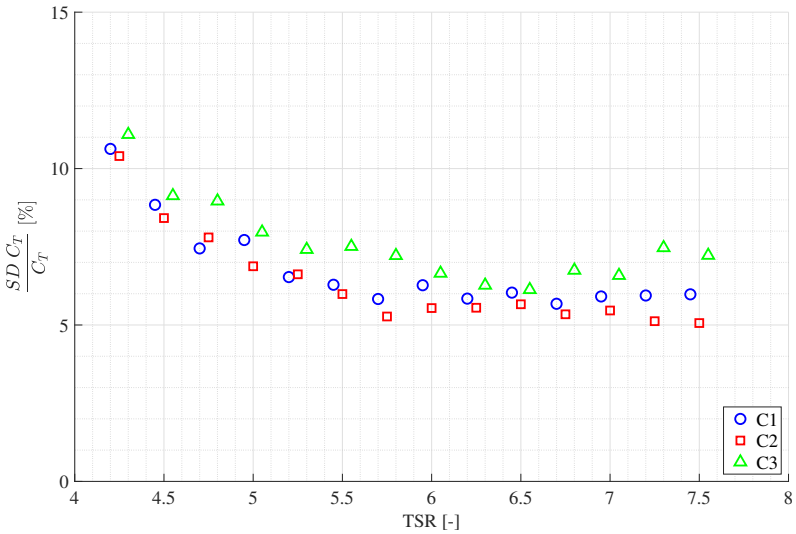


**Figure 7.7:** Standard deviation of $C_T$ normalised by the average $C_T$. Three yaw angles: C1:0°, C2:−10° and C3:−20°. No waves. C1 markers shifted by 0.05 to the left and C3 markers shifted by 0.05 to the right to avoid overlaps and improve visibility.

phenomenon was also observed by Frost (2016) but has not yet been satisfactorily explained. However, the difference in $C_P$ between C1 and C2 is so small that it could be compared with the experiments performed by Maganga et al. (2009, 2010), where the coefficient curves overlapped for yaw angles lower than 15°.

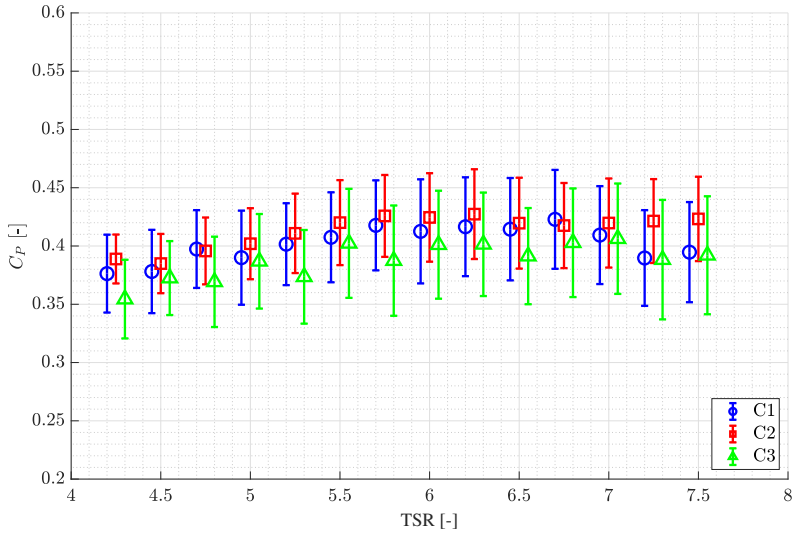


**Figure 7.8:** Variation of $C_P$ with $TSR$. Error bars indicate $C_P$ standard deviation. Three yaw angles: C1:0°, C2:−10° and C3:−20°. No waves. C1 markers shifted by 0.05 to the left and C3 markers shifted by 0.05 to the right to avoid overlaps and improve visibility.

Figure 7.9 shows the standard deviation of $C_P$ normalised by the average $C_P$ for the three flow angle cases C1, C2 and C3. Compared to $C_T$ in Figure 7.7, the standard deviation behaves in the opposite way, with a concave shape. In this case the curves have maximum values at $TSR \approx 6$. Although there seems to be a trend (C3 case with the highest $SD$ values, followed by C1 and, with the lowest values, C2), there is scatter in the $SD$ values, with the most noticeable being case C3 at $TSR \approx 6.5$. Similarly to Figure 7.7, it is not possible to draw any conclusions as no cause for the fluctuating values across the $TSR$ range has been identified.

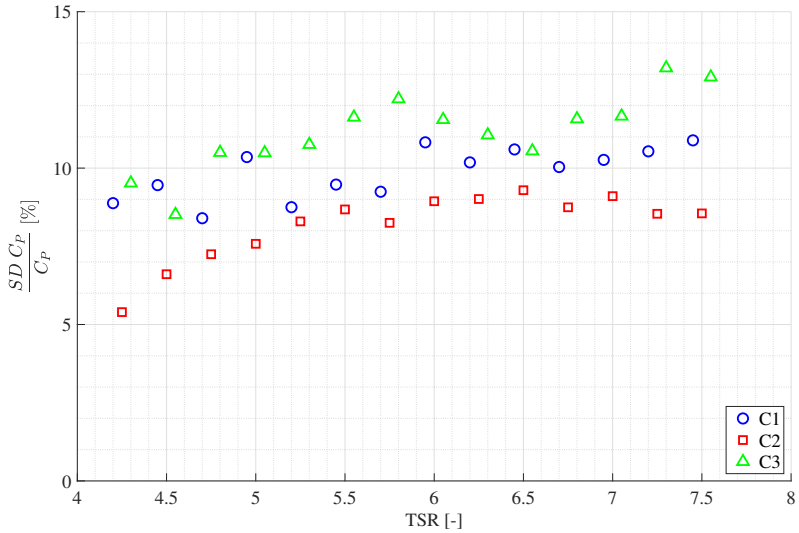


**Figure 7.9:** Standard deviation of $C_P$ normalised by the average $C_P$. Three yaw angles: C1:0°, C2:−10° and C3:−20°. No waves. C1 markers shifted by 0.05 to the left and C3 markers shifted by 0.05 to the right to avoid overlaps and improve visibility.

From Figure 7.7 and Figure 7.9, it can be noticed that $C_P$ and $C_T$ curves have standard deviations between 5% and 15% of the mean values. These values are not dissimilar to previous tests using the same turbine model (Payne et al., 2017a) at IFREMER with $TI = 12\%$.

## 7.5 Turbine testing at fixed TSR for all current and wave conditions

In this section, the turbine testing for all current and wave conditions at fixed $TSR$ is explored. Different analysis approaches are used. The section commences by

exploring the power and thrust coefficients at fixed $TSR$, then it moves to time domain testing, exploring the dependency of the loads on the wave fluctuations and on the rotor angular position. It concludes by exploring a frequency domain analysis of the data, from which some insights can be gained into the key frequency components of loading of the system.

### 7.5.1 Turbine performance under waves and current at fixed TSR - influence of wave period

Exploring the influence of wave period, Figures 7.10 and 7.11 show $C_T$ and $C_P$ respectively with error bars indicating their respective standard deviation based upon the full length of the coefficients time series. Each subplot is for wave angles of a) 0°, b) 45°, c)135° and d)-45°. For each wave angle, the current angle cases (C1, C2 and C3) and wave periods (2, 2.5 and 3 s) are grouped in each figure. The turbine $TSR$ is 7 at nominal flow velocity $U$=0.8 m/s. The coefficients were calculated using rotor-area- and time-averaged flow velocity $\overline{U_0}$ without waves. This approach helped isolate the influence of the waves in the coefficients and compare directly with the current-only cases. In both figures, similar trends are observed in the thrust and power coefficients, where C2 has the highest values, followed closely by C1 and at the bottom, with the lowest values, C3.

As it has been demonstrated previously (Bahaj et al., 2007a; Gaurier et al., 2015; Doman et al., 2015; Morandi et al., 2016), looking at waves with $\theta = 0°$ (Figure 7.10a), it is clear that the addition of waves with any period has little influence on the average $C_T$ values. However, it is seen that the addition of waves has a more evident influence on the $C_T$ standard deviation. Waves with period Tw=2.5 s and wave height H=91 mm present the highest $SD$ values of all the other wave cases for $\theta = 0°$ and 135°. The $C_T$ standard deviation with those waves at 0° is almost three times higher than the case with no waves. Similar behaviour has been observed by Gaurier et al. (2013); Barltrop et al. (2007); de Jesus Henriques et al. (2014b); Galloway et al. (2010); Porter et al. (2018); Ordonez-Sanchez et al. (2019); Martinez et al. (2019). What has not been reported in the literature before, is how rotor loading behaves for non-collinear waves and currents. Figures 7.10 b), c) and d) show

$C_T$ for all $\theta$ cases not-normal to the rotor plane. Waves with any wave height and period have average $C_T$ values within $\pm 2\%$ of the current-only cases for all $\theta$. In contrast, *SD* values are up to 30% the average $C_T$ values. Additionally, when waves occur at $\pm 45°$, $C_T$ standard deviation values for all wave cases are up to 1.5 times the values of the current-only cases. For $\theta = 135°$; however, waves with period Tw=2.5 s and H=91 mm have *SD* values almost three times the current-only cases, similar behaviour the same wave has at $\theta = 0°$.

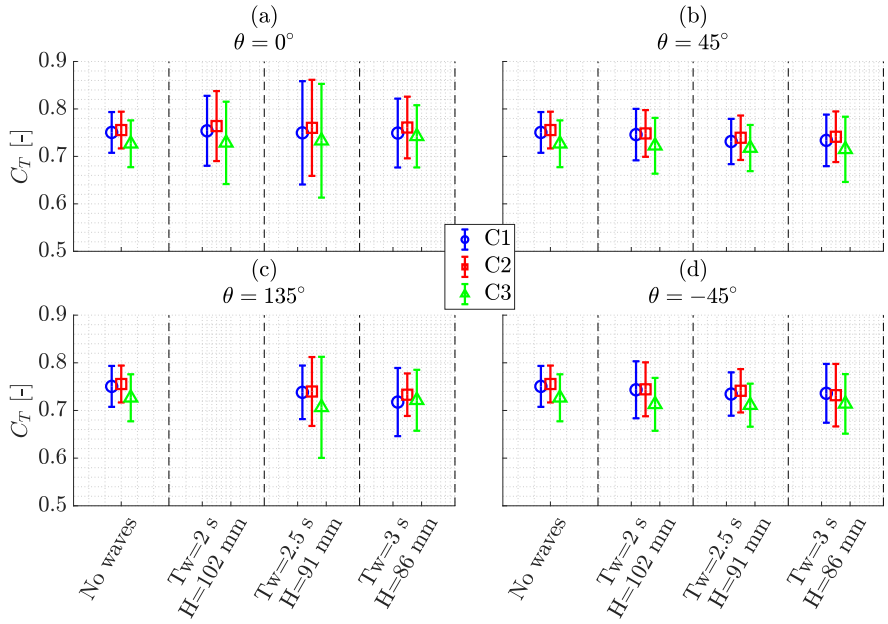


**Figure 7.10:** $C_T$ plots comparing the influence of wave period. Error bars indicate $C_T$ standard deviation. Plots grouped by wave angle: a) 0°, b) 45°, c)135° and d)-45°. *TSR*=7. Three flow angles: C1:0°, C2:$-10°$ and C3:$-20°$.

Looking into the power coefficient $C_P$, similar features seen in Figure 7.10 for $C_T$ are present in Figure 7.11 for $C_P$. Wave period and wave height have little effect on the average $C_P$ values. However, waves with Tw=2.5 s and H=91 mm have *SD* values up to 60% of the average $C_P$. All the different wave cases for $\theta = \pm 45°$ have *SD* values up to 1.5 times larger than the current-only cases. In contrast, waves with Tw=2.5 s and H=91 mm at 0° and 135° have *SD* values up to 2.5 times larger than the current-only cases. It is not yet understood why the wave with Tw=2.5 s has the largest influence on the *SD* of the coefficients. However, it is evident that the influence of wave height and period is closely dependent on the wave directionality.

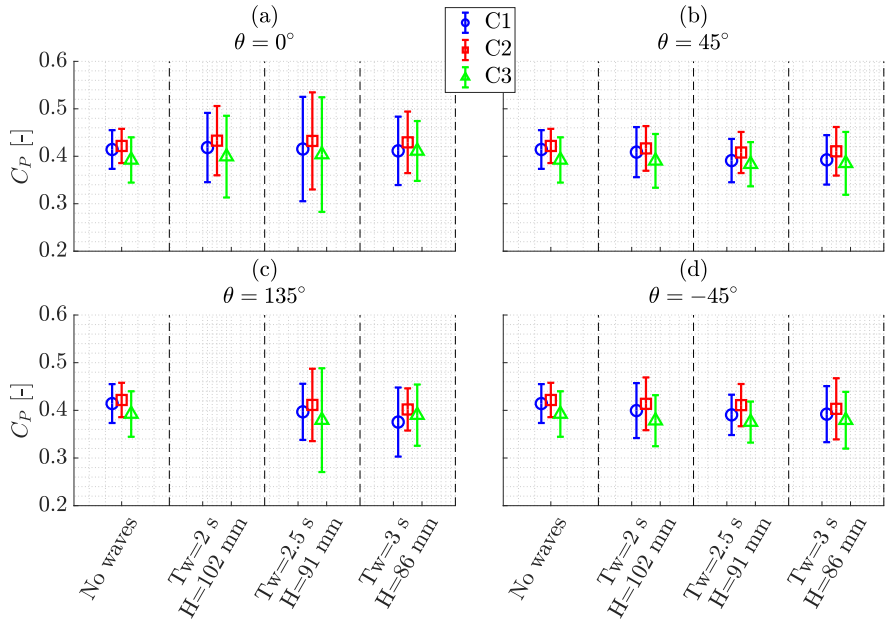


**Figure 7.11:** $C_P$ plots comparing the influence of wave period. Error bars indicate $C_P$ standard deviation. Waves at a) 0°, b) 45°, c)135° and d)-45°. $TSR$=7. Three flow angles: C1:0°, C2:$-10°$ and C3:$-20°$.

### 7.5.2 Turbine performance under waves and current at fixed tip-speed-ratio - influence of wave angle

Exploring the influence the wave angle has on $C_T$ and $C_P$, Figures 7.12 and 7.13 respectively, group tests by wave period. Each panel in both figures is for a specific $\theta$ value. Error bars indicate standard deviation.

The influence of the wave angle on the average $C_T$ values is more noticeable for waves with period Tw=3 s. At 135°, the average coefficient for C1 and C2 cases is $\sim 5\%$ lower than the $\theta = 0°$ case. For all wave conditions, cases C1 and C2 have very similar $C_T$ values. Case C3 also behaves similarly to cases C1 and C2 but with lower values. However, the gap between C3 and the two other cases decreases as the wave period increases. With the waves grouped by wave period, it is also possible to see how the waves with Tw=2.5 s have the largest influence on the standard deviation of $C_T$ with values up to 60% higher than other $\theta$ values. Wave cases at $\pm 45°$ have very similar values for $C_T$ at all wave periods. With waves

at 135° and current angle at 0° and -10°, $C_T$ is higher than for waves at ±45° for Tw=2.5 s and lower for waves with Tw=3 s.

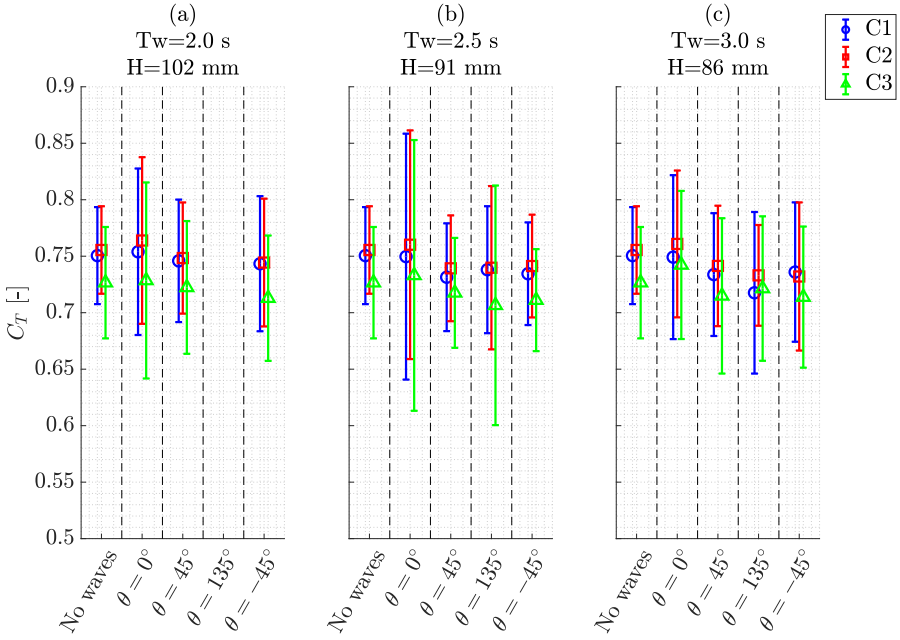


**Figure 7.12:** $C_T$ plots comparing the influence of wave angle. Error bars indicate $C_T$ standard deviation. Plots grouped by wave period: a) Tw=2.0 s, b) Tw=2.5 s, c) Tw=3.0 s. $TSR$=7. Three flow angles: C1:0°, C2:−10° and C3:−20°.

The power coefficient $C_P$ in Figure 7.13 has the same features as the thrust coefficient $C_T$ from Figure 7.12: for waves at 0°, $C_P$ has similar average values than for the cases without waves, waves not normal to the rotor plane show lower average values. Also, waves at 0° have the highest $SD$ values off all cases, specifically the wave case with period Tw=2.5 s.

In this Section, it was observed that wave-induced fluctuations have the highest influence on the thrust and power coefficients of a tidal turbine when they are normal to the rotor plane. However, as it was shown in Section 2.2.4, waves do not have a constant directionality as the tests presented here. In real sea conditions, wave directionality varies with time, therefore, the influence of waves normal to the rotor plane would not be constant. The same conclusion applies for the wave period. In real sea conditions, a tidal turbine will be subjected to a range of wave periods (Figure 2.5), with its particular influence on the turbine. As mentioned by Mullings

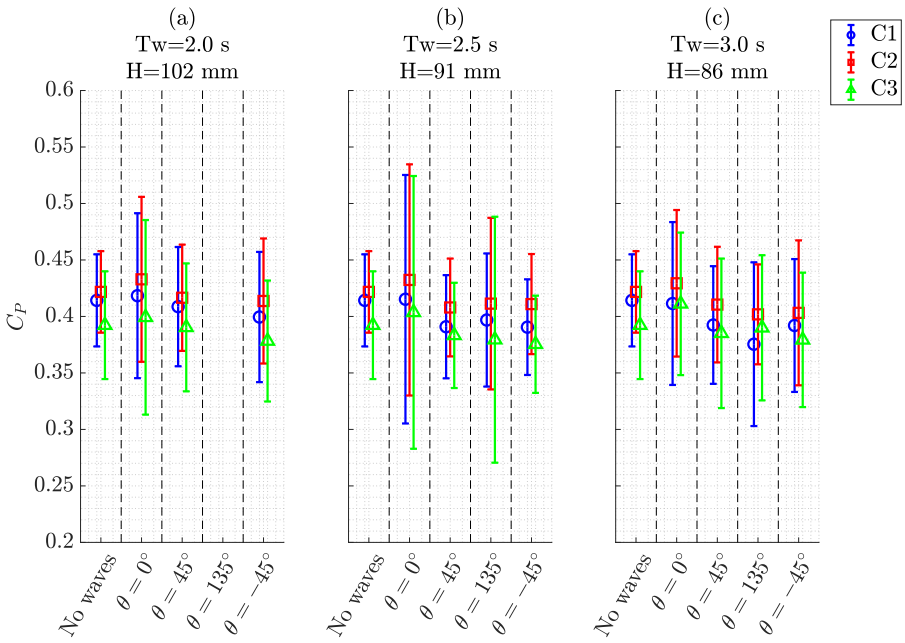


**Figure 7.13:** $C_P$ plots comparing the influence of wave angle. Error bars indicate $C_P$ standard deviation. Plots grouped by wave period: a) Tw=2.0 s, b) Tw=2.5 s, c) Tw=3.0 s. $TSR$=7. Three flow angles: C1:0°, C2:$-10°$ and C3:$-20°$.

et al. (2017), considering constant values overestimates the loading a turbine would experience in real sea conditions as no variable is constant in real sea conditions.

### 7.5.3 Rotational speed analysis

Analysing the influence the wave- and turbulence-induced flow fluctuations have on the rotor performance, the histogram in Figure 7.14 shows the rotational speed values of the rotor during combined wave and current case C1-W21. The histogram averages all the the rotational speed samples available in 0.667 s, which is equivalent to one full turn of the rotor. The magenta line indicates the target rotational speed of 90 RPM. These fluctuations are within the range of 86-89 RPM which is equivalent to $\sim 1-4\%$ of the target value. Assuming a constant flow velocity of 0.8 m/s, the turbine experiences a $TSR$ range of 5.75-5.95 during the test. This variation, although small, might have an influence in the turbine power production as the real $C_P$ is below the optimum $C_P$ value at $TSR \approx 6$.

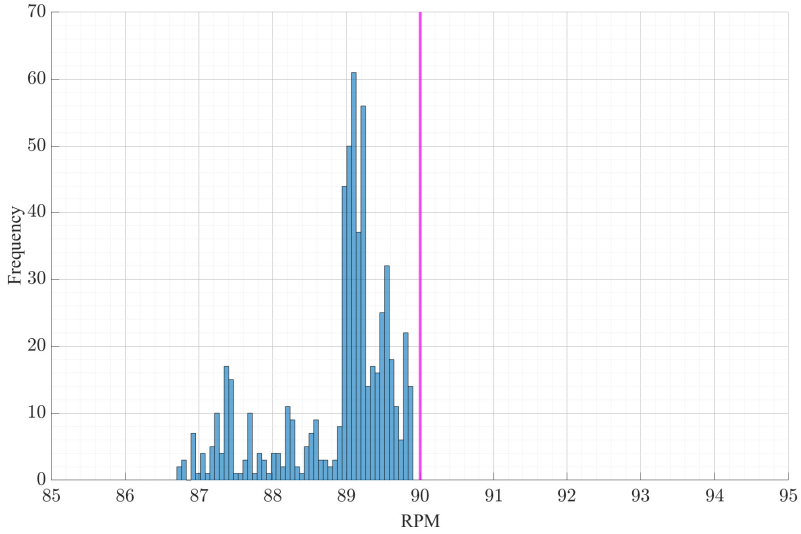


**Figure 7.14:** Histogram of rotational speed for case C1. Pink line represents the target rotational speed of 90 RPM.

### 7.5.4 Timeseries analysis of loading fluctuations due to waves

Sections 7.5.1 and 7.5.2 explored the influence of wave obliquity and period upon the dimensionless power and thrust coefficients. Although these measures are crucial, they are intrinsically time-averaged quantities. Here, the contributing time series are explored. Figure 7.15 shows time series of wave elevation and time-varying rotor thrust T for test C3-W12 with nominal velocity $U$=0.8 m/s, yaw angle -20°; waves Tw=2.0 s, H=102 mm and wave angle 45°. It is possible to see how the low frequency component of the thrust signal follows the period of the waves, highlighting the influence of the wave on the thrust forces. The two wave gauges and the lowest frequency part of the thrust spectra are slightly out of phase due to the angle of 45° at which the waves are generated. Looking at Figure 4.5, it can be seen that when waves come at an angle other than perpendicular to the rotor plane (45° in this case), one of the wave gauges will 'sense' the wave sooner than the other wave gauge, giving a phase difference. The slight wave height difference is not fully understood. The wave trains in the tank are not the only feature in the water surface. As the wave gauges are located exactly above the rotor, it could be possible that the rotation of the rotor has an influence on the wave propagation. However, the wave gauge that presents a higher amplitude is not always the same one, making it diffi-

cult to draw any conclusion. The high frequency oscillations observed in the thrust data are thought to be associated with the rotation of the three blades at $\sim 4.5$ Hz. This specific frequency is also explored in Sections 7.5.5 and 7.5.7.

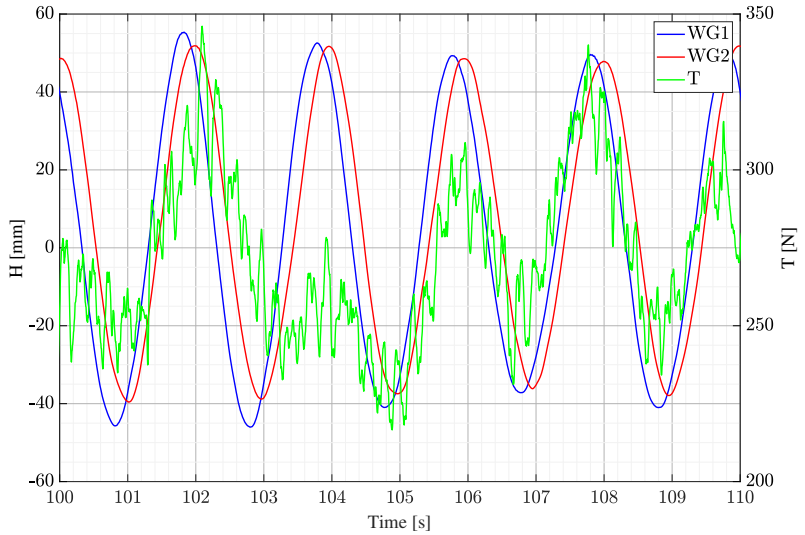


**Figure 7.15:** Time series of wave gauges (left axis) and thrust T (right axis). Case C3-W12.

Looking into the behaviour of the time-varying rotor torque $\tau$ in Figure 7.16, it is possible to see how it follows the waves' motion. The waves' influence on the rotor loading can be seen despite the high frequency noise in the data. The wave oscillations cross the mean thrust value at almost every cycle, with the result that the mean values between cases with and without waves are almost the same. These oscillations however, contribute to the high *SD* values of the power and thrust coefficients seen in Section 7.4 and 7.5.1. The high frequency fluctuations observed in the torque data are thought to be a mechanical/electrical artefact of the turbine. These fluctuations are also identified in the frequency domain as 'peak 7' on Figure 7.25.

### 7.5.5 Loading dependency on rotor angular position

In an attempt to understand the behaviour of the turbine loading in relation to the absolute position of the blades, polar plots are introduced in this subsection. Figure 3.4 shows the front view of the rotor with the blades, stanchion and rotational direction identified. All polar plots in this Section use this view as reference.

It can be anticipated that the instantaneous angular position of the blades will have an influence on the rotor loading. Also, changes in yaw angle and addition of

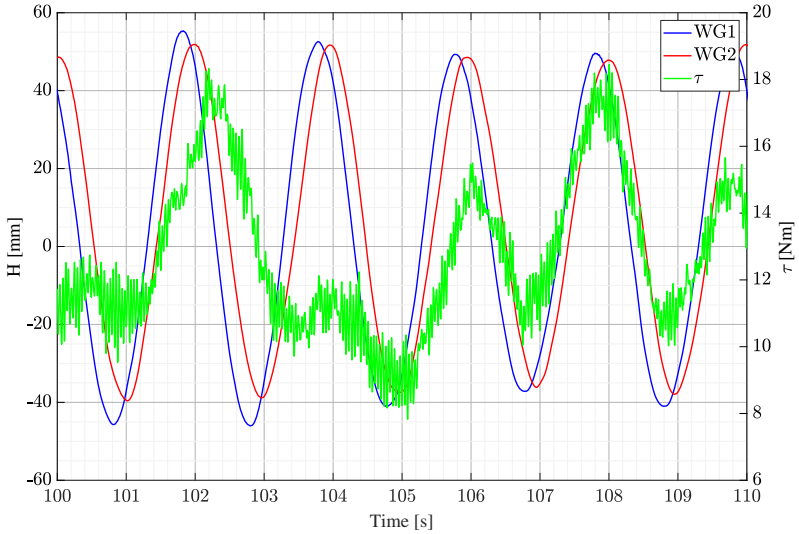


**Figure 7.16:** Time series of wave gauges (left axis) and torque $\tau$ (right axis). Case C3-W12.

waves are expected to have an influence on the rotor loading relative to the blades' angular position. To quantify this angular influence, Figures 7.17 to 7.22 are made by creating 1° bins and averaging all values of a given time series of any instrument that fall in each angular bin, giving an 'angle-averaged' polar plot. The angular position utilised is taken from the resolver data. In order to explore the angular behaviour of the rotor, thrust, *RBM*, torque and rotational speed (shown as RPM) are plotted in Figure 7.17 to Figure 7.20. The values plotted are the load variations as a percentage of the average. As an example, the 30° bin of the thrust measurements for, say, case C1, will have the average of all the thrust measurements that occurred when the motor shaft was at a 30° position.

Firstly, Figure 7.17 shows the thrust, *RBM*, torque and RPMs as a percentage of the mean values for cases C1, C2 and C3 to see the effect of yaw angle without the influence of waves. Each case has a specific colour: blue for C1 (0°), red for C2 (-10°) and green for C3 (-20°). The thrust plot shows different curves for each case, with a similarity being the clover-like shape that is somewhat lost at -10°. Despite the different shape, they all show a 120° pattern between each 'petal' of the clover-like shape. This clover-like shape is attributed to the tower 'shadow effect' that happens every time a blade passes in front of the support structure, hence three times per revolution of the rotor. The angular shift between the 'notches' and the

position of the tower has also been reported by Payne et al. (2018) and Ahmed et al. (2017) with experimental studies, and by Mason-Jones et al. (2013) with CFD simulations. The angular shift between cases C1 and C3 is $\sim$20°. This difference could be attributed to the difference between the cases' yaw angles of 0° and -20°, respectively.

The *RBM* curves for cases C1 and C3 show a fairly similar shape with their left-hand side narrower than the right-hand side. It is possible to see how at the bottom half of the rotor the blade experience lower *RBMs*. At the location of the tower (180°) the curves present a notch. These notches are thought to be attributed to the 'tower shadow' effect as the blade passes in front of the support structure once per revolution. Another possible contribution to the reduced loading at the notches is the decreasing flow velocity towards the bottom of the basin. The C2 curve shows a more rounded shape and slightly inclined to the left. Similar to the thrust curves, there is an angular difference between the notch in the *RBM* curves and the support structure.

It is interesting to see that in the torque plot, all case curves look very similar to each other. All of the curves show six peaks instead of three as in the thrust plot. Each of these peaks is now at 60° from each other, half of the 120° separation from thrust. All the peaks 'avoid' the tower, creating notches with 60° of separation. For $120° < \phi < 300°$ the peaks have a higher amplitude than for $120° > \phi > 300°$.

The RPM plot within Figure 7.17 shows the effect of the flow variability in the rotational speed and the efforts the drive goes through to keep the rotational speed constant. It can be seen that for roughly $120° < \phi < 300°$ the rotational speed experiences fewer variations but of higher amplitudes, phenomenon that matches the largest 'petal' in the thrust plot. For $120° > \phi > 300°$, the rotational speed appears to have higher frequency fluctuations but with smaller amplitude, meaning that the rotational speed is kept more constant in this area with more, but minor, fluctuations than the area below this line. This could mean that the area most influenced by the tower is the one for $120° < \phi < 300°$, generating larger fluctuations in the rotational speed. These fluctuations in the rotational speed could have a detrimental

effect in the drivetrain due to the fluctuations in the torque. The three curves present an elongated shape with centre line between 45° and 225°. The changes in RPM have a direct effect on the $TSR$ of the rotor and therefore on the $C_T$. For a given case C1, a rotational speed variation range of -3% to 2% from the average RPM and, if a constant flow velocity of 0.8 m/s is assumed, the turbine would experience a range of $TSR$ values of 6.5 to 7.1 during a test. These variations in $TSR$ will have an effect on the turbine's power and performance as seen from the standard deviation in Figures 7.6 and 7.8. Although the variations in the rotational speed could be a response to how the speed control is implemented, it is thought that this behaviour is not only specific to the scale model tested here as all the patterns seen in the curves are associated to some extent with the 'tower shadow' effect. Most common full-scale turbines have a tower-like support structure.

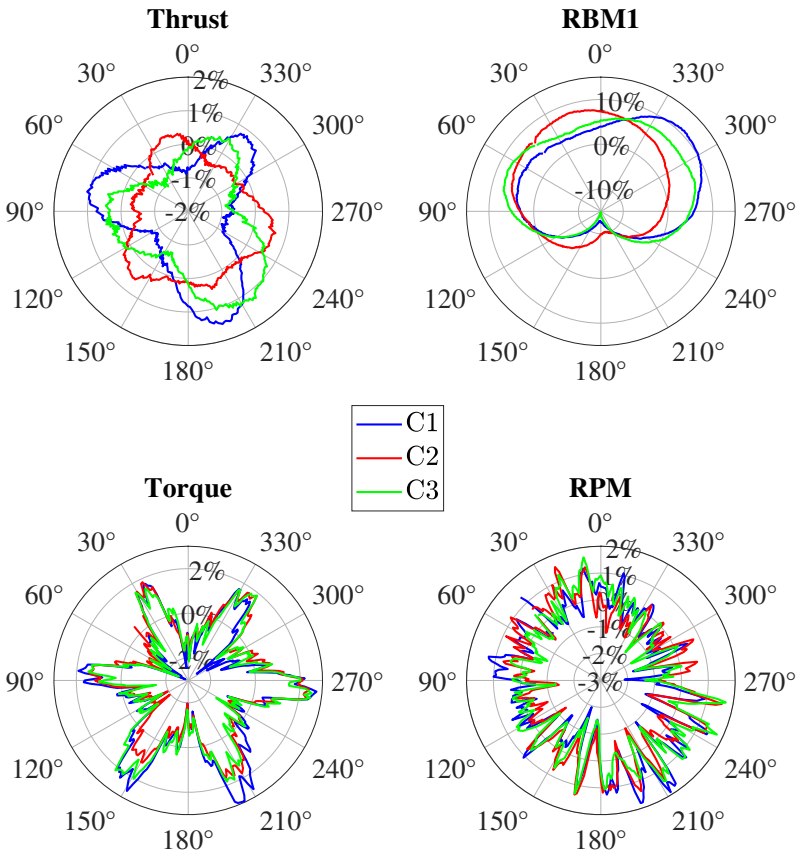


**Figure 7.17:** Polar plots of rotor loads and rotational speed variations as percentage of the mean values for cases C1, C2 and C3

Looking into the shape of the thrust curve on the C2 case from Figure 7.17, it is interesting to observe a similarity with cases in Figure 7.18, where the same yaw angle, and waves at 0° incidence show the same triangular shape. As has been seen throughout this work, the cases at -10° yaw have behaved somewhat differently to the C1 and C3 cases. No obvious explanation has been found. However, it is possible that the high flow variability seen in the rotor area that causes the $C_P$ and $C_T$ of case C2 (Section 6.5), is the same artefact that causes the more rounded shape of the *RBM* polar plots and the triangular shape of the thrust plots.

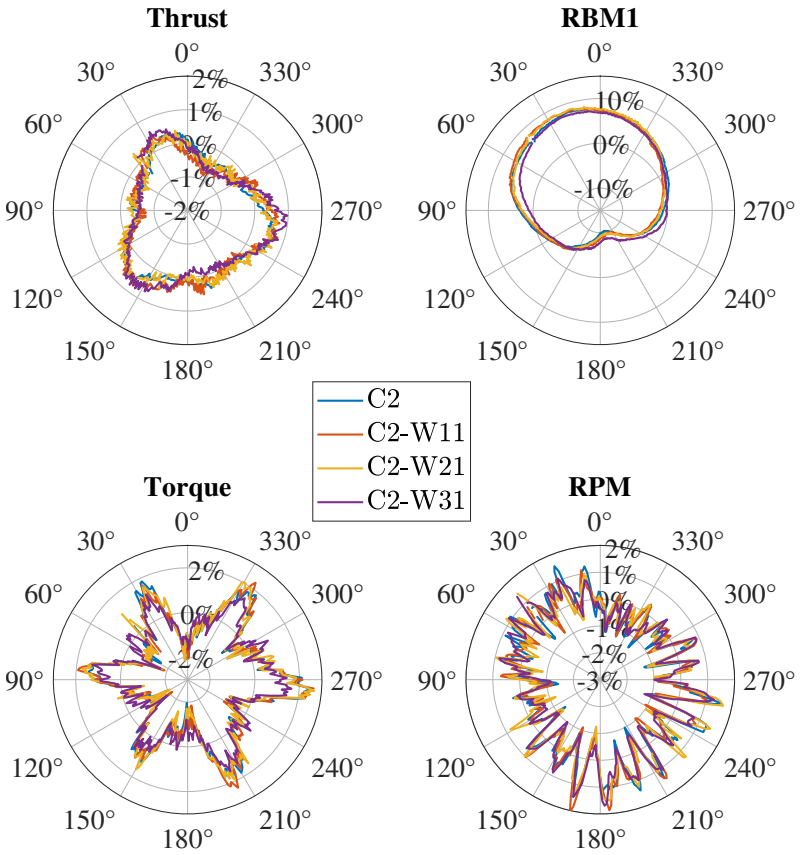


**Figure 7.18:** Polar plots of rotor loads and rotational speed variations (% from mean values) for all waves at 0° with -10° yaw.

It is relevant to see how fixing some parameters influence the turbine's behaviour. When this is done, it is possible to see patterns that otherwise would not be possible to identify and how the various parameters influence the turbine's behaviour.

Figure 7.19 explores the effect of wave period and height by keeping constant the yaw angle and wave angle at 0°. In all the subplots, it is possible to see that the wave period and height have little effect on the turbine's average loading and rotational speed with all the curves showing differences of no more than 0.5% between each other. This behaviour agrees with results shown in Sections 7.5.1 and 7.5.2

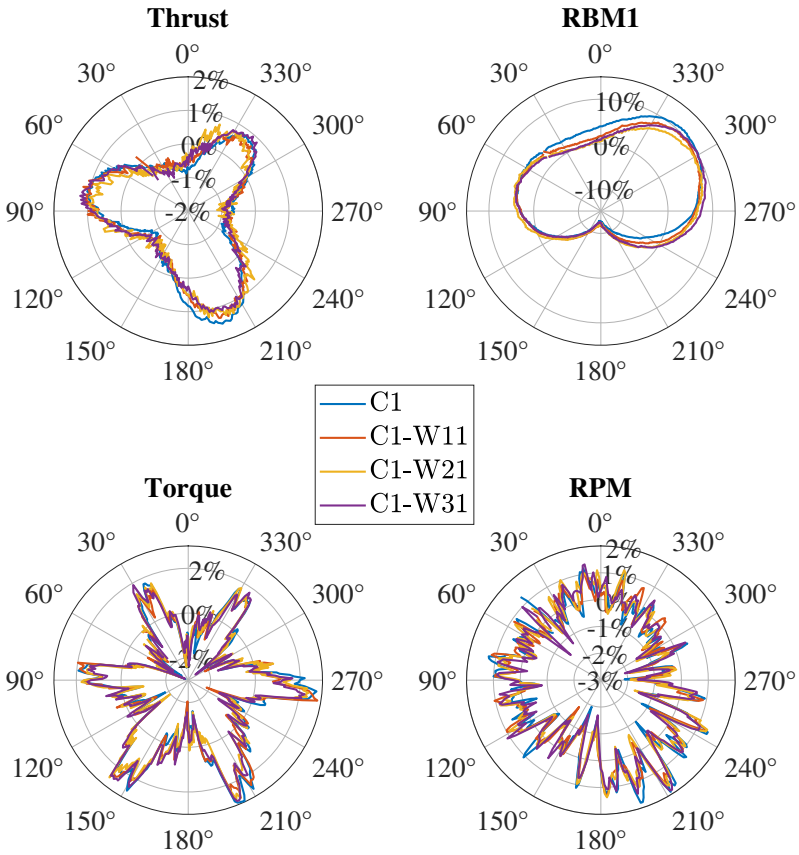


**Figure 7.19:** Polar plots of rotor loads and rotational speed variations (% from mean values) for all waves at 0° with 0° yaw.

Exploring the effect of wave angle, Figure 7.20 keeps a constant yaw angle of -20° and wave period Tw=2 s. Except for waves at -45°, thrust curves show a very similar shape with the largest petal at ∼200°. The *RBM* curves keep a similar shape with minor changes with the wave angle, giving it a narrower overall look but keeping the same distribution around the plot. The maximum difference between wave cases is no more than 5%. As this shape is kept almost constant at each given angle, little influence is to be expected on the rotor loading. Torque and RPM plots show no significant effect caused by wave angle.

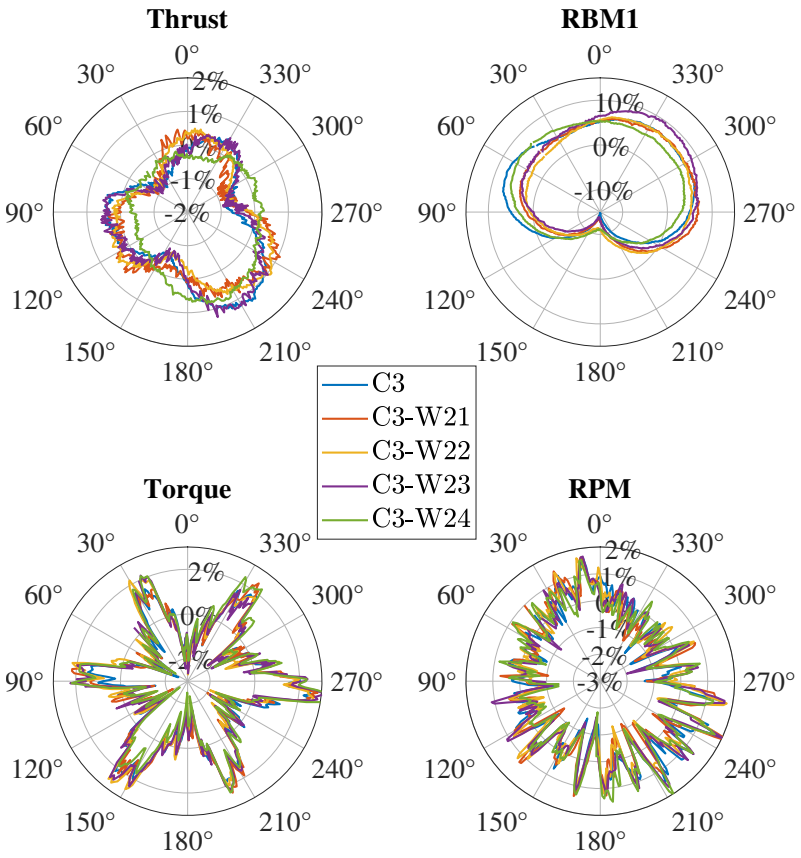


**Figure 7.20:** Polar plots of rotor loads and rotational speed variations (% from mean values) for waves with Tw=2.5 s, at all angles with -20° yaw.

In order to understand better the behaviour of the *RBMs*, thrust and torque, Figure 7.21 focuses on one single case: C3-W23. As has been mentioned before, the *RBM*3 transducer showed problems throughout the whole testing campaign so it is not included in this figure. In this case, the bottom left plot shows the two working *RBM* sensors with their absolute positions in the rotor. The bottom right plot shows the signals of *RBM*1 and *RBM*2. *RBM*2 in this case has been rotated so it matches the same position as *RBM*1. This correction is referred as 'angle-adjusted' and is used to compare how the blades behave during a full revolution. With the overlapped curves, it is possible to see that they both share the same shape, which indicates that, within a test, the two blades experience the same loading for every turn they make, independently of the flow characteristics. Due to the lack of a third *RBM*, it is not possible to compare the sum of the three *RBM* signals with the thrust signal.

The thrust (Figure 7.21, upper left) has the clover-like shape that is present in almost every case. It is possible to correlate the maximum value of the bottom 'petal' on the thrust curve (1.4%) with the highest value (10%) of the large, down-facing lobe of the *RBM*2 curve. A similar link can be made between the maximum value (1.1%) of the thrust's top 'petal' and the maximum value of 10% of the large lobe in the *RBM*1. If the third *RBM* were to be present, its shape would be likely associated to the maximum value (0.88%) of the third -unaccounted for- 'petal' from the thrust curve. Also, the notch at the lowest values on the *RBM* curves match the angular position of each of the notches -the lowest values- on the thrust curve.

The rotational speed (RPM) is shown in the top right plot. It shows higher frequency fluctuations than the loads in the same figure. The highest fluctuation amplitude ($\pm 2\%$ from the mean) appear to happen at $150^\circ > \phi > 300^\circ$. It is the same region where the highest thrust values of up to 1.5% from the mean are also present. This behaviour corresponds to the fact that, with a constant flow velocity, an increase in thrust corresponds to an increase in rotational speed (Figure 7.6). This phenomenon gives rise to a *TSR* range of 6.8-7.2 as the flow velocity is remained constant. This phenomenon was previously observed in Figure 7.17.

From the figures presented in this section, it is possible to observe that thrust, torque, *RBM* and rotational speed are influenced by the angular position of the rotor. The curve characteristics and fluctuation ranges of all the signals presented in this Section are similar to those observed by Payne et al. (2018). However, the shapes of the *RBM* curves are dissimilar (Figure 3.5 and 7.21). This difference is attributed to the flow characteristics of the facility in which the turbine was tested. This observation means that careful consideration has to be taken when selecting potential tidal sites as their unique flow characteristics will have a direct impact on any installed device.

### 7.5.6 Loading on support structure

The turbine is fixed to a support structure that is mounted on a six degrees of freedom load cell. When looking into the time-averaged streamwise loading ($\overline{\text{Fx}}$) on

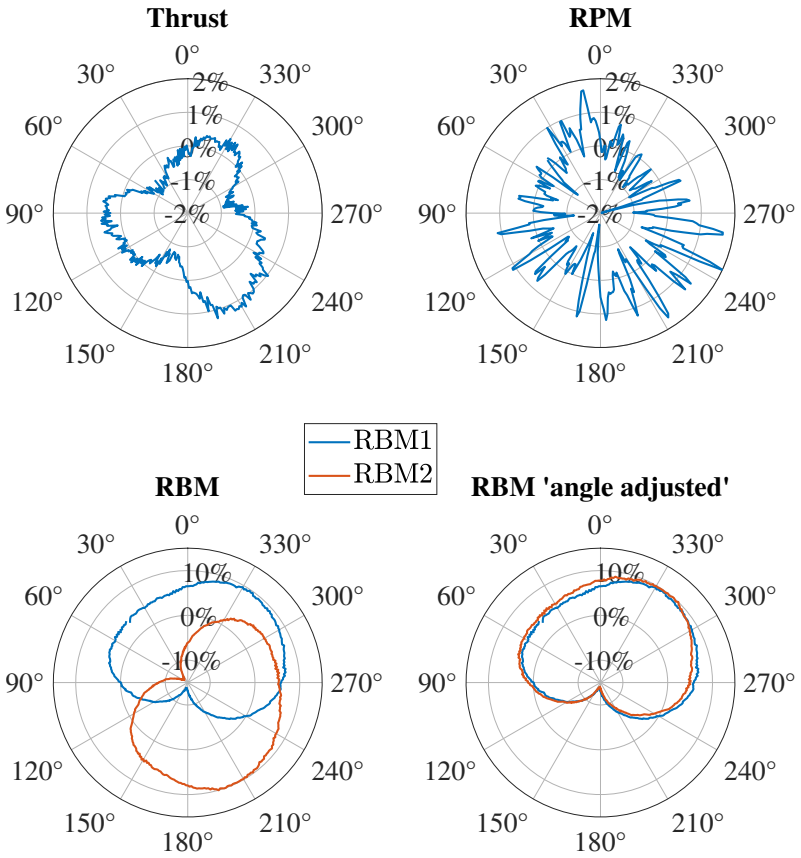


**Figure 7.21:** Polar plots rotor loads and rotational speed variations (% from mean values) for case C3-W23.

the support structure alongside the time-averaged rotor thrust $\overline{\mathrm{T}}$, it is possible to see (Figures 7.22 and 7.23) -as expected- that $\overline{\mathrm{Fx}}$ is higher throughout the $TSR$ range. This difference can be attributed to the drag on the turbine tower and nacelle that the thrust transducer mounted on the rotor would not be able to sense.

Considering the support structure diameter (0.1 m) as the characteristic length $l$ from Equation (2.43), a kinematic viscosity $\nu$ of $1.3E-06\ m^2/s$ at $10°C$ and a flow velocity of 0.8 m/s, it is possible to calculate Re=$6.1E04$. Consequently, a drag coefficient $C_D = 0.7$ is estimated using Figure 2.9. A support structure drag force of 20 N can be approximated using Equation (2.41) by assuming an average flow velocity of 0.8 m/s and a support structure projected area of 0.089 $m^2$. This estimate is a close approximation to the arithmetical difference between the streamwise load $\overline{\mathrm{Fx}}$ of the load cell and the rotor thrust $\overline{\mathrm{T}}$ (Figure 7.22). However, the difference between the streamwise load $\overline{\mathrm{Fx}}$ of the load cell and the rotor thrust is not constant.

Figure 7.23 shows the difference between $\overline{\mathrm{Fx}}$ and $\overline{\mathrm{T}}$ for the three yaw angles. The top graph is for the arithmetical difference of $\overline{\mathrm{Fx}} - \overline{\mathrm{T}}$ for the three current angles. The bottom graph is the relative difference of $\overline{\mathrm{Fx}}$ and $\overline{\mathrm{T}}$ as a percentage of $\overline{\mathrm{Fx}}$. In all the cases, the relative difference follows the same pattern, starting at around 8% for $TSR$=4.25 and decreasing monotonically to ∼4.5% as $TSR$ increases. The variation of the difference between Fx and thrust with $TSR$ appears to be influenced by the rotational speed of the rotor. At lower rotational speeds, the load difference is larger than at faster rotational speed. This increase in the load difference is attributed to the fact that the drag force is hardly influenced by the $TSR$ as it is mainly a function of the flow speed whereas thrust on the rotor increases with $TSR$ (Figure 7.6). Similar behaviour was observed by Payne et al. (2018).

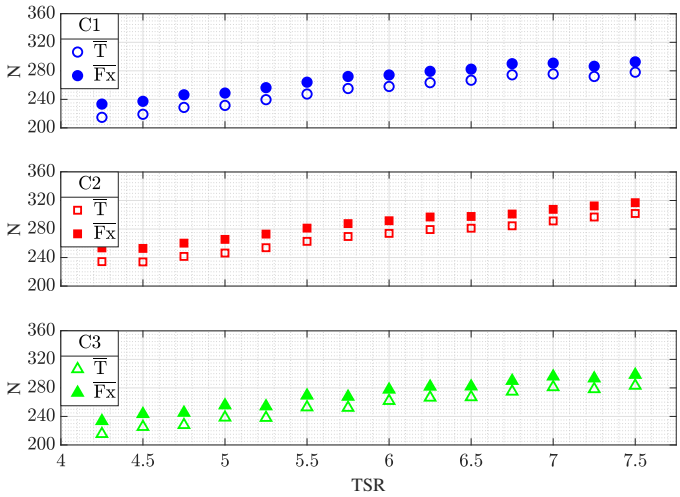


**Figure 7.22:** $\overline{\mathrm{T}}$ and $\overline{\mathrm{Fx}}$ comparison. Top to bottom: Current-only cases at 0°, -10° and -20°.

### 7.5.7 Frequency domain analysis

To understand the key frequency components that are present during the tests that could potentially have an influence in the loading fluctuation of the turbine, analysis in the frequency domain is utilised. This section starts by comparing the frequency spectra of the non-dimensional $C_T$ and $C_P$ in and out of the water against the flow velocity spectrum. It then moves to the analysis of the influence the different flow parameters have on the frequency spectra of $C_T$ and $C_P$. Finally, the $RBM$ spectrum in introduced and compared against the $C_T$ spectrum.

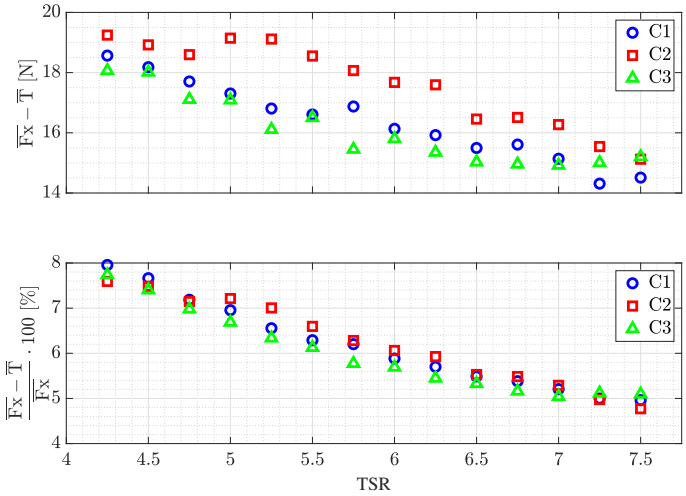


**Figure 7.23:** Difference between $\overline{Fx}$ and $\overline{T}$ from Figure 7.22.

Figure 7.24 shows the $C_T$ frequency spectrum ($S_{C_T}$) plotted against frequency normalised by the rotational frequency $f_0$. The test case is C3-W32 at $TSR$=7 with wave height H=86 mm and period Tw=3 s at $\theta = 45°$ and $U_0$=0.8 m/s at $\beta = -20°$. The $C_T$ spectrum with the turbine outside the water ('dry test') is also shown on the same plot. Finally, the normalised spectrum of the incident velocity is plotted and associated with the secondary (right-hand) y-axis. The -20° current angle was chosen to see how big an influence the most oblique current case has on the turbine loading spectrum.

Following the spectra from left to right, peak 1 at $f/f_0$=0.2 is associated with the wave frequency and peak 2 at $f/f_0$=0.4 is likely to be its harmonic. Comparing the slope in the $S_{C_T}$ and the $S_U$ spectra, it is possible to determine that the thrust coefficient follows the turbulent nature of the onset flow characterised by the Kolmogorov -5/3 slope (Figure 6.14). Peak 3 at $f/f_0$=1 happens once per revolution. As the frequency axis is normalised by the rotational frequency, it means that this peak is associated with the rotational frequency of the turbine. Peak 3 and its harmonic at $f/f_0$=2 (not labelled) are only visible on the 'dry test'. Therefore, these peaks are not associated to any hydrodynamic effect between the flow and the turbine but to a mechanical/electrical artefact of the turbine itself. Peak 4, at $f/f_0$=3, is associated to the frequency at which the three blades pass in front of the support

structure during each full revolution. It is the peak that is associated with the clover-like shape of the thrust polar plots from Section 7.5.5 (i.e. with the 'tower shadow' effect). Further harmonics of peak 4 (peaks 5 and 6) at exactly $f/f_0$= 6 and $f/f_0$=9 are clearly identifiable, each with successively smaller amplitudes. Same as peak 3, peak 7, at $f/f_0 \approx$15 is thought to be associated with a mechanical/electrical artefact of the turbine rather than with a hydrodynamic effect as it is also present in the 'dry test'.

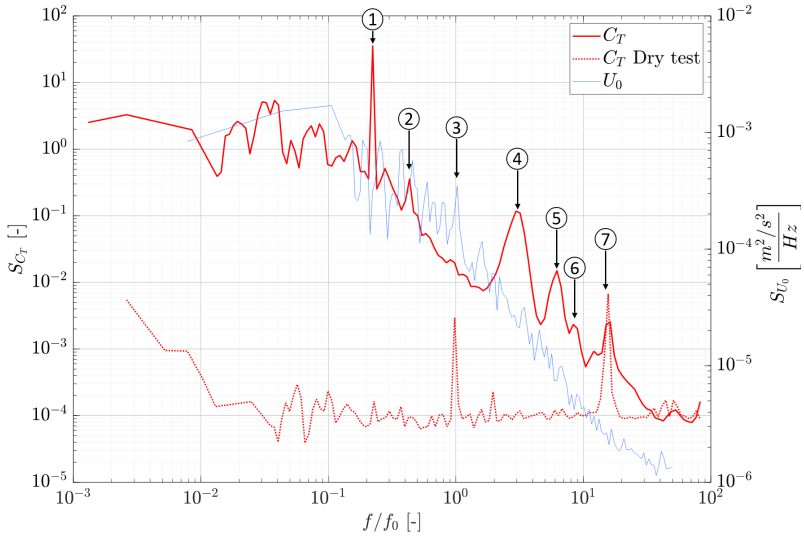


**Figure 7.24:** Spectral density of $C_T$ (left) and $U_0$ (right) against frequency normalised by the rotational frequency of the turbine $f_0$. Case C3-W32.

Figure 7.25 shows the $C_P$ frequency spectrum ($S_{C_P}$) for case C3-W32 at $TSR$=7 and $U_0$=0.8 m/s against the normalised frequency $f/f_0$. Similar to Figure 7.24, the wave frequency at $f/f_0$=0.2 (peak 1) and its first harmonic at $f/f_0$=0.4 (peak 2) can be seen. The peak associated to the passage of the three blades in front of the support structure at $f/f_0$=3 (peak 5) can also be seen. Although peak 6 falls at $f/f_0$=6, it is not believed to be a harmonic of peak 5 as it has a higher amplitude than peak 5 itself. Peaks 6, 7 and 8 at $f/f_0$=6, 16 and 35, respectively, are also present in the 'dry test' and are therefore not thought to be associated with fluid-blade interactions but with a mechanical/electrical artefact. Peak 3 is only present in the 'dry test' and it happens at $f/f_0$=1 or once per revolution and peak 4, at $f/f_0$=2 is its harmonic.

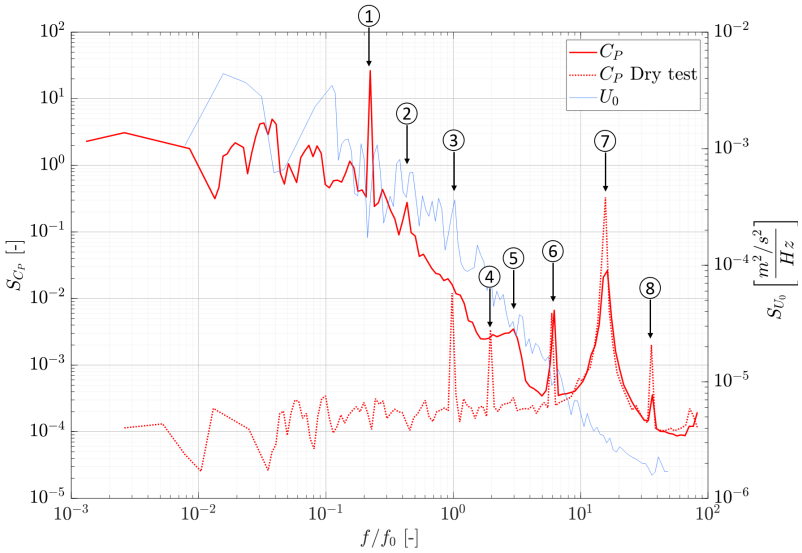


**Figure 7.25:** Spectral density of $C_P$ (left) and $U_0$ (right) against frequency normalised by the rotational frequency of the turbine $f_0$. Case C3-W32.

Exploring the influence of wave angle upon the $S_{C_P}$, Figure 7.26 groups cases with -20° yaw and waves with period Tw=2 s at different angles. All the curves are closely coincident, indicating an absence of any significant influence from the wave direction, except of course on the peaks associated to the wave's period. Figure 7.27 shows a close-up of the spectral peaks associated with the waves from Figure 7.26. The peaks associated with the wave frequency from cases C3-W12 and C3-W14 have similar amplitude, which is consistent with them both being associated with wave conditions symmetrical with respect to the rotor axis ($\theta = \pm 45°$). The C3-W11 case with waves at 0° shows the highest amplitude compared to the other wave angle cases. This is because the wave crest is parallel to the rotor plane. Therefore, the rotor experiences the whole magnitude of the wave-induced force and not only a component of it.

To compare the behaviour of $S_{C_T}$ from Figure 7.26 with current at -10° and 0°, Figures 7.28 and 7.29 show $S_{C_T}$ for the same waves cases as in Figure 7.26 (H=91 mm; Tw=2.5 s) but at different yaw angles, -10° and 0° respectively. The frequency spectra show very little change when a different current angle is applied, which means that the flow's frequency components behave in a similar manner independently of the current angle relative to the waves. The only visible changes are

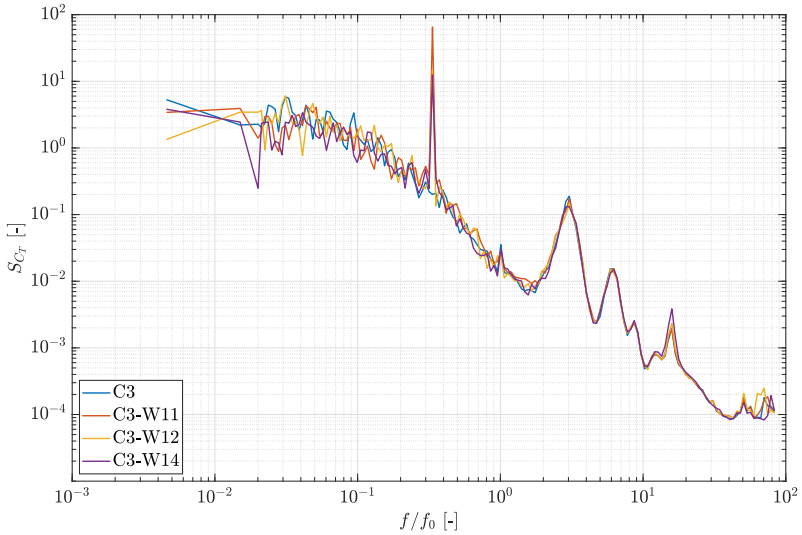


**Figure 7.26:** $S_{C_T}$ with current at -20°, exploring influence of wave angle with wave period Tw=2.0 s.

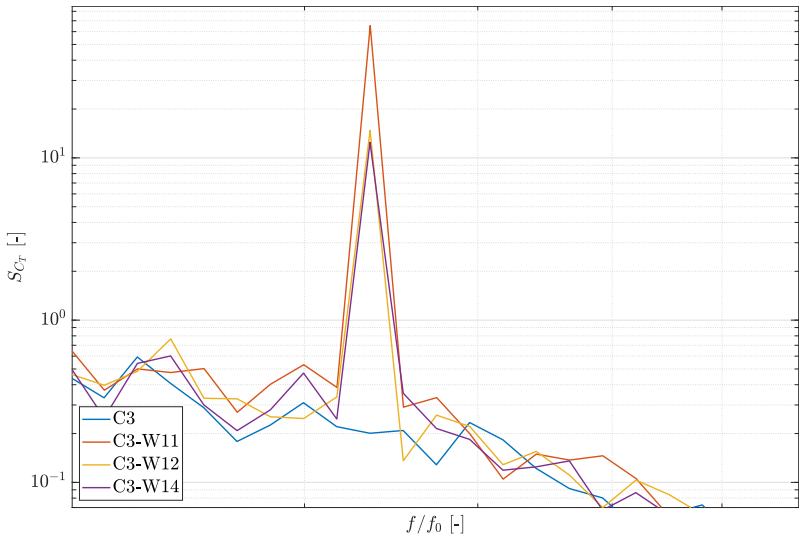


**Figure 7.27:** Zoom of the peak of the $S_{C_T}$ spectra from Figure 7.26 associated with the waves with period Tw=2.0 s.

the ones associated to the wave angles, with the waves at 0° showing higher energy values.

To see if the $S_{C_P}$ curves behave in the same fashion as $S_{C_T}$ in the presence of oblique waves and currents, Figure 7.30 shows $S_{C_P}$ at $TSR$=7 and $U_0$=0.8 m/s against the normalised frequency $f/f_0$. It is noticeable that, in fact, wave angle has no effect on the power coefficient spectra except for the energy content in the peaks associated with the wave period as in Figure 7.27.

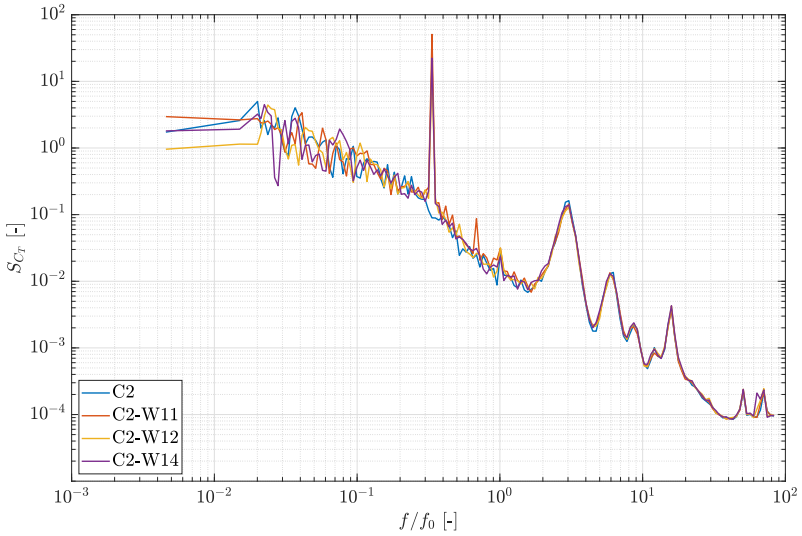


**Figure 7.28:** $S_{C_T}$ with current at -10°, exploring influence of wave angle with wave period Tw=2.0 s.

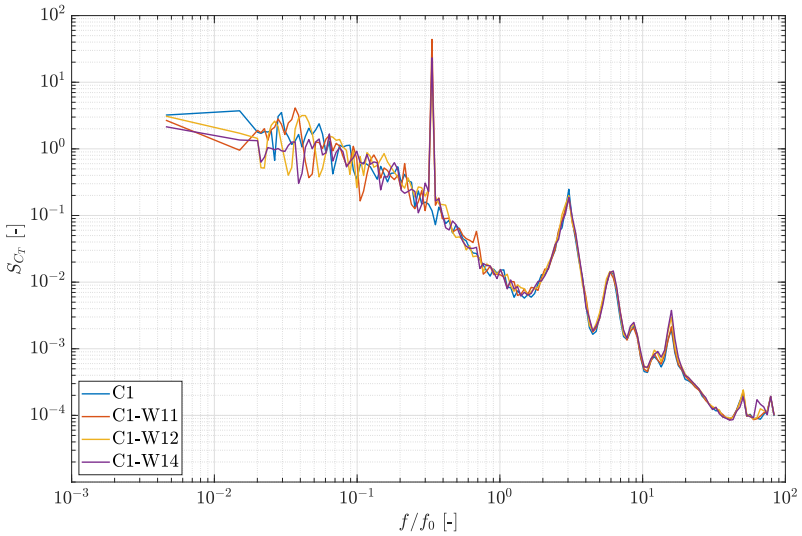


**Figure 7.29:** $S_{C_T}$ spectra with current at 0°, exploring influence of wave angle with wave period Tw=2.0 s.

In an attempt to understand the influence of the wave period in the frequency spectrum of the thrust coefficient, Figure 7.31 groups cases with same wave angle ($\theta$=-45°) and same current angle ($\beta$=-10°). The three peaks at $f/f_0$=0.22, 0.26 and 0.33 are associated with each of the wave periods Tw=3, 2.5 and 2 s, respectively. These peaks are the only difference between the three wave angle cases.

Summarising, Figure 7.32 gathers $S_{C_T}$ for cases C1-W11, C2-W22 and C3-W33 to compare all three current angles, all wave cases at three different wave

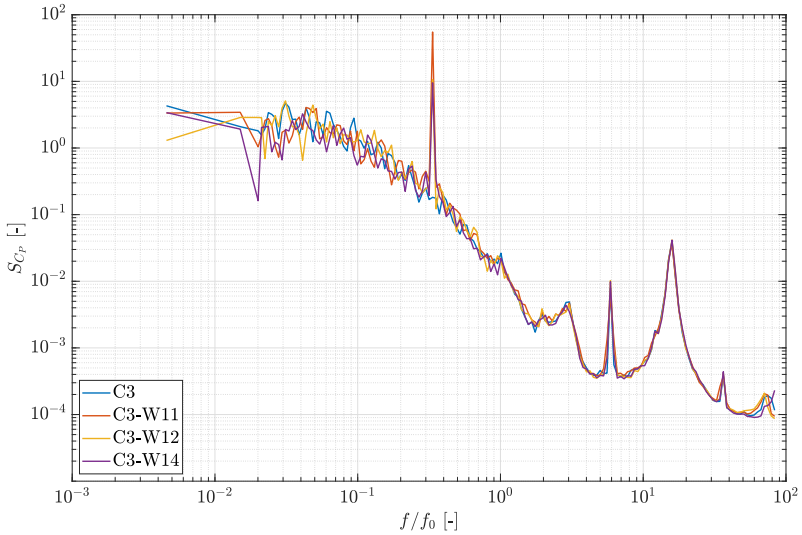


**Figure 7.30:** $S_{C_P}$ with current at -20°, exploring influence of wave angle with wave period Tw=2.0 s.

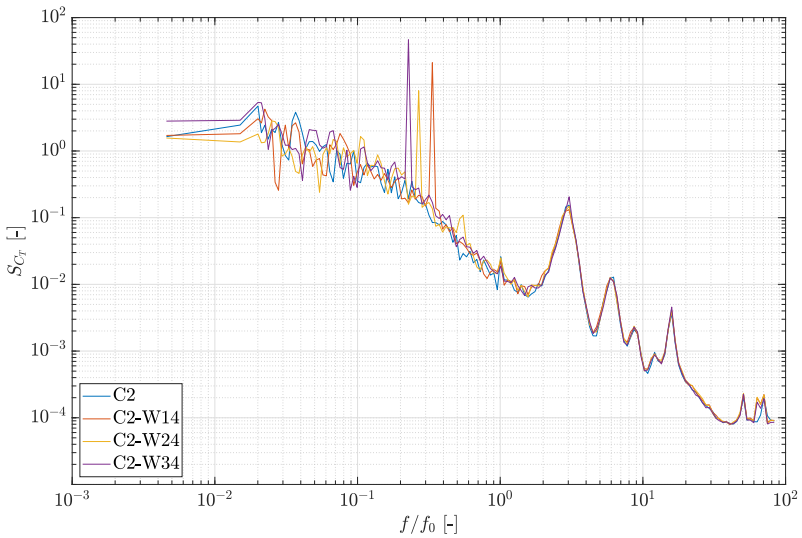


**Figure 7.31:** $S_{C_T}$ comparison of waves W1, W2 and W3 at 315° with a current angle of 0°

angles. From these spectra, it can be concluded that the frequency response of the turbine's power remains the same independent of the current angle, with the only changes being associated with the peaks associated to the waves.

The variation of the out-of-plane *RBM* in the frequency domain is now explored, using an *RBM* coefficient, defined as:

$$C_{RBM} = \frac{RBM}{D_{rotor} \cdot \left(\frac{1}{2} \cdot \rho \cdot A_{rotor} \cdot \overline{U_0}^2\right)} \tag{7.1}$$

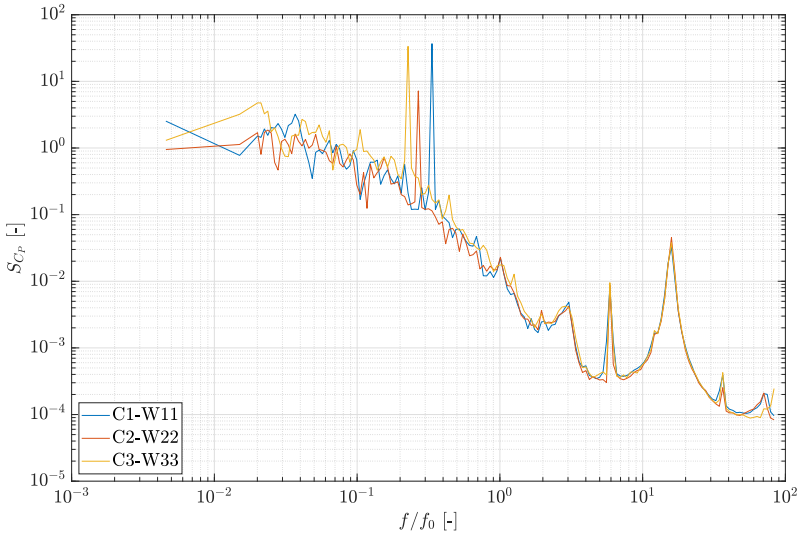


**Figure 7.32:** Spectral $C_P$ comparison of cases C1-W11, C2-W22 and C3-W33.

where $D_{rotor}$ is the rotor diameter, $\rho$ is the water density, $A_{rotor}$ is the rotor area and, $\overline{U_0}$ is the rotor-area- and time-averaged flow velocity.

Plotting the three $C_{RBM}$ spectra ($S_{C_{RBM}}$) from case C3-W32 (Figure 7.33) shows that the blade loadings have frequency spectra closely similar to each other. This similarity between blade bending moments gives confidence that the *RBM* sensors behave correctly. Figure 7.33 shows the spectral density of the three $C_{RBM}$ against the frequency normalised by the rotational frequency. Peak 1 ($f/f_0 = 0.22$) corresponds to the wave period, peak 2 ($f/f_0 = 1$) is associated with the 'tower shadow' effect which takes place once per revolution for each blade and peak 3 ($f/f_0 = 2$) is the first harmonic of peak 2.

Figure 7.34 presents the normalised spectral density of $C_T$ (blue) and $C_{RBM}$ for blade 1 (solid red) with its 'dry test' version (dotted red) plotted against the frequency normalised by the rotational frequency for case C3-W32. The figure also shows the spectrum of the summation of the three blades' *RBM*s time series ($S_{C_{\Sigma RBM}}$). All the spectra present the peak associated to the waves frequency (peak 1) except for the 'dry test'. Peak 2 is the once-per-revolution frequency associated with the passage of the blade in front of the tower with its first harmonic (peak 3). Peak 4 on $S_{C_T}$ and $S_{C_{\Sigma RBM}}$ is associated with the three blades passing by the tower. Peak 5 corresponds to the harmonic of peak 4. The far-right peak 6 appears in the

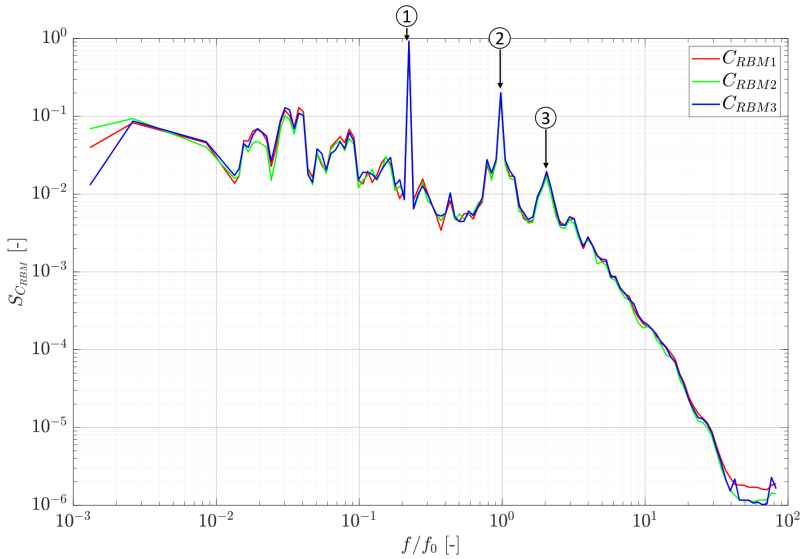


**Figure 7.33:** Comparison between spectral density of the three $C_{RBM}$ against frequency normalised by the rotational frequency of the turbine $f_0$. Case C3-W32.

$S_{C_T}$ and 'dry test' curves, which points to it being derived from a mechanical artefact of the turbine. When the three *RBM* signals are summed up, the once-per-revolution peak from $S_{C_{RBM}}$ does not show anymore and in turn, the three-times-per-revolution peak from $S_{C_T}$ is present in $S_{C_{\Sigma RBM}}$.

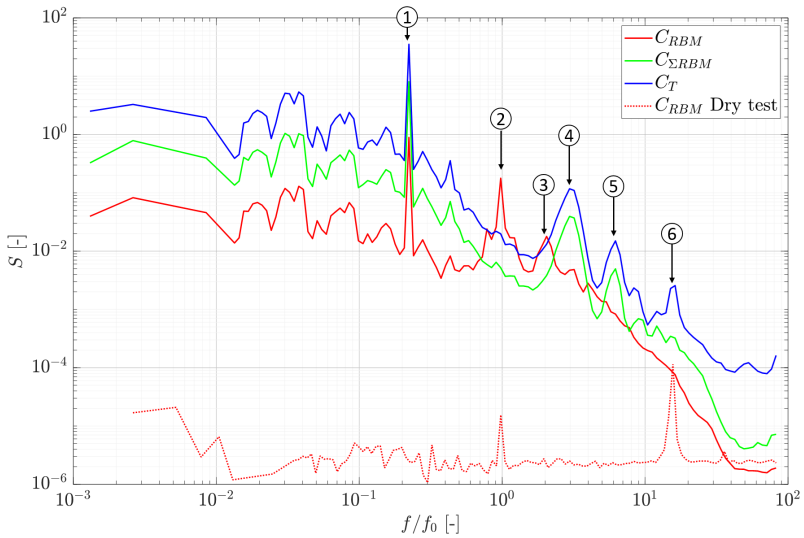


**Figure 7.34:** Comparison between spectral density of $C_T$ and $C_{RBM}$ and $S_{C_{\Sigma RBM}}$ against frequency normalised by the rotational frequency of the turbine $f_0$. Case C3-W32.

## 7.6 Summary of findings

In Section 7.4, it was observed that loading and performance of the turbine under three current angles across a range of $TSR$ values has little to no effect for the -10° case compared to the 0° case. However, the -20° yaw case experienced a reduction of up to 7% on $C_T$ and up to 10% on $C_P$ from the other yaw cases. Similar findings were reported by Maganga et al. (2010). In the case of $C_T$, *SD* values normalised by the average $C_T$ show a decrease with the increase in $TSR$ from ∼10% to ∼5%. For the $C_P$ case, the relative *SD* increases with $TSR$ from ∼5% to ∼10%. However, the $C_P$ standard deviation has a high degree of scatter.

Next, the influence of waves and current at different angles on the loading and performance of the turbine was explored in Section 7.5. Waves not normal to the rotor plane have average $C_T$ values up to 7% and $C_P$ up to 15% lower than waves normal to the rotor plane ($\theta = 0°$). Standard deviation values of $C_T$ and $C_P$ in the presence of waves is almost threefold the *SD* of the current-only cases. Current-only case at 0° corresponds to the lowest *SD* values of $C_T$ and $C_P$. Any current angle case with waves at 0° have the highest average and *SD* values for $C_T$ and $C_P$.

The influence of waves on the loading can be seen as the time series of thrust and torque follow the wave crests and troughs (Section 7.5.4). This effect gives mean loading values similar to those associated with tests performed without waves. However, tests in waves are associated with an increased standard deviation in the thrust.

The polar plots from Section 7.5.5 show how dependent upon the rotor angular position the loads are. For the current-only cases, thrust and torque fluctuations are up to ±2% the average thrust, root-bending-moment up to ±10% the average *RBM* and rotational speed varies from -3% to 2% the average RPM. The thrust and *RBM* signals show the effect of the tower behind the blades located at $\phi = 180°$. Thrust signal presents a clover-like shape for cases C1 and C3 that is created by the passage of the three blades in front of the tower. For case C2, however, the shape the thrust signal presents is triangular. Torque curves for all current angles have a six-point star figure with each point separated by 60°. This shape is not fully understood but

it is attributed to a mechanical/electrical phenomenon from the drivetrain as it was observed in the 'dry test' presented in the frequency spectrum of $C_P$. When plotting the three *RBM* signals together, they have the same shape but separated by a 120° angle corresponding to the geometry of the rotor. The summation of the three *RBM* signals ($\Sigma RBM$) has a similar clover-like shape to the shape of the thrust signal

In Section 7.5.6, comparison of the streamwise (Fx) loading on the foundation load cell with the rotor thrust measurements show similar behaviour. The difference between the two signals remains below 10% of the mean values throughout the whole $TSR$ range. This difference is due to the drag on the tower and nacelle being included in Fx. Additionally, the relative difference decreases as the $TSR$ increases. However, as $TSR$ increases, the mean loading increases. This behaviour was also observed by Payne et al. (2017a).

Finally, the frequency spectra of $C_T$ and $C_P$ explored in Section 7.5.7 have similarities in the peaks associated to the wave period and their harmonics. The peaks associated to the wave period have a higher energy content than the part of the curve associated with flow turbulence. As the flow energy decays, other peaks appear, e.g. each blade passing the tower ($f/f_0$=1 for the *RBM* and $f/f_0$=3 for the thrust and torque). Each of these peaks have their own harmonics with decreasing amplitude. Some of the peaks also happen during the dry tests performed to assess the behaviour of the turbine without hydrodynamic and hydrokinetic influences. These peaks are either mechanical or electrical artefacts that are sometimes also visible in the spectra during wet tests.

It has been shown that current angle has no effect on the frequency spectra. As expected, the addition of waves and their angle of incidence do. The peaks associated with waves have the highest amplitude, but this amplitude is affected by the wave angle of incidence. Waves at 0° lead to the highest amplitude and as the angle increases, the amplitude decreases.

The *RBM* frequency spectra of all the blades within a given test are almost identical except for a small discrepancy at higher frequencies. In comparison with the $C_T$ spectra, the single blade *RBM* spectra shows a peak at $f/f_0 = 1$ whereas

$C_T$ shows it at $f/f_0 = 3$ as it takes into consideration the three blades. This phenomenon can also be seen in the $\Sigma RBM$ spectrum.

# Chapter 8

# Conclusions

This thesis has presented results from basin testing of a 1:15 scale horizontal axis tidal turbine in oblique currents and waves at FloWave. To the knowledge of the author, the tests presented in this thesis are the first to investigate the effects of oblique waves and currents relative to the turbine axis. This thesis describes in detail and extends previous work by Martinez et al. (2017, 2018)

The author had a direct involvement in the procurement of parts for the turbine, assembling the turbine using jigs designed and built by the author as well as the design and build of the associated electrical cabinets. The author also designed and manufactured a water leakage sensor that covers the length of both aluminium sleeves that encase the turbine. The author was also responsible of assembling the waterproof connectors for the cabling.

Prior to the turbine tests, a set of flow characterisation tests was performed without the turbine present in the tank to determine the detail of the flow the turbine would be subjected to. These tests were performed with current-only conditions at three different current angles (0°, -10° and -20°) and a constant flow velocity (0.8 m/s). The experiments showed a flow velocity spatial variation of up to 18% across nine evenly-spread points in the rotor area. Hence, it was decided to use the average of the nine measurement points taken within the rotor area as the measure of the incident flow, instead of the commonly-used hub-height velocity measurement. Velocity depth profiles were then measured. Flow measurements were taken from $z$=-0.15 m to $z$=-1.9 m. In this 1.75 m depth range, flow velocity at $z$=-1.9 m

is up to 15% faster than the velocities measured at $z$=-0.15 m. A power law approximation of $10^{th}$ was fitted to the velocity depth profiles. Typically a power law approximation of $1/7^{th}$ is used to describe velocity depth profiles at potential tidal sites. However, it has been shown that a wide range of approximations can occur within a tidal cycle. The variation of turbulence intensity ($TI$) with depth was also measured. In this case, the highest $TI$ values were observed at $z$=-0.15 m, up to 76% higher than the lowest values observed at $z$=-1.9 m. These observations show the importance of incident flow characterisation for turbine performance assessment.

Turbine characterisation tests under current-only conditions explored the influence of flow misalignment on loading and performance of a tidal turbine via thrust and power coefficients, $C_T$ and $C_P$ respectively, over a range of $TSR$ values with a constant flow velocity of 0.8 m/s and the three different current angles used in the flow characterisation tests. These tests showed that $C_T$ values for currents at 20° are up to 5% lower than for current at 0° and 10°. On the other hand, $C_P$ is up to 10% lower for currents at 20°. Similar findings are reported by Frost (2016) and Maganga et al. (2010). For $C_T$, all of the yaw cases share a similar trend, increasing steadily as the $TSR$ increases. At the lower end of the $TSR$ range, the $SD$ of the thrust coefficient is around 10%. As $TSR$ increases, the $SD$ decreases. These $SD$ values are caused by the turbulent nature of the flow. The maximum of $C_P$ occurs at around $TSR$=6. In general, the variation of $C_P$ with $TSR$ is fairly flat and does not show a stall region because tests below $TSR$=4.25 were not possible to test without the turbine control becoming unstable. For the current case at -20°, $C_P$ standard deviation values increase with $TSR$ from a minimum of 10% to a maximum of 13% of the average $C_P$.

Next, the performance of, and loading on the turbine with the addition of waves was explored. The turbine was tested at a fixed $TSR$ of 7 and subjected to a combination of regular wave and current conditions to explore the influence of wave period and height over different wave directions on the loading and performance of the turbine. Flow velocity remained constant at a nominal 0.8 m/s for all tests. Current direction consisted of three current angles with respect to the rotor axis:

0°, -10° and -20°. Each current angle was tested on its own and in a combination with three different waves (H=102, 91 and 86 mm; Tw=2, 2.5 and 3 s, respectively) from four different directions ($\theta$=0°, 45°, 135° and -45°) with respect to the rotor axis. The combination of wave parameters was chosen to explore a wide range of conditions which could be found at potential tidal sites (Chapter 3).

The addition of waves normal to the rotor plane leads to average values of $C_P$ and $C_T$ hardly influenced by the different waves. However, average $C_P$ and $C_T$ values for waves not-normal to the rotor plane are up to 7% and 15%, respectively, lower than the wave cases normal to the rotor plane. As anticipated, the effect of waves on the average rotor loads at $\theta$=±45°, are very similar. A slight difference of ∼2% is thought to be associated to the direction of rotation of the rotor, although the mechanism for this influences is not understood. Standard deviation values for $C_P$ and $C_T$ with waves normal to the rotor plane are almost three times the values associated with current-only conditions.

Investigating the influence of flow misalignment and different wave directions on the turbine rotor according to its angular position, loads were sorted in 1° bins according to the rotor's absolute angular position. Thrust loads fluctuate around the average values by ±2%. Three peaks are observed 120° apart from each other, which corresponds to the blade angular spacing. Torque loads have the shape of a 6-point star and values fluctuate around the mean torque by 4%. The root bending moment data fluctuates ±10% around the mean values. *RBM* have a more semi-circular shape, with the lowest values happening at the location of the support structure associated with the 'tower shadow' effect. The 'angle-adjusted' *RBM* curves have similar shape, meaning that each blade experience the same loading each full revolution of the rotor. These are however, shifted from each other by an angle of 120° corresponding to the rotor geometry. The rotational speed data has the highest number of peaks with oscillations around the mean value of approximately 5%. The number of peaks are thought to be associated with the controller response to keep the rotational speed fixed. All the features seen in the polar plots agree with the peaks seen in the frequency domain.

Finally, the influence of waves with current on the turbine was explored in the frequency domain. The frequency spectra of the torque and thrust coefficients showed the following features:

- The peaks in the frequency response of $C_T$ and $C_P$ associated with the waves have the highest magnitudes for all test conditions.
- When comparing mirrored cases with waves at $\pm 45°$, the magnitude of the peaks associated to these waves are very similar.
- The peaks associated with waves normal to the rotor ($0°$) have the highest magnitude of all wave conditions. On the other hand, the peak associated with waves at $135°$ has the lowest.
- The second largest peak in any test case with waves is the one associated with the rotor blades experiencing the 'tower shadow' effect.

The work presented in this thesis contributes to the continuously growing knowledge of tidal energy technologies. It is the role of tank testing studies that try to further understand the influence of the incident flow characteristics on the performance and loading of the turbine. As mentioned before, the amount of tidal energy's density and predictability could help substantially in the need for renewable energy sources, but further research to mitigate the risks and uncertainties associated with every aspect of tidal energy conversion must continue.

# References


Adcock, T. A. A.; Draper, S.; Houlsby, G. T.; Borthwick, A. G. L., and Serhadlıoğlu, S.. The available power from tidal stream turbines in the Pentland Firth. *Proceedings of the Royal Society A: Mathematical, Physical and Engineering Sciences*, 469(2157), jul 2013. ISSN 1364-5021. doi: 10.1098/rspa.2013.0072. URL http://rspa.royalsocietypublishing.org/cgi/doi/10.1098/rspa.2013.0072.

Ahmed, U.; Apsley, D. D.; Afgan, I.; Stallard, T., and Stansby, P. K.. Fluctuating loads on a tidal turbine due to velocity shear and turbulence: Comparison of CFD with field data. *Renewable Energy*, 112:235–246, 2017. ISSN 18790682. doi: 10.1016/j.renene.2017.05.048. URL http://dx.doi.org/10.1016/j.renene.2017.05.048.

Andritz Hydro Hammerfest. AH1000 MK1 HATT, 2017. URL http://www.andritzhydrohammerfest.co.uk/. (Accessed October 2019).

Aqua-RET. Tidal stream - european resource map, 2012. URL https://www.aquaret.com/indexcd1b.html?option=com_content&view=article&id=112&Itemid=255&lang=en. (Accessed October 2019).

Atcheson, M.; MacKinnon, P., and Elsaesser, B.. A large scale model experimental study of a tidal turbine in uniform steady flow. *Ocean Engineering*, 110:51–61, 2015. ISSN 00298018. doi: 10.1016/j.oceaneng.2015.09.052.

Atlantis Resources. AR1500 HATT, 2017. URL `https://simecatlantis.com/services/turbines/`. (Accessed October 2019).

Bahaj, A. S.; Batten, W. M. J., and McCann, G. N.. Experimental verifications of numerical predictions for the hydrodynamic performance of horizontal axis marine current turbines. *Renewable Energy*, 32(15):2479–2490, 2007a. ISSN 09601481. doi: 10.1016/j.renene.2007.10.001.

Bahaj, A. S.; Molland, A. F.; Chaplin, J. R., and Batten, W. M. J.. Power and thrust measurements of marine current turbines under various hydrodynamic flow conditions in a cavitation tunnel and a towing tank. *Renewable Energy*, 32(3): 407–426, 2007b. ISSN 09601481. doi: 10.1016/j.renene.2006.01.012.

Barba, P. O.. *Large Eddy Simulation of Tidal Turbines*. PhD thesis, University of Cardiff, 2017.

Barltrop, N.; Varyani, K. S.; Grant, A. D.; Clelland, D., and Pham, X. P.. Wave-current interactions in marine current turbines. *Proceedings of the Institution of Mechanical Engineers, Part M: Journal of Engineering for the Maritime Environment*, 220(4):195–203, dec 2006. ISSN 1475-0902. doi: 10.1243/14750902JEME45.

Barltrop, N.; Varyani, K. S.; Grant, A. D.; Clelland, D., and Pham, X. P.. Investigation into wave—current interactions in marine current turbines. *Proceedings of the Institution of Mechanical Engineers, Part A: Journal of Power and Energy*, 221(2):233–242, mar 2007. ISSN 0957-6509. doi: 10.1243/09576509JPE315.

Batten, W. M. J.; Bahaj, A. S.; Molland, A. F., and Chaplin, J. R.. Experimentally validated numerical method for the hydrodynamic design of horizontal axis tidal turbines. *Ocean Engineering*, 34(7):1013–1020, 2007. ISSN 00298018. doi: 10.1016/j.oceaneng.2006.04.008.

Batten, W. M. J.; Bahaj, A. S.; Molland, A. F., and Chaplin, J. R.. The prediction of the hydrodynamic performance of marine current turbines. *Renewable Energy*, 33(5):1085–1096, 2008. ISSN 09601481. doi: 10.1016/j.renene.2007.05.043.

Bivol, I.; Jeffcoate, P.; Johanning, L., and Nicoll, R.. PLAT-O#2 at FloWave: A tank-scale validation of ProteusDS dynamic analysis tool for floating tidal. In *Proceedings of the 12th European Wave and Tidal Energy Conference*, pages 1–9, Cork, 2017.

Black & Veatch Consulting Ltd. Phase II - UK Tidal Stream Energy Resource Assessment. Technical report, The Carbon Trust, 2005.

Blackmore, T.; Gaurier, B.; Myers, L. E.; Germain, G., and Bahaj, A. S.. The effect of freestream turbulence on tidal turbines. In *Proceedings of the 11th European Wave and Tidal Energy Conference*, volume 1, pages 1–8, Nantes, France, 2015.

Blackmore, T.; Blunden, L. S.; Shah, K.; Myers, L. E., and Bahaj, A. S.. The impact of a real tidal flow on the fatigue loads acting on a tidal turbine. In *Proceedings of the 3rd Asian Wave and Tidal Energy Conference*, volume 1, pages 513–520, Singapore, 2016.

Chamorro, L. P.; Hill, C.; Morton, S.; Ellis, C.; Arndt, R. E. A., and Sotiropoulos, F.. On the interaction between a turbulent open channel flow and an axial-flow turbine. *Journal of Fluid Mechanics*, 716:658–670, 2013. ISSN 0022-1120. doi: 10.1017/jfm.2012.571.

Clarke, J. A.; Connor, G.; Grant, A. D., and Johnstone, C. M.. Design and testing of a contra-rotating tidal current turbine. *Proceedings of the Institution of Mechanical Engineers, Part A: Journal of Power and Energy*, 221(2):171–179, 2007. ISSN 09576509. doi: 10.1243/09576509JPE296.

Clarke, J.; Connor, G.; Grant, A.; Johnstone, C. M., and Ordonez-Sanchez, S.. Contra-rotating marine current turbines: single point tethered floating system - stabilty and performance. In *Proceedings of the 8th European Wave and Tidal Energy Conference*, pages 366–375, 2009.

Collombet, R.. Ocean Energy - Key trends and statistics 2018. Technical report, Ocean Energy Europe, Brussels, 2018.

de Jesus Henriques, T. A.; Hedges, T. S.; Owen, I., and Poole, R. J.. Influence of blade pitch angle on the performance of horizontal axis tidal stream turbines subject to wave-current interaction. In *Proceedings of the World Renewable Energy Congress*, London, UK, 2014a.

de Jesus Henriques, T. A.; Tedds, S. C.; Botsari, A.; Najafian, G.; Hedges, T. S.; Sutcliffe, C. J.; Owen, I., and Poole, R. J.. The effects of wave-current interaction on the performance of a model horizontal axis tidal turbine. *International Journal of Marine Energy*, 8:17–35, 2014b. ISSN 22141669. doi: 10.1016/j.ijome.2014.10.002.

de Jesus Henriques, T. A.; Hedges, T. S.; Owen, I., and Poole, R. J.. The influence of blade pitch angle on the performance of a model horizontal axis tidal stream turbine operating under wave–current interaction. *Energy*, 102:166–175, may 2016. ISSN 03605442. doi: 10.1016/j.energy.2016.02.066.

Dean, R. G. and Dalrymple, R. A.. *Water wave mechanics for engineers and scientists*. Prentice-Hall, Englewood Cliffs, 1984. ISBN 9789812385512.

Department for Business Energy & Industrial Strategy. Energy Trends December 2019. Technical Report December, 2019a. URL `https://www.gov.uk/government/statistics/energy-trends-december-2019`.

Department for Business Energy & Industrial Strategy. Digest of United Kingdom Energy Statistics. Technical report, 2019b. URL `https://www.gov.uk/government/statistics/digest-of-uk-energy-statistics-dukes-2019`.

Department of Energy and Climate Change. Electricity Generation Costs. Technical report, 2013. URL `https://www.gov.uk/government/publications/decc-electricity-generation-costs-2013`.

Doman, D. A.; Murray, R. E.; Pegg, M. J.; Gracie, K.; Johnstone, C. M., and Nevalainen, T. M.. Tow-tank testing of a 1/20th scale horizontal axis tidal turbine

with uncertainty analysis. *International Journal of Marine Energy*, 11:105–119, 2015. ISSN 22141669. doi: 10.1016/j.ijome.2015.06.003.

Draycott, S.; Davey, T.; Ingram, D. M.; Day, A., and Johanning, L.. The SPAIR method: Isolating incident and reflected directional wave spectra in multidirectional wave basins. *Coastal Engineering*, 114:265–283, 2016. ISSN 03783839. doi: 10.1016/j.coastaleng.2016.04.012.

Draycott, S.; Steynor, J.; Nambiar, A.; Sellar, B., and Venugopal, V.. Experimental assessment of tidal turbine loading from irregular waves over a tidal cycle. *Journal of Ocean Engineering and Marine Energy*, 5(2):173–187, may 2019. ISSN 2198-6444. doi: 10.1007/s40722-019-00136-9. URL https://doi.org/10.1007/s40722-019-00136-9.

Easton, M. C.. *An assessment of tidal energy and the environmental response to extraction at a site in the Pentland Firth*. PhD thesis, University of Aberdeen, 2013.

Easton, M. C.; Harendza, A.; Woolf, D. K., and Jackson, A. C.. Characterisation of a tidal energy site : hydrodynamics and seabed structure. In *Proceedings of the 9th European Wave and Tidal Energy Conference*, Southampton, UK, 2011.

Edge, G.; Davies, G., and Carcas, M.. Wave & Tidal Energy: State of the Industry. Technical report, ClimateXChange, 2017.

European Union. Directive (EU) 2018/2001 of the European Parliament and of the Council on the promotion of the use of energy from renewable sources. *Official Journal of the European Union*, 2018(L 328):82–209, 2018. URL https://eur-lex.europa.eu/legal-content/EN/TXT/PDF/?uri=CELEX:32018L2001&from=EN.

Evans, P. S.. *Hydrodynamic Characteristics of Macrotidal Straits and Implications for Tidal Stream Turbine Deployment*. PhD thesis, Cardiff University, 2014.

Fabre, R.; Trarieux, F.; Fiore, F., and Starzmann, R.. Turbine performance enhancement on the PLAT-O taut moored underwater tidal energy converter. *Proceedings of the 11th European Wave and Tidal Energy Conference*, pages 1–8, 2015.

Fernandez-Rodriguez, E.; Stallard, T. J., and Stansby, P. K.. Experimental study of extreme thrust on a tidal stream rotor due to turbulent flow and with opposing waves. *Journal of Fluids and Structures*, 51:354–361, 2014. ISSN 10958622. doi: 10.1016/j.jfluidstructs.2014.09.012.

Fraile, D. and Mbistrova, A.. Wind in power 2017. Technical report, Wind Europe, Brussels, 2018.

Frost, C. H.. *Flow Direction Effects On Tidal Stream Turbines*. PhD thesis, Cardiff University, 2016.

Frost, C. H.; Benson, I.; Elsaesser, B.; Starzmann, R., and Whittaker, T.. Mitigating uncertainty in tidal turbine performance characteristics from experimental testing. In *Proceedings of the 12th European Wave and Tidal Energy Conference*, pages 1–10, Cork, 2017.

Galloway, P. W.; Myers, L. E., and Bahaj, A. S.. Studies of a scale tidal turbine in close proximity to waves. *Proceedings of the 3rd International Conference on Ocean Energy*, (1):3–8, 2010.

Galloway, P. W.; Myers, L. E., and Bahaj, A. S.. Experimental and numerical results of rotor power and thrust of a tidal turbine operating at yaw and in waves. In *Proceedings World Renewable Energy Congress*, pages 2246–2253, Linköping, nov 2011. doi: 10.3384/ecp110572246.

Galloway, P. W.; Myers, L. E., and Bahaj, A. S.. Quantifying wave and yaw effects on a scale tidal stream turbine. *Renewable Energy*, 63:297–307, 2014. ISSN 09601481. doi: 10.1016/j.renene.2013.09.030.

Garrett, C. and Cummins, P.. The efficiency of a turbine in a tidal channel. *Journal of Fluid Mechanics*, 588:243–251, Oct 2007. doi: https://doi.org/10.1017/S0022112007007781.

Gaurier, B.; Davies, P.; Deuff, A., and Germain, G.. Flume tank characterization of marine current turbine blade behaviour under current and wave loading. *Renewable Energy*, 59:1–12, 2013. ISSN 09601481. doi: 10.1016/j.renene.2013.02.026.

Gaurier, B.; Germain, G.; Facq, J.-V.; Johnstone, C. M.; Grant, A. D.; Day, A. H.; Nixon, E.; Di Felice, F., and Costanzo, M.. Tidal energy "Round Robin" tests comparisons between towing tank and circulating tank results. *International Journal of Marine Energy*, 12:87–109, 2015. ISSN 22141669. doi: 10.1016/j.ijome.2015.05.005.

Goddijn-Murphy, L.; Woolf, D. K., and Easton, M. C.. Current patterns in the inner sound (Pentland Firth) from underway ADCP data. *Journal of Atmospheric and Oceanic Technology*, 30(1):96–111, 2013. ISSN 07390572. doi: 10.1175/JTECH-D-11-00223.1.

Gooch, S.; Thomson, J.; Polagye, B. L., and Meggit, D.. Site characterization for tidal power. In *Proceedings of OCEANS 2009*, pages 1–10, Biloxi, MS, USA, 2009. URL `http://ieeexplore.ieee.org/xpls/abs_all.jsp?arnumber=5422134`.

Good, A.; Hamill, G.; Whittaker, T., and Robinson, D.. PIV analysis of the near wake of a tidal turbine. In *Proceedings of the 21st International Offshore and Polar Engineering Conference*, volume 8, pages 770–776, 2011. ISBN 9781880653968.

Guo, X.; Gao, Z.; Yang, J.; Moan, T.; Lu, H., and Li, X.. The Effects of Surface Waves and Submergence on the Performance and Loading of a Tidal Turbine. In *Proceedings of the ASME 2017 36th International Conference on Ocean, Off-*

*shore and Arctic Engineering. Volume 7B: Ocean Engineering*, Trondheim, Norway, 2017. ASME. doi: https://doi.org/10.1115/OMAE2017-62233.

Hansen, M. O. L.. *Aerodynamics of Wind Turbines*. Earthscan, second edition, 2008. ISBN 978-1-84407-438-9.

Harding, S.; Payne, G. S., and Bryden, I.. Generating controllable velocity fluctuations using twin oscillating hydrofoils : experimental validation. *Journal of Fluid Mechanics*, 750:113–123, 2014. doi: 10.1017/jfm.2014.257.

Harrison, J.. ReDAPT - Deliverable MC7.3: Public Domain Report: FInal. Technical report, Alstom, 2015. URL `http://redapt.eng.ed.ac.uk/index.php?p=library_redapt_reports`.

Hedges, T. S.. Combinations of Waves and Currents: An Introduction. *Proceedings of the Institution of Civil Engineers*, 82(3):567–585, jun 1987. ISSN 1753-7789. doi: 10.1680/iicep.1987.319.

International Energy Agency. Energy security - Ensuring the uninterrupted availability of energy sources at an affordable price, 2019. URL `https://www.iea.org/areas-of-work/ensuring-energy-security/`.

Jeffcoate, P. and McDowell, J.. Performance of PLAT-I , a Floating Tidal Energy Platform for Inshore Applications. In *Proceedings of the 12th European Wave and Tidal Energy Conference*, pages 1–8, Cork, 2017.

Jeffcoate, P.; Elsaesser, B.; Whittaker, T., and Boake, C.. Testing Tidal Turbines - Part I: Steady Towing Tests vs. Tidal Mooring Tests. *International Conference on Offshore Renewable Energy*, (2014):1–9, 2014.

Jeffcoate, P.; Salvatore, F.; Boake, C.; Elsaesser, B., and Vallerano, V.. Effect of Submergence on Tidal Turbine Performance. In *Proceedings of the 11th European Wave and Tidal Energy Conference*, pages 3–9, 2015.

Jeffcoate, P.; Whittaker, T.; Boake, C., and Elsaesser, B.. Field tests of multiple 1/10 scale tidal turbines in steady flows. *Renewable Energy*, 87:240–252, 2016. ISSN 18790682. doi: 10.1016/j.renene.2015.10.004.

Lewis, M. J.; Neill, S. P.; Robins, P. E.; Hashemi, M. R., and Ward, S. L.. Characteristics of the velocity profile at tidal-stream energy sites. *Renewable Energy*, 114:258–272, 2017. ISSN 18790682. doi: 10.1016/j.renene.2017.03.096.

Lienhard, H. J.. *Synopsis of Lift, Drag, and Vortex Frequency Data for Rigid Circular Cylinders*. Technical Extension Service, Washington State University, Pullman, Washington, 1966.

Lust, E. E.; Luznik, L.; Flack, K. A.; Walker, J. M., and Van Benthem, M. C.. The influence of surface gravity waves on marine current turbine performance. *International Journal of Marine Energy*, 3-4:27–40, 2013. ISSN 22141669. doi: 10.1016/j.ijome.2013.11.003.

Luznik, L.; Flack, K. A.; Lust, E. E., and Taylor, K.. The effect of surface waves on the performance characteristics of a model tidal turbine. *Renewable Energy*, 58: 108–114, 2013. ISSN 09601481. doi: 10.1016/j.renene.2013.02.022.

Maganga, F.; Germain, G.; King, J.; Pinon, G., and Rivoalen, E.. Experimental study to determine flow characteristic effects on marine current turbine behaviour. In *Proceedings of the 8th European Wave and Tidal Energy Conference*, pages 661–667, 2009. doi: http://dx.doi.org/10.1049/iet-rpg.2009.0205.

Maganga, F.; Germain, G.; King, J.; Pinon, G., and Rivoalen, E.. Experimental characterisation of flow effects on marine current turbine behaviour and on its wake properties. *IET Renewable Power Generation*, 4(6):498–509, 2010.

Martinez, R.; Payne, G. S., and Bruce, T.. Preliminary results on the effects of oblique current and waves on the loadings and performance of tidal turbines. In *Proceedings of the 12th European Wave and Tidal Energy Conference*, pages 1–8, Cork, 2017.

Martinez, R.; Payne, G. S., and Bruce, T.. The effects of oblique waves and currents on the loadings and performance of tidal turbines. *Ocean Engineering*, 164: 55–64, 2018. ISSN 00298018. doi: 10.1016/j.oceaneng.2018.05.057. URL https://doi.org/10.1016/j.oceaneng.2018.05.057.

Martinez, R.; Ordonez-sanchez, S.; Johnstone, C. M.; Allmark, M.; Lloyd, C.; O'Doherty, T.; Gaurier, B., and Germain, G.. Analysis of the effects of control strategies and wave climates on the loading and performance of a laboratory scale horizontal axis tidal turbine. *Manuscript submitted for publication*, 2019.

Mason-Jones, A.; O'Doherty, D. M.; Morris, C. E., and O'Doherty, T.. Influence of a velocity profile & support structure on tidal stream turbine performance. *Renewable Energy*, 52:23–30, 2013. ISSN 09601481. doi: 10.1016/j.renene.2012.10.022.

McCann, G. N.; Hitchcock, S., and Lane, S.. Implications of site-specific conditions on the prediction of loading and power performance of a tidal stream device. *Proceedings of the 2nd International Conference of Ocean Energy*, pages 1–9, 2008.

McCombes, T. and Iyer, A. S.. D2.2: Collation of Tidal Test Options. Technical report, MARINET, 2012. URL http://www.marinet2.eu/wp-content/uploads/2017/04/D2.02-Collation-of-Tidal-Test-Options.pdf.

McNaughton, J.; Harper, S.; Sinclair, R., and Sellar, B. G.. Measuring and Modelling the Power Curve of a Commercial-Scale Tidal Turbine. In *Proceedings of the 11th European Wave and Tidal Energy Conference*, pages 1–9, 2015.

Milne, I. A.; Sharma, R. N.; Flay, R. G. J., and Bickerton, S.. Characteristics of the turbulence in the flow at a tidal stream power site. *Philosophical Transactions of the Royal Society A: Mathematical, Physical and Engineering Sciences*, 371 (1985):20120196–20120196, jan 2013. ISSN 1364-503X. doi: 10.1098/rsta.2012.0196.

Morandi, B.; Di Felice, F.; Costanzo, M.; Romano, G. P.; Dhomé, D., and Allo, J.-C.. Experimental investigation of the near wake of a horizontal axis tidal current turbine. *International Journal of Marine Energy*, 14:229–247, 2016. ISSN 22141669. doi: 10.1016/j.ijome.2016.02.004.

Mullings, H. R.; Stallard, T. J., and Payne, G. S.. Operational loads on a tidal turbine due to environmental conditions. In *Proceedings of the 27th International Offshore and Polar Engineering Conference*, San Francisco, CA, USA, 2017.

Munk, W. H.. Origin and generation of waves. In *Proceedings of the 1st conference on coastal engineering*, pages 1–4, California, USA, 1950.

Mycek, P.; Gaurier, B.; Germain, G.; Pinon, G., and Rivoalen, E.. Experimental study of the turbulence intensity effects on marine current turbines behaviour. Part I: One single turbine. *Renewable Energy*, 66:729–746, 2014. ISSN 09601481. doi: 10.1016/j.renene.2013.12.036.

Nautricity. CoRMaT, 2017. URL `https://www.nautricity.com/`. (Accessed October 2019).

Neill, S. P.; Vögler, A.; Goward-Brown, A. J.; Baston, S.; Lewis, M. J.; Gillibrand, P. A.; Waldman, S., and Woolf, D. K.. The wave and tidal resource of Scotland. *Renewable Energy*, 114:3–17, 2017. ISSN 18790682. doi: 10.1016/j.renene.2017.03.027.

Newman, J. N.. *Marine hydrodynamics*. The MIT Press, 40th anniversary edition, 1977. ISBN 9780262534826.

Nilfanion. UK maps, 2017. URL `https://commons.wikimedia.org/wiki/User:Nilfanion/Maps/National#/media/File:United_Kingdom_police_areas_map.svg`. (Accessed October 2019).

Noble, D. R.; Davey, T. A. D.; Smith, H. C. M.; Kaklis, P.; Robinson, A., and Bruce, T.. Spatial variation in currents generated in the FloWave Ocean Energy Research

Facility. *Proceedings of the 11th European Wave and Tidal Energy Conference*, pages 1–8, 2015.

Nortek Group. The Comprehensive Manual, 2017. URL https://support.nortekgroup.com/hc/en-us/article_attachments/360031694212/N3015-030-Comprehensive-Manual-Velocimeters_1118.pdf. (Accessed October 2019).

Nova Innovation. M100 HATT, 2017. URL https://www.novainnovation.com/nova-m100. (Accessed October 2019).

Oceanflowenergy. Evopod HATT, 2017. URL http://www.oceanflowenergy.com/Evopod-Technology.html. (Accessed October 2019).

O'Connor, E. J.; Illingworth, A. J.; Brooks, I. M.; Westbrook, C. D.; Hogan, R. J.; Davies, F., and Brooks, B. J.. A method for estimating the turbulence kinetic energy dissipation rate from a vertically pointing Doppler lidar, and independent evaluation from balloon-borne in situ measurements. *J. Atmos. Ocean. Tech.*, 27: 1652–1664, 2010.

O'Neill, P. L.; Nicolaides, D.; Honnery, D., and Soria, J.. Autocorrelation functions and the determination of integral length with reference to experimental and numerical data. In *Proceedings of the 15th Australasian Fluid Mechanics Conference*, Sydney, Australia, 2004.

Orbital Marine. Orbital O2, 2018. URL https://orbitalmarine.com/. (Accessed October 2019).

Ordonez-Sanchez, S.; Porter, K.; Frost, C. H.; Allmark, M.; Johnstone, C. M., and O'Doherty, T.. Effects of wave-current interactions on the performance of tidal stream turbines. In *Proceedings of the 3rd Asian Wave and Tidal Energy Conference*, pages 978–981, Singapore, 2016. ISBN 9789811107825. doi: 10.3850/978-981-11-0782-5.

Ordonez-Sanchez, S.; Allmark, M.; Porter, K. E.; Ellis, R.; Lloyd, C.; Santic, I.; O'Doherty, T., and Johnstone, C.. Analysis of a horizontal-axis tidal turbine performance in the presence of regular and irregular waves using two control strategies. *Energies*, 12(3):367, jan 2019. ISSN 1996-1073. doi: 10.3390/en12030367. URL http://www.mdpi.com/1996-1073/12/3/367.

Ouro, P.; Ramírez, L., and Harrold, M.. Analysis of array spacing on tidal stream turbine farm performance using Large-Eddy Simulation. *Journal of Fluids and Structures*, 91:102732, nov 2019. ISSN 08899746. doi: 10.1016/j.jfluidstructs.2019.102732. URL https://doi.org/10.1016/j.jfluidstructs.2019.102732.

Payne, G. S.. Guidance for the experimental tank testing of wave energy converters. Technical report, SuperGen Marine, University of Edinburgh, 2008. URL http://www.supergen-marine.org.uk/drupal/files/reports/WEC_tank_testing.pdf.

Payne, G. S.; Stallard, T. J., and Martinez, R.. Design and manufacture of a bed supported tidal turbine model for blade and shaft load measurement in turbulent flow and waves. *Renewable Energy*, 107:312–326, 2017a. ISSN 09601481. doi: 10.1016/j.renene.2017.01.068.

Payne, G. S.; Stallard, T. J.; Mullings, H. R., and Martinez, R.. Experimental investigation into unsteady loads on horizontal axis tidal turbines. In *Proceedings of the 12th European Wave and Tidal Energy Conference*, pages 1–6, 2017b.

Payne, G. S.; Stallard, T. J.; Martinez, R., and Bruce, T.. Variation of loads on a three-bladed horizontal axis tidal turbine with frequency and blade position. *Journal of Fluids and Structures*, 83(2018):156–170, nov 2018. ISSN 10958622. doi: 10.1016/j.jfluidstructs.2018.08.010.

Peregrine, D.. Interaction of water waves and currents. volume 16 of *Advances in Applied Mechanics*, pages 9 – 117. Elsevier, 1976. doi: https://doi.org/

10.1016/S0065-2156(08)70087-5. URL http://www.sciencedirect.com/science/article/pii/S0065215608700875.

Pope, S. B.. *Turblent Flows*. Cambridge University Press, 2000.

Porter, K. E.; Ordonez-Sanchez, S.; Allmark, M.; Ellis, R.; Lloyd, C.; O'Doherty, T., and Johnstone, C. M.. Laboratory study of tidal turbine performance in irregular waves. In *Proceedings of the 4th Asian Wave and Tidal Energy Conference*, Taipei, Taiwan, 2018.

Robinson, A.; Ingram, D. M.; Bryden, I., and Bruce, T.. The effect of inlet design on the flow within a combined waves and current flumes, test tank and basins. *Coastal Engineering*, 95:117–129, 2015a. ISSN 03783839. doi: 10.1016/j.coastaleng.2014.10.004.

Robinson, A.; Ingram, D. M.; Bryden, I., and Bruce, T.. The generation of 3D flows in a combined current and wave tank. *Ocean Engineering*, 93:1–10, 2015b. ISSN 00298018. doi: 10.1016/j.oceaneng.2014.10.008.

Sabella. D10 HATT, 2017. URL https://www.sabella.bzh/en/projects/d10. (Accessed October 2019).

Salter, S. H. and Taylor, J. R. M.. Vertical-axis tidal-current generators and the Pentland Firth. *Proceedings of the Institution of Mechanical Engineers, Part A: Journal of Power and Energy*, 221(2):181–199, 2007. ISSN 09576509. doi: 10.1243/09576509JPE295.

Salvatore, F.; Iyer, A. S.; Day, A. H., and Di Felice, F.. D2.23 - Review of Tow Tank Limitations. Technical report, MARINET, 2014. URL http://www.marinet2.eu/wp-content/uploads/2017/04/D2.23-Review-of-Tow-Tank-Limitations-1.pdf.

Schluntz, J. and Willden, R. H. J.. The effect of blockage on tidal turbine rotor design and performance. *Renewable Energy*, 81:432–441, 2015. ISSN 0960-

1481. doi: 10.1016/j.renene.2015.02.050. URL http://dx.doi.org/10.1016/j.renene.2015.02.050.

Schmitt, P. and Elsäßer, B.. The application of Froude scaling to model tests of Oscillating Wave Surge Converters. *Ocean Engineering*, 141:108–115, 2017. ISSN 0029-8018. doi: 10.1016/j.oceaneng.2017.06.003. URL http://dx.doi.org/10.1016/j.oceaneng.2017.06.003.

Sellar, B. and Wakelam, G.. Characterisation of tidal flows at the European Marine Energy Centre in the absence of ocean waves. *Energies*, 11(1):176, jan 2018. ISSN 1996-1073. doi: 10.3390/en11010176. URL http://www.mdpi.com/1996-1073/11/1/176.

Shigley, J. E. and Mischke, C. R.. *Mechanical Engineering Design*. McGraw-Hill, 5th edition, 1989. ISBN 0-07-056899-5.

SIEMENS. S-N Curve, 2019. URL https://community.sw.siemens.com/s/article/what-is-a-sn-curve. (Accessed October 2019).

Solomon Jr., O. M.. PSD Computations Using Welch's Method. Technical Report December, Sandia Laboratories, 1991.

Soulsby, R.; Hamm, L.; Klopman, G.; Myrhaug, D.; Simons, R., and Thomas, G.. Wave-current interaction within and outside the bottom boundary layer. *Coastal Engineering*, 21(1-3):41–69, dec 1993. ISSN 03783839. doi: 10.1016/0378-3839(93)90045-A. URL https://linkinghub.elsevier.com/retrieve/pii/037838399390045A.

Starzmann, R.; Baldus, M.; Groh, E.; Hirsch, N.; Lange, N. A., and Scholl, S.. Full-scale testing of a tidal energy converter using a tug boat. In *Proceedings of the 10th European Wave and Tidal Energy Conference*, pages 1–8, Aalborg, 2013.

Sustainable Marine Energy Ltd. Plat-O HATT, 2017. URL https://sustainablemarine.com/plat-o. (Accessed October 2019).

Sutherland, D.; Ordonez-sanchez, S.; Belmont, M. R.; Moon, I.; Steynor, J.; Davey, T., and Bruce, T.. Experimental optimisation of power for large arrays of cross- fl ow tidal turbines. *Renewable Energy*, 116:685–696, 2018. ISSN 0960-1481. doi: doi.org/10.1016/j.renene.2017.10.011. URL https://doi.org/10.1016/j.renene.2017.10.011.

Sutherland, D. R. J.; Sellar, B. G.; Harding, S., and Bryden, I.. Initial flow characterisation utilising turbine and seabed installed acoustic sensor arrays. In *Proceedings of the 10th European Wave and Tidal Energy Conference*, pages 1–8, Aalborg, 2013.

Sutherland, D. R. J.; Noble, D. R.; Steynor, J.; Davey, T. A. D., and Bruce, T.. Characterisation of current and turbulence in the FloWave Ocean Energy Research Facility. *Ocean Engineering*, 139(2):103–115, jul 2017. ISSN 00298018. doi: 10.1016/j.oceaneng.2017.02.028.

The British Government. Wave and tidal energy: part of the UK's energy mix, 2013. URL https://www.gov.uk/guidance/wave-and-tidal-energy-part-of-the-uks-energy-mix.

The Scottish Government. 2020 Routemap for Renewable Energy in Scotland - Update. Technical Report December, 2013. URL https://www2.gov.scot/Resource/0044/00441628.pdf.

The Scottish Government. Facts and figures about Scotland's sea area (coastline length, sea area in sq kms), 2018. URL http://marine.gov.scot/data/facts-and-figures-about-scotlands-sea-area-coastline-length-sea-area-sq-kms.

The Scottish Government. Annual energy statement 2019. Technical report, 2019. URL https://www.gov.scot/publications/annual-energy-statement-2019/.

Thiébaut, F.. D2.28 - Model Construction Methods. Technical report, MARINET, 2015. URL http://www.marinet2.eu/wp-content/uploads/2017/04/D2.28-Protocol-for-Model-Construction-1.pdf.

Thiébaut, M. and Sentchev, A.. Tidal stream resource assessment in the Dover Strait (eastern English Channel). *International Journal of Marine Energy*, 16:262–278, December 2016. ISSN 22141669. doi: 10.1016/j.ijome.2016.08.004.

Thorpe, S. A.. *An Introduction to Ocean Turbulence*. Cambridge University Press, Cambridge, 2007. ISBN 9780511801198. doi: 10.1017/CBO9780511801198.

Tian, W.; Mao, Z., and Ding, H.. Design, test and numerical simulation of a low-speed horizontal axis hydrokinetic turbine. *International Journal of Naval Architecture and Ocean Engineering*, 10(6):782 – 793, 2018. ISSN 2092-6782. doi: https://doi.org/10.1016/j.ijnaoe.2017.10.006. URL http://www.sciencedirect.com/science/article/pii/S2092678217301978.

van Dyke, M.. *An album of fluid motion*. The parabolic press, Stanford, California, 1982. ISBN 978-0915760022.

Vennell, R.. Exceeding the Betz limit with tidal turbines. *Renewable Energy*, 55:277–285, jul 2013. ISSN 09601481. doi: 10.1016/j.renene.2012.12.016. URL http://dx.doi.org/10.1016/j.renene.2012.12.016.

Vinod, A.; Lawrence, A., and Banerjee, A.. Effects of free stream turbulence on tidal turbines . Part II – Turbine performance and near wake characteristics. In *Proceedings of the 12th European Wave and Tidal Energy Conference*, pages 1–10, Cork, 2017.

White, F. M.. *Fluid Mechanics*. McGraw-Hill, 7 edition, 2010. ISBN 0073529346, 9780073529349.

Xu, Q.; Li, W.; Lin, Y.; Liu, H., and Gu, Y.. Investigation of the performance of a stand-alone horizontal axis tidal current turbine based on in situ

experiment. *Ocean Engineering*, 113:111–120, 2016. ISSN 00298018. doi: 10.1016/j.oceaneng.2015.12.051.

# Appendix A. RBM calibration tables

**Table A.1:** Calibration table for RBM1. Output columns are at different lever arm lengths. Data provided by manufacturer Applied Measurements Ltd.

| **Applied** | **Output [mA]** | | | |
|---|---|---|---|---|
| **load [N]** | **@ 125 mm** | **@ 250 mm** | **@ 375 mm** | **@ 500 mm** |
| 0 | 4.657 | 4.656 | 4.656 | 4.656 |
| 50 | 5.489 | 6.245 | 6.962 | 7.697 |
| 100 | 6.323 | 7.826 | 9.266 | 10.739 |
| 150 | 7.15 | 9.409 | 11.576 | 13.796 |
| 200 | 7.981 | 10.993 | 13.899 | 16.879 |
| 250 | 8.811 | 12.58 | 16.233 | 19.971 |
| 200 | 7.982 | 10.993 | 13.903 | 16.874 |
| 150 | 7.153 | 9.406 | 11.58 | 13.791 |
| 100 | 6.321 | 7.821 | 9.266 | 10.729 |
| 50 | 5.503 | 6.241 | 6.96 | 7.688 |
| 0 | 4.658 | 4.657 | 4.656 | 4.654 |

**Table A.2:** Calibration table for RBM2. Output columns are at different lever arm lengths. Data provided by manufacturer Applied Measurements Ltd.

| **Applied** | **Output [mA]** | | | |
|---|---|---|---|---|
| **load [N]** | **@ 125 mm** | **@ 250 mm** | **@ 375 mm** | **@ 500 mm** |
| 0 | 4.852 | 4.853 | 4.852 | 4.85 |
| 50 | 5.724 | 6.461 | 7.224 | 7.985 |
| 100 | 6.595 | 8.082 | 9.629 | 11.169 |
| 150 | 7.47 | 9.717 | 12.054 | 14.381 |
| 200 | 8.35 | 11.366 | 14.509 | 17.613 |
| 250 | 9.232 | 13.025 | 16.949 | 20.84 |
| 200 | 8.35 | 11.372 | 14.513 | 17.615 |
| 150 | 7.471 | 9.723 | 12.063 | 14.39 |
| 100 | 6.593 | 8.088 | 9.634 | 11.17 |
| 50 | 5.72 | 6.465 | 7.234 | 7.985 |
| 0 | 4.853 | 4.854 | 4.854 | 4.853 |

**Table A.3:** Calibration table for RBM3. Output columns are at different lever arm lengths. Data provided by manufacturer Applied Measurements Ltd.

| **Applied** | **Output [mA]** | | | |
|---|---|---|---|---|
| **load [N]** | **@ 125 mm** | **@ 250 mm** | **@ 375 mm** | **@ 500 mm** |
| 0 | 4.527 | 4.528 | 4.528 | 4.529 |
| 50 | 5.375 | 6.101 | 6.839 | 7.528 |
| 100 | 6.221 | 7.678 | 9.157 | 10.638 |
| 150 | 7.065 | 9.256 | 11.49 | 13.727 |
| 200 | 7.916 | 10.84 | 13.838 | 16.845 |
| 250 | 8.767 | 12.435 | 16.209 | 19.959 |
| 200 | 7.918 | 10.844 | 13.84 | 16.837 |
| 150 | 7.067 | 9.258 | 11.489 | 13.718 |
| 100 | 6.22 | 7.673 | 9.151 | 10.629 |
| 50 | 5.375 | 6.098 | 6.833 | 7.571 |
| 0 | 4.527 | 4.526 | 4.526 | 4.526 |

# Appendix B. Test matrix

**Table B.1:** Test Matrix

| No. | Code | U [m/s] | Flow Angle [°] | Wave Period [s] | Wave Height [mm] | Wave Angle [°] |
|---|---|---|---|---|---|---|
| 1 | C1 | 0.8 | 0 | 0 | 0 | 0 |
| 2 | C1-W11 | 0.8 | 0 | 2 | 102 | 0 |
| 3 | C1-W21 | 0.8 | 0 | 2.5 | 91 | 0 |
| 4 | C1-W31 | 0.8 | 0 | 3 | 86 | 0 |
| 5 | C1-W12 | 0.8 | 0 | 2 | 102 | 45 |
| 6 | C1-W22 | 0.8 | 0 | 2.5 | 91 | 45 |
| 7 | C1-W32 | 0.8 | 0 | 3 | 86 | 45 |
| 8 | C1-W23 | 0.8 | 0 | 2.5 | 91 | 135 |
| 9 | C1-W33 | 0.8 | 0 | 3 | 86 | 135 |
| 10 | C1-W14 | 0.8 | 0 | 2 | 102 | 315 |
| 11 | C1-W24 | 0.8 | 0 | 2.5 | 91 | 315 |
| 12 | C1-W34 | 0.8 | 0 | 3 | 86 | 315 |
| 13 | C2 | 0.8 | -10 | 0 | 0 | 0 |
| 14 | C2-W11 | 0.8 | -10 | 2 | 102 | 0 |
| 15 | C2-W21 | 0.8 | -10 | 2.5 | 91 | 0 |
| 16 | C2-W31 | 0.8 | -10 | 2 | 102 | 45 |
| 17 | C2-W12 | 0.8 | -10 | 2.5 | 91 | 45 |
| 18 | C2-W22 | 0.8 | -10 | 3 | 86 | 45 |
| 19 | C2-W32 | 0.8 | -10 | 2.5 | 91 | 135 |
| 20 | C2-W23 | 0.8 | -10 | 3 | 86 | 135 |
| 21 | C2-W33 | 0.8 | -10 | 2 | 102 | 315 |
| 22 | C2-W14 | 0.8 | -10 | 2.5 | 91 | 315 |
| 23 | C2-W24 | 0.8 | -10 | 3 | 86 | 315 |
| 24 | C2-W34 | 0.8 | -10 | 3 | 86 | 0 |
| 25 | C3 | 0.8 | -20 | 0 | 0 | 0 |
| 26 | C3-W11 | 0.8 | -20 | 2 | 102 | 0 |
| 27 | C3-W21 | 0.8 | -20 | 2.5 | 91 | 0 |
| 28 | C3-W31 | 0.8 | -20 | 3 | 86 | 0 |
| 29 | C3-W12 | 0.8 | -20 | 2 | 102 | 45 |
| 30 | C3-W22 | 0.8 | -20 | 2.5 | 91 | 45 |
| 31 | C3-W32 | 0.8 | -20 | 3 | 86 | 45 |
| 32 | C3-W23 | 0.8 | -20 | 2.5 | 91 | 135 |
| 33 | C3-W33 | 0.8 | -20 | 3 | 86 | 135 |
| 34 | C3-W14 | 0.8 | -20 | 2 | 102 | 315 |
| 35 | C3-W24 | 0.8 | -20 | 2.5 | 91 | 315 |
| 36 | C3-W34 | 0.8 | -20 | 3 | 86 | 315 |

# Appendix C. Time series - all tests

Thrust

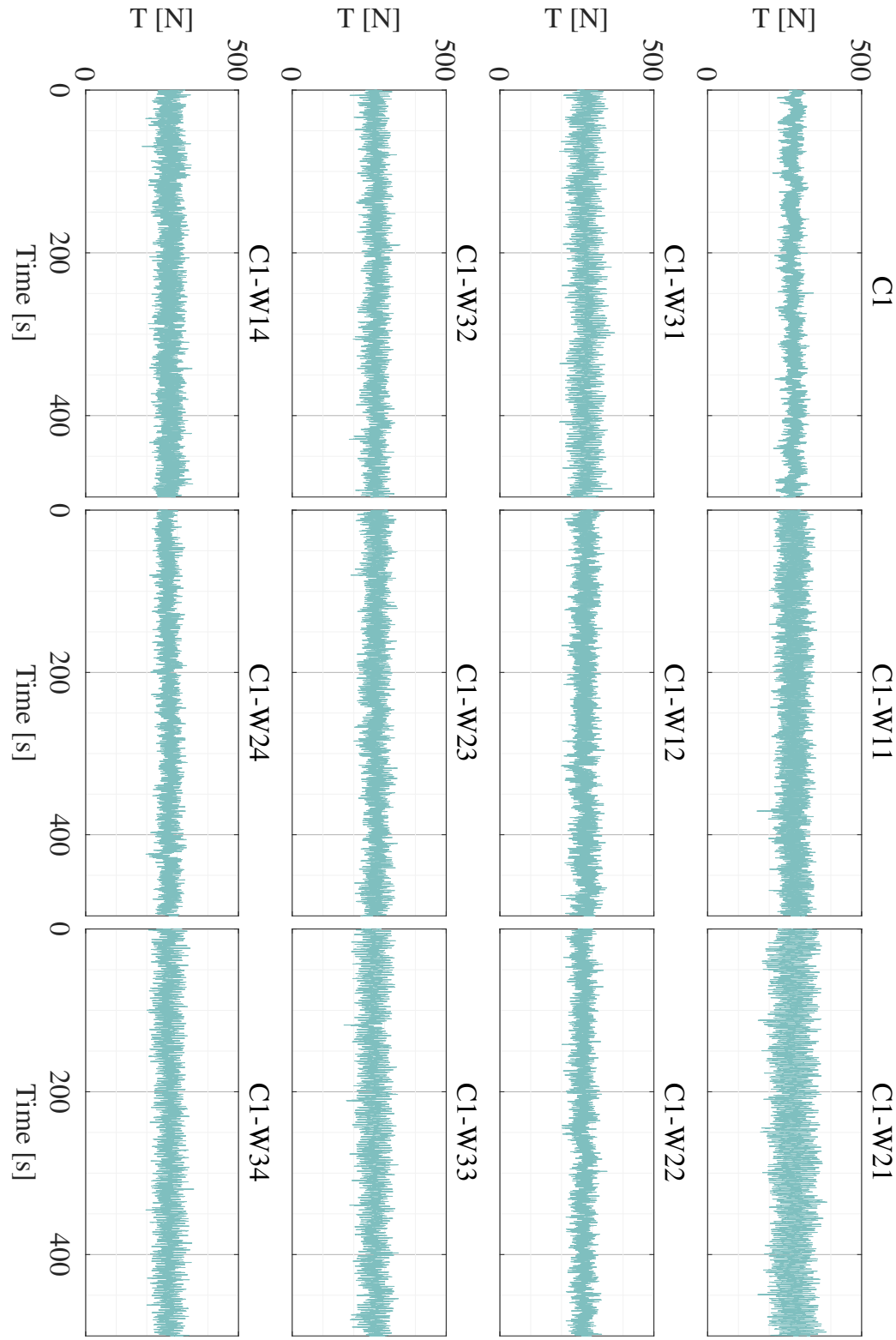


**Figure C.1:** Thrust signals for all tests at $\beta = 0°$

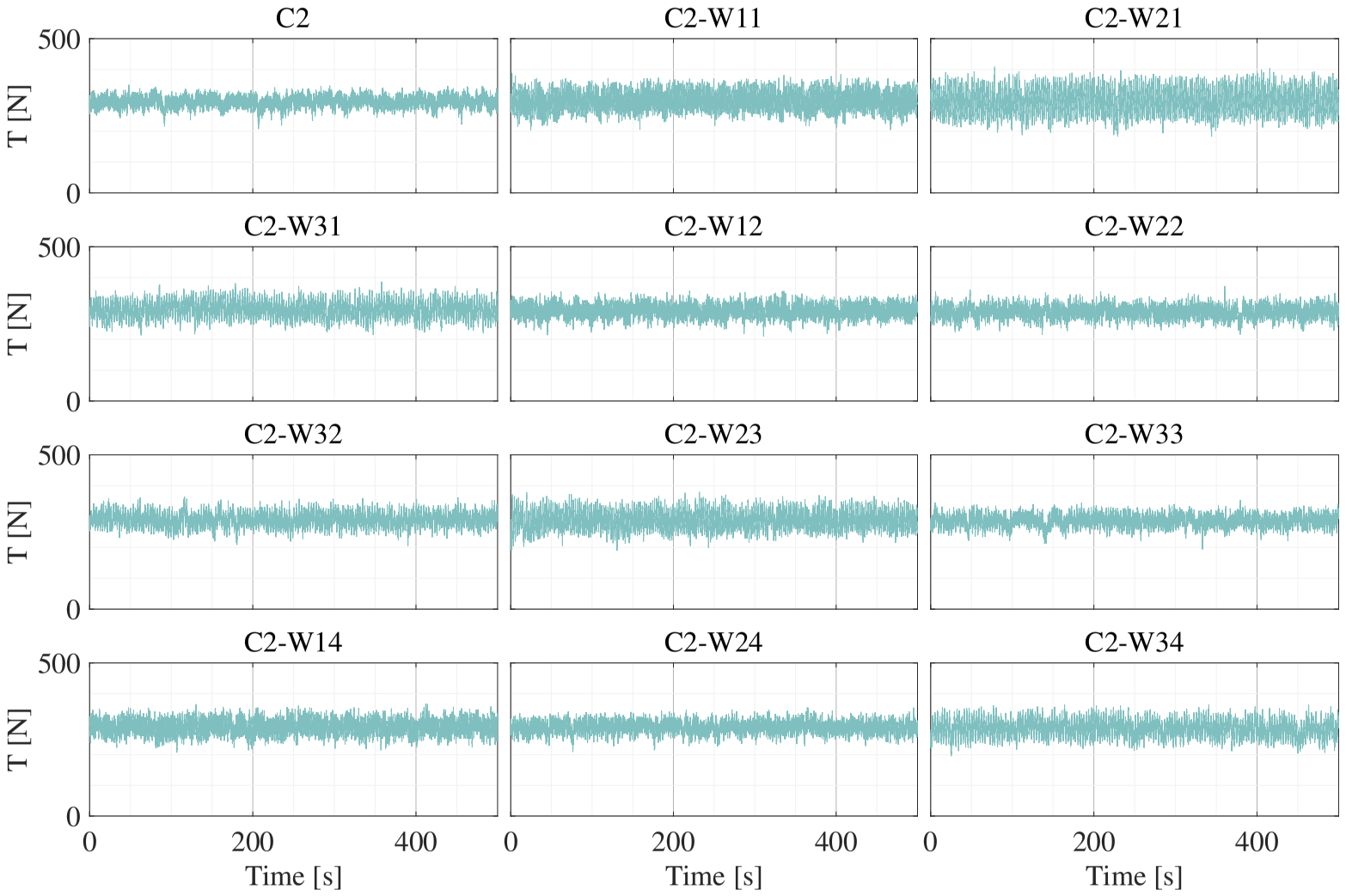


**Figure C.2:** Thrust signals for all tests at $\beta = 10°$

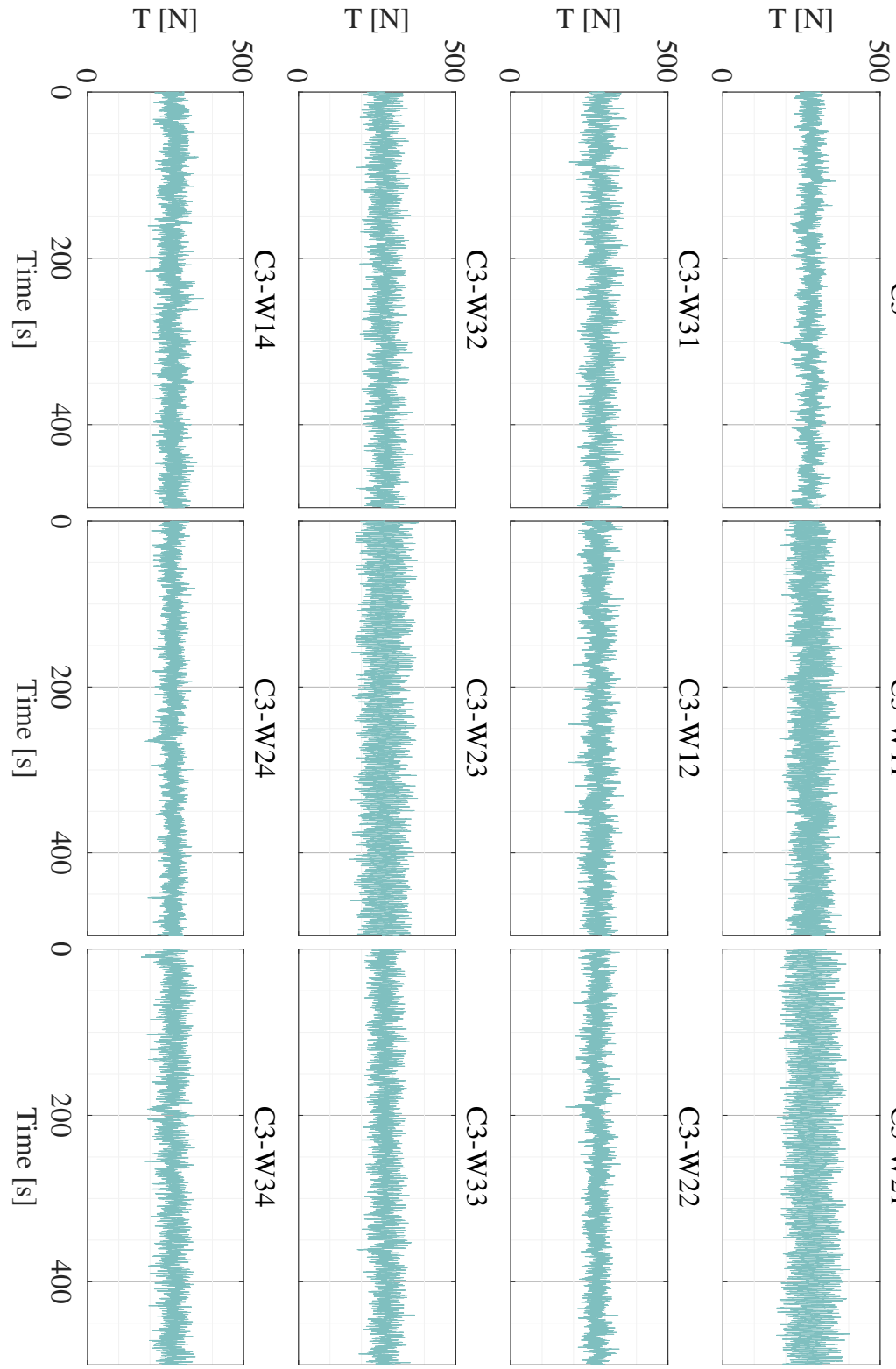


**Figure C.3:** Thrust signals for all tests at $\beta = 20°$

# Torque

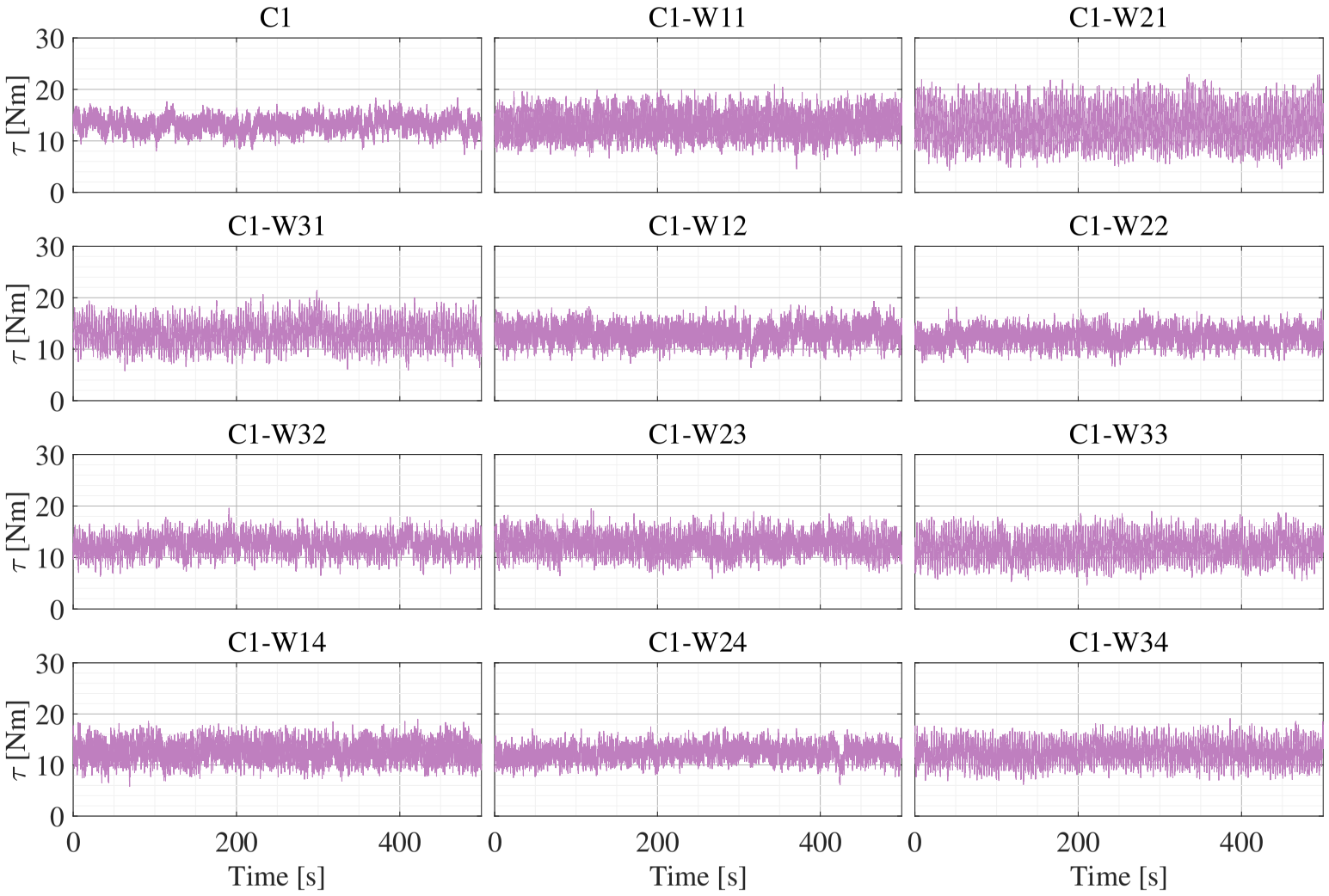


**Figure C.4:** Torque signals for all tests at $\beta = 0°$

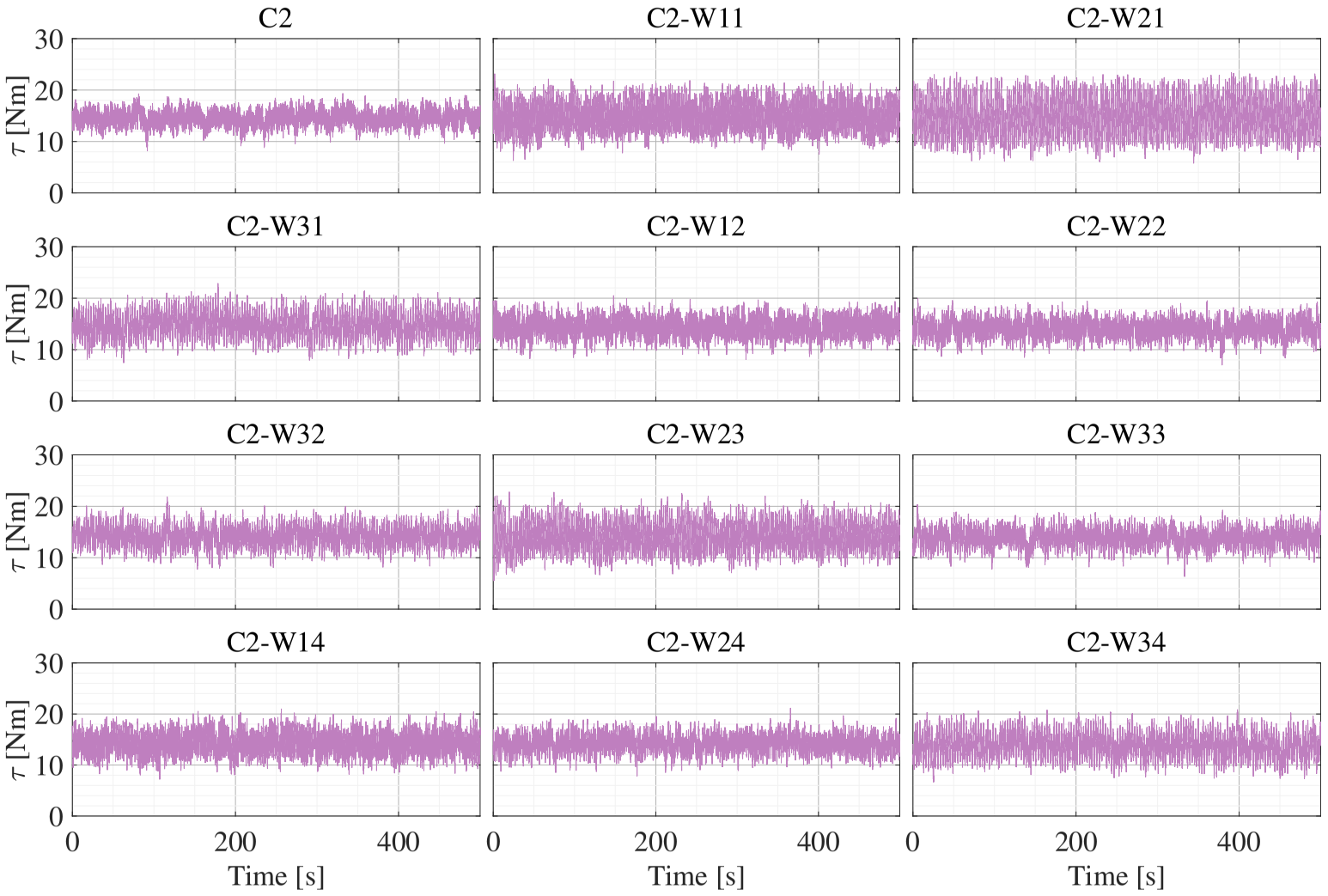


**Figure C.5:** Torque signals for all tests at $\beta = 10°$

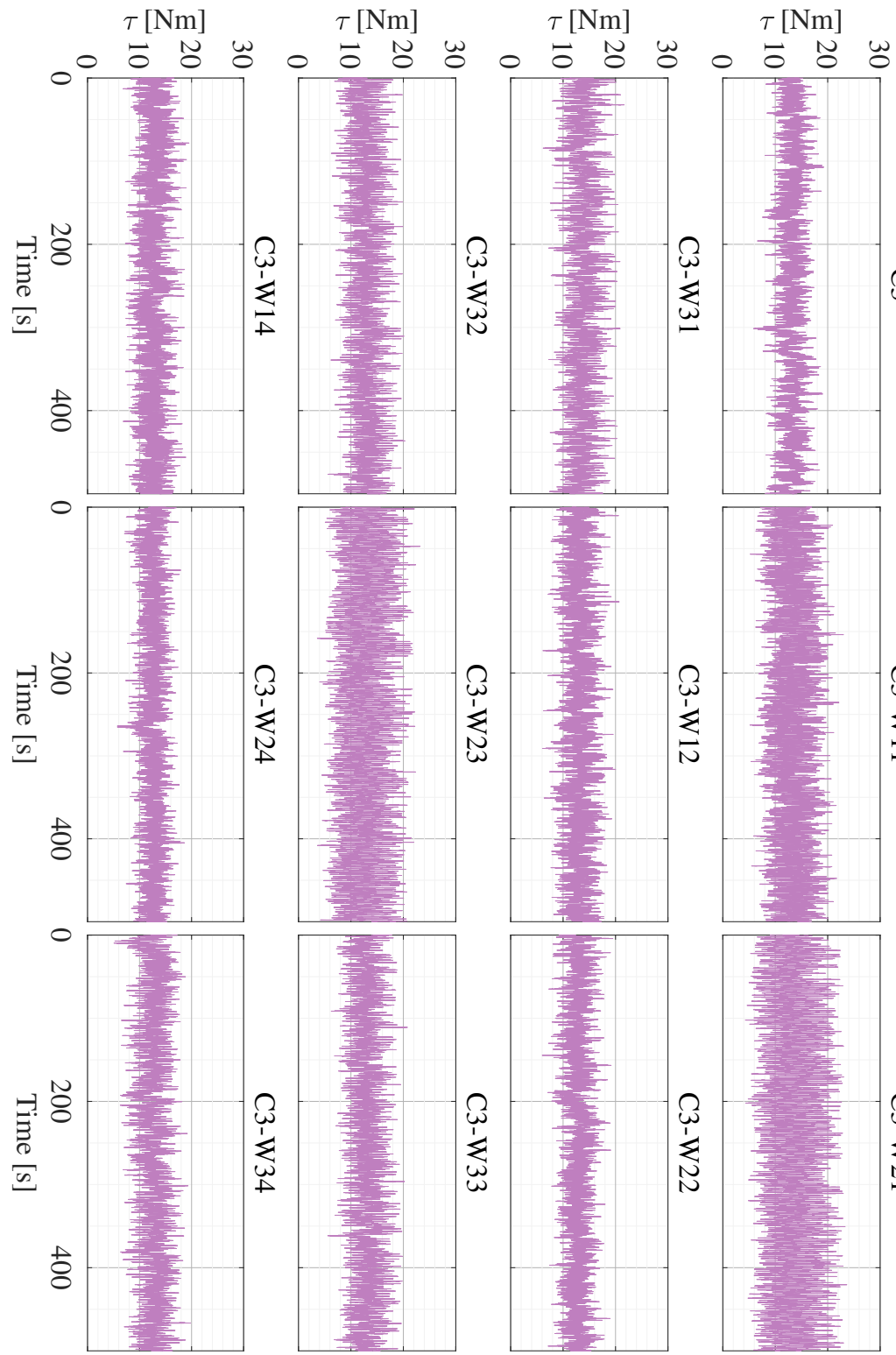


**Figure C.6:** Torque signals for all tests at $\beta = 20°$

RBM

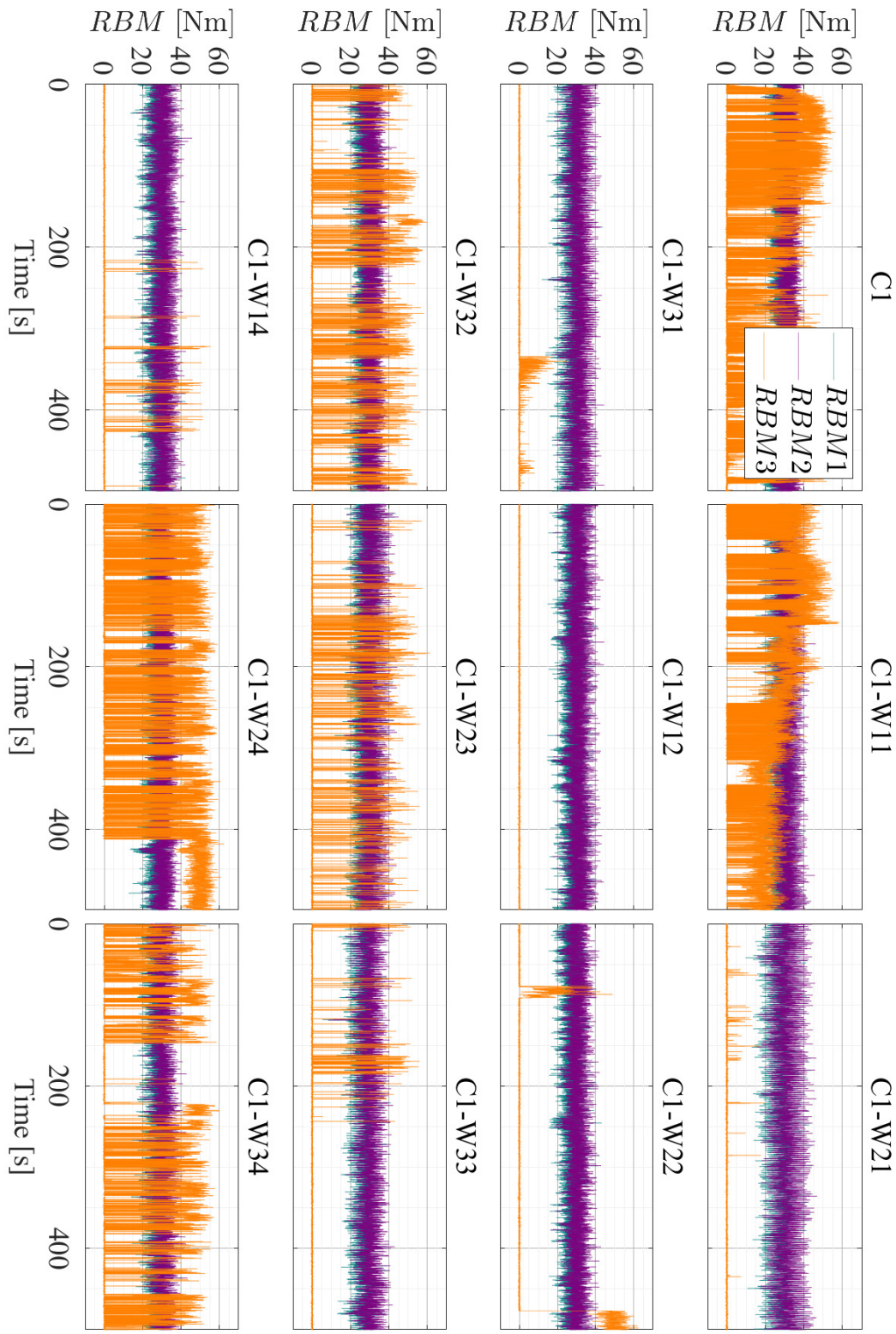


**Figure C.7:** RBM signals for all tests at $\beta = 0°$

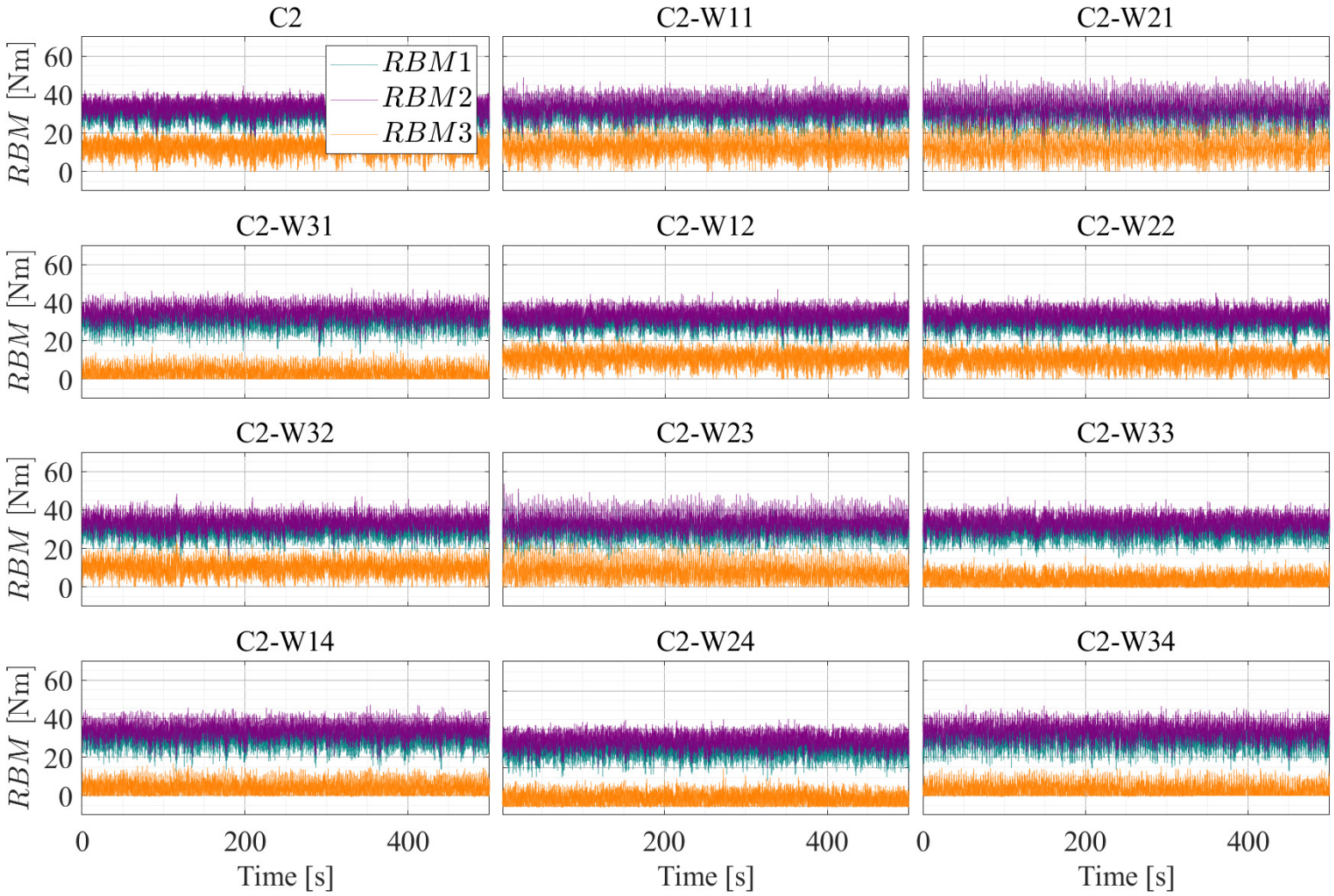


**Figure C.8:** RBM signals for all tests at $\beta = 10°$

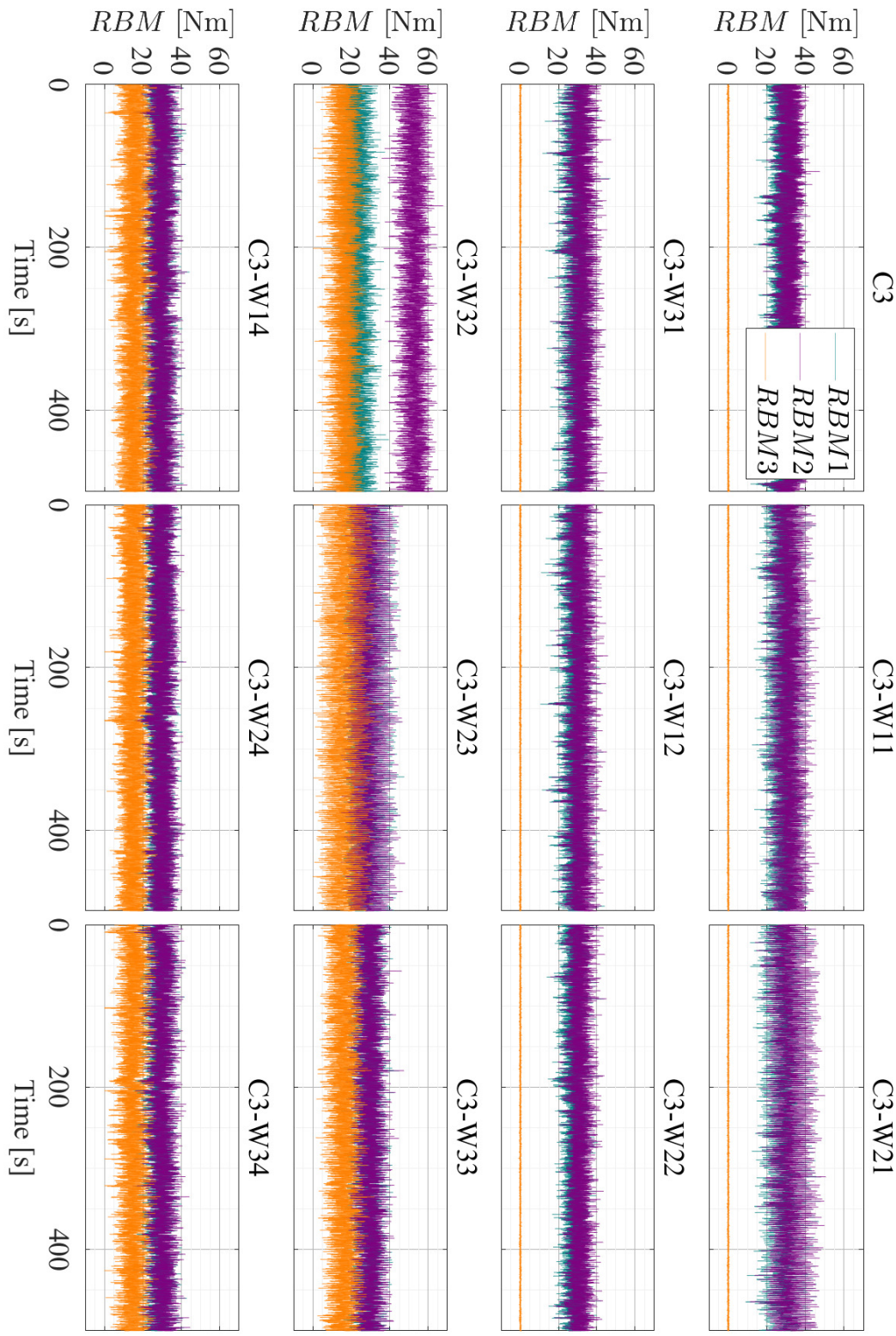


**Figure C.9:** RBM signals for all tests at $\beta = 20°$

# Load cell

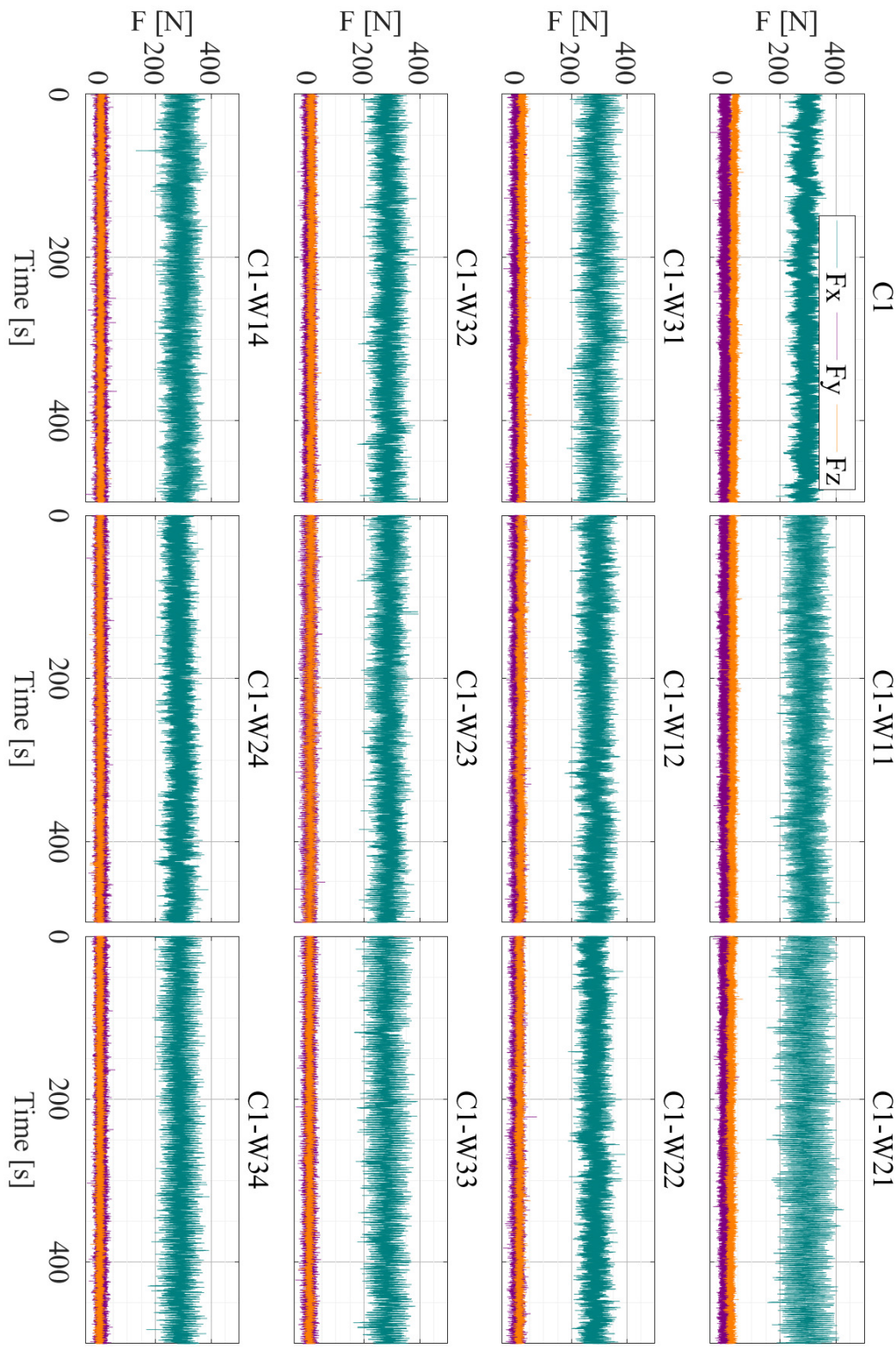


**Figure C.10:** Load cell signals for all tests at $\beta = 0°$

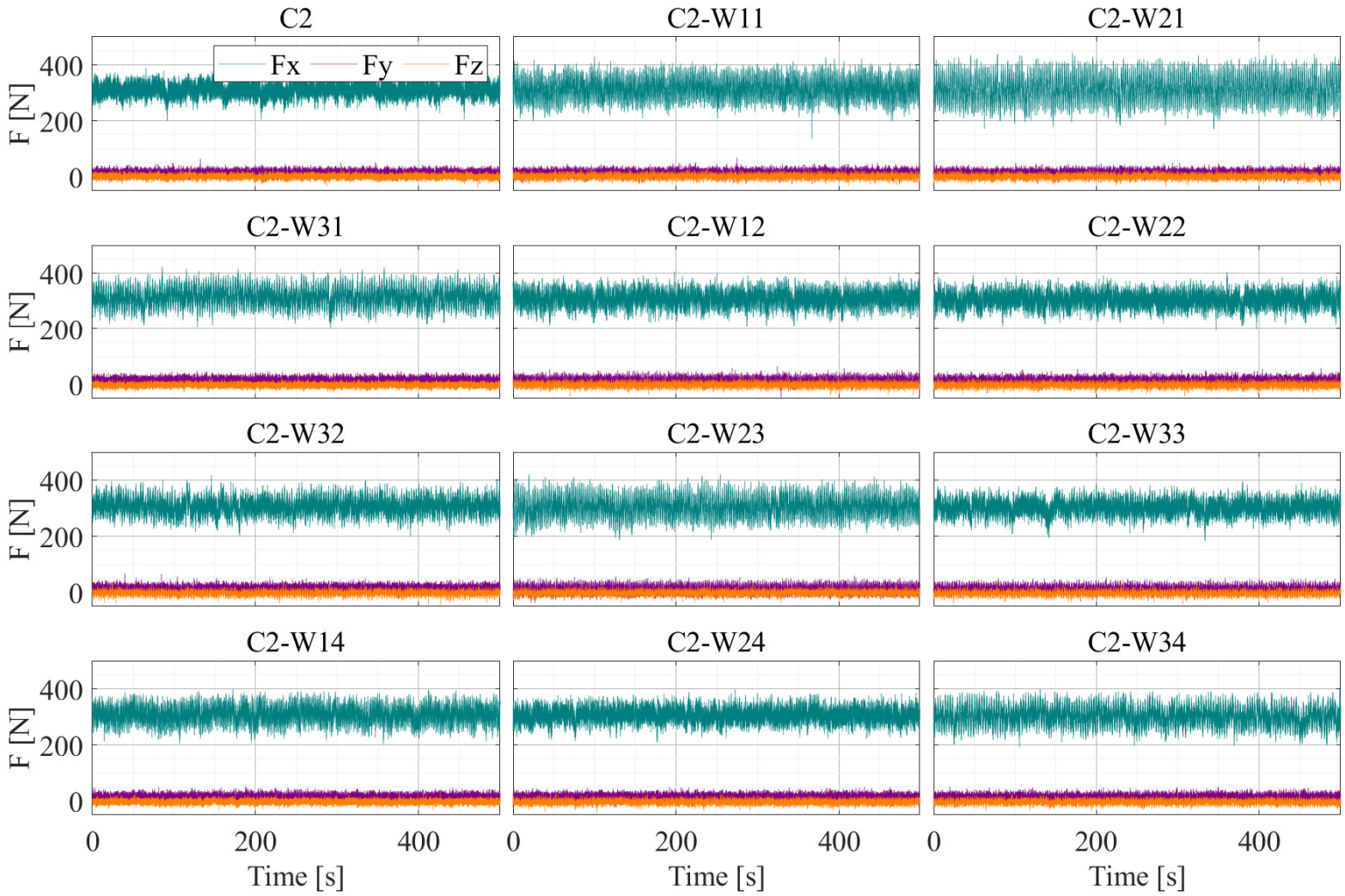


**Figure C.11:** Load cell signals for all tests at $\beta = 10°$

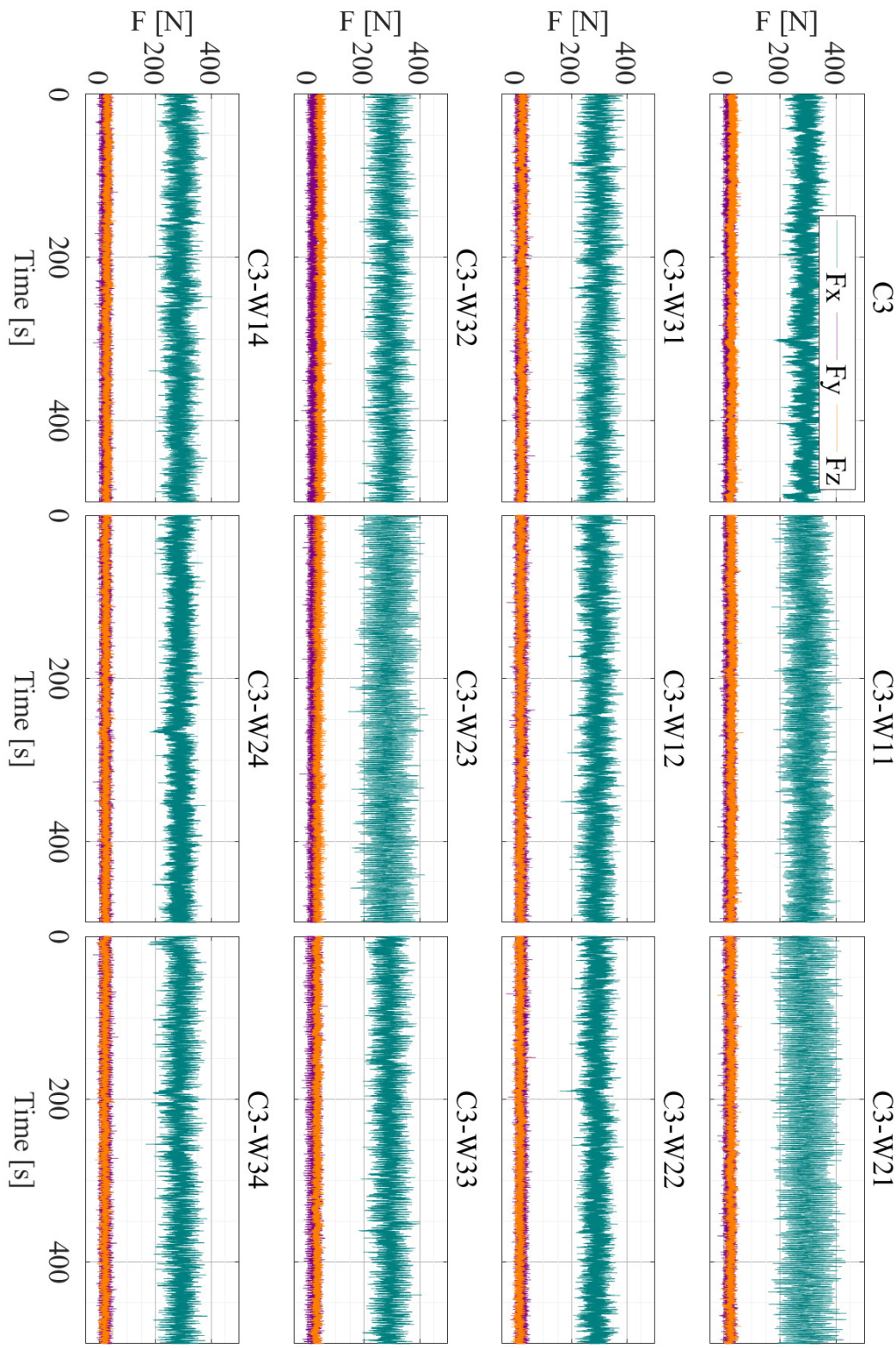


**Figure C.12:** Load cell signals for all tests at $\beta = 20°$

# Wave gauges

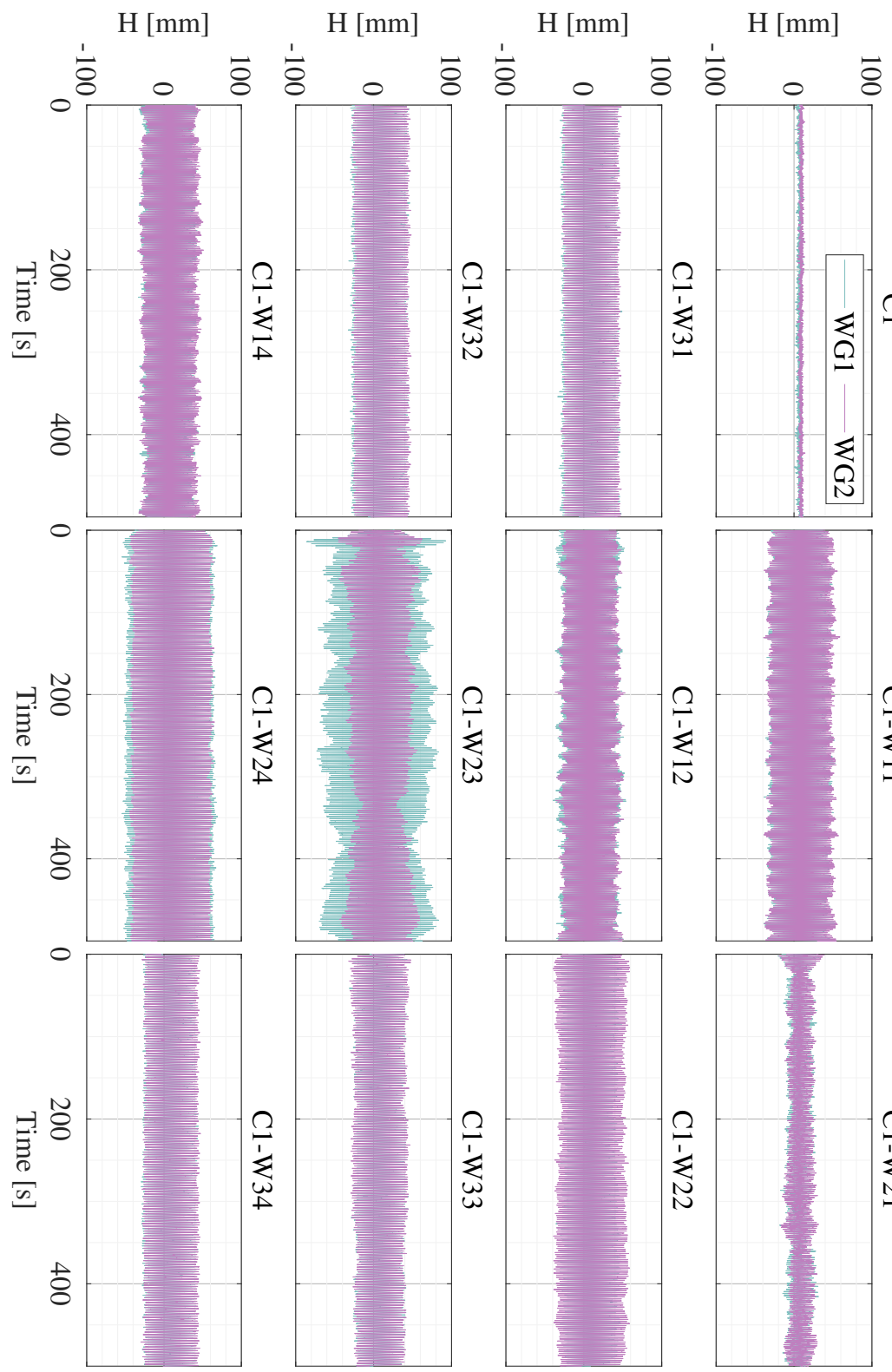


**Figure C.13:** Wave gauges signals for all tests at $\beta = 0°$

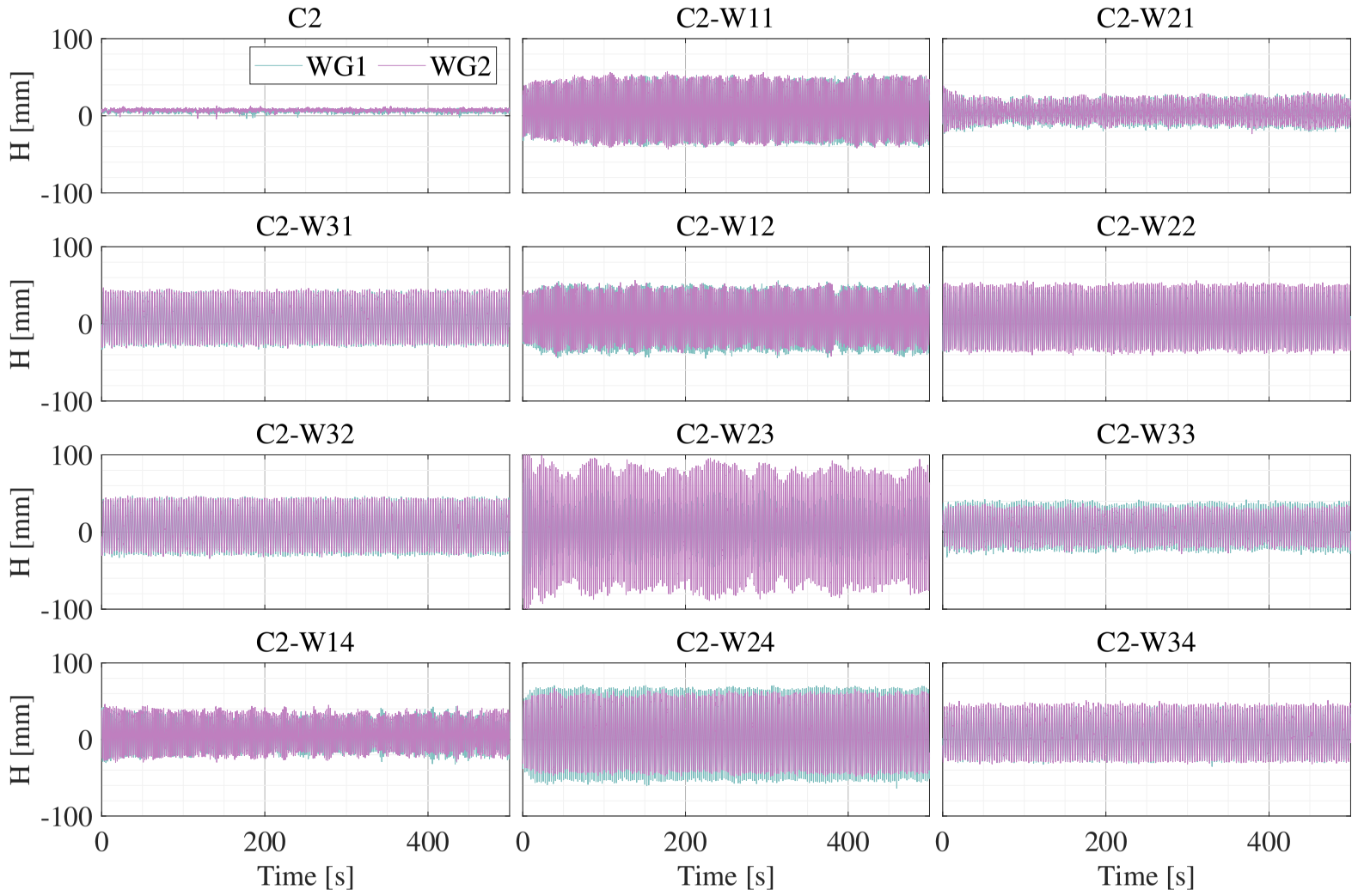


**Figure C.14:** Wave gauges signals for all tests at $\beta = 10°$

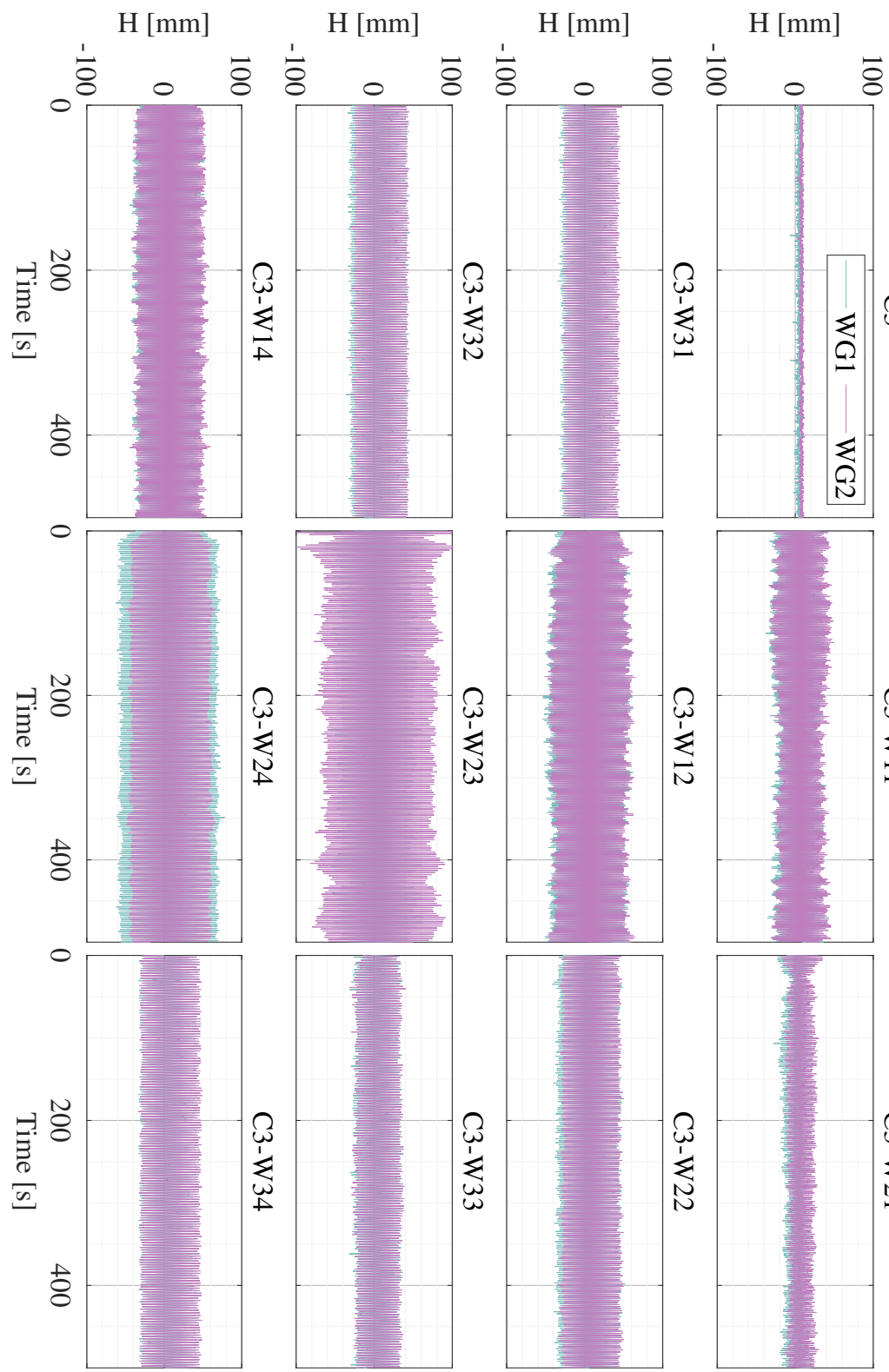


**Figure C.15:** Wave gauges signals for all tests at $\beta = 20°$

## Appendix D. Author contributions

Journal publications as first author

Ocean Engineering 164 (2018) 55–64

Contents lists available at ScienceDirect

Ocean Engineering

journal homepage: www.elsevier.com/locate/oceaneng

# The effects of oblique waves and currents on the loadings and performance of tidal turbines

Rodrigo Martinez*, Grégory S. Payne[1], Tom Bruce

*School of Engineering, University of Edinburgh, UK*

ARTICLE INFO

*Keywords:*
Tidal energy
Horizontal axis tidal rotor
Wave-current interaction
Performance characterisation
Tank testing
Physical modelling

ABSTRACT

Tidal energy exploitation is at an early deployment stage and costs need to be reduced to improve the long term economic viability of the sector. High costs of tidal turbines are, in part, the result of load uncertainties, which lead to the use of high factors of safety in the design to ensure survival. One of the most important causes of uncertainty is hydrodynamic loadings. To date, most of the scaled model experiments with horizontal axis turbines investigating this issue have been carried out with collinear wave and current directions. To the authors' knowledge, the work presented herein is the first experimental investigation of a horizontal axis turbine model subjected to combined oblique waves and current. Turbine performance and loading are measured for a 1:15 scale model tested in the FloWave circular, combined wave and current basin at the University of Edinburgh (UK). Three different flow directions were tested and each of them were also combined with regular waves in three different directions non-collinear with the flow. Fifteen physical quantities were measured including flow velocity, rotor and foundation loads and turbine speed. Characterisation of loads and turbine performance in those oblique current and wave conditions are presented. Waves affect means and standard deviation of rotor power and thrust, but off-axis waves are associated with lower thrust loads than head-on waves. Compared to current only, rotor torque and thrust standard deviations are higher in the presence of waves and almost twice as high when the wave crest is parallel to the rotor plan. The experimental data associated with this article can be downloaded from http://dx.doi.org/10.7488/ds/2360.

## 1. General introduction

Due to the ever greater urgency to address global warming issues, the Scottish Government (2013) has set a target of generating the equivalent of 100% of Scotland's electricity from renewable sources by 2020 with the added challenge of maintaining the country as a global lead in tidal and wave energy developments. Compared with other renewables such as wind and solar PV, tidal energy is at a relatively early stage on its maturity and needs continued research into fundamentals of machine loading and performance in realistic conditions to enhance reliability and cost effectiveness.

According to the Department of Energy and Climate Change (2013), the levelised cost of electricity (LCOE) from tidal stream sources is expected to reduce from 190£/MWh in 2025 to 171£/MWh by 2030 for shallow water deployments, and from 148£/MWh to 129£/MWh for deep water deployments. This is still not a competitive generation method compared to onshore wind turbines over 5 MW per unit which is forecasted to have in 2030 a LCOE of 97£/MWh. This is due to the high cost of capital expenditure (CapEx) and operational expenditure (OpEx). A solution to lower the LCOE is to reduce CapEx by optimising the structural design of the device whilst maintaining the device's performance and survivability. A possible approach is to lower the factors of safety (FS) that account for the design and performance uncertainties arising from loads in naturally occurring flows. A way to assess the effect of these loads is physical testing of scale models.

There is an extensive literature on tidal turbine testing based upon physical models. Bahaj et al. (2007) used a 0.8m rotor in a towing tank, finding that the highest performance for their tidal turbine model was at a tip-speed ratio (TSR) $\lambda = 5–7$ with pitch angle of 20°. They found that the power coefficient ($C_P$) of the turbine decreases as the rotor is yawed and when the turbine tip is around 0.19D from the water surface. Mycek et al. (2014), with a 0.7m rotor, Gaurier et al. (2013) with a 0.9m rotor and de Jesus Henriques et al. (2014) with a 0.5m rotor, all in a recirculating tank, observed that wave-induced fatigue loads show a standard deviation two to three times higher than for the current-only induced fatigue loads and represents a significant risk of failure. The average $C_P$ and the average thrust coefficient ($C_T$) are however not affected. In addition, they found that the ambient turbulence affects the

* Corresponding author.
*E-mail address:* r.martinez@ed.ac.uk (R. Martinez).
[1] Present address: Department of Naval Architecture, Ocean & Marine Engineering, University of Strathclyde.

https://doi.org/10.1016/j.oceaneng.2018.05.057
Received 23 December 2017; Received in revised form 25 May 2018; Accepted 28 May 2018
Available online 20 June 2018

fatigue loadings on the turbine, but not its performance. At higher turbulence intensity (TI), the wake was observed to recover faster than at lower TI. Luznik et al. (2013) with a 0.46m rotor tested in a towing tank, observed that in the absence of waves the turbine can operate at lower TSR values.

Evans (2014) and Easton (2013), using ADCP measurements at Ramsey Sound (Pembrokeshire, Wales, UK) and the Inner Sound (Pentland Firth, Scotland, UK) respectively, showed that the main flow direction at potential tidal sites can vary by up to 20° between flood and ebb. Their findings were used to inform the range of directionalities explored in the present work. In the field, although there is a predominant wave direction, there will be occasions when the wave direction varies from this. The wave direction is independent of the tidal flow direction. To the authors' knowledge however, the influence of waves not collinear to the current has not been explored in the literature, perhaps in part due to the limited number of testing facilities capable of producing such conditions.

The turbine model used for this project is described in Payne et al. (2017). The article details the design process of the turbine. Blade Element Momentum (BEM) is first used estimate the loads the turbine would be subjected to, which in turn informs the specifications for the force sensors and for the drive train. Finite Element Analysis (FEA) is used to ensure that the blades can structurally withstand the loads. Preliminary results from testing carried out in the recirculating flume of IFREMER in Boulogne-sur-Mer, France is also presented including $C_P$ and $C_T$ curves, load time series and wake measurements.

The tests for this project were carried out in the FloWave basin of the University of Edinburgh whose characteristics have been documented in Noble et al. (2015) and Sutherland et al. (2017). Both articles describe a fairly straight velocity depth profile from the surface up to mid-depth with slower speeds closer to the bottom of the basin. They observed that at 1.5m above the floor, the measured flow speed experiences significant spatial variation throughout the basin's raiseable floor area and it can be up to 50% lower than the prescribed value. The velocity depth profiles change considerably as the flow measurements are performed further away from the basin's centre, especially on the transverse direction to the flow. Significant changes become noticeable outside a ~5 meters radius. Noble et al. (2015) propose a working area of 8-by-6 meters outside of which the spatial variations are of the order of 10% of the nominal speeds. Inside this working area, all speed measurements are within 5% of the nominal speed.

The main objective of this study is to identify the effects of oblique waves and currents on the root bending moment of the blades, on the rotor thrust and torque loadings and on the performance of a tidal turbine. Presently, the use of Factors of Safety (FS) protect the devices from damage due to uncertain flow characteristics, the aim of this work is to reduce these design uncertainties. Tests were undertaken in a circular tank that allows the generation of waves and currents at any desired angle. This research used a 1.2 m diameter horizontal axis turbine model and a matrix of wave and current parameters ranging from collinear to oblique interactions. This work expands the findings from Martinez et al. (2017).

This work is divided in two main sections: flow characterisation and turbine testing. These sections are preceded by a general introduction of the testing facility and turbine model.

## 2. The experimental facility and turbine model

### 2.1. Wave-current basin and instrumentation

The FloWave facility, shown in Fig. 1, is located at The University of Edinburgh in Scotland, UK. It is a 25m diameter circular basin with a 2m working depth and a 15m diameter elevating floor to facilitate access to the basin bottom when setting up models. Current is generated by 28 5-bladed, 1.7m diameter impellers arranged around the full circumference of the basin. Multidirectional wave generation is archived by 168 absorbing flap type wavemakers, also arranged around the full circumference. This facility has the advantage of creating flow and waves independently at any given angle (Robinson et al., 2015). It was specifically designed to support tidal and wave energy research and development in intermediate water depths.

An Acoustic Doppler Velocimeter (ADV) was used for all flow measurements. The specific instruments used was a Vectrino Profiler from Nortek. This instrument can measure flow velocities up to 3.0 m/s at a sample rate of up to 100Hz.

Wave elevation are measured using resistive wave gauges. These are sampled at 64Hz and were calibrated every day before testing.

### 2.2. Turbine model

The turbine model used for the tests was designed and built by Payne et al. (2017) at the University of Edinburgh under The Engineering and Physical Sciences Research Council (EPSRC) funded project “X-MED” (EP/J010235/1). It consists of a 1:15 scale, 1.2m diameter rotor that represents an 18m diameter turbine at full scale. The blade profile is a NACA 63-8XX made of aluminium, manufactured by computer numerical control (CNC) machining. For these experiments, the turbine was operated under speed control. Fig. 2 shows the turbine mounted on the basin floor. All the instrumentation is kept protected inside the black and silver cylindrical sleeves.

The turbine was first tested at IFREMER in Boulogne-sur-Mer, France with results presented by Payne et al. (2017).

#### 2.2.1. Turbine instrumentation

The turbine model is fitted with a transducer measuring rotor torque and thrust on the rotor only. It also includes sensors measuring the stream-wise root bending moment at the root of each blade. A resolver records the absolute angular position of the rotor. All the turbine sensors are sampled synchronously at 256Hz. The root bending moment load cells developed a fault during the tests and their measurements are therefore not analysed herein.

## 3. Flow characterisation

### 3.1. Introduction and methodology

In order to understand the onset flow the turbine was going to be exposed to, a campaign of flow characterisation tests was carried out before putting the turbine in the water. This section describes the tested conditions and findings.

Fig. 3 shows a top view of the basin, with a blue marker representing the location of the turbine. The dashed lines represent the wave angles selected and the solid, coloured lines, represent the flow angles. A flow speed of 0.8 m/s was selected. This is the design speed for the turbine model presented by Payne et al. (2017). From Froude scaling, this corresponds to a full-scale velocity of 3.1 m/s which, according to McNaughton et al. (2015), is a realistic flow speed for deployment sites such as the European Marine Energy Centre (EMEC). The wave directions were chosen to provide a broad range of conditions within the testing time allocated and the technical capability of the facility. In that context, tests in 180° opposing wave were not carried out as it limits the range of wave period available (because of the Doppler effect). 90° waves were also excluded because the associated wave induced velocity will be parallel to the rotor disc and will therefore have limited influence on its load. Wave heights and periods were chosen to produce (according to linear wave theory) a horizontal wave induced velocity at hub height of 0.1 m/s. Such a flow speed fluctuation is within the capability of the turbine model and would be associated at full scale with a 1.5m wave height and 8s wave period.

Wave heights and periods were selected to generate a wave-induced horizontal water particle velocity at hub height of 0.1 m/s. Three regular waves were used with the characteristics shown in Table 1.

**Fig. 1.** View of the FloWave basin.

**Fig. 2.** The turbine mounted on the basin floor (shown in the floor's raised position).

These tests were performed without the turbine and measurements of the flow speed were taken in the plane where the rotor would be. Fig. 4 shows a front view of the rotor plane indicating where the wave gauges (yellow lines) were positioned during the tests and the flow velocity measurement positions (red markers) to create vertical and transverse profiles. The dashed circle represents the rotor swept area. The figure also shows the coordinate system used to describe the flow velocity components.

All the flow characterisation tests were recorded for 160s with a 32s ramp-up at the beginning to allow for the first waves generated to reach the centre of the basin, yielding an effective test duration of 128s after trimming off the run-up seconds.

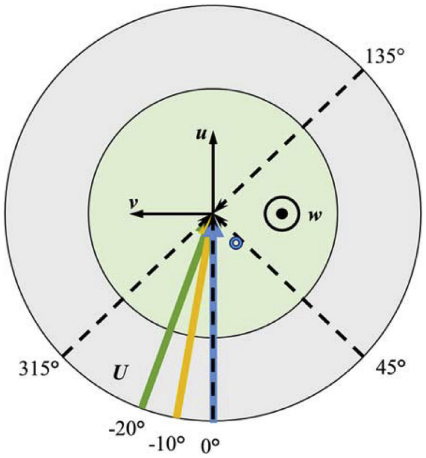


**Fig. 3.** Plan view of the basin indicating flow (solid) and wave (dashed) angles selected for testing. Blue marker represents the turbine position. (For interpretation of the references to colour in this figure legend, the reader is referred to the Web version of this article.)

**Table 1**
Wave parameters.

| Period [s] | Wave height [mm] |
|---|---|
| 2.0 | 102 |
| 2.5 | 91 |
| 3.0 | 86 |

### 3.2. Results

First, the case of no waves and zero yaw is considered. Fig. 5 shows

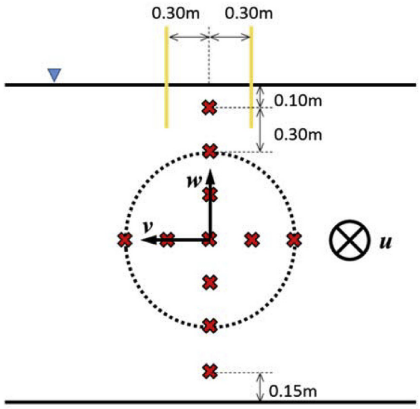


**Fig. 4.** Front view of the rotor plane delimited by the dashed circle. Wave gauges (yellow lines) and flow velocity measurement points (red crosses). (For interpretation of the references to colour in this figure legend, the reader is referred to the Web version of this article.)

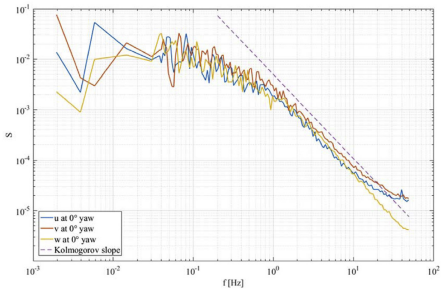


**Fig. 5.** Spectral comparison of the flow components at 0° without waves.

the spectral density of the onset velocity components $\boldsymbol{u}$, $\boldsymbol{v}$, and $\boldsymbol{w}$ at hub height plotted against frequency. Both axes use a logarithmic scale. These curves were obtained using a method where the data is downsampled logarithmically, meaning that at lower frequencies, the bins contain fewer frequency components than at higher frequencies, giving smother curves at high frequencies. Two distinct regions of the spectrum are visible in the figure. For frequencies $< 0.2$ Hz, the trend of the spectra of the three velocity components is broadly horizontal, corresponding to the energy containing range. For higher frequencies, the fall away of the spectral density indicates the inertial range. All the velocity components are observed to follow closely the Kolmogorov slope of $-5/3$, indicating that measured flow is similar to the idealised case of 3D isotropic homogeneous turbulent flow conditions modelled by Kolmogorov's theory as presented by Thorpe (2007). The levelling-off of the spectra at the highest frequencies (above 30 Hz or so) is due to the limits of the instrumentation. This is discussed in Section 3.3.

The flow velocity magnitude $\boldsymbol{U}$ comprises both horizontal components of the flow ($\boldsymbol{u}$ and $\boldsymbol{v}$) and is defined by:

$$\boldsymbol{U} = \sqrt{\boldsymbol{u}^2 + \boldsymbol{v}^2} \quad (1)$$

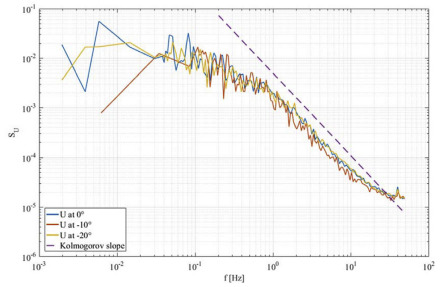


**Fig. 6.** Spectral comparison exploring the effect of yaw angle in **U** with no waves.

As the vertical flow component $\boldsymbol{w} << \boldsymbol{u}, \boldsymbol{v}$ it was decided not to be included in $\boldsymbol{U}$.

Fig. 6 shows the spectral density of the onset flow velocity $\boldsymbol{U}$ at hub height without waves for three flow directions. The spectra are very similar for the three directions. Comparing Figs. 5 and 6, it can be seen that $\boldsymbol{U}$ has a similar spectral density to the individual velocity components, henceforth, $\boldsymbol{S_U}$ will replace the use of the components' spectra $\boldsymbol{S_u}$, $\boldsymbol{S_v}$ and $\boldsymbol{S_w}$.

Focussing on the $-20°$ yaw case, the influence of waves was explored by the addition of waves (period T = 2.0s; height H = 102 mm) from three different directions: 0°, 45° and 315°. Fig. 7 shows the resulting spectral density functions of the velocity $\boldsymbol{U}$. It is interesting to note the size of the spectral peaks associated with the wave period are about an order of magnitude higher than those associated with turbulence. This suggests that at the wave frequency, the energy contained in the waves is more significant than the energy contained in the turbulence.

In order to explore the uniformity of the flow within the rotor area and later on assess its effect on the turbine, the nine $\boldsymbol{U}$ point measurements located within the rotor area shown in Fig. 4, were calculated with **(1)**, time averaged and then spatial averaged, giving one single velocity value $\boldsymbol{U_0}$. Fig. 8 shows three different rotor area velocity maps. There are nine point measurements represented by red crosses. The dashed circle shows the rotor disc area. The subfigures are for flow at: *a)* 0°, *b)* $-10°$ and *c)* $-20°$ respectively. It can be seen that closer to the bottom of the basin the velocity is slower. This is due to bed friction-induced velocity shear profile and also due to the way in which the water is projected from the turning vanes in the basin - see Noble et al.

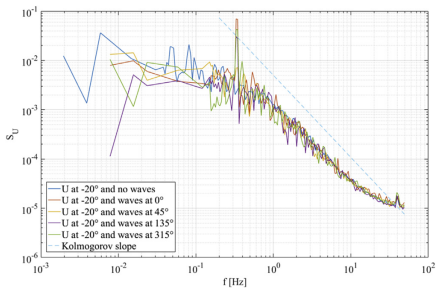


**Fig. 7.** Spectral comparison of U at $-20°$ with waves with T = 2.0s from all different directions.

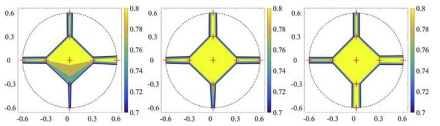

**Fig. 8.** Rotor velocities (U) maps for the 3 different flow angles. Colour bar units are m/s. a) 0° flow, no waves; b) −10° flow, no waves; c) −20° flow, no waves. (For interpretation of the references to colour in this figure legend, the reader is referred to the Web version of this article.)

(2015). It can also be observed that in the 0° and −20° cases, the right-hand side of the rotor disc experiences a faster flow with a relative increase to the rotor averaged velocity $\boldsymbol{U_0}$ of 8.5% and 7.7% respectively. The −10° case is more uniform throughout the rotor area although at the rotor axis, the velocity is slightly higher than the rotor area average. Bare basin measurements reported in Noble et al. (2015) and Sutherland et al. (2017) give the turbulence intensity varying between 5% and 11% in the stream-wise direction. All the cases show a transverse profile with the left-hand side showing slower velocities than the right side. On the other hand, 0° and −10° cases show also a depth profile that is not as pronounced in the −20° case. These variations in flow are not dissimilar to those of Noble et al. (2015).

### 3.3. Discussion

A feature of the spectral density data in Figs. 5–7 is an apparent levelling off for highest frequencies. The instrument's geometry shown in Fig. 9 is responsible for this artefact, the so-called "noise floor" seen in Fig. 6 where $\boldsymbol{u}$ and $\boldsymbol{v}$ curve start to become horizontal and detach from the −5/3 slope at around 10 Hz while the vertical component $\boldsymbol{w}$ keeps following the −5/3 slope up to 50 Hz. This is due to the 60° angle at which the probe's receivers are mounted relative to the emitter. The vertical direction is therefore "better aligned" with the receivers compared horizontal. This phenomenon was also observed by Harding et al. (2014). It is worth noting that the instrument was never rotated between tests and the basin velocity input values were always the same.

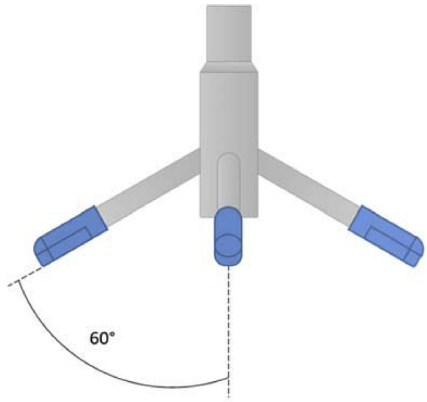


**Fig. 9.** Vectrino probe geometry. The emitter is located in the centre while four (only three shown in diagram) protruding arms represent the receivers.

Bare-basin testing gave a better understanding of how the flow behaves at the same position where the turbine sits. Although the flow showed some non-uniformity within the rotor area of the order of 10% or less, the quality of the data and the different conditions tested gave confidence that the data is fit for purpose and it was now possible to move on to the next stage of the data analysis with the turbine tests.

## 4. Turbine testing

### 4.1. Introduction

The objective of these tests is to determine how big an influence oblique waves and flows have on a horizontal axis turbine and to assist designers in choosing less conservative factors of safety. For this to happen it is necessary to understand how the conditions selected affect the performance and loadings of the turbine. The performance of the turbine is assessed through power and thrust coefficients across a range of tip speed ratio.

Turbine testing allows to understand the behaviour of the turbine loadings under oblique waves and currents, conditions that are poorly represented in the literature.

### 4.2. Methodology

The torque and thrust sensors were calibrated by the manufacturer. Previous experience has given confidence that the torque and thrust transducer show no drift during operation.

To improve the frequency analysis utilising fast Fourier transforms (FFT), the duration of each test was selected so that the number of measurement samples is a power of two. However, to allow for the waves to travel to the turbine's position, 30s had to be added to each test's duration but was removed prior to analysis.

From previous experience, operating the turbine below a particular TSR value in steady flow conditions leads to instability in the rotor's rotational speed as presented by Payne et al. (2017). Therefore, special care had to be taken while choosing the tests parameters. Here, a set of tests aimed at characterising turbine performance ($C_P$ and $C_T$) across a range of TSR from 4.25 to 7.5 were performed. In these tests, the flow velocity remained fixed at 0.8 m/s and the rotor's speed was varied from 45 RPM and 95 RPM. It is thought that there is a hydrodynamic limitation that triggers instabilities for TSR < 4. All the turbine characterisation tests were performed without waves and at three different flow angles as shown in Fig. 10, and were based upon a measurement duration of 256s.

The location of the wave gauges (yellow markers) and Vectrino (red marker) relative to the turbine is shown in Fig. 11.

Shown in Fig. 3 are the flow and wave angles used for flow characterisation. These same conditions were also used for testing the turbine. The difference between the two sets of tests is that there is only one point measurement for the flow velocity, as shown in Fig. 12.

To limit the potential for damage to the turbine and its instrumentation, a cycle of tests was performed with the turbine configuration where all the load sensors were removed and replaced with dummy solid metal parts to make sure that the test program did not include conditions triggering the instabilities observed by Payne et al. (2017) in previous tests. Also, special care was taken during testing (with instrumentation) by constantly monitoring the live instruments' data stream looking for signal clipping or signals out of the expected range or shape.

All the loading tests were performed at a rated TSR of ~7 with prescribed flow speed of 0.8 m/s and 90 RPM, they were all recorded for 512s with a 33s buffer at the beginning to allow for the first waves generated to reach the centre of the basin.

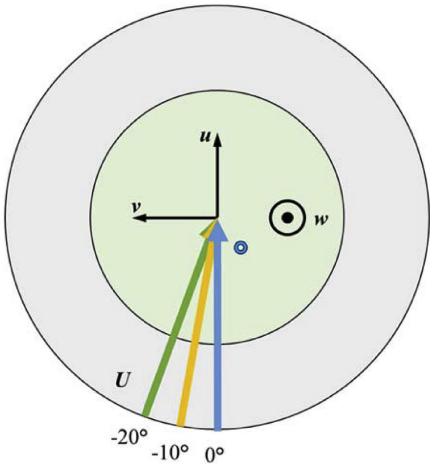


**Fig. 10.** Plan view of the basin indicating flow angles used during turbine characterisation and turbine position (blue marker). (For interpretation of the references to colour in this figure legend, the reader is referred to the Web version of this article.)

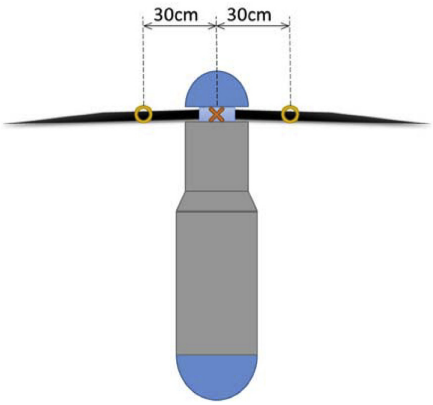


**Fig. 11.** Plan view of the turbine with position of instrumentation indicated by markers. Cross for ADV and circles for wave gauges.

### 4.3. Results

For calculating the power and thrust coefficients, $C_P$ and $C_T$ respectively, the following familiar definitions were used:

$$C_P = \frac{P}{\frac{1}{2}\cdot\rho\cdot A\cdot\overline{U_0^3}} \quad (2)$$

$$C_T = \frac{T}{\frac{1}{2}\cdot\rho\cdot A\cdot\overline{U_0^2}} \quad (3)$$

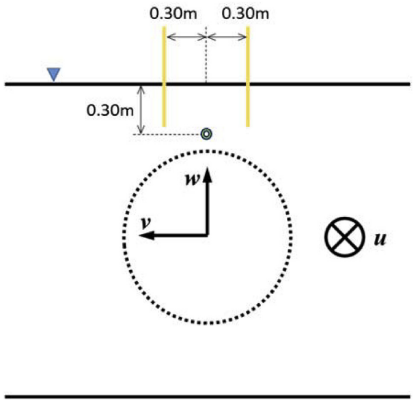


**Fig. 12.** Front view of the rotor plane shown by the dashed circle. Wave gauges (yellow lines) and flow velocity measurement point (green circle). (For interpretation of the references to colour in this figure legend, the reader is referred to the Web version of this article.)

where $P$ is the power generated, $T$ is the thrust experienced by the rotor ρ is the water density, $A$ is the rotor area and, $U_0$ is the rotor-area-averaged flow velocity. Before calculating the spatial averaged $\overline{U_0^3}$ and $\overline{U_0^2}$, each single point measurement $U$ needs to be calculated using equation **(1)**. For calculating $\overline{U_0^3}$ and $\overline{U_0^2}$, it is important to emphasise that each point measurement in the rotor area is cubed or squared before time averaging and then averaged over the nine measured points. This allows a more realistic representation of the flow as this method takes into account the dynamic nature of the flow and also gives a true RMS value as presented by Blackmore et al. (2016).

In Fig. 13 the $C_T$ curves for flow at the three different yaw angles and without waves are presented against the TSR. Markers are the experimental data and the dashed lines show a quadratic fit. It is possible to note a decreasing trend that goes with the increasing yaw angle. The shadings in the background show the uncertainty bounds associated with standard deviation. The standard deviation is defined as the variation of the measurements from their mean and it is the square root of the variance.

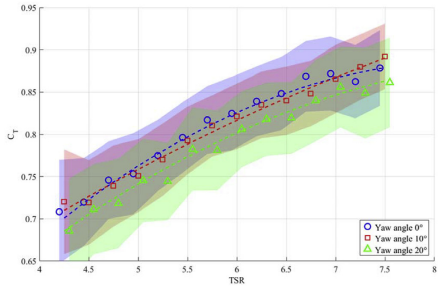


**Fig. 13.** Variation of $C_T$ with TSR, for three yaw angles. No waves. The standard deviation associated with each yaw is shown using shading with the same colour as the data markers. (For interpretation of the references to colour in this figure legend, the reader is referred to the Web version of this article.)

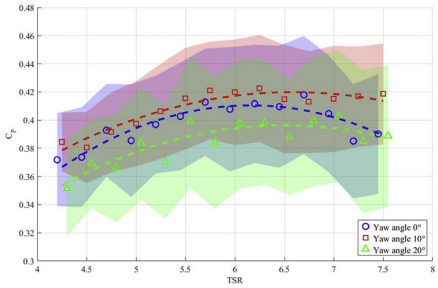


**Fig. 14.** Variation of $C_P$ with TSR, for three yaw angles. No waves. The standard deviation associated with each curve is shown using shading with the same colour as the data markers. (For interpretation of the references to colour in this figure legend, the reader is referred to the Web version of this article.)

Fig. 14 shows the $C_P$ variation with TSR for the same tests covering three yaw angles, without waves. Again, quadratic fits have been done to try to assist in the visual interpretation of the data. In this case, the curves do not follow the same intuitive variation with yaw that was followed by $C_T$. The red $-10^\circ$ yaw angle curve has a higher $C_P$ while the $-20^\circ$ curve shows a considerably lower curve, with the 0° yaw curve lying between. This phenomenon was also observed by Frost (2016) but has not yet been satisfactorily explained. It could possibly be due to the significant variation in onset flow velocity observed over the rotor disc (see section 3.2). The flow characterisation used for the $C_T$ and $C_P$ calculations rely on only nine points. It is thought that using denser velocity mapping across the rotor area could yield different results.

It can be noticed that both $C_P$ and $C_T$ have very high standard deviation which arises from the high turbulence intensities and velocity variability across the rotor area.

Now introducing waves: Fig. 15 shows $C_T$ and $C_P$ for different flow yaw angle and for waves at 0°. The turbine TSR is 7 at nominal flow speed $\boldsymbol{U} = 0.8$ m/s. In this case the coefficients were calculated using rotor averaged $\boldsymbol{U_o}$ without waves. This approach helped identify the influence of the waves in the coefficients. It is possible to see the same trend in $C_P$ as seen in Fig. 14 where the curve for the $-10^\circ$ flow case is higher than 0° curve. For $C_T$, similarly to Fig. 14, both 0° and $-10^\circ$ are very close to each other when waves are present. It is also worth noting how both 0° and $-10^\circ$ decrease as the wave period increases but the $-20^\circ$ flow case behaves the opposite way.

In Fig. 16, $C_P$ and $C_T$ curves for three flow angles with no waves and waves with T = 2.0 s at 0°, 45° and 315° are presented. For all, TSR = 7 and the flow speed is 0.8 m/s. As for Fig. 15, the coefficients were calculated using rotor averaged $\boldsymbol{U_o}$ without waves. Again, it is the cases at 0° and $-10^\circ$ which show similar behaviour. The $-20^\circ$ case follows the other two flow angles, contrary to Fig. 15. Here, comparing the same wave shows that as the waves' incidence angle increases, the coefficients decrease.

Plotted against frequency normalised by rotational frequency $f_o$, the $C_T$ frequency spectra at TSR 7 and $\boldsymbol{U_o} = 0.8$ m/s (Fig. 17) where several noticeable peaks can be observed. The $-20^\circ$ yawed flow was chosen to keep consistency with the other cases presented in this work, to see how big of an impact the most oblique flow has on the turbine. Following the spectra from left to right, the first large peak is associated with the wave frequency. The next peak at exactly $3f/f_o$ is the frequency with the passage of the three blades. Further harmonics of this at exactly 6, 9 and 12 $f/f_o$ are clearly identifiable, each with successively smaller amplitudes. The peak at 16 $f/f_o$ is believed to be caused by a mechanical artefact. Indeed, tests carried out at the same rotational speed but with the turbine outside the water ('dry test') show the same peak.

Fig. 18 shows a close up of the spectral peaks associated with the waves. The 45° and 315° peaks have similar amplitude which is consistent with them both being associated with wave conditions symmetrical with respect to the rotor axis. The peak at 0° shows the highest amplitude compared to the same wave at other angles. This is because the wave crest is parallel to the rotor plane. Therefore, the rotor experiences the whole force magnitude of the waves and not a component of this force.

Fig. 19 shows the $C_P$ spectra at TSR 7 and $\boldsymbol{U_o} = 0.8$ m/s against the normalized frequency $f/f_o$. In this case the wave frequency and blade frequency ($3f/f_o$) peaks can be seen. The $6f/f_o$ peak is not believed to be a harmonic of the blade frequency since it is higher than the $3f/f_o$ peak. The $6f/f_o$ peak as well as the 18 $f/f_o$ and the 26 $f/f_o$ peaks are also present in 'dry tests' and are therefore not thought to be associated with fluid-blade interactions.

The mean and SD values for all the tests performed with waves with period T = 2.0s, TSR = 7 and $\boldsymbol{U_o} = 0.8$ m/s are presented in Table 2. At all flow angles, cases B, F and J with waves at 0° show the highest means and standard deviations for both torque and thrust compared to all the other cases with the same wave at different angles. The high SD values mean that the waves aligned with the rotor have a higher impact

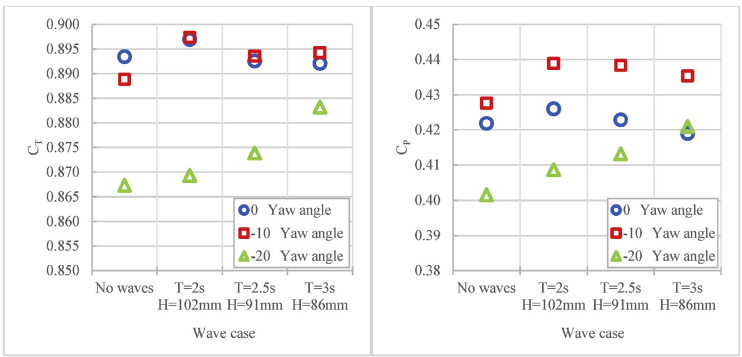


**Fig. 15.** $C_T$ and $C_P$ with all flow angles and all waves at 0° incidence.

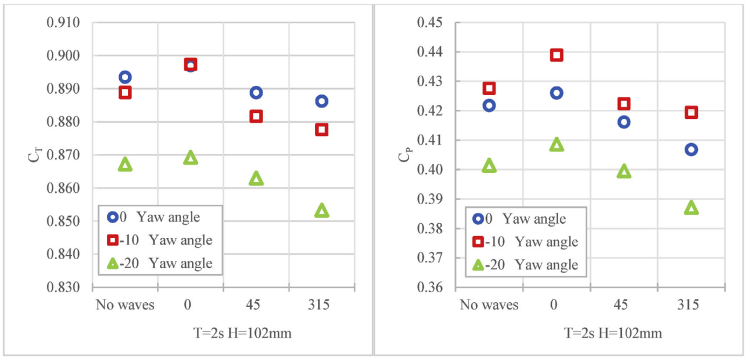


**Fig. 16.** $C_T$ and $C_P$ with flow at all angles and wave T = 2.0 s at all angles.

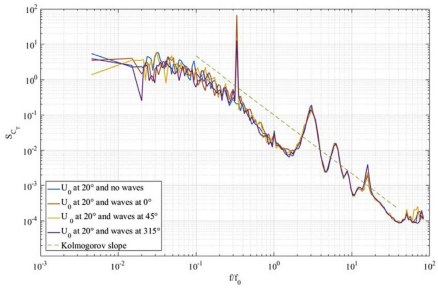


**Fig. 17.** $C_T$ spectra with flow at −20°, exploring influence of wave angle.

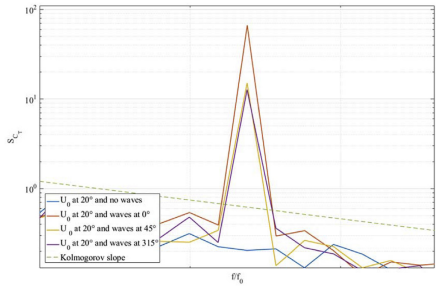


**Fig. 18.** Zoom of the peak of the $C_T$ spectra associated with the waves with period T = 2.0s.

on the load variability because the rotor experiences the whole magnitude of the waves' forces and not a smaller component when the waves have an angle relative to the turbines axis. This will affect the fatigue loads directly. Cases D, H and L with waves at 315° show the lowest mean values for both torque and thrust. The difference between the values at 45° and the 315° cases is due to the relative angle between the flow and the wave. At 315° both have a NE direction while in the

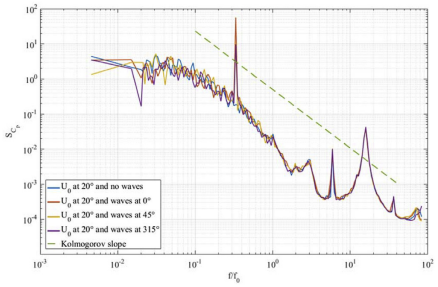


**Fig. 19.** $C_P$ spectra with flow at −20°, exploring influence of wave angle.

45° case, the flow goes NE while the waves are moving NW. At all the flow angles, the cases with no waves have the lowest SD values for torque and thrust. The cases A, E and I with no waves show the lowest SD values.

Fig. 20 shows time series of wave elevation and rotor thrust for a test with nominal velocity $\boldsymbol{U}$ = 0.8 m/s, yaw angle −20°; waves T = 2.0s, H = 102 mm and wave angle 45°. It is possible to see how the low frequency component of the thrust signal follows the quasi period of the wave gauges, highlighting the influence of the wave on the thrust forces. The two wave gauges are slightly out of phase due to the angle of 45° at which the waves are generated. Looking at Fig. 11, it can be seen that when waves come at an angle other than perpendicular to the rotor plane, one of the wave gauges will 'sense' the wave sooner than the other wave gauge, giving a phase difference.

### 4.4. Discussion

The data presented in this section, proved to be of great use despite the faults with the root bending moment sensors and the high variability in the flow that accounted for such high SD on $C_T$ and $C_P$. These values were expected after the non-uniformity presented on Section 3.

Turbine testing allowed to understand the impact of waves and current at different angles on the loadings and performance of the turbine. It is the standard deviation values of the torque and thrust that are highly affected by them. With flow at −20° and waves at 315° the torque has the lowest mean values. Flow at 0° with no waves has the

**Table 2**
Means and standard deviation of torque and thrust for all flow angles at **U** = 0.8 m/s and T = 2.0s waves at all angles. TSR = 7.

| Line | Current | | Waves | | | Torque [Nm] | SD Torque [Nm] | Thrust [N] | SD Thrust [N] |
|---|---|---|---|---|---|---|---|---|---|
| | $U_0$ [m/s] | Angle | Period T [s] | Height H [mm] | Angle | | | | |
| A | 0.78 | 0° | – | – | – | 13.2 | 1.29 | 326 | 15.9 |
| B | 0.77 | 0° | 2.0 | 102 | 0° | 13.3 | 2.32 | 327 | 27.2 |
| C | 0.77 | 0° | 2.0 | 102 | 45° | 13.0 | 1.68 | 324 | 20.0 |
| D | 0.78 | 0° | 2.0 | 102 | 315° | 12.7 | 1.83 | 323 | 22.1 |
| E | 0.81 | −10° | – | – | – | 14.6 | 1.24 | 343 | 15.1 |
| F | 0.81 | −10° | 2.0 | 102 | 0° | 15.0 | 2.52 | 347 | 28.8 |
| G | 0.80 | −10° | 2.0 | 102 | 45° | 14.4 | 1.62 | 341 | 19.2 |
| H | 0.80 | −10° | 2.0 | 102 | 315° | 14.3 | 1.91 | 339 | 22.1 |
| I | 0.77 | −20° | – | – | – | 13.2 | 1.60 | 327 | 18.9 |
| J | 0.77 | −20° | 2.0 | 102 | 0° | 13.5 | 2.90 | 328 | 33.2 |
| K | 0.78 | −20° | 2.0 | 102 | 45° | 13.2 | 1.90 | 326 | 22.5 |
| L | 0.77 | −20° | 2.0 | 102 | 315° | 12.7 | 1.80 | 322 | 21.3 |

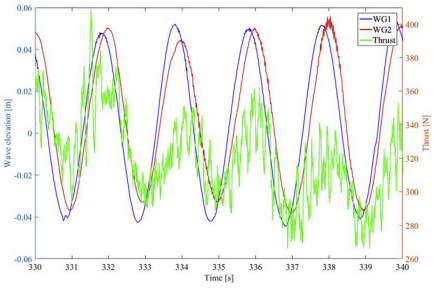


**Fig. 20.** Time series of both wave gauges (left y axis) and thrust (right y axis).

lowest SD values and any flow case with waves at 0° gave the highest means and SD. This tests reduce some of the uncertainties associated with the effect of the onset flow on a tidal stream turbine.

## 5. Conclusions

The work reported results from basin testing of a 1:15 scale horizontal axis tidal turbine in oblique currents and waves at FloWave. To the knowledge of the authors, the tests are the first of their kind.

The flow characterisation for the current only cases showed some flow velocity spatial variation across the rotor area. It was decided to use all the measurement points taken within the rotor area to give a better representation of the flow. The case with flow at −10° yaw had the highest $C_P$ values, followed by 0° and −20°. Similar findings are reported by Frost (2016). This counterintuitive trend could be related to the significant velocity variations in the onset flow. The velocity value used in the computation of $C_P$ and $C_T$ are based on the nine measurement points across the rotor but a higher number of points within the rotor area would yield a more accurate representation of the onset flow which could have consequences on power coefficient values. These results show the importance of onset flow characterisation for turbine performance assessment.

The $C_T$ at −10° showed the expected trend where the thrust coefficient decreases with flow angle.

The presence of waves, especially at 0° incidence to the turbine axis, leads to SD values for torque and thrust which are almost double those associated with current only. This would have a detrimental impact for fatigue loading. The mean values of the torque and thrust are however, hardly affect by waves compared to current only conditions.

Unlike the flow with yaw angles of 0° and −10°, −20° yawed current in combination with waves at 0° show an increase in the $C_T$ and $C_P$ with wave period. Once again, this trend should be treated with caution given the importance and uncertainties associated with the onset flow velocity used in the power and thrust coefficients calculations.

In the frequency analysis, the peaks in $S_{C_T}$ and $S_{C_P}$ associated with waves at 45° and 315° have similar magnitude which is consistent with the fact that these two wave directions are symmetrical with respect to the rotor axis. The peaks associated with the waves at 0° have the highest magnitude compared to all the other wave angles. The peaks associated with waves at 135° have the lowest magnitude.

The different parameters used to test the turbine covered a wide range of cases which could be found in the ocean and which, to the authors' knowledge, had not been tested at scale previously.

The findings presented herein provide original and important elements for considerations in the design process of tidal turbine. The spectral analysis of loads could be a key input for turbine components design and specifications. With a better understanding of the frequency distribution of loads, safety factors could be reduced and the turbine structure can be designed to ensure that no vibration mode corresponds to significant load frequencies.

## Acknowledgments

The first author would like to acknowledge the financial support of Consejo Nacional de Ciencia y Tecnología (CONACYT). The authors would like to thank the FloWave staff, Jeff Steynor, Tom Davey and Martin Lennon, for their help with the testing. This work would not have been possible without the funding from the EPSRC via the Marine Challenge grant EP/J010235/1 (X-MED) for the development of the turbine model. The experimental data used to create the plots can be downloaded from http://dx.doi.org/10.7488/ds/2360.

## References

Bahaj, A.S., Molland, A.F., Chaplin, J.R., Batten, W.M.J., 2007. Power and thrust measurements of marine current turbines under various hydrodynamic flow conditions in a cavitation tunnel and a towing tank. Renew. Energy 32 (3), 407–426. http://dx.doi.org/10.1016/j.renene.2006.01.012. Elsevier.

Blackmore, T., Myers, L.E., Bahaj, A.S., 2016. Effects of turbulence on tidal turbines: implications to performance, blade loads, and condition monitoring. Int. J. Mar. Energy 14, 1–26. http://dx.doi.org/10.1016/j.ijome.2016.04.017. Elsevier Ltd.

Department of Energy and Climate Change, 2013. Electricity Generation Costs. doi: 267393///1/1 25 May 2010.

Easton, M.C., 2013. An Assessment of Tidal Energy and the Environmental Response to Extraction at a Site in the Pentland Firth. University of Aberdeen.

Evans, P.S., 2014. Hydrodynamic Characteristics of Macrotidal Straits and Implications for Tidal Stream Turbine Deployment. PhD thesis. Cardiff University, Cardiff, UK.

Frost, C.H., 2016. Flow Direction Effects on Tidal Stream Turbines. PhD thesis. Cardiff University, Cardiff, UK.

Gaurier, B., Davies, P., Deuff, A., Germain, G., 2013. Flume tank characterization of marine current turbine blade behaviour under current and wave loading. Renew.

Energy 59, 1–12. http://dx.doi.org/10.1016/j.renene.2013.02.026. Elsevier.
Harding, S., Payne, G.S., Bryden, I., 2014. Generating controllable velocity fluctuations using twin oscillating hydrofoils : experimental validation. J. Fluid Mech. 750, 113–123. http://dx.doi.org/10.1017/jfm.2014.257. Cambridge University Press.
de Jesus Henriques, T.A., Tedds, S.C., Botsari, A., Najafian, G., Hedges, T.S., Sutcliffe, C.J., Owen, I., Poole, R.J., 2014. The effects of wave-current interaction on the performance of a model horizontal axis tidal turbine. International Journal of Marine Energy 8 (December 2014), 17–35. http://dx.doi.org/10.1016/j.ijome.2014.10.002. Elsevier Ltd.
Luznik, L., Flack, K.A., Lust, E.E., Taylor, K., 2013. The effect of surface waves on the performance characteristics of a model tidal turbine. Renew. Energy 58, 108–114. http://dx.doi.org/10.1016/j.renene.2013.02.022. Elsevier.
Martinez, R., Payne, G.S., Bruce, T., 2017. Preliminary results on the effects of oblique current and waves on the loadings and performance of tidal turbines. In: Proceedings of the 12th European Wave and Tidal Energy Conference. Cork, Ireland, pp. 1–8.
McNaughton, J., Harper, S., Sinclair, R., Sellar, B.G., 2015. Measuring and modelling the power curve of a commercial-scale tidal turbine. In: Proceedings of the 11th European Wave and Tidal Energy Conference, pp. 1–9.
Mycek, P., Gaurier, B., Germain, G., Pinon, G., Rivoalen, E., 2014. Experimental study of the turbulence intensity effects on marine current turbines behaviour. Part I: one single turbine. Renew. Energy 66, 729–746. http://dx.doi.org/10.1016/j.renene.2013.12.036. Elsevier Ltd.
Noble, D.R., Davey, T.A.D., Smith, H.C.M., Kaklis, P., Robinson, A., Bruce, T., 2015. Spatial variation in currents generated in the FloWave ocean energy research facility. In: Proceedings of the 11th European Wave and Tidal Energy Conference, pp. 1–8.
Payne, G.S., Stallard, T.J., Martinez, R., 2017. Design and manufacture of a bed supported tidal turbine model for blade and shaft load measurement in turbulent flow and waves. Renew. Energy 107, 312–326. http://dx.doi.org/10.1016/j.renene.2017.01.068. Elsevier.
Robinson, A., Ingram, D.M., Bryden, I., Bruce, T., 2015. The generation of 3D flows in a combined current and wave tank. Ocean Eng. 93, 1–10. http://dx.doi.org/10.1016/j.oceaneng.2014.10.008. Elsevier.
Sutherland, D.R.J., Noble, D.R., Steynor, J., Davey, T.A.D., Bruce, T., 2017. Characterisation of current and turbulence in the FloWave ocean energy research facility. Ocean Eng. 139 (2), 103–115. http://dx.doi.org/10.1016/j.oceaneng.2017.02.028. Elsevier.
The Scottish Government, 2013. 2020 Routemap for Renewable Energy in Scotland - Update. Edinburgh. Available at: http://www.gov.scot/Resource/0044/00441628.pdf.
Thorpe, S.A., 2007. An Introduction to Ocean Turbulence, an Introduction to Ocean Turbulence. Cambridge University Press, Cambridge. http://dx.doi.org/10.1017/CBO9780511801198.

# Journal publications as contributing author

Journal of Fluids and Structures 83 (2018) 156–170

Contents lists available at ScienceDirect

Journal of Fluids and Structures

journal homepage: www.elsevier.com/locate/jfs

# Variation of loads on a three-bladed horizontal axis tidal turbine with frequency and blade position

Grégory S. Payne [a,*], Tim Stallard [b], Rodrigo Martinez [c], Tom Bruce [c]

[a] Department of Naval Architecture, Ocean & Marine Engineering, University of Strathclyde, Glasgow G4 0LZ, UK
[b] School of Mechanical, Aerospace and Civil Engineering, University of Manchester, Manchester M13 9PL, UK
[c] Institute for Energy Systems, School of Engineering, University of Edinburgh, King's Buildings, Mayfield Road, Edinburgh EH9 3FB, UK

ARTICLE INFO

*Article history:*
Received 10 October 2017
Received in revised form 17 August 2018
Accepted 22 August 2018
Available online 18 September 2018

*Keywords:*
Tidal turbine
Frequency analysis
Loads
Physical experiment

ABSTRACT

Sustainable and cost effective design for tidal current turbines requires knowledge of the complex nature of unsteady loads on turbine components including blades, rotor and support structure. This study investigates experimentally the variation with frequency of rotor thrust and torque loads, of streamwise root bending moment on individual blades and of loads on foundation at the bed. Comparisons between these different load spectra are also established. The impact of absolute rotor angular position on blade and rotor thrust loads is also examined. The study is based on measurements from a 1/15 scale, three-bladed, horizontal axis machine tested in a recirculating flume, in onset flows of 3% and 12% turbulence intensity. It is found that for frequencies below the rotational frequency, load spectra are correlated to spectral density of the onset flow velocity. Above the rotational frequency, loads are mainly affected by turbine operation phenomena. The tower shadowing effect is clearly identified through frequency and angular analysis. Finally, thrust loads as experienced by the rotor alone are for the first time compared with streamwise and transverse foundation loads. Higher frequency loads experienced by the tower are shown to be affected by different vortex shedding regimes associated with different regions of the wake. All the experimental measurements presented in this article can be accessed from http://dx.doi.org/10.7488/ds/2423.


## 1. Introduction

Systems for generation of electricity from tidal streams have attracted increasing interest in recent decades. Although a variety of design concepts have been developed, the most widely studied systems are horizontal axis turbines, similar in configuration to wind turbines. Several developers have now deployed such turbines at full-scale test sites (Parkinson and Collier, 2016; MayGen Ltd., 2016). However, there remain challenges for design, particularly with regard to accurate prediction of the unsteady loads that determine component specification for adequate operational life. For the similar case of a wind turbine, unsteady loading on blades, and hence on the turbine, is due to the rotation of the blades through a non-uniform onset flow and in proximity to a fixed support structure. Onset turbulence also play a role in the unsteady loading. The influence of these factors on wind turbine design have received attention through experimental studies such as the MEXICO campaign (Schepers et al., 2014) and CFD analysis, particularly suited to complex onset flows (Thé and Yu, 2017; Storey et al., 2016). Such studies have informed development of engineering tools for prediction of the time-varying loads and component load spectra (Moriarty and Hansen, 2005; Smilden et al., 2016) that are required for fatigue design.

* Corresponding author.
*E-mail address:* gregory.payne@strath.ac.uk (G.S. Payne).

https://doi.org/10.1016/j.jfluidstructs.2018.08.010

Similar information is required for tidal stream turbines for which the operating environment comprises a depth constrained turbulent flow, potentially with free surface waves, and for which the supporting structure is typically much larger, relative to the turbine, than for wind turbines. Experimental datasets provide a crucial basis for development of understanding of the processes contributing to component loading and for validation of numerical models. Tidal turbine loading and performance have been analysed for three-bladed horizontal axis turbine models of various diameter, (Bahaj et al., 2007a; Kolekar and Banerjee, 2015; Gaurier et al., 2015; Payne et al., 2017a). Several studies have also addressed unsteady loading of rotors or turbines due to waves, in towing tanks (Lust et al., 2013; Luznik et al., 2013; Galloway et al., 2014; Doman et al., 2015) and in flumes and tanks (Gaurier et al., 2013; de Jesus Henriques et al., 2014; Fernandez-Rodriguez et al., 2014; Martinez et al., 2017). The impact of turbulences on turbine performance and loading has also been explored (Chamorro et al., 2013; Mycek et al., 2014; Fernandez-Rodriguez et al., 2014; Milne et al., 2016; Blackmore et al., 2016). Durán Medina et al. (2017) carried out an in-depth analysis of the correlations between onset flow velocity and turbine power production based on spectral methods, empirical mode decomposition and time-dependent intrinsic correlation. However, there has, to-date, been limited in-depth analysis of the frequency variation of loading of horizontal axis tidal turbine blades and the turbine supporting structure. This work analyses the relationship between the frequency variation of principal components of loading of a horizontal axis tidal stream turbine focusing on streamwise blade loading, thrust and power developed by the three-bladed rotor, and the streamwise and transverse loading on the entire turbine assembly comprising rotor, nacelle and tower.

The experimental approach and flow conditions studied are summarised in Section 2, variation of rotor and blade loading are investigated in Section 3 and factors leading to unsteady loading of the support structure are analysed in Section 4. Conclusions are provided in Section 5.

## 2. Experimental apparatus and considerations

### 2.1. Turbine model

The experimental turbine model used was a bed mounted three-bladed horizontal axis machine with a rotor diameter $D = 1200$ mm. The blade design was developed to produce a radial variation of the rotor thrust coefficient at a specific tip speed ratio similar to that of a full scale generic turbine (Stallard et al., 2015). The idea behind this approach is that highest rotor loads and wakes are phenomena which are predominantly affected by the thrust characteristics of turbines. The turbine model was developed to integrate a high level of instrumentation in order to measure the following quantities:

- streamwise root bending moment for each blade
- rotor torque
- rotor thrust
- rotor absolute angular position

A detailed description of the experimental model, of its design and manufacture can be found in Payne et al. (2017a) and a section view of the model is reproduced in Fig. 1.

A primary consideration for the model design was to maximise quality of load measurements. This approach was implemented by locating the sensors as close as possible to where the loads they are measuring are applied. When considering the load path, the sensors are located 'upstream' of the shaft rotary seals so that their associated parasitic friction does not affect the load measurements. As a consequence, these sensors are in a wet environment and so were designed to be waterproof. The turbine generator was simulated by a brushless servo motor controlled in speed.

The turbine model was installed so that the rotor axis was located at mid-depth (1 m deep). The bottom of the turbine tower was mounted to a fixed mooring structure via a six-axis load cell of the type TYPR FX2.6 manufactured by the company SIXAXES.

Signal from all turbine sensors (including the six-axis foundation load cell) were synchronously sampled at 256 Hz. Sample measurement time series can be found in Payne et al. (2017a).

### 2.2. Testing facility

The study was conducted in the flow recirculating facility of IFREMER in Boulogne-sur-Mer, France shown on Fig. 2(a). The flow channel is 4 m wide, has a useable length of 18 m and was operated at 2 m depth (Germain, 2008). The blockage ratio, taking into account the rotor, the tower and support structure is 0.2. The inlet of the flume is fitted with removable flow conditioning units (see Fig. 2(b)) which produced two levels of streamwise turbulence intensity $TI_u$: 3% with the flow conditioning units and 12% without. $TI_u$ is defined by:

$$TI_u = 100\frac{\sigma(u)}{\overline{u}} \tag{1}$$

where $\sigma(u)$ is the standard deviation of the streamwise velocity component $u$ and $\overline{u}$ is the mean of $u$.

The facility is equipped with a two-component fibre optical laser Doppler anemometry (LDA) system consisting of a FiberFlow transmitter and manipulators made by Dantec and of two Genesis MX SLM series lasers produced by Coherent,

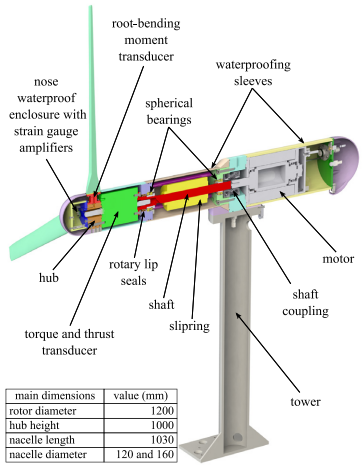


| main dimensions | value (mm) |
|---|---|
| rotor diameter | 1200 |
| hub height | 1000 |
| nacelle length | 1030 |
| nacelle diameter | 120 and 160 |

**Fig. 1.** CAD section view of the experimental turbine model.

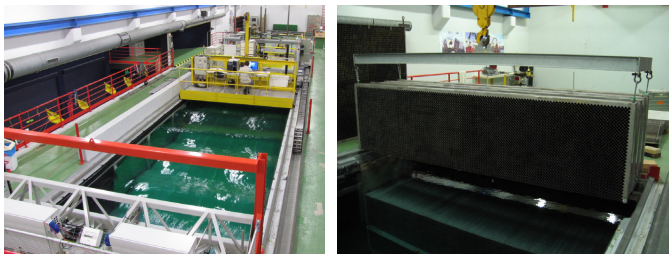

(a) (b)

**Fig. 2.** IFREMER recirculating flow and wave facility 2(a) and its removable inlet flow conditioning screen 2(b).
*Source:* (images courtesy of IFREMER).

one green (514 nm wavelength) and the other blue (488 nm wavelength). The LDA probe is mounted on a motorised gantry allowing automated movement in the vertical and cross flow directions.

Measurements were taken at turbine hub location in the absence of the turbine. The streamwise mean velocity was 0.814 m s$^{-1}$ for $TI_u = 3\%$ and 0.819 m s$^{-1}$ for $TI_u = 12\%$. With LDA, the sampling frequency is not constant as measurements take place each time a seeding particle passes through the measurement volume. It is also different for the two velocity components measured. The mean sampling frequency for the high and low turbulence conditions were 283 and 941 Hz respectively in the streamwise direction and 71 and 258 Hz respectively in the transverse direction. The sampling durations were 256 and 200 s for the high and low turbulence conditions respectively. In order to carry out spectral analyses of flow velocities, the LDA timeseries are first re-sampled at a constant frequency corresponding to the mean sampling frequency of the timeseries. The re-sampling is applied using linear interpolation and alternative sampling frequencies were tested to ensure that the chosen frequency was sufficient to resolve the frequency range shown. Alternative methods to compute periodigrams without re-sampling, such as the Empirical Mode Decomposition-Hilbert Spectral Analysis lead to comparable results, as shown by Durán Medina et al. (2017) for the Empirical Mode Decomposition-Hilbert Spectral Analysis method. The spectral density of the velocity fluctuations with respect to the mean is shown in Fig. 3 for streamwise ($u'$) and transverse ($v'$) fluctuations for the two $TI_u$ levels. The spectral densities are normalised by $\overline{u}^2$. The spectral density curves shown were

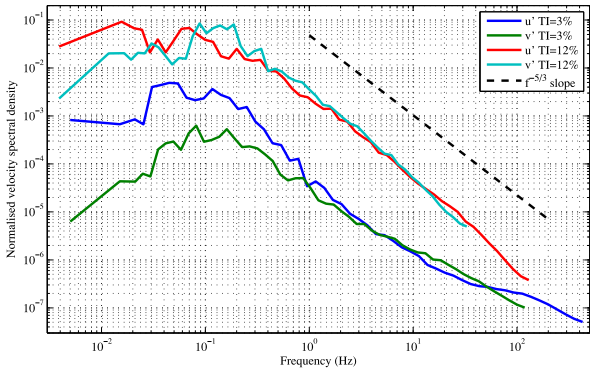


**Fig. 3.** Normalised velocity spectral density in the streamwise ($u'$) and transverse ($v'$) direction for $TI = 3$ and 12%.
*Source:* ($TI = 3\%$ data are courtesy of IFREMER).

obtained by averaging components over bins whose frequency widths are evenly distributed on a log scale. This means that high frequency bins contain a wider frequency range than low frequency bins which leads to curves being smoother toward higher frequencies. This processing was applied to all spectral density plots in this article. As expected, there is higher turbulent kinematic energy density across the frequency range for the flow with higher turbulence intensity. For $TI_u = 12\%$, $u'$ and $v'$ spectra are relatively close, implying isotropic turbulence. However, for $TI_u = 3\%$, the flow is anisotropic with $u'/v' > 1$ for frequencies below 2 Hz and this ratio increases with decreasing frequency. This difference is due to the fact that for the low TI conditions, the flow enters the test section of the flume through a honeycomb structure (shown in Fig. 2(b)). This constrains the flow in the cross-flow direction, hence limiting variance of transverse fluctuations. In the inertial sub-range (at frequencies roughly above 1 Hz here) it can be seen that all curves have a slope which broadly follows the Kolmogorov minus five thirds power law. However towards the higher frequencies, $u'$ at low TI departs significantly from that slope. This can be attributed to the anisotropy of the flow which implies that the Kolmogorov dissipation scale no longer fully applies (see Durán Medina et al. (2015) and Thorpe (2007)).

### 2.3. Reynolds and Froude numbers

The chord based Reynolds number associated with the blade profile at radius $r$ is defined as follows:

$$Re_c(r) = \frac{\rho \cdot \lambda \cdot r \cdot \overline{u} \cdot c(r)}{\mu \cdot R} \tag{2}$$

where $\rho$ is the water density, $\lambda$ is the tip speed ratio (TSR), $R$ is the rotor radius, $c(r)$ the blade chord length at radius $r$ and $\mu$ the dynamic viscosity of water. For $r/R \geqslant 0.2$, $c(r)$ varies little with $r$ compared with $r/R$ (see table 2 of Payne et al. (2017a)). From (2) $Re_c(r)$ can therefore be assumed to be a linear function of $r$ for $r/R \geqslant 0.2$. For the experiments reported herein where TSR ranges from 4.5–7 and for $r/R \geqslant 0.2$, $49\,000 \leqslant Re_c \leqslant 252\,000$.

The rotor diameter based Reynolds number is given by:

$$Re_D = \frac{\rho \cdot \overline{u} \cdot 2R}{\mu} \tag{3}$$

$Re_D = 975\,000$ throughout this article.

The Froude number of the test channel is defined by:

$$Fr = \frac{\overline{u}}{\sqrt{gh}} \tag{4}$$

where $g$ is the gravitational acceleration and $h$ the channel water depth. For the experiments reported in this article, $Fr = 0.18$.

### 2.4. Root bending moment sensor quality check

Each blade was mounted to the hub through a root bending moment sensor. More details on the sensor design and calibration can be found in Payne et al. (2017a). As noted previously by the authors, the sensors developed a slow drift

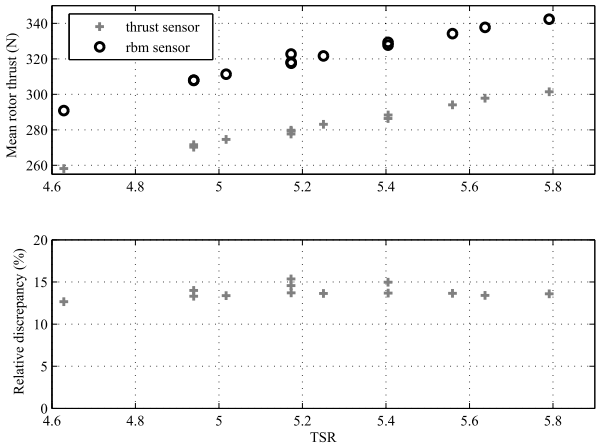


**Fig. 4.** Comparison between mean rotor thrust measured with the torque and thrust transducer and inferred from the blade root bending moment (rbm) sensors (top graph). The bottom graph shows the corresponding relative discrepancy with respect to the torque and thrust transducer measurements. Measurements were carried out over a range of tip speed ratios with an onset flow velocity of 0.814 $m \cdot s^{-1}$ and a $TI_u = 3\%$.

fault during the initial test programme. That drift progressed slowly, so providing that the signal remained within the saturation limits of the amplifier and that the sensors were 'zeroed' several times per day, measurements were deemed to be accurate within the 5% band established through calibration, especially for investigating the fluctuating component of the load. For time series which met this quality criteria, agreement between the streamwise force on the rotor inferred from the root bending sensor and the rotor thrust measured directly at the shaft was checked. The root bending moment sensors measure bending moment on the blades in the streamwise direction. The corresponding streamwise force on the blade is a function of the radial position of the centroid of the streamwise load on the blades. This 'lever arm' distance cannot be measured experimentally and was instead estimated with a blade element moment (BEM) theory model. The BEM tool is as described in Hansen (2008), with Spera high axial induction factor correction. The lever arm distance obtained by this method (see Payne et al. (2017a)) varies only by 2.3% over the tip speed ratio (TSR) range 4.5 to 6.0 and a constant value of 330 mm was therefore used to infer the mean streamwise force on the blade from the mean of the root bending moment signal. Comparison is shown in Fig. 4 for tests at $TI_u = 3\%$. The discrepancy varies little (between 13 and 15%) over the TSR range and can therefore be considered as consistent. The discrepancy itself is not surprising and can be attributed to the following factors.

- The lever arm distance is computed using a standard BEM approach which does not account for the blockage factor (20%), onset flow profile or flow turbulence, which are all present in the physical experiment.
- Due to space restrictions, the geometry of the flexure of the root bending moment sensors was that of a beam. Flexure deflection is mainly driven by bending moment but the sensor is also, to a lesser degree, affected by shear force to the extent that calibration exhibited a maximum error of 5% (Payne et al., 2017a).

## 3. Rotor loads

The rotor loads are partly analysed using the standard thrust and power coefficients which are defined respectively by:

$$C_T = \frac{T}{\frac{1}{2} \cdot \rho \cdot A_r \cdot \overline{u}^2} \quad \text{and} \quad C_P = \frac{Q \cdot \overline{\omega}}{\frac{1}{2} \cdot \rho \cdot A_r \cdot \overline{u}^3} \tag{5}$$

where $T$ is the rotor thrust, $Q$ its torque, $\overline{\omega}$ its averaged rotational speed and $A_r$ the rotor area.

### 3.1. Angular dependency

In order to investigate the impact of the absolute angular position of the rotor on its thrust loads, measurements from sensors are binned into 360 angular sectors (each 1° wide) based on the rotor absolute angular position at the time of

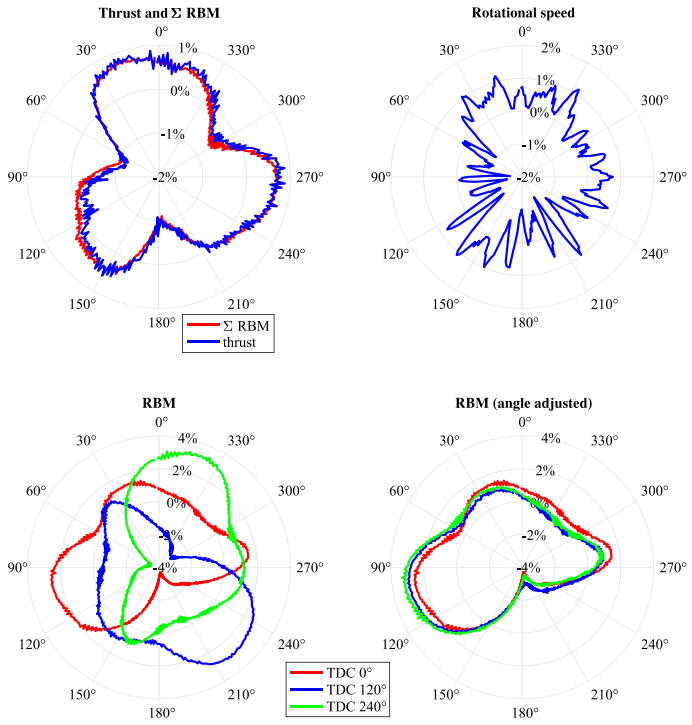


**Fig. 5.** 'phase-averaged' rotor loads and rotational velocity variations (in %) plotted against rotor absolute angular position. $\Sigma$ RBM corresponds to the sum of the measurements from the three root bending moment (RBM) sensors. The legend for the two bottom plots indicates the absolute angular position of the rotor when a given blade is at top dead centre (TDC). In the bottom right plot, the angular positions for two blades have been adjusted by 120° and 240° respectively to directly compare the azimuthal variation of the root bending moment on each blade. Measurements were carried out with an onset flow velocity of 0.814 m · s$^{-1}$, $TI_u = 3\%$ and TSR = 6.9.

the measurement. Values in each bin are then averaged to yield 'phase-averaged' measurements for each 1° sector of the rotor full revolution. Fig. 5 shows the relative variation (in percent) with respect to the mean of those 'phase-averaged' measurements plotted in polar coordinates.

Azimuthal variation of thrust is in close agreement with the sum of the three root bending moment signals (see top left frame) and this provides further confidence in the root bending moment quality control process of Section 2.4. The variations of the thrust (and $\Sigma$ RBM) curve are overall small (within a 2% range) but two clear patterns can be observed. The first pattern is exhibited by three distinct lobes about 120° apart, which is believed to be associated with the tower shadowing effect. The second pattern is a small distortion of the three lobe pattern with mainly the part of the lobe in the 60°–120° sector being slightly smaller than for the two other lobes. This pattern, which takes place once per revolution, is also observed in Fig. 8 of Section 3.2 on frequency analysis (peak A taking place at frequency $f_0$). This is correlated with the angular variation of the rotor rotational velocity (see top right frame) which indicates a lower speed in the 60°–120° region. Given that the onset flow velocity remains constant, this translates into a lower thrust as can be seen on the $C_T$ versus TSR curve shown in Fig. 6. This rotational velocity variation is believed to be due to either a mechanical artifact of the drive train or something to do with the motor speed control.

The two bottom frames show the variations in root bending moment experienced by each blade. It can be seen that the three curves are, as expected, similar and that when no angular position adjustment is applied (bottom left graph) they are 120° apart. Those two plots show very clearly the sharp dip in root bending moment associated with the tower shadowing effect. It can be seen that this minimum does not occur exactly when the blade passes the tower (180° on the bottom right plot) but that there is a lag of around 15°. Occurrence of this lag is consistent with observations from CFD

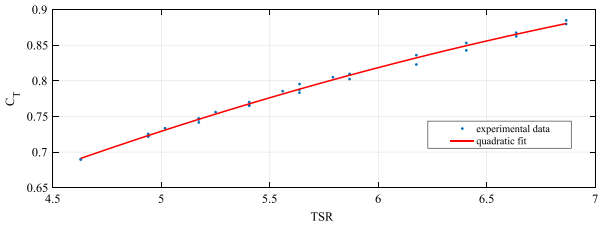


**Fig. 6.** $C_T$ versus TSR curve obtained by a quadratic fit on experimental data measured with an onset flow of 0.814 m s$^{-1}$ and TI = 3%.

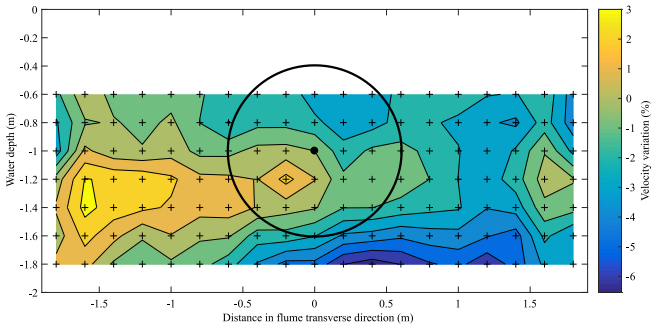


**Fig. 7.** Velocity variation map across the section of the flume at the location where the turbine was deployed but in the absence of the turbine. The velocity variations (in %) are calculated with respect to the hub velocity (0.814 m · s$^{-1}$) measured at the location indicated by the black dot. The circle corresponds to the location of the turbine rotor and the crosses are the measurement points.
*Source:* (raw velocity data courtesy of IFREMER).

studies (Mason-Jones et al., 2013), (McNaughton, 2013) and from measurements from full-scale prototype trials (Ahmed et al., 2017), although with some difference of magnitude between each case due to differences of turbine operating point and geometry, including position of tower relative to rotor plane. Beyond the tower shadowing effect, there are other significant variations in root bending moment over the full rotor revolution, especially in the transverse direction. To understand these better, it is useful to look at the variation in onset flow velocity over the flume cross section. Fig. 7 shows the variation of the streamwise velocity with respect to the hub velocity over the flume cross section where the turbine was deployed but in the absence of the turbine. The measurements do not quite cover the whole area of the rotor (indicated by the black circle) but a transverse asymmetry is clearly visible and consistent with the similar asymmetry in root bending moment loads observed in Fig. 5. The transverse asymmetry in the flow is due to the fact that it is generated by two impellers, located side by side in the bottom recirculation channel of the flume, which are both spinning in the same direction (see Germain (2008) for further detail on the flume layout). The flow conditioning units fitted to the flume reduced the transverse flow asymmetry to some extend but did not suppress it completely.

### 3.2. Thrust and torque loads frequency analysis

Frequency dependency of rotor loads are first investigated considering the spectral density of the thrust and power coefficients defined by Eq. (5). These spectral densities $S_{C_T}$ and $S_{C_P}$ are plotted in Figs. 8 and 9 for the two different turbulence intensity regimes and also for when the turbine is rotating under dry test conditions, in air. The spectra are plotted against frequency normalised by the rotor rotational frequency $f_0$. The rotor is spinning at 80 RPM, corresponding to TSR values of 6.14 and 6.18 for $TI_u = 3\%$ and $TI_u = 12\%$ respectively. The time series durations used to compute these spectral densities are 256, 128 and 3584 s for the dry test, the low and high turbulence conditions respectively. The normalised spectral density of the streamwise flow velocities of Fig. 3 are also shown.

For both turbulence intensity values studied, the general trend of the curves of thrust $S_{C_T}$ and power $S_{C_P}$ spectra are similar. For $f/f_0 < 1$ both curves (3% and 12% TI as green and red curves respectively) are approximately parallel to each other and

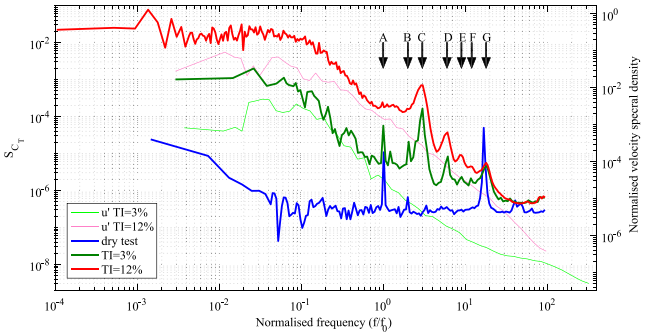


**Fig. 8.** Spectral densities of $C_T$ (thick lines, left hand side vertical axis) and normalised velocity spectral density (thin lines, right hand side vertical axis) plotted against frequency normalised by turbine rotational frequency $f_0$.

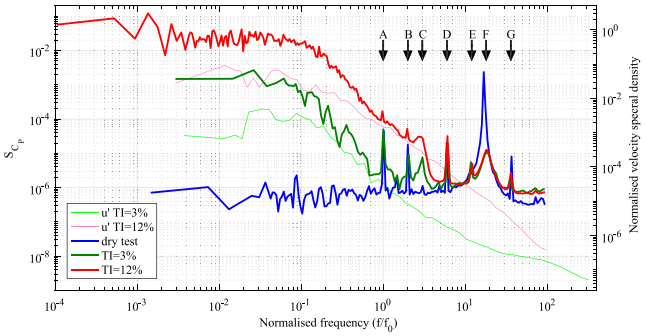


**Fig. 9.** Spectral densities of $C_P$ (thick lines, left hand side vertical axis) and normalised velocity spectral density (thin lines, right hand side vertical axis) plotted against frequency normalised by turbine rotational frequency $f_0$.

roughly in-line with the velocity spectral density for the same turbulence intensity. The slope of the thrust coefficient spectra is similar to that of the velocity spectra. However, the slope of the power coefficient spectra is steeper than that of the onset velocity spectral density in the inertial sub-range. A similar observation was also reported by Durán Medina et al. (2015) who suggest that this may be related to maintaining rotor velocity constant through speed control. Nevertheless, Figs. 8 and 9 show a clear correlation between the velocity fluctuation in the onset flow and the thrust and torque loads with the TI = 12% load curves consistently above their TI = 3% counterparts by about one order of magnitude. As the frequency increases ($f/f_0 > 1$) the load spectra converge and tend to a plateau at high frequency, departing from the trend of the velocity spectral density. This plateau is thought to be due to background noise associated with the sensors. This is corroborated by the fact that the level of the plateau is independent of the turbulence intensity of the flow.

Multiple specific peaks are observed in the $S_{C_T}$ spectra for both turbulence intensities. For the sake of convenience these have been labelled in Fig. 8. The highest peak for both curves is peak C, which takes place at three times the rotational frequency. This is due to the shadowing effect of the tower, taking place when each blade passes the tower i.e. three times per rotor revolution. Peaks D, E and F take place at $6f_0$, $9f_0$ and $12f_0$ respectively and their amplitude decreases with increased frequency indicating that they are harmonics of the $3f_0$ peak. Peak A, B and G take place respectively once, twice and 18 times per revolution and could not be explained by any obvious hydrodynamic phenomenon. It was therefore decided to investigate $S_{C_T}$ with the turbine model taken out of the flume ('dry test') which corresponds to the thick blue line in Fig. 8. The general trend of that curve is flat since there cannot be any correlation with onset flow velocity fluctuations and this is indicative of the flat, broad band noise floor inherent to the sensor. The $S_{C_T}$ values appear to increase at the lowest frequencies. This is believed to be due to noise in the spectral density whose computation for low frequencies involves no or only little averaging (as explained in Section 2.2). The curve exhibits two clear peaks (labelled A and G). Peak A occurs

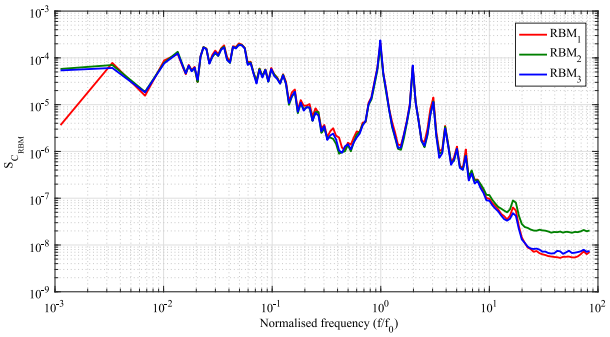


**Fig. 10.** Spectral density of $C_{RBM}$ for the three rotor blades plotted against frequency normalised by turbine rotational frequency $f_0$. The onset flow has a TI = 3% and the TSR = 6.9 (rotor speed: 89 rpm). The sampling duration is 600 s.

once per revolution and is attributed to a mechanical artifact of the turbine model drive train, e.g. a slight misalignment between the motor and turbine shafts or a slight imbalance in the rotor. It can be seen that this affects $S_{C_T}$ for TI = 3% and to a much lesser extent at TI = 12%. This makes sense as ambient level of load fluctuation is significantly higher for TI at 12% than at 3%. Peak B is lower than peak A and appears to be a harmonic of peak A. Peak G occurs at $18f_0$ and, as this is quite high for a mechanical artifact, this is thought to be either due to vibration induced by pole cogging in the motor or a function of the motor speed controller or possibly some electromagnetic interference. Irrespective of the phenomenon at play, it is an artifact of the turbine model itself and not of its interaction with the flow. However, it is evident that it is affecting the $S_{C_T}$ curves corresponding to the turbine in the flume on which peak G is clearly of higher magnitude than a harmonic of the lower frequency hydrodynamic forcing.

The analysis of the peaks in the $S_{C_T}$ curves of Fig. 8 broadly also applies to the $S_{C_P}$ curves of Fig. 9. However, peak C is of different magnitude and further peaks are observed (D, E and G). The peak associated with the tower shadowing effect (peak C) is less pronounced than for $S_{C_T}$ which can be explained by the fact that this phenomenon is mainly a streamwise wake effect and affects therefore more significantly rotor thrust than torque. The 'dry test' $S_{C_P}$ curve exhibits three extra peak (D, E and G) compared with its $S_{C_T}$ counterpart. The reason for peak D, which takes place at $6f_0$, is not fully understood but is obviously a 'dry' phenomenon associated with the turbine model. It nevertheless clearly affects $S_{C_P}$ when the turbine is in the flow. Peak E occurs at $12f_0$ and is believed to be a harmonic of peak D. Peak F takes place at $18f_0$ and corresponds to peak G in Fig. 8. Peak G (of Fig. 9) occurs at $36f_0$ and is believed to be a harmonic of peak F.

### 3.3. Frequency variation of blade root bending moment

As mentioned in Section 2.1, each turbine blade is fitted at its root with a sensor measuring fluctuation of bending moment due to the streamwise load (contributing to thrust) experienced by the blades. The root bending moment ($RBM$) signals are rendered dimensionless using a similar approach as for the thrust coefficient $C_T$ (see (5)):

$$C_{RBM} = \frac{RBM}{\frac{1}{3} \cdot D \cdot \left(\frac{1}{2} \cdot \rho \cdot A_r \cdot \overline{u}^2\right)} \tag{6}$$

where $D$ is the rotor diameter and the other symbols are the same as for Eq. (5). Fig. 10 shows the spectral densities of $C_{RBM}$ for each blade. It can be seen that the load spectra are nearly identical for all blades, except for small discrepancies at both ends of the frequency spectrum. At high frequency, the difference is likely to be due to slight mechanical and/or electronic inconsistencies of the $RBM_2$ sensor with respect to the two others, leading to a higher background noise level.

With the consistency in spectral density of the root bending moment established across all three blade sensors, the relationship between spectra of velocity, of blade loading and of rotor loading is now considered. Fig. 11 compares the spectra of $C_{RBM_1}$ (corresponding to blade 1 only) with that of $C_T$, with the normalised velocity spectral density of the onset flow ($u'$) and with the spectral density of $C_{\Sigma RBM}$ defined as follows:

$$C_{\Sigma RBM} = \frac{\sum_{i=1}^{3} RBM_i}{D \cdot \left(\frac{1}{2} \cdot \rho \cdot A_r \cdot \overline{u}^2\right)} \tag{7}$$

where suffix $i$ is the blade index. $\sum_{i=1}^{3} RBM_i$ corresponds to the summation of the three root bending moment time series. In other words, at each time step, the three root bending moments measured simultaneously for the three blades are added

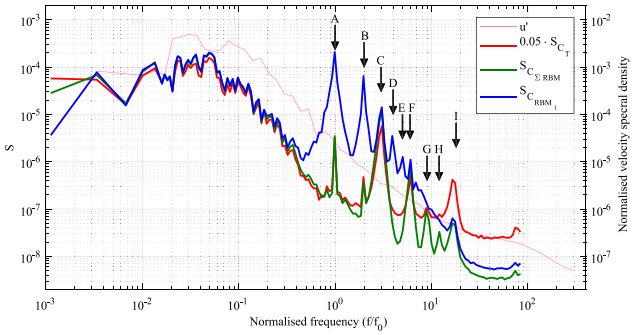


**Fig. 11.** Comparison between spectral densities of $C_{RBM_1}$, $C_T$ and $C_{\Sigma RBM}$. $S_{C_T}$ is multiplied by 0.05 to shift its curve vertically and facilitate comparison to the RBM curves. The normalised velocity spectral density of the onset flow $u'$ is also plotted on a different vertical scale (right axis). All quantities are plotted against frequency normalised by turbine rotational frequency $f_0$. The onset flow has a TI = 3% and the TSR = 6.9 (rotor speed: 89 rpm). The sampling duration is 600 s.

together. To facilitate visual comparison of the trend between the $C_T$ and RBM curves, the spectral density of $C_T$ is shown multiplied by 0.05. Curve peaks have also once again been labelled for convenience.

Over the low frequency range, both the $C_{RBM_1}$ and $C_{\Sigma RBM}$ curves follow the same trend as the velocity spectrum indicating that root bending moment loads are strongly correlated with turbulence of the onset flow. However, the spectrum associated with rotor loads ($C_{\Sigma RBM}$) is correlated with the onset flow to a higher frequency (for $f/f_0 \leqslant 1.5$ aside from a narrow spike at $f/f_0 \simeq 1$) than that of an individual blade (for $f/f_0 \leqslant 0.5$).

For $f/f_0 > 0.5$ the $C_{RBM_1}$ curve exhibits a series of sharp peaks (labelled A to F) of decreasing amplitude and whose frequencies correspond to $f/f_0 = 1, 2, 3, 4, 5$ and 6 respectively. Peak A is expected to be due to the tower shadowing effect which affects each blade once per rotor revolution. This has a similar amplitude to that of the low frequency turbulence induced loads. The frequencies and amplitudes of peaks B to F suggest that they are harmonics of peak A.

The main peak exhibited by the $C_{\Sigma RBM}$ curve is at $3f_0$ (peak C) corresponding to the tower shadowing effect on each blade once per revolution. Peaks F, G and H on that curve, taking place respectively at $6f_0$, $9f_0$ and $12f_0$ are harmonics of peak C. Peaks A, B and I of the $C_{\Sigma RBM}$ curve are not believed to be due to hydrodynamic phenomena but to mechanical and/or motor artifacts (see Fig. 8 and Section 3.2).

There is agreement between the spectra of thrust and of sum of root bending moment sensors over much of the frequency range (to about $3f_0$) but the RBM sensors have a lower noise floor and so capture greater detail on the frequency dependency to about $20f_0$. Over this range, the distinct three harmonics of peak C are observed (peaks F, G and H).

Fig. 12 compares the spectral density of $C_{RBM_1}$ for the two levels of onset flow turbulence intensity (3% and 12%) and also shows the normalised velocity spectral density of the corresponding onset flows. The vertical gap between the two $C_{RBM_1}$ curves is qualitatively consistent with that between the velocity spectral density curves. The frequency at which blade loading becomes uncorrelated with the onset flow spectrum is around $0.6f_0$. This is slightly higher than observed in Fig. 11 and this is likely to be due to the different operating point (see related discussion in Payne et al. (2017b), Chamorro et al. (2013)). It can be seen that for the flow with higher turbulence intensity, the peaks of the blade loading spectrum associated with the effects of the turbine structure are less pronounced. This is believed to be due to the higher level of turbulence induced loads which reduces the apparent amplitude of the peaks. Qualitatively, similar behaviour has been observed through CFD simulation with a time-varying turbulent onset velocity field imposed to represent similar magnitude of turbulence (Ahmed et al., 2017). For frequencies greater than the third harmonic of the tower shadowing effect, the slope of blade loading spectra is steeper than that of the corresponding velocity spectra. For TI = 3% this rapid decay is obscured by the narrow spike at $20f_0$ and by the sensor noise floor. However, for TI = 12% a similarly steep slope is observed over a wider frequency range before the sensor noise floor is reached, resulting in lower variance over frequencies greater than $20f_0$ than would be expected if loads were correlated with the onset velocity spectral density over this high frequency range.

## 4. Loads on support structure

To the authors' knowledge, in previously reported experimental investigation of horizontal axis tidal turbine, thrust loads were measured either at the level of the nacelle or at the base of the supporting structure. Typical examples of the former are (Bahaj et al., 2007b) and Milne et al. (2013) where the thrust sensor spins with the shaft and is located between the hub and the component simulating the generator. (Kolekar and Banerjee, 2015) employed a slightly different approach with a

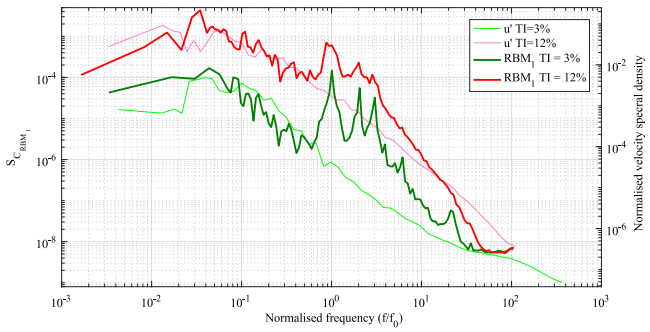


**Fig. 12.** Spectral densities of $C_{RBM_1}$ in onset flows of turbulence intensity of 3% and 12% for TSR = 5.4. The normalised velocity spectral densities of the onset flow $u'$ for both levels of turbulence are also plotted on a different vertical scale (right axis). All quantities are plotted against frequency normalised by turbine rotational frequency $f_0$. The sampling durations for the RBM measurements are 128 s and 256 s for the low and high turbulence intensity conditions respectively.

static thrust sensor located at the back of the nacelle, between the motor and the support structure. On the other hand Gaurier et al. (2015), de Jesus Henriques et al. (2014), Mason-Jones et al. (2012) and Stallard et al. (2015) estimate thrust loads using a load cell located above waterline on the supporting tower. The latter approach cannot isolate thrust on the rotor alone from loads on the nacelle and support structure as is pointed out in Gaurier et al. (2015). McTavish et al. (2014) adopted an interesting technique to mitigate this issue by enclosing the turbine tower (which is connected to the load cell) into a hollow tube held rigidly but not mechanically connected to the tower or the load cell. This way, the tower does not experience any drag. This method does not however suppress the contribution of the drag on the nacelle to the thrust measurements.

In this experiment, the model was fitted with a torque and thrust transducer located between the shaft and the hub, and the entire turbine and support structure assembly was mounted on a six-axis load cell at the base of the tower. Data from this arrangement provided the opportunity to compare thrust loads experienced by the rotor alone with those acting on the turbine as whole. Such a comparison for mean load values over a range of TSR is shown in Fig. 13. The vertical position of the centroid of the streamwise force is also computed, using both $F_x$ and the moment along the transverse axis $M_y$, from the load cell and this is shown in the bottom frame.

As would be expected, Fig. 13 clearly shows that the mean streamwise force $F_x$ on the overall turbine exceeds the mean thrust load on the rotor alone. The standard deviation of turbine force $F_x$ is also larger than that of shaft thrust. This can be explained by the fact that the main additional contribution to $F_x$ compared to rotor thrust loads is drag on the tower. The tower is located in the near wake of the rotor (0.4D downstream) and is therefore subjected to a more turbulent flow than the rotor itself. This leads to more variability in the tower drag force than in the rotor thrust, hence the larger standard deviation in $F_x$ than in thrust.

Mean force on the rotor is around 10% less than the mean force on the turbine. However this disparity (middle graph) decreases with increasing TSR. To understand this trend, it is useful to consider BEM theory, as derived in detail in Hansen (2008, chap. 4), which implies that:

$$T \propto a \cdot (1 - a) \cdot u^2 \tag{8}$$

where $T$ is the rotor thrust, $a$ the axial induction factor, $u$ the onset velocity and $\propto$ means "proportional to". The streamwise flow velocity $u_1$ directly in the wake of the turbine is given by:

$$u_1 = (1 - 2 \cdot a) \cdot u \tag{9}$$

Given that the drag force $F_D$ on the tower is proportional to $u_1^2$:

$$F_D \propto (1 - 2 \cdot a)^2 \cdot u^2 \tag{10}$$

Combining (8) and (10) yields after simplification:

$$\frac{F_D}{T} \propto \frac{1}{a \cdot (1 - a)} - 4 \tag{11}$$

From BEM, the right-hand side of (11) decreases with TSR which is consistent with the middle graph of Fig. 13.

The bottom graph of Fig. 13 shows that the vertical position of the centroid of $F_x$ is slightly above the rotor axis, even though the streamwise loads on the tower are applied below the rotor axis. This is the case because $F_x$ is dominated by rotor

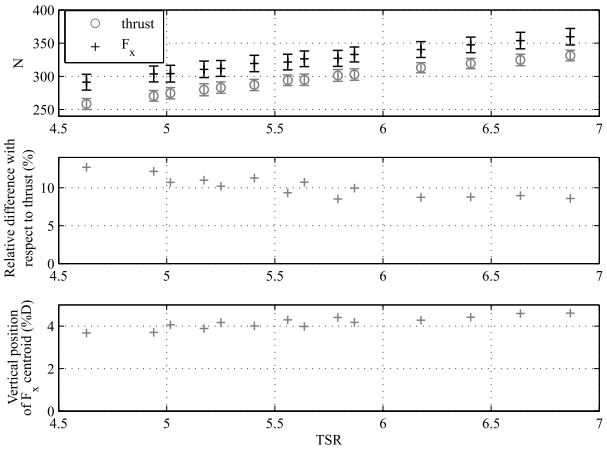


**Fig. 13.** Comparison between thrust loads on the rotor alone and the overall streamwise force $F_x$ on the turbine model (top graph). The error bars correspond to the standard deviation. The middle graph shows the discrepancy between the two measurements relative to thrust. The bottom graph shows the vertical position of the centroid of $F_x$ with respect to the rotor axis. This position is normalised by the rotor diameter D and given in %. Measurements were carried out over a range of tip speed ratios with an onset flow velocity of 0.814 $m \cdot s^{-1}$ and a $TI_u = 3\%$.

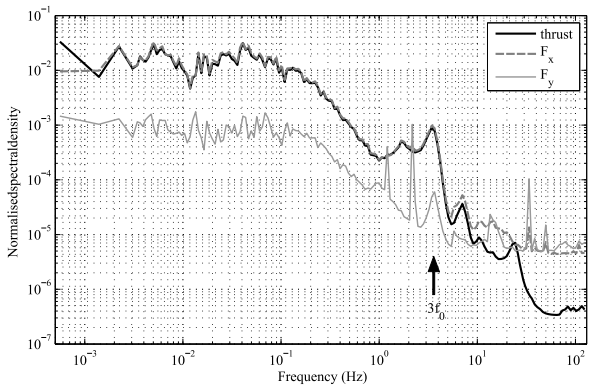


**Fig. 14.** Spectral comparison of rotor thrust, overall streamwise ($F_x$) and transverse ($F_y$) forces. Measurements were carried out with a free stream velocity of 0.819 $m \cdot s^{-1}$, $TI_u = 12\%$, TSR = 5.53 and the sampling duration is 3584 s. $f_0$ is the rotational frequency of the turbine.

thrust and the thrust on individual blades (see Fig. 5 (bottom right)) is larger whilst blades are rotating through the upper half of the depth.

It is also interesting to compare rotor thrust and turbine loading in terms of spectral density. Fig. 14 shows the spectral density of these forces together with that of the transverse force $F_y$ due to the whole turbine as measured by the load cell. Although the area on which force acts differs, all three forces are normalised by $\frac{1}{2} \cdot \rho \cdot A_r \cdot u^2$ (where $A_r$ the rotor area) to facilitate comparison.

For frequencies less than 5 Hz, turbine streamwise loading ($F_x$) is nearly identical to rotor thrust. For higher frequencies the $F_x$ spectrum is of higher magnitude than the rotor loading spectrum. This is partly due to the higher noise floor of the load

cell ($\sim 5 \times 10^{-6}$ for both $F_x$ and $F_y$ components reached at about 30 Hz) compared to the thrust sensor ($\sim 4 \times 10^{-7}$ reached at 60 Hz). The $F_y$ curve is consistently lower than the $F_x$ one despite the fact that the flow is nearly isotropic, with the level of turbulence similar in the $x$ and $y$ directions, as can be seen in Fig. 3 ($TI_u = 12\%$). This is partly due to the disparity between projected area of the tower and nacelle associated with transverse force and the much larger swept area of the rotor which determines the rotor thrust.

All the major peaks of the thrust curve are explained in Section 3. The $F_y$ curve exhibits a peak at the blade frequency ($3f_0$) which is most likely due to the tower shadowing effect. The two narrow peaks, at 2.18 and 1.21 Hz do not appear on the thrust or $F_x$ curves. These can be associated with vortex shedding behind the tower which is subjected to two flow regimes; the rotor wake across the upper portion and the bypass in the portion below the swept area of the rotor. To assess whether this is due to shedding the normalised shedding frequency is considered. Rearrangement of the Strouhal number yields the streamwise velocity $u_{tow}$ to which the tower is subjected:

$$u_{tow} = \frac{f_{tow} \cdot D_{tow}}{St} \tag{12}$$

where $f_{tow}$ is the frequency of oscillation of the vortices, $D_{tow}$ the tower diameter and $St$ the Strouhal number. Streamwise velocity in the turbine wake was measured in the vertical plane above the turbine axis at 0.5D downstream of the rotor and is reported in Payne et al. (2017a, Fig. 18). This velocity varies from 0.5 $\mathrm{m \cdot s^{-1}}$ to 0.9 $\mathrm{m \cdot s^{-1}}$ from the wake to the bypass region. The tower is actually located 0.4D downstream of the rotor and below the turbine axis where the wake and bypass velocities might be slightly different than the ones measured above. However, assuming $0.5 \leqslant u_{tow} \leqslant 0.9$ $\mathrm{m \cdot s^{-1}}$ is a reasonable starting point to estimate the Strouhal numbers for each section of the tower. For this velocity range the Reynolds number of the flow incident to the tower, $Re_{tow}$, is in the range $5.1 \cdot 10^4 \leqslant Re_{tow} \leqslant 9.1 \cdot 10^4$. The Strouhal number varies little for Reynolds numbers ranging from $3 \cdot 10^4$ to $2 \cdot 10^5$ and is equal to 0.19 (Bearman, 1969). With these numbers, (12) yields $u_{tow} = 1.17$ $\mathrm{m \cdot s^{-1}}$ and 0.7 $\mathrm{m \cdot s^{-1}}$ which are slightly higher but reasonably close to the velocities which can be expected in the bypass flow and rotor wake respectively. The 1.17 $\mathrm{m \cdot s^{-1}}$ velocity corresponds to $Re_{tow} = 1.2 \cdot 10^5$ which is also within the range for which the Strouhal number is stable at 0.19. This strongly suggests that the peaks in $F_y$ at 2.18 and 1.21 Hz are indeed due to vortex shedding on the tower with the different frequencies associated with the velocities of the bypass flow and wake respectively.

The support structure considered here is a simple cylinder. Developers may consider different forms, such as for reduced drag and hence reduced momentum extraction or for structural requirements. For design of both blades and supporting structures, consideration should be given to the impact of the unsteady loads due to onset flow and the support structure shedding regimes on fatigue design and avoidance of coincidence with driving forces at harmonics of the rotor frequency.

## 5. Conclusions

Unsteady loading of a three-bladed horizontal axis turbine has been analysed. The system studied comprises a three bladed rotor on a bed mounted support structure subject to a nearly uniform onset flow. The frequency variation of unsteady loads on the rotor, the supporting structure and the blades are analysed and related to characteristics of the turbulent onset flow and of the turbine.

For low frequencies, the spectra of blade loading, of rotor thrust and of the streamwise force on the turbine are correlated with the spectrum of the streamwise onset velocity. However, a steeper slope is observed for the spectra of power coefficient. Correlation of streamwise load spectra with the onset velocity spectra occurs up to a frequency equal to half the rotational frequency for blade loading, but to around three times this frequency for the rotor loading. For low onset turbulence (3% turbulence intensity) blade loading peaks are clearly observed at the rotational frequency and at five higher harmonics. This is associated with the tower-shadow effect with a reduction of blade load observed once per cycle when the blade is approximately 15–20 degrees misaligned with the tower. The amplitude of the peak at rotational frequency is similar to that of the highest onset flow induced loads at low frequencies. Similar fluctuations of load are observed when aggregated across the three blades and in the rotor thrust spectrum, with each harmonic at three times that of the blade load. For higher value of onset turbulence (12% turbulence intensity) blade loading is observed at the rotational frequency and the first two harmonics but with greater variation at intervening frequencies. For the high frequency range, greater than fifth and third harmonic for low and high turbulence cases respectively, the slope of blade loading spectra is observed to be greater than that of the corresponding onset velocity spectra.

Although the turbine is bed-mounted and its tower is therefore generating drag force below the rotor axis, the centroid of the streamwise force over the entire turbine (rotor, nacelle and tower) is above the axis of rotation (by about 4% of the rotor diameter). This is mainly associated with the tower shadowing effect which reduces blade loads in the lower part of the rotor disc. Mean streamwise load on the nacelle and supporting structure is approximately ten percent of rotor thrust although this reduces slightly with increasing tip-speed ratio, due to variation of thrust and hence wake velocity over this range. Analysis of both streamwise and transverse force on the tower indicates that two vortex shedding regimes occur along the tower associated with the wake and bypass flow.

The analysis presented provides a benchmark for evaluating the capability of numerical models for unsteady load prediction.

**Acknowledgements**

This work was supported by the UK Engineering and Physical Sciences Research Council via the Marine Challenge grant EP/J010235/1 (X-MED). The authors would like to thank the IFREMER team of Boulogne-sur-Mer (France) for their help with the testing of the model, for granting access to some of their flow characterisation data used in this article and for the useful discussions during the data analysis phase of the project.

All the experimental measurements presented in this article can be accessed from http://dx.doi.org/10.7488/ds/2423.

**Authors' contributions**

G.P. and T.S developed the turbine model specifications and design, the tank test programme and the analysis plan, G.P led the tank testing, the data analysis and drafted this manuscript, T.S was co-investigator on the project and contributed to the analysis presented and to manuscript preparation; R.M. contributed to the assembly of the physical model and to tank testing; T.B. was co-investigator for the project and contributed to specification of tank test programme and to manuscript review.

**References**

Ahmed, U., Apsley, D., Afgan, I., Stallard, T., Stansby, P., 2017. Fluctuating loads on a tidal turbine due to velocity shear and turbulence: comparison of CFD with field data. Renew. Energy 112, 235–246.

Bahaj, A., Batten, W., McCann, G., 2007a. Experimental verifications of numerical predictions for the hydrodynamic performance of horizontal axis marine current turbines. Renew. Energy 32 (15), 2479–2490.

Bahaj, A., Molland, A., Chaplin, J., Batten, W., 2007b. Power and thrust measurements of marine current turbines under various hydrodynamic flow conditions in a cavitation tunnel and a towing tank. Renew. Energy 32 (3), 407–426.

Bearman, P.W., 1969. On vortex shedding from a circular cylinder in the critical Reynolds number regime. J. Fluid Mech. 37 (3), 577–585.

Blackmore, T., Myers, L.E., Bahaj, A.S., 2016. Effects of turbulence on tidal turbines: Implications to performance, blade loads, and condition monitoring. Int. J. Marine Energy 14, 1–26. http://www.sciencedirect.com/science/article/pii/S2214166916300297.

Chamorro, L.P., Hill, C., Morton, S., Ellis, C., Arndt, R.E.a., Sotiropoulos, F., 2013. On the interaction between a turbulent open channel flow and an axial-flow turbine. J. Fluid Mech. 716, 658–670.

de Jesus Henrique, T., Tedds, S., Botsari, A., Najafian, G., Hedges, T., Sutcliffe, C., Owen, I., Poole, R., 2014. The effects of wave-current interaction on the performance of a model horizontal axis tidal turbine. Int. J. Marine Energy 8, 17–35.

Doman, D.a., Murray, R.E., Pegg, M.J., Gracie, K., Johnstone, C.M., Nevalainen, T., 2015. Tow-tank testing of a 1/20th scale horizontal axis tidal turbine with uncertainty analysis. Int. J. Marine Energy 11, 105–119. http://linkinghub.elsevier.com/retrieve/pii/S2214166915000259.

Durán Medina, O., Schmitt, F., Calif, R., Germain, G., Gaurier, B., 2015. Correlation between synchronised power and flow measurements, a way to characterize turbulence effects on a marine current turbine. In: Proceedings of the 11th European Wave and Tidal Energy Conference.

Durán Medina, O., Schmitt, F.G., Calif, R., Germain, G., Gaurier, B., 2017. Turbulence analysis and multiscale correlations between synchronized flow velocity and marine turbine power production. Renew. Energy 112, 314–327.

Fernandez-Rodriguez, E., Stallard, T., Stansby, P., 2014. Experimental study of extreme thrust on a tidal stream rotor due to turbulent flow and with opposing waves. J. Fluids Struct. 51 (December 2015), 354–361.

Galloway, P.W., Myers, L.E., Bahaj, A.S., 2014. Quantifying wave and yaw effects on a scale tidal stream turbine. Renew. Energy 63, 297–307.

Gaurier, B., Davies, P., Deuff, A., Germain, G., 2013. Flume tank characterization of marine current turbine blade behaviour under current and wave loading. Renew. Energy 59, 1–12.

Gaurier, B., Germain, G., Facq, J., Johnstone, C., Grant, A., Day, a.H., Nixon, E., Di Felice, F., Costanzo, M., 2015. Tidal energy "Round Robin" tests comparisons between towing tank and circulating tank results. Int. J. Marine Energy 12 (2015), 87–109.

Germain, G., 2008. Marine current energy converter tank testing practices. In: 2nd International Conference on Ocean Energy (ICOE 2008) October pp. 2–7, Brest, France, http://archimer.ifremer.fr/doc/00022/13366/.

Hansen, M.O.L., 2008. Aerodynamics of Wind Turbines, second ed. Earthscan.

Kolekar, N., Banerjee, A., 2015. Performance characterization and placement of a marine hydrokinetic turbine in a tidal channel under boundary proximity and blockage effects. Appl. Energy 148, 121–133. http://www.sciencedirect.com/science/article/pii/S0306261915003360.

Lust, E.E., Luznik, L., Flack, K.A., Walker, J.M., Van Benthem, M.C., 2013. The influence of surface gravity waves on marine current turbine performance. Int. J. Marine Energy 3–4, 27–40.

Luznik, L., Flack, K.A., Lust, E.E., Taylor, K., 2013. The effect of surface waves on the performance characteristics of a model tidal turbine. Renew. Energy 58, 108–114. http://dx.doi.org/10.1016/j.renene.2013.02.022.

Martinez, R., Payne, G.S., Bruce, T., 2017. Preliminary results on the effects of oblique current and waves on the loadings and performance of tidal turbines. In: Proceedings of the 12th European Wave and Tidal Energy Conference, Cork, Ireland.

Mason-Jones, A., O'Doherty, D.M., Morris, C.E., O'Doherty, T., 2013. Influence of a velocity profile & support structure on tidal stream turbine performance. Renew. Energy 52, 23–30.

Mason-Jones, A., O'Doherty, D.M., Morris, C.E., O'Doherty, T., Byrne, C.B., Prickett, P.W., Grosvenor, R.I., Owen, I., Tedds, S., Poole, R.J., 2012. Non-dimensional scaling of tidal stream turbines. Energy 44 (1), 820–829. http://dx.doi.org/10.1016/j.energy.2012.05.010.

MayGen Ltd, 2016. MeyGen Tidal Energy Project Phase 1. Project Environmental Monitoring Programme, Technical Report MEY-1A-70-HSE-018-I-PEMP.

McNaughton, J., 2013. Turbulence Modelling in the near Field of an Axial Flow Turbine Using Code Saturne. University of Manchester.

McTavish, S., Feszty, D., Nitzche, F., 2014. An experimental and computational assessment of blockage effects on wind turbine wake development. Wind Energy 17, 1515–1529. http://onlinelibrary.wiley.com/doi/10.1002/we.1648/full.

Milne, I., Day, A., Sharma, R., Flay, R., 2013. Blade loads on tidal turbines in planar oscillatory flow. Ocean Eng. 60, 163–174. http://linkinghub.elsevier.com/retrieve/pii/S0029801812004465.

Milne, I.A., Day, A.H., Sharma, R.N., Flay, R.G., 2016. The characterisation of the hydrodynamic loads on tidal turbines due to turbulence. Renew. Sustain. Energy Rev. 56, 851–864. http://dx.doi.org/10.1016/j.rser.2015.11.095.

Moriarty, P.J., Hansen, A.C., 2005. AeroDyn Theory Manual, NREL/TP-500-36881, National Renewable Energy Laboratory http://www.nrel.gov/docs/fy05osti/36881.pdf.

Mycek, P., Gaurier, B., Germain, G., Pinon, G., Rivoalen, E., 2014. Experimental study of the turbulence intensity effects on marine current turbines behaviour. Part I: One single turbine. Renew. Energy 66, 729–746.

Parkinson, S.G., Collier, W.J., 2016. Model validation of hydrodynamic loads and performance of a full-scale tidal turbine using Tidal Bladed. Int. J. Marine Energy 16, 279–297.
Payne, G.S., Stallard, T., Martinez, R., 2017a. Design and manufacture of a bed supported tidal turbine model for blade and shaft load measurement in turbulent flow and waves. Renew. Energy 107, 312–326.
Payne, G.S., Stallard, T., Mullings, H.R., Martinez, R., 2017b. Experimental investigation into unsteady loads on horizontal axis tidal turbines. In: 12$^{th}$ European Wave and Tidal Energy Conference, Cork, Ireland.
Schepers, J.G., Boorsma, K., Gomez-Iradi, S., Schaffarczyk, P., Madsen, H.A., Sørensen, N.N., Shen, W.Z., Lutz, T., Schulz, C., Herraez, I., Schreck, S., 2014. Final report of IEA Task 29: Mexnext (Phase 2), ECN-E–14-060, Energieonderzoek Centrum Nederland (ECN) https://www.ecn.nl/publications/PdfFetch.aspx?nr=ECN-E--14-060.
Smilden, E., Sørensen, A., Eliassen, L., 2016. Wind model for simulation of thrust variations on a wind turbine. Energy Procedia 94 (1876), 306–318. http://dx.doi.org/10.1016/j.egypro.2016.09.188.
Stallard, T., Feng, T., Stansby, P., 2015. Experimental study of the mean wake of a tidal stream rotor in a shallow turbulent flow. J. Fluids Struct. 54, 235–246.
Storey, R.C., Cater, J.E., Norris, S.E., 2016. Large eddy simulation of turbine loading and performance in a wind farm. Renew. Energy 95, 31–42. http://dx.doi.org/10.1016/j.renene.2016.03.067.
Thé, J., Yu, H., 2017. A critical review on the simulations of wind turbine aerodynamics focusing on hybrid RANS-LES methods. Energy 138, 257–289.
Thorpe, S., 2007. An Introduction to Ocean Turbulence. Cambridge University Press.

Renewable Energy 107 (2017) 312–326

Contents lists available at ScienceDirect

Renewable Energy

journal homepage: www.elsevier.com/locate/renene

# Design and manufacture of a bed supported tidal turbine model for blade and shaft load measurement in turbulent flow and waves

Grégory S. Payne [a, *], Tim Stallard [b], Rodrigo Martinez [a]

[a] School of Engineering, University of Edinburgh, Edinburgh, EH9 3FB, UK
[b] School of Mechanical, Aerospace and Civil Engineering, University of Manchester, Manchester, M13 9PL, UK

ARTICLE INFO

*Article history:*
Received 1 February 2016
Received in revised form
4 January 2017
Accepted 31 January 2017
Available online 3 February 2017

*Keywords:*
Tidal stream turbine
Experimental testing
Instrumentation
Turbulence loading

ABSTRACT

Laboratory testing of tidal turbine models is an essential tool to investigate hydrodynamic interactions between turbines and the flow. Such tests can be used to calibrate numerical models and to estimate rotor loading and wake development to inform the design of full scale machines and array layout. The details of the design and manufacturing techniques used to develop a highly instrumented turbine model are presented. The model has a 1.2 m diameter, three bladed horizontal axis rotor and is bottom mounted. Particular attention is given to the instrumentation which can measure streamwise root bending moment for each blade and torque and thrust for the overall rotor. The model is mainly designed to investigate blade and shaft loads due to both turbulence and waves. Initial results from tests in a 2 m deep by 4 m wide flume are also presented.



## 1. Introduction

Tidal energy has seen a rapid development over recent years with several developers now conducting offshore trials of full-scale prototypes generating electricity to the grid. These machines are pre-commercial (Technology Readiness Level (TRL) 8) and it is expected that further technological development will reduce cost towards the range required for TRL 9. As part of that process, numerical modelling tools such as Blade Element Momentum (BEM) and Computational Fluid Dynamics (CFD) are widely used for load predictions and wake analysis. However, the interactions between tidal turbines and the water flow are complex and there remain limitations to these numerical methods, particularly concerning methodologies for representing the complexity of turbulent tidal flows, including with waves, and the effect of these flows on loading and wake recovery. Physical testing in laboratory conditions is therefore an essential tool to provide validation data for numerical models and insight into the physical processes of these flow/turbine interactions to inform improvements to machine design. This paper details the design and manufacture of a turbine developed to study peak loading on tidal turbines associated with flow, turbulence, waves and impact.

Several prototype tidal stream turbines have now been developed and evaluated at offshore test-centres such as the European Marine Energy Centre (EMEC). The most widely trialled designs comprise a two- or three-bladed horizontal axis turbine with nacelle supported on a rigid bed connected structure (Alstom/GE, Hammerfest, Atlantis). Prototypes are of the order of 18–24 m diameter, designed for operation in water depths greater than approximately 30 m. Fatigue design of turbines and components is critical and requires accurate prediction of load-cycles through the operating life. Unsteady loading of full-scale turbines is due to complex onset flow with mean velocity and velocity profile varying continuously during the tidal cycle and unsteady onset velocity due to turbulence and free-surface waves. Prediction of peak loads is also required and this may be due to environmental loads or impact with immersed bodies, for which it is crucial to predict the flow field incident to the rotor plane [5]. For large-scale electricity generation it is expected that farms comprising multiple turbines would be deployed. To predict energy yield from farms, accurate prediction is required of the effect of energy extraction on the flow (Garrett and Cummins [12], of the effect of flow constraint on turbine performance (e.g. due to blockage [27]) and in particular, of development of wakes from isolated turbines and from groups of turbines.

* Corresponding author.
*E-mail addresses:* gregory.payne@ed.ac.uk (G.S. Payne), Tim.Stallard@manchester.ac.uk (T. Stallard), R.Martinez@ed.ac.uk (R. Martinez).

http://dx.doi.org/10.1016/j.renene.2017.01.068

A number of laboratory scale studies of tidal stream turbines have been conducted. The motivation for such studies has generally been for acquiring experimental data for validation of numerical models for prediction of either, or both, aspects of turbine performance or characteristics of turbine wakes. Turbine performance is typically characterised by variation of time-averaged power and thrust coefficient with tip speed ratio. Such data has been reported from experimental studies of several different turbine geometries, including 3-bladed turbines with diameters of 0.8 m [4], 0.7 m [24], 0.6 m [32], 0.28 m [18] and 0.27 m [31] amongst others. Dual rotor horizontal axis turbine systems have also been studied experimentally including adjacent 0.5 m diameter turbines on a central spar [16] and 0.82 m diameter contra-rotating concept [6]. For these turbine geometries, thrust and power variation due to waves has been studied, using a towing tank [9,11,19], with waves following a flow with around 3% turbulence [8,13] and with waves opposing a shallow flow with 12% turbulence [10]. Velocity and turbulence of the wake has also been reported, typically from downstream distance defined by the supporting structure [24,25,31,32]. Blade loads have been measured for a 0.78 m diameter turbine subjected to oscillatory motion in a towing tank [23]. Limited datasets have now also been published from field trials including blade load variation due to turbulence on the Alstom 500 kW turbine [7] and the power curve of the Alstom/GE 1 MW turbine [20] each deployed at the EMEC site. The power curve of a smaller scale (1.5 m diameter) four bladed turbine has also been measured through field tests in Strangford Lough Narrows (Northern Ireland) [17].

Although a large body of literature reports on experimental testing of tidal turbine models (see previous paragraph), little information on the actual design and manufacturing of turbine models is available (to the notable exception of Bahaj et al. [3] which, however, is over a decade old).

The present article aims at addressing this issue by providing a comprehensive and detailed description of the design process and of the manufacturing techniques implemented for a laboratory scale tidal turbine with both blade and shaft instrumentation. The design motivation and requirements are first presented (section 2). They are followed by a description of the overall turbine model design (section 3). More detail is then given on the rotor design and on the numerical approach taken to estimate blade and rotor loads (section 4). Development of bespoke instrumentation and the process of generator selection are described (sections 5 and 6 respectively). The main characteristics of the system, as measured through tank testing, are then presented (section 7). Finally, the appendices provide details on the waterproofing of the model (section A), the manufacturing techniques employed (section B) and discuss further improvements to the design (section C).

## 2. Design requirements

The design was developed to provide experimental measurement of rotor thrust and torque and individual blade loads. It was therefore desirable to maximise geometric scale to facilitate incorporation of blade instrumentation. Maximising geometric scale of the rotor is also desirable to minimise the variation of blade performance with Reynolds number. Overall dimensions are subject to flume dimensions and the turbine was designed for nominal flume water depth of 2 m, suitable for large-scale facilities including IFREMER [14] and FloWaveTT [28] with typical test velocities of around 0.8 m $s^{-1}$. A bed mounted support structure was considered to represent the majority of prototype turbines, minimising disruption to propagating waves and disrupting the wake near bed rather than near surface. In practical terms this configuration also facilitates measurement of the wake velocity to within a short distance downstream of the rotor plane, allowing analysis of the tip vortex region.

The overall configuration was selected to study peak loading due to waves and turbulence representing operation of a full-scale turbine at low tide water level. For given flow speed, wave height and period, peak loads would thus occur at low water level due to increased blockage and lower rate of depth decay of wave induced velocities. A depth to diameter ratio of 1.67 and wave conditions providing hub height velocities of up to 30% of the mean velocity were defined. This ratio is consistent with prior reduced scale studies of turbine wakes and loading conducted in a wide flume [31] with blades designed to produce a thrust curve similar to a generic full-scale turbine. To focus on the effect of environmental conditions on peak loads, blades were designed to represent the radial variation of thrust of the same generic turbine at a particular tip speed ratio. During the design process emphasis was placed on defining a wetted geometry to minimise effort required for development of computational meshes. To this end, blades were designed for high rigidity to minimise deflection due to peak combination of wave and current loading. The aim was to keep blade tip deflection within 2% of the rotor radius which corresponds to a coning angle of 1.15°. Both nacelle and structure were also defined by simple cylindrical sections.

## 3. Overall turbine model design

The ability of the model to provide high quality measurements was considered a key objective and instrumentation was therefore taken into consideration from the start of the overall design process. Three main features followed on from that design approach:

1. The sensors are configured in a way to measure as directly as possible the physical quantities of interest.
2. As a consequence all force sensors are located ‘upstream’ of water seals so that parasitic friction associated with those seals do not affect measurements.
3. Low voltage signals from the sensors are amplified as close as possible from the sensor themselves and the signal cables are sheltered as much as possible from electromagnetic noise to improve the signal to noise ratio of the measurements.

The rotor design, the model instrumentation and the drive system are described in section 4, 5 and 6 respectively. Practical aspects of the waterproofing and manufacturing of the turbine as well as the lessons learnt from developing and testing the model are provided in Appendix A, Appendix B and Appendix C respectively.

An overview of the design is given in Fig. 1 which shows a section view of the CAD model of the turbine.

The main characteristics and components of the model are summarised in Table 1. CAD files providing the outer geometry of the turbine including the blades can be downloaded from http://dx.doi.org/10.7488/ds/1707.

The selected configuration is described from hub downstream to generator. The root of each blade is attached to the hub via a transducer to measure the streamwise root bending moment. These transducers rely on strain gauge bridges whose low voltage signals are amplified by electronic signal processing units housed in a waterproof enclosure located immediately upstream of the hub, in the nose cone of the turbine, hence minimising the length of the low voltage signal cables exposed to external noise. Detail on the root-bending moment sensors is given in section 5.2.

The hub is affixed directly to a torque and thrust transducer. This is a stiff arrangement which minimises any structural

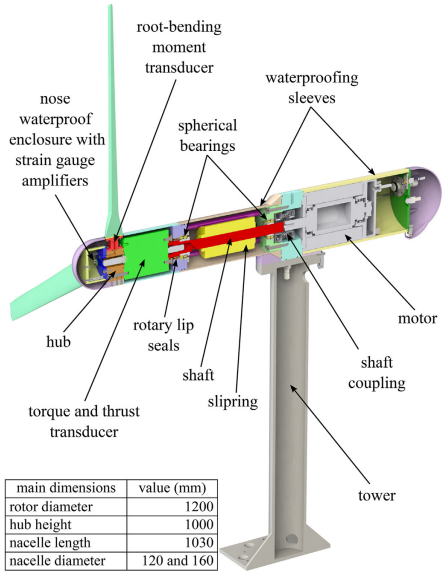


| main dimensions | value (mm) |
|---|---|
| rotor diameter | 1200 |
| hub height | 1000 |
| nacelle length | 1030 |
| nacelle diameter | 120 and 160 |

**Fig. 1.** Section view of the turbine model and its key dimensions.

compliance between the two parts which could otherwise adversely affect measurements. Signal conditioning units are built into the sensors which output amplified signals (see section 5.1 for more detail).

The torque and thrust transducer is bolted to a 304 stainless steel shaft with a solid main section of 25.4 mm in diameter. For the first 60 mm (on the side of the transducer) the shaft is hollow to allow the instrumentation cable to go through and exit at 45° to connect to the rotor of the slipring. The cable from the slipring stator is routed through the model to exit at the top of the hollow tower via a waterproof connector (shown in white in Fig. 1). The shaft is held in place by two spherical bearings (SKF 22206E and 22205E) suitable for the expected thrust load and allowing for potential angular misalignment. Selection was mainly driven by their internal diameter and the load and rotation per minute (rpm) ratings for these bearings are overspecified for the design conditions (summarised in Table 1). The two parts housing the bearings on either side of the shaft are rigidly connected by four 14 mm diameter solid 304 stainless steel rods (two of them are visible in magenta in Fig. 1). This 'cage' arrangement is stiff and ensures alignment between the two bearing housings while providing access to the slipring connections when the waterproofing sleeve is removed.

The rotary shaft seals are located just 'downstream' of the torque and thrust transducer. Thus, the interior of the housing shown in Fig. 1 'on the right' of the seals, which contain the slipring, the shaft coupling and the motor is a dry environment. More details on the shaft seal arrangement can be found in section A.1.2.

A motor is used to provide controllable resistance to the rotor motion induced by the flow. The motor shaft is directly connected to the turbine shaft without a gearbox. This approach is typically

**Table 1**
Turbine specifications.

| | |
|---|---|
| Rotor diameter (mm) | 1200 |
| Nacelle length (mm) | 1030 |
| Nacelle diameter (mm) | 120 from hub up to tower 160 beyond tower |
| Hub height (mm) | 1000 |
| Tower diameter (mm) | 102 |
| Distance from rotor plan to tower axis (mm) | 486 (0.4D) |
| Model mass, excluding tower (kg) | 35 |
| Number of blades | 3 |
| Drivetrain | Direct drive with brushless servo motor manufactured by the company Alxion |
| Load sensors | Rotor torque and thrust and streamwise root bending moment for each blade developed with the company Applied Measurements |
| Position sensor | Absolute angular position through motor feedback resolver |
| Maximum continuous torque (Nm) | 26 |
| Peak torque (Nm) | 100 |
| Maximum measurable torque (Nm) | 100 |
| Torque transducer proof rating (Nm) | 150 |
| Maximum measurable thrust (N) | 1300 |
| Thrust transducer proof rating (N) | 1950 |
| Maximum measurable streamwise blade root bending moment (Nm) | 62 |
| Root bending moment proof rating (Nm) | 93 |
| Maximum rotational speed (rpm) | 250 |

described as 'direct drive'. A Smartflex coupling made by the company Mayr (www.mayr.com) is used to connect the two shafts. This coupling is compact while offering suitable torque rating. The motor is located at the rear of the nacelle with cables exiting at the back to minimise the impact of electro magnetic interference on the instrumentation. More information on the drive system is given in section 6.

The non waterproof components of the model (mainly the drive train and the slipring) are protected from water by thin aluminium alloy cylindrical sleeves. Sharp corners and blunt surfaces are covered as much as possible by fairings to avoid disturbing the flow and to facilitate meshing of the geometry when simulated in CFD. They are shown in light purple in Fig. 1. These fairings play no structural roles. To ensure precise fitting, manufacture was by 3D printing from ABS plastic.

## 4. Rotor design

### 4.1. Design process

The simulation tool used to estimate the rotor performance and design loads was a standard BEM with Spera high axial induction factor correction as described by Hansen [15]. The code was written in Matlab and a given rotor configuration was simulated in about a second on a standard desktop. The blade sections used are based on the NACA 63-8XX series whose drag and lift coefficients used for the BEM simulations can be found in Bahaj et al. [2].

Radial variation of streamwise and azimuthal loads on the blade computed by the BEM code were used as input to a structural analysis. Initially, it was desirable to be able to quickly assess a range of rotor designs and so the structural analysis needed to be computationally efficient. Beam theory was used to assess the maximum tip deflection and to carry out vibration analysis. The blades were discretised spanwise in 80 blade elements (see Fig. 2a), each of constant section. The mechanical properties of each section were computed using the software ABAQUS Simulia which then solves the beam equations for the full blade to compute deflection

and vibration modes. ABAQUS Simulia was run in batch mode using Python scripting to integrate the BEM Matlab code with the structural analysis. With this approach, it was possible to carry out the combined BEM and structural assessment of a given rotor design in an automated way.

Once the rotor design had been selected with the method described above, a detailed CAD model of the blades was generated. It was used to carry out a more time consuming three dimensional finite element analysis (FEA) to provide a more in-depth structural analysis taking into account the root attachment feature not represented in the beam model. The loads were once again computed from BEM and input into SolidWorks Simulation. The FEA analysis was used to confirm the blade deflection predicted by beam theory (which was within 6% of the FEA results) and to check that the level of stress throughout the blades is acceptable. Fig. 2b shows the maximum deflection predicted by the FEA analysis. The dimensions of final blade shape used for the turbine is given in Table 2.

### 4.2. Detailed blade design

#### 4.2.1. Blade CAD design

Using the dimensions from Table 2 a CAD model of the blade was constructed. The shape of each of the ten foil profiles was obtained from the software JavaFoil (developed by Martin Hepperle and available from www.mh-aerotools.de/airfoils/javafoil.htm) which was used to provide the coordinates of 60 points describing each profile. The coordinates were rotated by the twist angles indicated in Table 2. The centre of rotation used is located at a quarter of the chord line from the leading edge. This corresponds approximately to the aerodynamic centre of the foil sections ([1]; Ch. 4). The points were then imported in a CAD software at the appropriate radial location (given in Table 2) with the axis of the blade going through the quarter-chord point of each foil section. The discreet points describing each section were used to generate smooth interpolated curves which were in turn used as support for

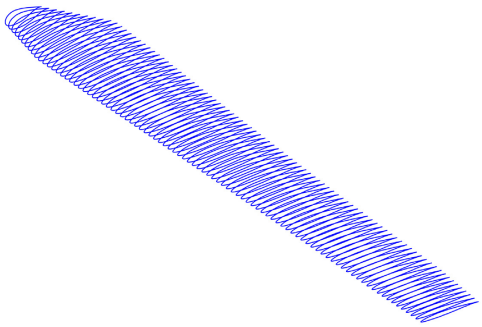

(a) Blade discreetisation for beam theory analysis

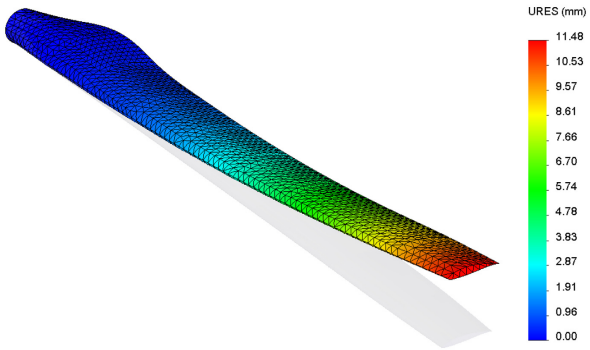


(b) FEA deflection analysis

**Fig. 2.** Discretisation of the blade for beam theory analysis (a) and FEA analysis showing the overall blade deflection in mm (color bar) (b). (For interpretation of the references to colour in this figure legend, the reader is referred to the web version of this article.)

an interpolated lofted surface. The blade CAD model was originally constructed with SolidWorks but it was found difficult to build a smooth transition from the circular root attachment to the blade main section. In the end, the MultiSurf/SurfaceWorks (developed by AeroHydro) add-in to SolidWorks was used as it provides better control of lofted surfaces. It should be noted that because of the feature at the blade root necessary to attach it to the hub, the blade section at the very root ($r/R = 0.1$) is a circle 44 mm in diameter rather than the foil section whose characteristics are given in Table 2. The blade section then rapidly and smoothly morphs from the circular shape of the root into a foil section so that from $r/R = 0.2$ it corresponds exactly to the dimensions given in Table 2. The data of the table were nevertheless used without alteration for the BEM modelling. This approximation was considered acceptable given that the blade root makes a relatively small contribution to torque, thrust, and bending moment.

#### 4.2.2. Blade pitch angle adjustment

Being able to set the pitch angle of turbine blades accurately is important as even small angular errors will affect the angle of attack of the blade profile and hence its performance. It is also key to ensure that the pitch angle is consistent across the three blades as they would otherwise perform differently even if their profiles are identical. Finally, in a scale turbine model used for research and development, it is desirable to be able to accurately modify the blade pitch angle to investigate its impact on performance. The arrangement developed to fastened the blade roots to the hub is shown from two different angles by exploded views in Fig. 3.

The square face of the root attachment part (which is also the root bending moment transducer, as detailed in section 5.2) is bolted onto the hub. The pitch angle of the blade with respect to the root attachment part is set by the angular adjustment disc and locating pins. The centring pin goes through the blade, the disc and into the root attachment part and defines the pitch axis of the blade. A combination of two smaller pins, one going through the blade root and the disc and the other going through the root attachment part and the disc locks the pitch angular position. The pins are ground and the locating holes reamed thus providing a tight fit which prevents any angular play. The two small locating pins are as far out from the pitch axis as possible, thus providing a high degree of accuracy in pitch angle positioning. Assuming a machining accuracy of 0.02 mm for the location of the holes and given that the angular locating pins are placed at a radius of 19 mm from the pitch axis, this yields an accuracy of 0.12° in pitch angle.

Once the pitch angular position has been locked with the pins, the six cap screws shown in Fig. 3 can be fastened to secure the blade, with no risk of modifying the angle while tightening the screws. If the blades need to be mounted at a different pitch, new discs, with different hole patterns need to be made. However, no modification is required on the blades and on the root attachment parts as the latter are fitted with kidney slots for the screws to go through. This makes it possible to adjust the angle by ±5° from the central position.

**Table 2**
Blade dimensions based on NACA 63-8XX profile. r is the local radius, R the overall blade radius (0.6 m), c the chord length and t the thickness. *As explained in more detail in the main text, that section was different in manufactured blade.

| r/R | r (mm) | c/R | c (mm) | t/c (%) | t (mm) | twist (°) |
|---|---|---|---|---|---|---|
| 0.1* | 60 | 0.0483 | 29 | 58 | 16.82 | 23 |
| 0.2 | 120 | 0.1117 | 67 | 25 | 16.75 | 19 |
| 0.3 | 180 | 0.1109 | 66.56 | 23.45 | 15.61 | 12.35 |
| 0.4 | 240 | 0.1045 | 62.72 | 21.9 | 13.73 | 9.96 |
| 0.5 | 300 | 0.0988 | 59.3 | 20.35 | 12.07 | 8.91 |
| 0.6 | 360 | 0.0932 | 55.92 | 18.8 | 10.51 | 8 |
| 0.7 | 420 | 0.0883 | 52.98 | 17.25 | 9.14 | 7.03 |
| 0.8 | 480 | 0.0857 | 51.44 | 15.7 | 8.08 | 6.21 |
| 0.9 | 540 | 0.083 | 49.82 | 14.15 | 7.05 | 5.74 |
| 0.99 | 594 | 0.0733 | 44 | 12.6 | 5.54 | 5.5 |

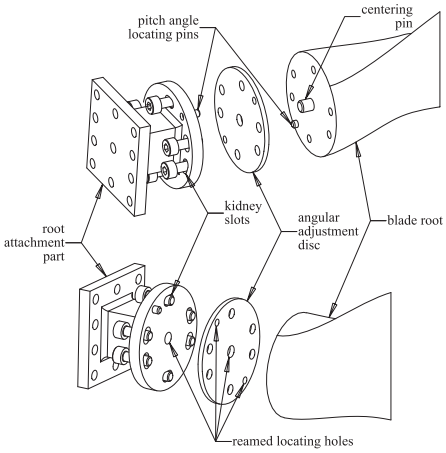


**Fig. 3.** Exploded views of blade root attachment system.

## 5. Instrumentation

### 5.1. Torque and thrust transducer

The torque and thrust transducer was custom made by the company Applied Measurements Ltd (www.appmeas.co.uk). As it is located 'upstream' of shaft seal, and therefore in contact with the surrounding water, it was designed to be waterproof and is made of stainless steel. The specifications for its measurement range were based on the maximum rotor loads predicted by the BEM model, with a safety factor of 2 applied. They are summarised in Table 1. From calibration, the 'interactions' of thrust loads on torque readings and of torque loads on thrust readings are respectively within 0.06% and 0.11% of the load ratings.

One of the key bespoke features of this sensor for this application is the cable routing. In addition to the six cables required to supply power and to output torque and thrust signals, 15 are routed through the body of the transducer to supply power to instruments in the turbine nose and return measured signals. The transducer is fitted with a 19 way connector (model DBPU 104 Z092-139 made by Fischer) on the face bolted to the shaft and with a 16 way connector (model DBEU 104 A086-130 made by Fischer) on the face attached to the hub (see Fig. 1). O-rings are fitted at the interfaces between the transducer and the hub and between the transducer and the shaft. This approach makes it possible to conveniently route cables from the waterproof enclosure in the nose cone to the hollow section of the shaft through a waterproof environment.

### 5.2. Root bending moment transducer

The blade root bending moment transducers are located between the hub and the blades. In addition to their role as a

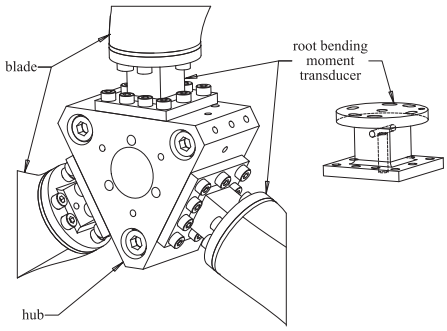


**Fig. 4.** Close-up view of the turbine model hub, blades and root bending moment transducer arrangement (left). Root bending moment transducers on its own with hidden edges partially visible to show the internal galleries for cable routing (right).

measurement instrument they are also an integral part of the mechanical structure of the turbine and their form factor is tightly constrained to keep the nacelle shape streamlined. As such their design is deeply interwoven with those of the hub and the blade. Small load cells with suitable load ratings, such as the Mini series produced by the company ATI Industrial Automation, are available off the shelf. They offer the advantage of measuring not only bending moment but also loads along the standard 6-axis. Although the load cells themselves would probably be small enough to fit within the nacelle diameter, they would however require special adaptor parts to interface between their standard mounting features and the specific mounting feature of the blades. Moreover, these 6-axis load cells are expensive. It was therefore decided to keep the design of the root bending moment transducer 'in-house' and to supply the manufactured flexures to Applied Measurements Ltd for strain gauging, waterproofing and calibration.

The overall arrangement of the root bending moment flexures with the hub and the blades is shown in Fig. 4. The square beam section of the flexure is strained gauged on the two faces perpendicular to the flow direction to measure the streamwise blade root bending moment. A gallery connects the two instrumented faces with the bottom face of the flexure so that the four cables necessary to operate the strain gauge bridge are routed to come out at the bottom.

The design of the transducer was based on load predictions from BEM. The dimensions of the 'deforming' section of the flexure was first computed using beam theory [30] based solely on the maximum root bending moment in the streamwise direction. A comprehensive CAD model of the complete part was then developed and used as a geometrical input for FEA calculations to investigate strain and stress distributions and to finalise the shape of the flexure. At this stage root bending moment and resultant force in the streamwise and in the cross-flow directions were taken into account. Fig. 5 shows the vertical strain distribution predicted by the FEA on the face of the flexure in tension for the final design. The pair of grey inner rectangles shows the planned location for the active section of the strain gauge. The strain distribution is clearly not symmetrical with respect to the vertical axis of the part view. This is to be expected as the flexure also experiences loads in the cross-flow direction. The hole in the upper part of the flexure affect significantly the strain pattern but it can be seen that vertical strain distribution within the active part of the strain gauge varies only within about 9%, which is below the 10% limit recommended to reduce gauge fatigue and variations in transducer creep [22]. The vertical strain predicted over the active gauge section ranges between 750 and 800$\mu\varepsilon$. Given that the recommended maximum strain is between 1000 and 1700$\mu\varepsilon$ [22] this was thought to provide a sufficient safety factor.

To avoid significant hysteresis, it is recommended to keep the stress in the flexure below 30% of the yield strength of the material [29]. The flexures were therefore made of grade 2014 T6 aluminium alloy which has a high yield strength of 415 MPa. The maximum stress predicted by the FEA around the active region of the strain gauge is 54 MPa which corresponds to 13% of the material yield strength, thus providing a good safety factor. 2014 T6 aluminium

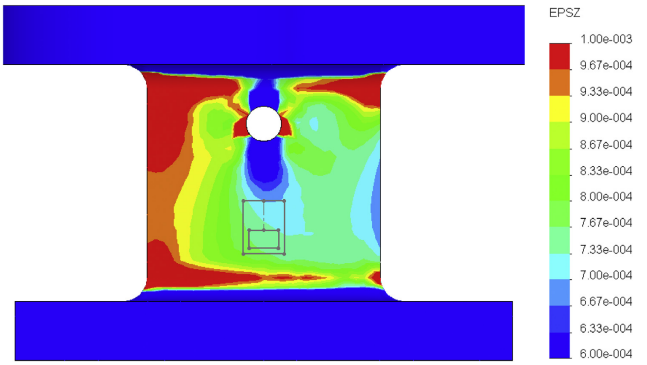


**Fig. 5.** Vertical strain distribution of the face of the flexure experiencing tension. The color bar scale is given in strain. The grey rectangles indicate the footprint of the strain gauge with the inner rectangle corresponding to the active part of the gauge. (For interpretation of the references to colour in this figure legend, the reader is referred to the web version of this article.)

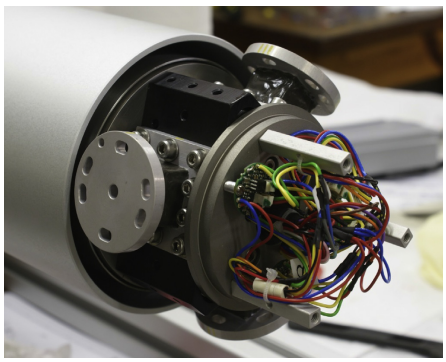

**Fig. 6.** Hub of the turbine model with the root bending moment transducers mounted and the nose waterproof enclosure open.

alloy does not have good corrosion resistance. The flexures were therefore treated with chromic anodising for corrosion protection. Fig. 6 shows the transducer completed with their waterproof coating. They are mounted onto the hub of the turbine. The nose waterproof enclosure is open and the strain gauge bridge amplifiers can be seen.

The cantilever beam type of transducer is compact and this is the main reason why it was used in this turbine model. However, with such a transducer geometry, although the strain measured is mainly due to streamwise blade root bending moment, it is also affected by the streamwise resultant shear force on the blade and, to a lesser extent, by the cross-flow loads. The FEA model predicts that the vertical strain in the active region of the gauge when the transducer is loaded by bending moment and resultant force in the streamwise and in the cross-flow directions is 4% higher than when it is loaded by the streamwise bending moment only. This difference was deemed small and it was therefore considered that the strain measurement would provide a good indication of streamwise blade root bending moment. To check that this assumption held true with the physical transducer, an extensive calibration program was commissioned. The principle of the calibration carried out is summarised by Fig. 7.

The base of the transducer was bolted on a vertical reference and the blade was replaced by round bar 500 mm in length. The bar was horizontal and featured four attachment points (shown as black dots in Fig. 7) evenly spread over its length to which accurate weight could be attached thus applying a vertical force onto the bar (**F** in Fig. 7). The weights ranged from 0 to 125 N and readings from the transducer were taken for each weight at each attachment point thus providing a range of bending moment and shear force combinations. This operation was first carried out with the force applied in the streamwise direction. Fig. 8 shows the resulting calibration line and the relative error between fitted and actual bending moment values. On the graphs, different markers are used for the different lever arm lengths at which force is applied. The relative error is quite significant when the load is applied with a short lever arm (125 mm).

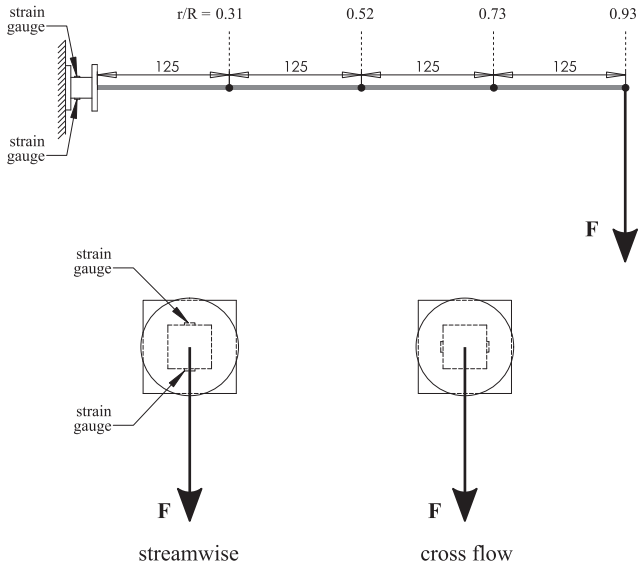


**Fig. 7.** Schematic of the root bending moment transducer calibration. Dimensions are given in mm. The location at which the calibration forces are applied are also given as a function of the rotor radius (r/R).

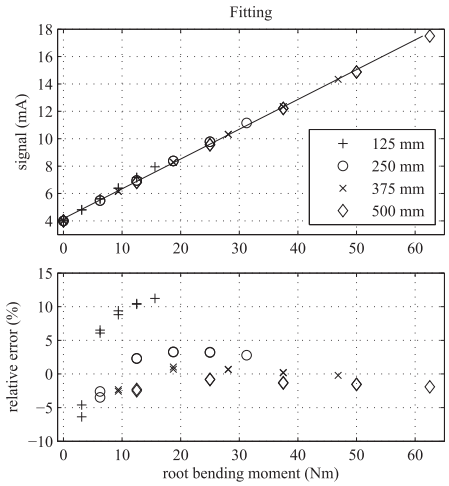


**Fig. 8.** Calibration curve of the transducer (top) and calibration relative error (bottom). The different markers are associated with different lever arm length at which the vertical force is applied.

This makes physical sense since that, in this configuration, the ratio of shear force to bending moment is at its largest and shear force is therefore more likely to have a significant impact on the transducer reading. However, as the length of the lever arm increases to 250 mm and above, the relative error falls below 5%.

To investigate the 'interactions' of cross-flow loading on streamwise readings, the calibration coefficients corresponding to Fig. 8 have been applied the transducer signal when it is loaded purely in the cross-flow direction (corresponding to the bottom right configuration of Fig. 7). Fig. 9 shows the outcome in terms of streamwise root bending moment readings as a function of cross-flow loads applied.

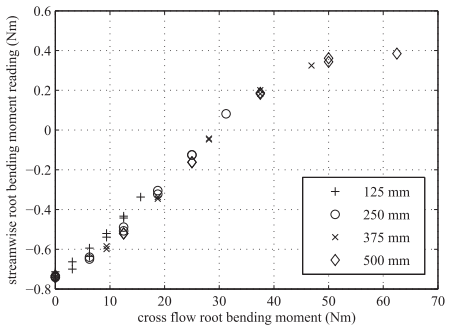


**Fig. 9.** Cross-flow load 'interactions' on streamwise readings when the transducer is loaded purely in the cross-flow direction. The different markers are associated with different lever arm length at which the force is applied.

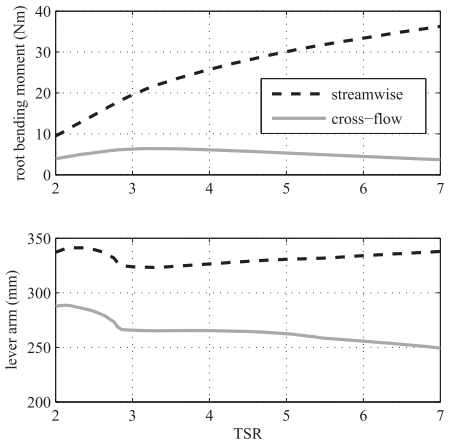


**Fig. 10.** Root bending moment (top) and lever arm length at which resultant force is applied on the blade (bottom). Both are plotted against tip speed ratio.

The 'interactions' are overall small compared to the range of bending moment applied. They vary from −0.75 to 0.4 Nm with shorter lever arms tending to lead to more 'negative' offsets and longer arms being associated with positive ones.

To establish the overall impact of the streamwise calibration errors combined with 'interactions' on measurements, it is useful to consider streamwise and cross-flow loads and their point of application as predicted by BEM. The point of application of the force varies with TSR because the radial variation of thrust load on the blades varies with TSR. This is shown in Fig. 10 with a free stream velocity is 0.8 m $s^{-1}$. From these graphs it can be seen that in the cross-flow direction the root bending moment does not exceed 10 Nm and that the lever arm length is between 250 and 290 mm. From Fig. 9, this load configuration corresponds to an offset of approximately −0.7 Nm. Superimposing this offset to the streamwise calibration error plotted in Fig. 8 yields the overall estimated measurement error and is plotted in Fig. 11.

For low streamwise root bending moments and short lever arm lengths, the relative error is significant (above 25%). However, according to the BEM computations (Fig. 10) this load configuration is not expected for tip speed ratio (TSR) values above 3, which is the main operating region of interest for the model. In that TSR range, the streamwise lever arm length varies between 325 and 340 mm and the associated root bending moment is above 20 Nm. This corresponds in Fig. 11 to an overall relative error below ±5% which tends to decrease as root bending moment values increase. It can also be seen from Fig. 11 that the relative error is not symmetrical with respect to zero and that their is a slight bias for the transducer to underestimate loads.

Overall the measurement error inferred from calibration are below ±5% and they are in line with the FEA predictions over the operating region of interest of the turbine model.

### 5.3. Slipring and cabling

The torque and thrust transducer and the root bending moments sensors are all rotating with the turbine shaft but their

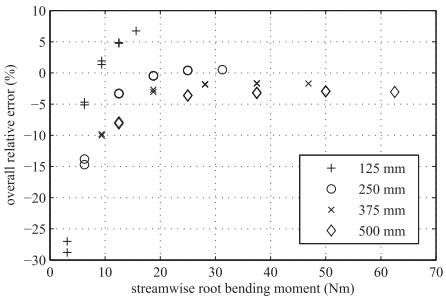


**Fig. 11.** Estimate of the overall relative error in root bending moment measurement as a function of streamwise loads. The different markers are associated with different lever arm length at which the force is applied.

cabling needs to be eventually routed through the non moving part of the nacelle. This is achieved using a through bore slipring whose arrangement is shown in Fig. 12. The slipring model used is an AC6349-18 made by the company Moog Components Group and it has 18 circuits.

To make it possible to disassemble the model easily, the cable coming out of the torque and thrust transducer could not be directly soldered to the slipring and a connector was used instead. Given the tight space requirement a high density circular micro connector with 16 ways manufactured by Omnetics was used. (see close-up in Fig. 12).

To avoid sensor signals being polluted by electromagnetic noise from the motor/generator or from the environment, signal cables were wherever possible screened cable (with tinned copper braid).

### 5.4. Data acquisition system

The data acquisition system is based on a National Instruments CompactDAQ USB chassis (cDAQ-9174). A digital I/O module (NI 9401) is used to log the encoder signal generated by the motor (see section 6 for more detail). The strain gauge bridge amplifiers used with all sensors provide current signal (4–20 mA) rather than voltage as it is more resilient to electromagnetic interference. A current analogue input module (NI 9203) is therefore used to log these.

To reduce further the impact of electromagnetic interferences onto measured signals, the data acquisition system is enclosed in a grounded metal cabinet and special care was taken in grounding the screen of the signal cables at their point of entry into the cabinet. Moreover, opto-isolators are used to electrically decouple the motor encoder signal output by the motor drive from the data acquisition system. The data acquisition cabinet can be seen in Fig. 13.

## 6. Drive system

Resistance to the torque induced by the flow onto the rotor is provided by a brushless permanent magnet servo motor. This type of electrical machines was preferred over a generator because a wide range is readily available and because they are highly controllable in speed and in torque with an off the shelf motor drive. Their drawback is that they have poor efficiency when operating as generators but electricity production is not the purpose of the model.

The motor torque specifications were inferred from BEM predictions. The other main requirement was the form factor. The hub and nacelle diameter were originally selected to be around 10% of the rotor diameter to minimise influence on the rotor wake. The motor length however is not critical. In the end the diameter requirement had to be relaxed to find a machine with suitable torque rating and consequently, as can be seen in Fig. 1, the back of the nacelle has a larger diameter (160 mm) than the front (120 mm).

The motor used is a 145ST4M017 model made by the company Alxion (www.alxion.com). It is 145 mm in diameter and 213 mm long (plus shaft). Its continuous torque rating is 26 Nm and the maximum peak torque is 110 Nm. It is fitted with a resolver whose signal is used as an input to the speed control loop but also to record the rotor angular position with the data acquisition system. Fig. 12 shows the turbine nacelle stripped of its waterproofing sleeves. The motor can be seen on the left.

Given that the motor operates most of the time as a generator and with therefore a poor efficiency, cooling was an important design consideration. The flow of water around the nacelle provides excellent cooling but it is not directly in contact with the motor body. The motor waterproofing sleeve is therefore made of aluminium alloy which as a good thermal conductivity. The air gap between the motor and the sleeve is kept to minimum (0.5 mm radially) to minimise thermal insulation between the two components. The sleeve is black anodised to absorb radiated heat better.

The motor is powered by three phase 400 VAC mains supply through a four quadrant drive which is capable of operating the motor as a break/generator and which can dump the generated electricity into a recovery resistor located next to the drive. In

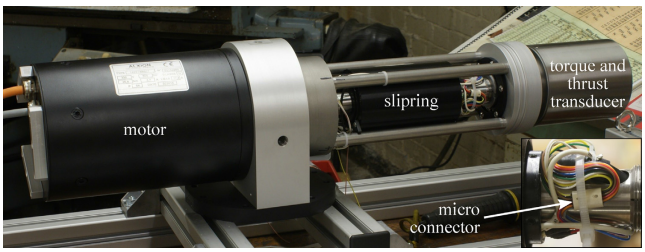


**Fig. 12.** Turbine drive train. The main picture shows the nacelle stripped of its waterproofing sleeves with the torque and thrust transducer, the slipring with the shaft going through and the motor. The close-up picture shows the connection between the cable coming out of the shaft and the rotor of slip ring.

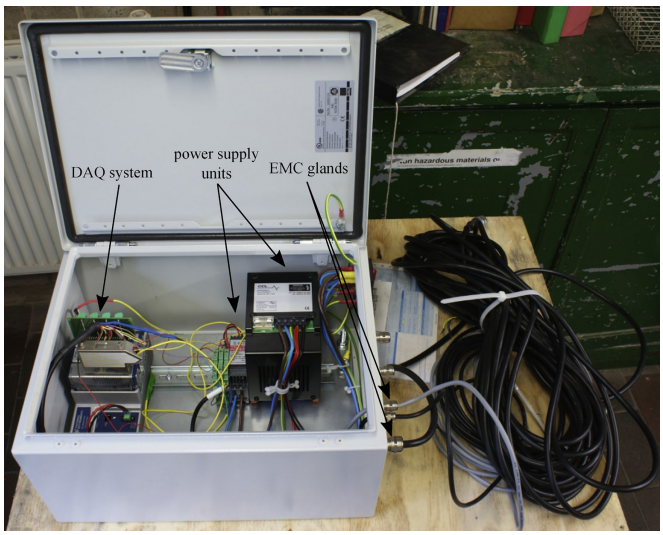


**Fig. 13.** Data acquisition cabinet with the CompactDAQ chassis on the left and power supplies on the right. On the right of the cabinet, signal cables are routed through EMC glands.

addition to a standard miniature circuit breaker (MCB), the drive supply circuit is also fitted with a 30 mA residual current device (RCD) to make the system trip in case of accidental current leakage which could arise from water ingress into the motor or its wiring. The RCD is an important safety feature as accidental electrical connection between the motor circuitry and the water of the tank is a potential hazard for operators. The electrical cabinet containing the motor drive and associated supply circuit is shown in Fig. 14.

## 7. Initial tests and measured turbine characteristics

Initial measurements of loading and wake due to turbulent flow and waves were carried out at the IFREMER flow recirculating flume in Boulogne-sur-Mer, France. The flume has a usable section 18 m long, 4 m wide and 2 m deep. It is fitted with a two-dimensional laser Doppler velocimetry (LDV) system mounted on a two-axis automated gantry. More information on the IFREMER

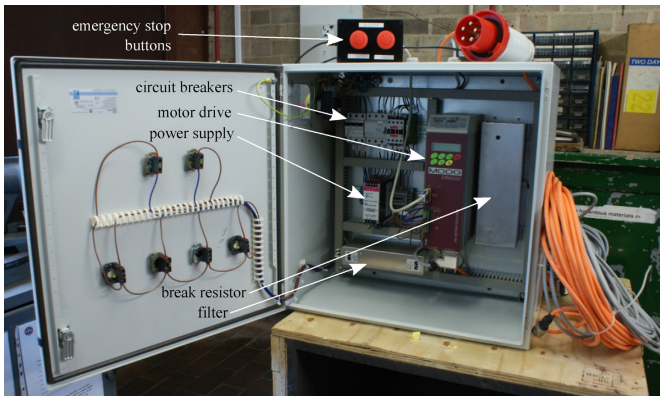


**Fig. 14.** Drive cabinet and its main components.

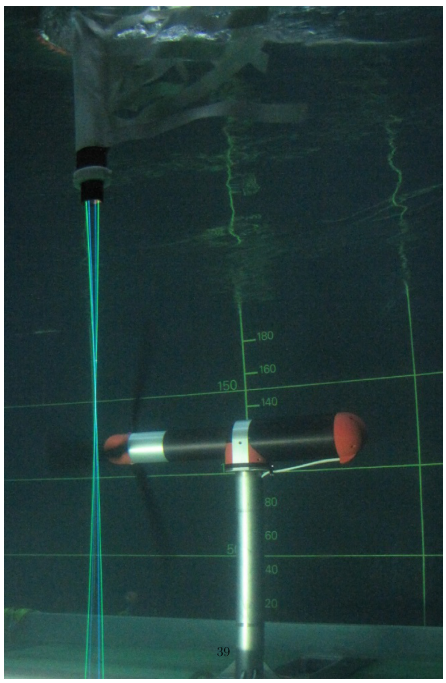

**Fig. 15.** Turbine model being tested at the IFREMER flume with the LDV system on the left.

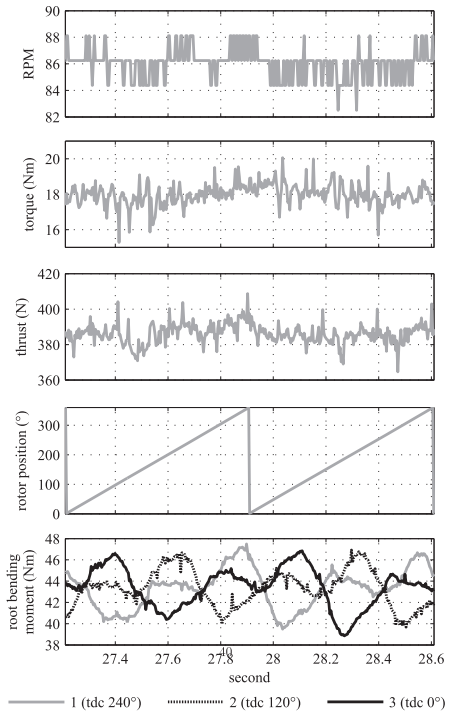


**Fig. 16.** Time series of turbine model sensors. The legend at the bottom only applies to the bottom graph. It indicates, for each blade, indexed 1 to 3, the rotor angular position when it is at top dead centre.

flow facility can be found in Ref. [14]. Fig. 15 shows the turbine being tested with LDV system measuring flow velocity in the turbine wake.

Fig. 16 shows time series of all the sensors of the model for a test in a mean flow velocity of 0.81 m $s^{-1}$ at TSR 6.75 (86 rpm). Sensors were sampled at 256 Hz and are all synchronised as they were all recorded simultaneously over different channels of the same data acquisition system. The measurements shown are a short interval from the overall time series focusing on two full rotations of the rotor. Rotational speed was computed by differentiating with respect to time the rotor angular position reported by a digital encoder signal. This explains the 'digital aspect' of the time series of rotational speed. The bottom graph shows the root bending moment of the blades. Each blade is referred to in the legend by its index and by the rotor angular position when the blade is at top dead centre (denoted 'tdc'). It can be seen that the root bending moment time series for each blade is periodic and that the period corresponds to a full rotation of the rotor. The phase shift between the three time series is about a third of the time taken for a full rotor rotation, consistent with 120° blade separation. Finally a dip in root bending moment is visible for each blade when close to (but not exactly at) bottom dead centre (corresponding to a rotor position of 60° for blade 1, 300° for blade 2 and 180° for blade 3). This is associated with the shadowing effect of the turbine tower whose centreline is located 0.4 rotor diameter (0.4D or 486 mm) downstream of the rotor plane.

To characterise performance and confirm the operating range of angular speeds, measurements were initially obtained of blade and rotor loading due to turbulent flows with 3% and 12% turbulence intensity (see Germain [14]) over a range of tip speed ratios. Measurements were subsequently obtained for the low turbulence case with following waves. The measured variation of mean and standard deviation of thrust $C_T$ and power $C_P$ coefficient is shown in Fig. 17. These are computed from the experimental measurements as follows:

$$C_T = \frac{T}{\frac{1}{2}\rho U_0^2 A} \text{and} \quad C_P = \frac{Q\omega R}{\frac{1}{2}\rho U_0^3 A} \tag{1}$$

where $T$ is rotor thrust in N, $\rho$ is water density in kg $m^{-3}$, $U_0$ the free stream velocity in m $s^{-1}$, $A$ the rotor area in $m^2$, $Q$ is the rotor torque

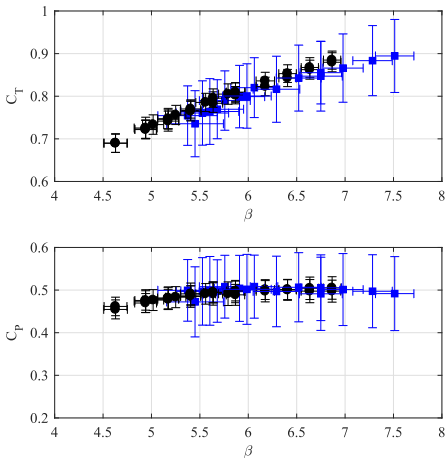


**Fig. 17.** Variation of thrust coefficient (top) and power coefficient (bottom) with tip speed ratio ($\beta$). Mean values (markers) and standard deviation of both coefficients and tip-speed ratio shown for ambient flow with turbulence intensity of 3% (black circle (●) and range) and 12% (blue square (■) and range). (For interpretation of the references to colour in this figure legend, the reader is referred to the web version of this article.)

in Nm, $\omega$ the rotational speed of the rotor in rads$^{-1}$ and $R$ the rotor radius in m. The coefficients were computed using mean values of $T$, $Q$ and $\omega$. The free stream velocity $U_0$ used was the mean flow velocity at hub height in the absence of the turbine. For low turbulence thrust and power vary with a standard deviation of 3–5% of the mean. For high turbulence mean coefficients are slightly reduced due to the increased range of tip-speed ratio and standard deviation increases to 10% and 18% for thrust and power respectively.

A bed mounted support structure was employed to minimise disruption to propagating waves and to facilitate measurement of the near-wake region. An example of the wake velocity profiles measured for onset turbulence of 12% is shown in Fig. 18. The rate of wake expansion is lower in the vertical direction than horizontal due to closer proximity of free surface (at $z/R = 1.67$) than flume wall (at $y = 2.33R$). This indicates a nearly axisymmetric form as observed for comparable depth to diameter ratio at smaller geometric scale [31], although expansion rate may be expected to differ with tip vortex strength (e.g. Ref. [21]) and ambient turbulence.

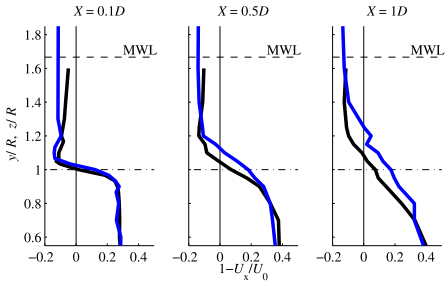


**Fig. 18.** Variation of normalised streamwise velocity along both transverse ($U_x(y/R)$, blue curve) and vertical ($U_x(z/R)$, black curve) axes intersecting the rotor axis. $y$ and $z$ are the transverse and vertical coordinates respectively. Mean water line (MWL) at $z = 1.67R$ and flume wall at $y = 2.33R$. Profiles shown for the positions 0.1$D$, 0.5$D$ and 1$D$ downstream of rotor plane at $X = 0D$. (For interpretation of the references to colour in this figure legend, the reader is referred to the web version of this article.)

## 8. Conclusions

Experimental tank testing is an essential tool to investigate the hydrodynamics of tidal turbines. It provides valuable data on rotor loading and wake development which are key to improving turbine design and tidal array layout. Acquisition of quality experimental data requires detailed consideration of instrumentation and system configuration throughout the design and manufacturing process. This study details the development of a highly instrumented tidal turbine model, developed for measurement of peak loading due to combined turbulent flow and waves. The main requirement for the model was therefore a high level of instrumentation. The rotor was designed to produce radial variation of thrust and torque to represent typical operation of a full-scale generic turbine. The model structure, instrumentation and drivetrain are described comprehensively and supplier details for key components are provided. The in-depth information provided about design processes and manufacturing techniques for this turbine and the instrumentation contribute to the state of the art in turbine model laboratory testing. Key features of the system include bespoke instrumentation for measurement of blade root bending and shaft loading and configuration of instrumentation outboard of the shaft seal to avoid parasitic losses and maximise signal quality. The novel approach to blade-root bending flexure design enables a compact design facilitating integration within a small diameter hub. This design approach is applicable to flexures for other applications.

The measurement capabilities of the model have been demonstrated through time-series of the signal produced by each of the sensors. Hydrodynamic characteristics of the rotor have been presented in the form of torque and thrust curves derived experimentally confirming similar mean performance but elevated variance of loading due to elevated onset turbulence. Initial measurements of wake velocity are also provided clearly indicating that depth constraint limits the rate of vertical expansion to lower than the rate of horizontal expansion. The commissioned system thus provides a platform for obtaining high fidelity data on blade, shaft and tower loading due to complex combinations of shear, turbulence and waves.

## Acknowledgements

This work was supported by the EPSRC via the Marine Challenge grant EP/J010235/1 (X-MED). The authors would like to thank Strathclyde University, Cardiff University, Southampton University and Edinburgh Designs Ltd in the UK and IFREMER in France for providing valuable insight of their experience with designing and making their own turbine models.

CAD files providing the outer geometry of the turbine including

the blades as well as the experimental data used to create figures 16, 17 and 18 can be downloaded from http://dx.doi.org/10.7488/ds/1707.

**Appendices**

*A. Waterproofing*

Some components of the turbine model such as the motor, bearings, the slipring and wiring are only designed to operate in a dry environment. It is therefore a vital requirement to keep some sections of the model and some of the electrical connections watertight.

*A.1. Seals*

In this model two types of seals are required: static and dynamic. The former are used to prevent water ingress between parts which need to be moved only for assembly and disassembly purposes. The latter are only used to for the shaft, to keep water away while it is rotating.

*A.1.1. Static seals.* The type of static seals used for this models is o-ring. They are cheap and widely available. Given the benign pressures (typically less than 1 bar), temperatures and fluid (water) they have to operate in for this application, standard nitrile buna rubber (NBR) o-ring were used.

O-ring can be either be mounted radially or axially. In the former case, the dimensions of both the o-ring groove and of the radial gap between the two parts to seal are important. With the latter approach, only the groove dimensions (and mainly its depth) matters which makes axial seal more reliable and therefore a preferred option. If radial seals must be used, reliability can be increased by having two of these seals in series.

Larger cord section o-rings offer a larger sealing area and as such tend to be more tolerant to dirt and to small scratches on the surface to seal. On the other hand, they take more space which is not always available when designing a compact model. For the turbine model described herein, o-rings with a cord diameter between 2 and 3 mm have been used. All o-ring seals were greased using Molykote 111 silicon grease made by Dow Corning.

It is highly recommended to use factory made circular o-rings rather than to manually glue o-ring cord to a specific circumference. The latter approach creates an uneven singularity in the o-ring over which sealing and strength are poor and which can lead to leaks. Factory made circular o-rings are available in a large range of circumferences and can be stretch by up to 3% to fit groove dimensions.

Groove and gap dimensions as well as required surface finish and stretch recommendations can be found in numerous o-ring handbooks, often published by o-ring manufacturers (see Ref. [26] for example).

*A.1.2. Dynamic seal.* The sealing of the rotating shaft was done using two lip seals made by Tai Tsuang Oil (TTO) similar to the one shown in Fig. 19. These are made of Viton and rated to 0.5 bar. Viton, as a material, is over specified for sealing just water at room temperature but these Viton lip seals come with their metal parts either fully covered with Viton (seal frame) or made of stainless steel (lip spring). This is important since the spring is exposed to the high pressure side i.e. the water side.

**Fig. 19.** Viton lip seal with visible stainless steel lip spring.

Two identical lip seals were installed in series along the shaft. This approach provides redundancy and makes it possible to lubricate the seals by having water resistant grease (3752 Almagard made by Lubrication Engineers) between the two lips. This design was inspired by that of shaft seals found in outboard trolling motors.

*A.2. Connectors*

Water ingress in model circuitry can lead to faults in the instrumentation signals which can be difficult do diagnose as the symptoms are not always those of a clear short-cut. In the power circuit of the motor, water leak can have dramatic consequences for the model and can potentially be dangerous if the voltage is high. Waterproof electrical connectors therefore need to be carefully chosen.

Standard IP68 connectors are not designed for immersion over long durations, especially for depths below 1 m. Rubber moulded marine underwater connectors on the other hand can withstand pressure of tens of bars but tend to be bulky and expensive. Lemo W series connectors have been found to be a suitable compromise between the two above. They feature two o-rings arranged in series which are compressed axially.

*A.3. Moisture absorption*

Moisture inside sealed containers kept underwater can condense and have severe adverse effects on electrical components. This issue can easily be addressed by fitting bags of silica gel inside the waterproof housings to absorb moisture. In rotating waterproof compartments or in compartments containing moving parts, the bags should be securely fastened, using elastic band for example. Some types of silica gel change colour when saturated with moisture. It is recommended to use these as they also provide a way to detect moisture ingress.

*B. Manufacturing*

Most metal parts are made of aluminium alloy (grade 6082T6) with some made of stainless steel (grade 304) for extra stiffness and

strength. Conventional and CNC machining were used for most parts.

The turbine tower (see Figs. 1 and 15) is made of stainless steel 304. The two flanges were first welded on either side of the tube and were then machined to ensure that their respective outside face are well parallel to each other.

The most challenging parts to make were the blades. They were CNC machined from solid metal. The machine used was a three axis CNC mill. The blades were machined in three stages:

1. A bar of rectangular section was first machined to accurate dimensions. Locations and tapped holes on what was to become the face of the blade root were machined. Holes were also made just beyond what was to become the blade tip.
2. The bar was laid flat on the mill bed and held at a precise location with a special jig using the location holes of the bar. The first side of the blade profile was then machined (see Fig. 20a).
3. The bar was flipped over and the second side of the blade profile was machined (see Fig. 20b).

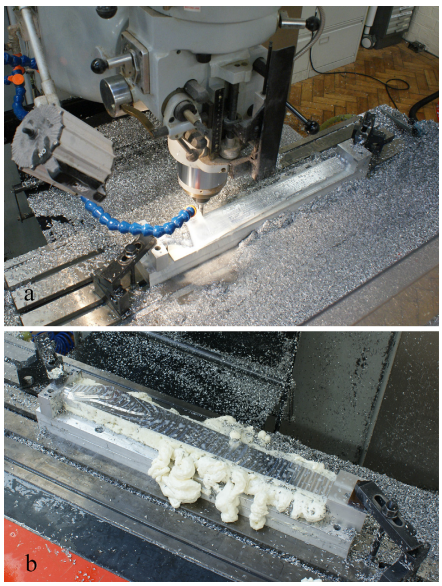


**Fig. 20.** CNC machining of turbine blade. (a) shows machining of the first side and (b) shows the set-up for machining of the second side with foam packing.3

When machining the first side, the part is supported all along its span by the material underneath but once it has been flipped onto its other side, it is only supported underneath at the root and at the tip. This brings about a lack of rigidity which in turns leads to vibration during machining. Packing the underneath of the part with expanding polyurethane foam (of the type used for building insulation) was found to provide sufficient support to reduce vibrations to an acceptable level. This type of foam comes in different hardness and it is recommended to use the hardest possible. To prevent the foam from sticking to the parts, these were protected by cling film. After machining, the blades were hand polished to remove the ridges left by the ball nose cutter. The completed blades can be seen in Fig. 21.

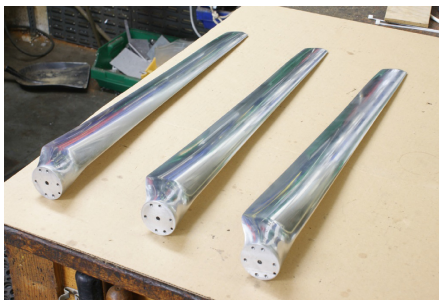

**Fig. 21.** Completed turbine blades.4

The initial design was to manufacture blades of stainless steel 304 to maximise rigidity. However, due to time constraints, the initial set of blades was manufactured from aluminium alloy 6082T6 which is much faster to machine. According to the FEA analysis, this increases the maximum blade tip deflection from 4.2 mm to 11.5 mm, which is still within 2% of the blade radius and was therefore deemed acceptable. All the aluminium parts were anodised to improve their corrosion resistance. Hard anodising was used except of the parts with tight tolerances. For these, standard anodising, whose growth is smaller, was used.

### *C. Issues encountered and further improvements*

#### *C.1. Rotational speed instability*

The initial tests of the turbine model were overall successful but some minor issues were encountered. The most serious one was an instability in the turbine rotational speed. This phenomenon only occurred for specific combinations of flow and rotational speeds. Running the turbine at these rpm values but in the absence of flow did not lead to instability which suggests that the phenomenon has to do with the interaction between hydrodynamics and motor control. In the most severe instances, as the rotor was spinning normally, in the direction induced by the flow, it would abruptly start spinning in the opposite direction for few degrees and then sharply go back to the 'correct' direction for about half a turn before reversing direction for few degrees and so on. The only way to break this cycle was to change either flow or rotational speed. Those jerky oscillations caused significant dynamic loads which the force sensors had not been designed to withstand. The root bending moment transducers were eventually damaged beyond use.

Two steps are currently being taken to address this issue.

- The control parameters of the motor drive are to be optimised. The idea is to test the model with all its force sensors replaced by non-instrumented structural dummies. This way the control parameters can be explored comprehensively with no risk of damaging the sensors.
- New flexures, to make the root bending moment transducers more robust, have been manufactured out of stainless steel,

which will reduce by a factor of about three the level of strain experienced by the stain gauges for the same load. It will also reduce the sensor sensitivity by the same factor but this can be partly compensated by increasing the gain of the strain gauge bridge amplifiers.

### C.2. Water ingress detector

Because of time constraints it was not possible to fit the turbine model with water ingress detectors. Although the model did not leak during these initial tests, given the potentially dramatic consequences of water ingress, such detectors are being developed. They consist of two strips of thin (about 0.2 mm) stainless steel sheet glued inside and along the length of the water proofing cylindrical sleeves. They are glued using double sided tape which ensures electrical insulation between the strips and the sleeves on top of the insulation already provided by the anodising. The smaller the gap between the strips, the better as long as they are not touching. Even small drops of water in that gap will create some electrical conductivity between the two strips. The fact that the strips stretch over the whole length of the sleeve provides an earlier leak detection than if the two contacts were located only at one point.

## References


[1] I. Abbot, A. Von Doenhoff, Theory of Wing Sections, Dover Publications, 1959.
[2] A. Bahaj, W. Batten, G. McCann, Experimental verifications of numerical predictions for the hydrodynamic performance of horizontal axis marine current turbines, Renew. Energy 32 (15) (2007a) 2479–2490.
[3] A. Bahaj, W. Batten, A. Molland, J. Chaplin, Experimental Investigation into the Hydrodynamics Performance of Marine Current Turbines. Tech. Rep. ISSN 1747-0544, University of Southampton, 2005 sustainable Energy Series Report 3.
[4] A. Bahaj, A. Molland, J. Chaplin, W. Batten, Power and thrust measurements of marine current turbines under various hydrodynamic flow conditions in a cavitation tunnel and a towing tank, Renew. Energy 32 (3) (March 2007b) 407–426.
[5] T. Carlson, B. Watson, J. Elster, A. Copping, M. Jones, M. Watkins, R. Jepsen, K. Metzinger, Assessment of Strike of Adult Killer Whales by an Openhydro Tidal Turbine Blade. Tech. Rep. PNNL-22041, Pacific Northwest National Laboratory, 2012.
[6] J.A. Clarke, G. Connor, A.D. Grant, C.M. Johnstone, Design and testing of a contra-rotating tidal current turbine, Proc. Institut. Mech. Eng. Part A J. Power Energy 221 (2) (Jan. 2007) 171–179. URL, http://pia.sagepub.com/lookup/doi/10.1243/09576509JPE296.
[7] W. Collier, S. Way, Full-scale validation study of a numerical tool for the prediction of the loading and hydrodynamic performance of axial flow tidal turbines, in: 10th European Wave and Tidal Energy Conference (EWTEC 2013). Aalborg, Danemark, 2013.
[8] T. de Jesus Henriques, S. Tedds, A. Botsari, G. Najafian, T. Hedges, C. Sutcliffe, I. Owen, R. Poole, The effects of wave-current interaction on the performance of a model horizontal axis tidal turbine, Int. J. Mar. Energy 8 (2014) 17–35.
[9] D. a. Doman, R.E. Murray, M.J. Pegg, K. Gracie, C.M. Johnstone, T. Nevalainen, Tow-tank testing of a 1/20th scale horizontal axis tidal turbine with uncertainty analysis, Int. J. Mar. Energy 11 (Sep. 2015) 105–119. URL, http://linkinghub.elsevier.com/retrieve/pii/S2214166915000259.
[10] E. Fernandez-Rodriguez, T. Stallard, P. Stansby, Experimental study of extreme thrust on a tidal stream rotor due to turbulent flow and with opposing waves, J. Fluids Struct. 51 (December 2015) (2014) 354–361.
[11] P.W. Galloway, L.E. Myers, A.S. Bahaj, Quantifying wave and yaw effects on a scale tidal stream turbine, Renew. Energy 63 (2014) 297–307.
[12] C. Garrett, P. Cummins, The power potential of tidal currents in channels, Proc. R. Soc. A Math. Phys. Eng. Sci. 461 (2060) (2005) 2563–2572.
[13] B. Gaurier, G. Germain, J. Facq, C. Johnstone, A. Grant, a.H. Day, E. Nixon, F. Di Felice, M. Costanzo, Tidal energy "Round Robin" tests comparisons between towing tank and circulating tank results, Int. J. Mar. Energy 12 (2015) (2015) 87–109.
[14] G. Germain, Marine current energy converter tank testing practices, in: 2nd International Conference on Ocean Energy (ICOE 2008). No. October. Brest, France, 2008, pp. 2–7. URL, http://archimer.ifremer.fr/doc/00022/13366/.
[15] M.O.L. Hansen, Aerodynamics of Wind Turbines, second ed., Earthscan, 2008.
[16] C. Hill, V.S. Neary, B. Gunawan, M. Guala, F. Sotiropoulos, U. S. Department of Energy Reference Model Program RM1 : Experimental Results. Tech. Rep. SAND2014–18783R, Sandia National Laboratories, 2014. URL, http://energy.sandia.gov/download/24671/.
[17] P. Jeffcoate, B. Elsaesser, T. Whittaker, C. Boake, Testing tidal turbines - part 1: steady towing tests vs tidal moored tests, in: Proceedings of the International Conference on Offshore Renewable Energy. Glasgow, UK, 2014.
[18] N. Kolekar, A. Banerjee, Performance characterization and placement of a marine hydrokinetic turbine in a tidal channel under boundary proximity and blockage effects, Appl. Energy 148 (2015) 121–133. URL, http://www.sciencedirect.com/science/article/pii/S0306261915003360.
[19] E.E. Lust, L. Luznik, K.A. Flack, J.M. Walker, M.C. Van Benthem, The influence of surface gravity waves on marine current turbine performance, Int. J. Mar. Energy 3–4 (2013) 27–40.
[20] J. McNaughton, S. Harper, R. Sinclair, B. Sellar, Measuring and modelling the power curve of a commercial-scale tidal turbine, in: Proceedings of 11th European Wave and Tidal Energy Conference. Nantes, France, 2015.
[21] S. McTavish, D. Feszty, F. Nitzche, An experimental and computational assessment of blockage effects on wind turbine wake development, Wind Energy 17 (2014) 1515–1529. URL, http://onlinelibrary.wiley.com/doi/10.1002/we.1648/full.
[22] Measurements Group, Strain Gage Based Transducers, Their Design and Construction, Measurements Group, Raleigh, USA, 1988.
[23] I. Milne, A. Day, R. Sharma, R. Flay, Blade loads on tidal turbines in planar oscillatory flow, Ocean Eng. 60 (Mar. 2013) 163–174. URL, http://linkinghub.elsevier.com/retrieve/pii/S0029801812004465.
[24] P. Mycek, B. Gaurier, G. Germain, G. Pinon, E. Rivoalen, Experimental study of the turbulence intensity effects on marine current turbines behaviour. Part I: one single turbine, Renew. Energy 66 (June 2014) 729–746.
[25] L.E. Myers, A.S. Bahaj, Experimental analysis of the flow field around horizontal axis tidal turbines by use of scale mesh disk rotor simulators, Ocean Eng. 37 (2–3) (2010) 218–227.
[26] NewDealSeals, The World's Best o-ring Handbook. Tech. Rep, NewDealSeals, 2015. URL, http://newdealseals.com/en/brochures/14/o-ring-handbook/7/o-ring-technical-handbook.html.
[27] T. Nishino, R.H.J. Willden, Effects of 3-D channel blockage and turbulent wake mixing on the limit of power extraction by tidal turbines, Int. J. Heat Fluid Flow 37 (2012) 123–135, http://dx.doi.org/10.1016/j.ijheatfluidflow.2012.05.002. URL.
[28] D.R. Noble, T. Davey, H.C.M. Smith, P. Kaklis, A. Robinson, T. Bruce, Characterisation of spatial variation in currents generated in the FloWave ocean energy research facility, in: 11th European Wave and Tidal Energy Conference. Nantes, France, 2015.
[29] C.C. Perry, H.R. Lissner, The Strain Gage Primer, McGraw-Hill, 1955.
[30] R. Roark, W. Young, Roark's Formulas for Stress and Strain, McGraw-Hill, 1989.
[31] T. Stallard, T. Feng, P. Stansby, Experimental study of the mean wake of a tidal stream rotor in a shallow turbulent flow, J. Fluids Struct. 54 (2015) 235–246.
[32] S.C. Tedds, I. Owen, R.J. Poole, Near-wake characteristics of a model horizontal axis tidal stream turbine, Renew. Energy 63 (2014) 222–235.